Fast-Forward Full-Duplex Strategies to Mitigate Reactive Jamming Attacks on Low-Latency Communication

A THESIS

submitted by

VIVEK CHAUDHARY

in fulfillment of the requirements of the degree

of

DOCTOR OF PHILOSOPHY

DEPARTMENT OF ELECTRICAL ENGINEERING
INDIAN INSTITUTE OF TECHNOLOGY DELHI.

SEPTEMBER 2022

CERTIFICATE

This is to certify that the thesis titled **Fast-Forward Full-Duplex Strategies to Mitigate Reactive Jamming Attacks on Low-Latency Communication**, submitted by **Vivek Chaudhary**, to the Indian Institute of Technology, Delhi, for the award of the degree of **Doctor of Philosophy**, is a bona fide record of the research work done by him under my supervision.

The contents of this thesis, in full or in parts, have not been submitted to any other Institute or University for the award of any degree or diploma.

Prof. Harshan Jagadeesh
Thesis Supervisor
Department of Electrical Engineering
Indian Institute of Technology, Delhi
Hauz Khas New Delhi 110016

Place: New Delhi

ACKNOWLEDGEMENTS

This thesis would not have been possible without the help of some fantastic people around me. I take this opportunity to thank them for making my stay at IIT Delhi memorable and enjoyable.

First, I would like to thank my advisor, Prof. Harshan Jagadeesh, for his tremendous patience, timely advice and support throughout my spell as a graduate student. He has given me invaluable insights into our research work, taught me the art of problem-solving, along with helping me to strive for an excellent work-life balance. His inspiring thoughts and the constant pursuit of excellence and perfection have made me a better person and a researcher.

I thank my student research committee members, Prof. Shiv Dutt Joshi, Prof. Saif Khan Mohammed, and Prof. Prabhu Babu, for their valuable comments and suggestions. Their invaluable comments and suggestions have helped me substantially streamline my work and progress.

Life as a PhD student is incomplete without a technically interactive and intellectually vibrant lab. I take this opportunity to thank my colleagues, Kamal Agrawal, Anand Jee, Amit Patel, Deebakshi Dey, Amar Mishra, Manish Bansal, and Rohit Joshi, who have always motivated me during the course of my journey at IIT Delhi.

The PhD duration is long and tends to have so many highs and lows. I thank my friends, Anuj Jain, Ritij Chaudhary, Vishal Patel, Aakar Srivastav, Shashank Shekshar, Rahul Neema, Chetan Singh, Abhinay Pardeshi, Anuj Srivastav, Anand Jee, Abhishek Shukla, and Himanshu Rai for being with me in my lows and celebrate my high times.

I would also like to thank my cycling mates, Anand Jee, Himanshu Rai, Kamal Agrawal, Kalyan Dash, and Dr Amit Prasad, for memorable cycling rides on weekends exploring the capital city.

Finally, last but not least, I am genuinely indebted to my parents, Smt. Sudha Singh and Dr Vijay Singh, and my brother, Abhishek, for believing in me and helping me

through my PhD program. I sincerely thank my friend Preeti for always being by my side and supporting me during difficult times. Thanks for always being there for me.

I once again thank everybody from the bottom of my heart.

ABSTRACT

In the context of 5G/5G+, securing wireless links becomes crucial due to the services offered by the applications running on these networks. Since some of these applications have mission-critical data with low-latency constraints, a slight delay in the reception could have undesirable effects—for instance, autonomous vehicles, unmanned aerial vehicles, and the industrial internet of things. The low-latency constraints of these applications attract a plethora of attacks, mainly jamming attacks since these attacks are easy to execute. Moreover, radio architecture advancements have also created a new class of jammers, known as reactive jammers. Unlike a traditional jammer, a reactive jammer may monitor the network for possible countermeasures and change its attacking strategies based on its observations. While countermeasures like frequency hopping are known to provide reliable communication amidst traditional jamming attacks, using them against reactive jammers might not offer the anticipated outcome. Thus, this thesis aims to provide new mitigation strategies against reactive jammers to facilitate reliable, low-latency communication to the victim with the help of a nearby full-duplex helper. Under the framework of fast-forward full-duplex strategies, we design constellations for the victim and the helper that minimize the error rates at the destination. In particular, we solve optimal constellations at the victim and the helper, subject to average energy constraints at the victim and the helper, under various channel conditions and radio architectures at the full-duplex helper. In addition to minimizing the error rates, we also analyze the covertness of our proposed schemes in deceiving a family of countermeasure detectors deployed by the reactive jammer.

TABLE OF CONTENTS

LIST OF TABLES

LIST OF FIGURES

ABBREVIATIONS

DoS	Denial of Service
SNR	Signal-to-Noise Ratio
MIMO	Multiple-Input Multiple-Output
WLAN	Wireless Large Area Network
FH	Frequency Hopping
DSSS	Direct Sequence Spread Spectrum
FDD	Frequency Division Duplex
FD	Full-Duplex
HD	Half-Duplex
CR	Cognitive Radio
CRN	Cognitive Radio Network
FDCA	Full-Duplex Cognitive Adversary
SI	Self-Interference
SIC	Self-Interference Cancellation
RSS	Received Signal Strength
CST	Carrier Sensing Time
PER	Packet Error Rate
RTS	Request to Send
CTS	Clear to Send
ACK	Acknowledgement
LoS	Line of Sight
ADC	Analogue to Digital Converter
DAC	Digital to Analogue Converter
LNA	Low Noise Amplifier
DSP	Digital Signal Processing
OFDM	Orthogonal Frequency Division Multiplexing
MAP	Maximum A Posteriori
FFFD	Fast-Forward Full-Duplex

OOK	On-Off Keying
ASK	Amplitude Shift Keying
PSK	Phase Shift Keying
CSI	Channel State Information
JDD	Joint Dominant Decoder
AWGN	Additive White Gaussian Noise
MAC	Multiple Access Channel
SC-F2HD	Semi-Coherent Fast-Forward Half-Duplex
SC-F2FD	Semi-Coherent Fast-Forward Full-Duplex
NC-FFFD	Non-Coherent Fast-Forward Full-Duplex
DT NC-FFFD	Delay Tolerant NC-FFFD
DASC-MF	Delay-Aware Semi-Coherent Multiplex-and-Forward
SC-MAC	Semi-Coherent Multiple Access Channel
NR	Newton Raphson

NOTATION

α,	Energy-splitting factor
$\gamma(\cdot,\cdot)$	Lower-incomplete Gamma function
$\Gamma(\cdot,\cdot)$	Upper-Incomplete Gamma function
$\Gamma(\cdot)$	Complete Gamma function
$Q(\cdot)$	Q-function
$\delta(\cdot)$	Dirac-delta function
$Q_1(\cdot,\cdot)$	Marcum-Q function
N_o	Noise variance
N_C	Receive antennas at Charlie
N_B	Receive antennas at Bob
$\mathbf{0}_{N_C}$	$N_C \times 1$ vector of zeros
$\mathbf{I}_{N_C}$	$N_C \times N_C$ Identity Matrix
$\max$	Maximum
$\min$	Minimum
$\mathbb{E}[\cdot]$	Expectation operator
$\mathbf{P}_{FA}$	Probability of false-alarm
$\mathbb{P}_{MD}$	Probability of miss-detection
Φ_{ij}	Probability of decoding bit-i and bit-j at Charlie
$(\cdot)^H$	Hermitian operator
σ_{AC}^2	Variance of Alice-to-Charlie link
σ_{AB}^2	Variance of Alice-to-Bob link
σ_{CB}^2	Variance of Charlie-to-Bob link
$\mathcal{CN}(\cdot,\cdot)$	Complex Normal distribution
$\bar{i}$	complement of i
$\ln(\cdot)$	Natural logarithm
λ	Residual SI
f_{AB}	Alice-to-Bob uplink frequency
f_{CB}	Charlie-to-Bob uplink frequency

$\mathcal{E}_{AB}$	Average energy level on f_{AB}
$\mathcal{E}_{CB}$	Average energy level on f_{CB}
h_{AB}	Rayleigh fading channel coefficient of Alice-to-Bob link
h_{CB}	Rayleigh fading channel coefficient of Charlie-to-Bob link
h_{AC}	Rayleigh fading channel coefficient of Alice-to-Charlie link
$I(X;Y)$	Mutual Information between X and Y

CHAPTER 1

INTRODUCTION

1.1 Overview

Communication has been an integral part of human lives since its inception. However, Marconi's experiment in 1895 laid the foundation and framework for the communication system we experience today. Since then, wireless communication has evolved at an unprecedented rate and is an essential aspect of our lives, thanks to a large number of connected devices around us. Technologies, such as polar codes [4, 5], Multiple-Input Multiple-Output (MIMO) [6–8], carrier aggregation [9], millimetre-wave [10], and non-orthogonal multiple access [11, 12] have greatly enhanced the quality and widespread connectivity of wireless communication. Because of these advancements, the vision of the internet of everything seems realizable.

The *Mathematical Theory of Communication* by Shannon [13] states that given a sufficiently long time and a sufficient number of channel usage, one can nearly achieve an error-free data transmission, where the channel capacity governs the transmission rate. However, the latency constraints in the 5G/5G+ wireless networks limit long transmission time and the number of channel usage. In particular, virtual/augmented reality (AR), public safety, factory automation, and autonomous vehicles have latency requirements of less than one-millisecond [14]. Thus, it is needless to say that latency is probably one of the most influential performance measures of 5G/5G+ [15]. Amongst the various use cases of low-latency applications, specific applications have strict latency constraints, and even a delay of a few milliseconds can have catastrophic effects. For instance, a self-driving car on the road must recognize other vehicles, pedestrians, bikes, and other objects from other vehicles or base stations in real-time. Therefore, while it is crucial to design physical layer solutions that provide reliable low-latency communication of symbols, securing these applications against adversaries is equally essential. In particular, it is necessary to secure these applications from adversaries which introduce a delay in the received messages at the intended base station. Denial of

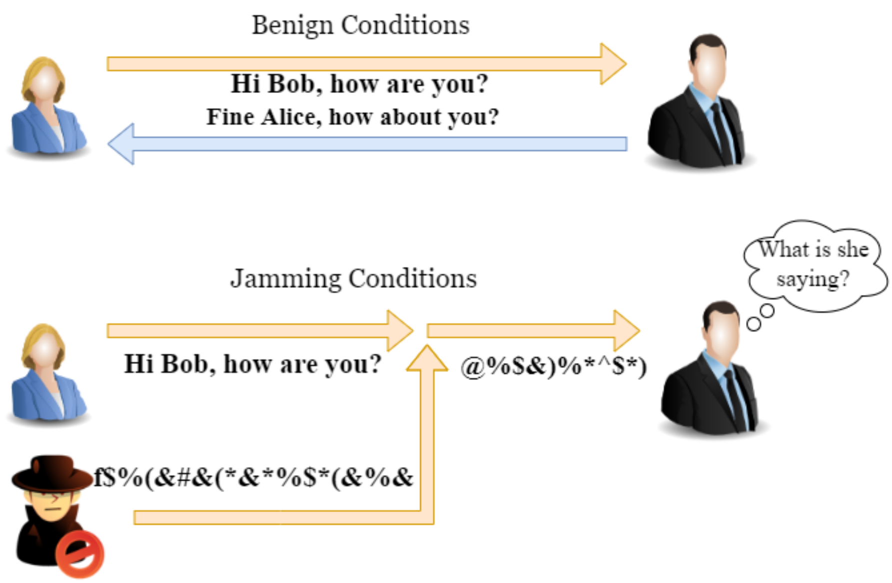

Figure 1.1: Pictorial representation of jamming.

Service (DoS) attack is a well-known threat wherein an adversary blocks a source from accessing the network using a radio built with off-the-shelf components [16]. One such specific form of DOS attack is the jamming attack, wherein the adversary injects jamming energy on the victim's frequency, thereby reducing the effective Signal-to-Noise Ratio (SNR) at the base station below the required threshold. As a result, the base station may not decode the victim's symbols at the first attempt, thus requiring multiple retransmissions leading to deadline violations. Jamming attacks are more preferred attack models due to the following reasons. Firstly, jamming attacks can be launched easily. For instance, a small USB dongle worth $10 is capable of emitting a jamming power of 100mW in 20MHz bandwidth below 6GHz. Such devices can easily disrupt the WiFi services in offices and homes [17]. Further, software defined radios such as USRP and WARP are more powerful and give more flexibility to the jammer. Secondly, jamming attacks can only be mitigated at the physical layer. This is because, during the jamming attack, the receiver is unable to decode the bits at the lower layers. Thus, any mitigation scheme at medium access control layer or higher are incapable of addressing the jamming attacks. Further, besides hampering decoding process at the destination, a jamming attacker can prohibit a legitimate user to access the network by keeping the channel busy. Thus, addressing jamming attacks on low-latency communication is crucial since the victim node must ensure timely delivery of symbols after implementing the countermeasures.

There are limited countermeasures against the jamming attacks. Thus, an attacker can leverage on these vulnerabilities to disrupt the communication. [18, 19] proposed Frequency Hopping (FH) based schemes to mitigate jamming attacks for Wireless Large Area Network (WLAN). In particular, [18] proposed FH based scheme for WiFi networks against all types of jammers and [19] proposed adaptive FH and window dwelling based countermeasures against reactive jammers [20]. Further, [21,22] proposed Direct Sequence Spread Spectrum (DSSS) based countermeasures against constant jamming attacks and frequency-sweeping jamming attacks [23]. Furthermore, [24–27] proposed MIMO mitigation schemes against reactive jamming attacks and constant jamming attacks. In particular, the solutions proposed in [24, 25] projected the received signal on a subspace orthogonal to the jamming signal. Whereas, the solution proposed in [26, 27] used multi-channel ratio decoding and jamming resilient synchronization. Further, [28, 29] proposed the use of an alternative road side unit to relay the traffic from the jammed region in vehicular networks. [30] proposed random channel hopping against primary user enumalation attack [31].

It is worthwhile to note that in most of the mitigation schemes discussed above, the victim vacates the jammed band and operates on a different frequency band, i.e., FH. Now consider a cognitive jamming adversary who besides jamming, can also measure the average energy level on the jammed band. As a result, if the victim node uses FH, then, it might detect the countermeasure owing to a significant drop in the average energy level of the jammed band. The detection may compel the adversary to execute the jamming attack on another frequency bands thereby guaranteeing degradation in the network performance, especially in a crowded network that do not have unused frequencies. Therefore, in order to mitigate this cognitive jamming adversary, a new framework is required to facilitate reliable communication of low-latency symbols of the victim node, and to engage the adversary to the jammed frequency band. This implies that the framework should force the adversary to observe identical network conditions before and after its implementation. If the mitigation scheme succeeds in achieving this objective, then we refer it as a covert scheme. This is because the threat model resembles the conventional setting of covert communication wherein the legitimate nodes must communicate with each other without getting noticed by a third-party warden [32]. Thus, the notion of cognitive jamming adversaries opens up problems on how to design countermeasures that ensure that the victim's symbols reliably reach the base station within the deadline, amidst the presence of a cognitive jamming adversary.

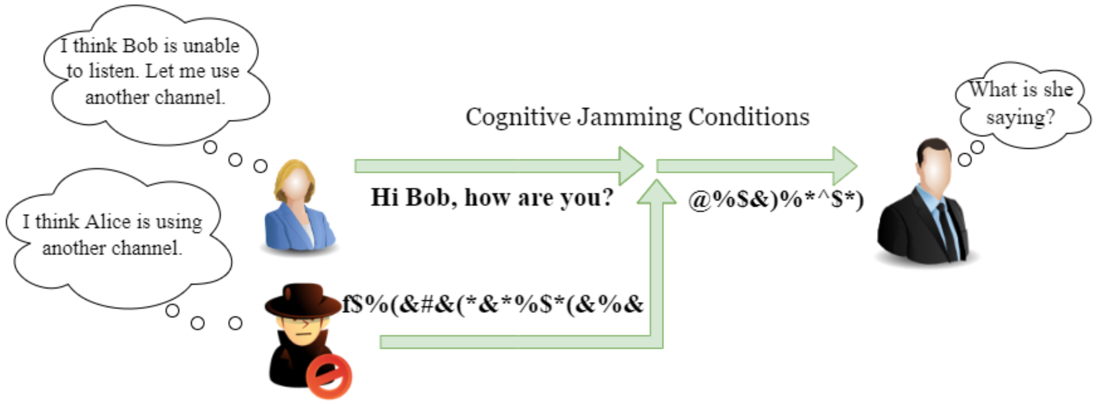

Figure 1.2: Pictorial depiction of cognitive jamming.

1.2 Objective and Scope of the Thesis

Consider a *crowded* wireless network wherein a number of nodes intend to communicate with a base station using Frequency Division Duplex (FDD) mode. The network is crowded since the nodes have used all the uplink frequencies, and no unused frequency is available. As shown in Fig. 1.3, let Alice be a single-antenna transmitter node, who wants to communicate her low-latency symbols to Bob on a frequency band centred around f_{AB}. Now, consider a reactive Full-Duplex Cognitive Adversary (FDCA), Dave, who wants to jam Alice's symbol to Bob. Due to Dave's sophisticated radio hardware, he is able to observe the network for possible countermeasures and based on his observations, he may change his attacking strategy. A straightforward reactive attacking strategy would be to randomly choose a frequency band and pour the jamming energy on it, thus, ensuring guaranteed degradation in the networks performance. Therefore, while it is necessary for Alice to communicate her low-latency symbols to Bob, the implemented countermeasure must be such that Dave is always engaged on the jammed band.

Within this network, also consider a node nearby Alice, Charlie, who is communicating his symbols to Bob on a frequency band centred around f_{CB}. Charlie is a Full-Duplex (FD) radio enabled node, capable of instantaneous manipulation of incoming symbols. The data requirements of Alice and Charlie are heterogeneous, such that Charlie transmits his symbols with arbitrary data-rate with relaxed latency constraints, whereas, Alice transmits her symbols with low data-rate. Towards mitigating the jamming attack from a reactive FDCA, this research explores possible solutions wherein Charlie assists Alice in evading jamming attack from Dave, while adhering to the strict

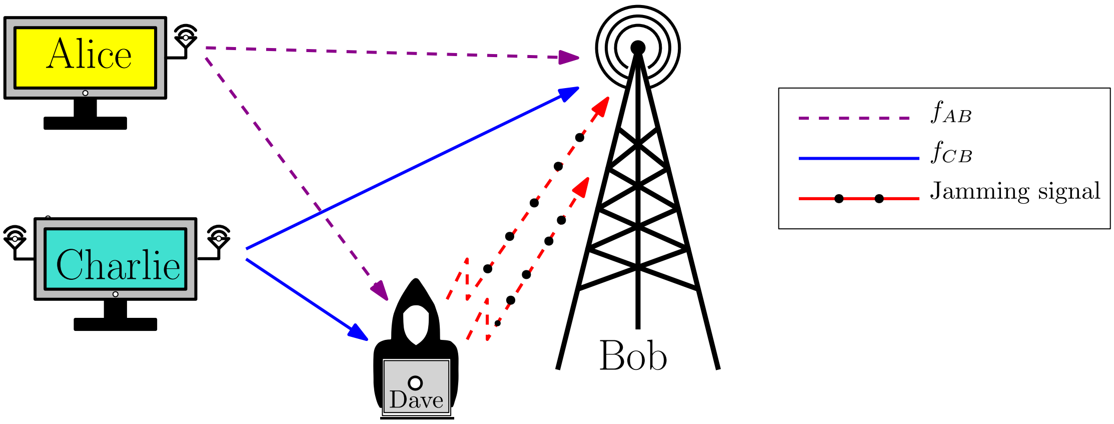

Figure 1.3: System model for jamming attack by a cognitive adversary.

latency constraints on Alice's symbols, subject to various channel conditions, the type of countermeasure detectors deployed by Dave, and Charlie's ability to instantaneously manipulate the incoming symbols. Through this research, we explore:

1. New mitigation strategies against reactive FDCA to facilitate reliable, low-latency communication to the victim with the help of a nearby FD helper.
2. New constellations designs for the victim and the helper that minimize the error rates at the base station. In particular, we design optimal constellations at the victim and the helper, subject to average energy constraints at the victim and the helper, under various channel conditions and also under various radio architectures at the FD helper node.
3. The ability of the proposed constellation designs in deceiving a family of countermeasure detectors deployed by the reactive cognitive jammer.

A detailed discussion on various types of jamming attacks, FD radios, cognitive radios, and FDCA is given in Chapter 2.

1.3 Contributions and Outline of the Thesis

The main contributions of this thesis in mitigating reactive jamming attacks are as follows.

Chapter 3, addresses a DoS attack on low-latency communication by an FDCA, armed with a perfect FD radio, such that it can simultaneously measure the average energy level on the victim's frequency band besides jamming it. Thus, the FDCA can detect FH-based countermeasures and subsequently change the target frequency band. To mitigate the adversary, we propose a fast-forward framework wherein the victim node seeks the assistance of a helper node in its vicinity to relay its symbols to the base station. In this chapter, we propose two cooperative relaying schemes: semi-coherent fast-forward half-duplex and semi-coherent fast-forward full-duplex relaying schemes, wherein the helper node can either work in Half-Duplex (HD) or FD mode depending on the distance between the helper and the jammer. In both schemes, the helper nodes instantaneously multiplex the victim's messages to its messages and forward them to the base station. In the former scheme, the victim continues its transmission on the jammed band, whereas the helper node overhears the victim's frequency band to multiplex their information in its frequency band. In the latter scheme, the victim and the helper node cooperatively pour fractions of their energies on both frequency bands to reliably communicate their messages on the helper's frequency band. Assuming the channel between the helper and the base station is slow-fading, this chapter presents an extensive analysis of the choice of the energy-splitting factor between the frequency bands, besides proving that both schemes successfully engage the adversary on the jammed frequency band. Contents of this chapter are published in [33–35].

With potential applications to short-packet communication in fast-fading channels, in Chapter 4, we address the transmission of low-latency messages in fast-fading channels under the presence of an FDCA. Unlike the adversary in Chapter 3, the FDCA in this chapter scans all the frequency bands to detect FH and repetition-coding across frequency based countermeasures. Subsequently, the adversary changes its target frequency band if it detects a countermeasure. To facilitate reliable communication amidst a strong adversary, we propose a non-coherent fast-forward full-duplex relaying scheme wherein the victim uses a helper in its vicinity to fast-forward its messages to the base station, in addition to ensuring that the countermeasures are undetected by the FDCA. Towards designing the constellations for the proposed scheme, we identify that existing non-coherent constellations for fast-fading channels are not applicable owing to the cooperative nature of the fast-forward scheme. As a result, we formulate an optimization problem of designing the non-coherent constellations at the victim and the helper such that the symbol-error probability at the base station is minimized. We theoretically analyze the optimization problem and propose several strategies to compute near-optimal constellations based on the helper's data-rate and fast-forwarding abilities. We show that the proposed constellations provide near-optimal error performance and help the victim evade jamming. Finally, we also prove the efficacy of the proposed schemes in deceiving the countermeasure detectors at the jammer. Contents of this chapter are published in [36–40].

In Chapter 5, we also examine a reactive jamming attack by an FDCA on the low-latency messages of a victim. However, in addition to the countermeasure detection mechanisms in Chapter 3 and Chapter 4, the FDCA in this chapter also measures the average energy level on all the frequency bands and changes its target frequency in an event of a detection. We highlight that the existing schemes against FDCA use relays with instantaneous FD radios to evade the attack. However, due to the limitation of the radio architecture of the FD helper, instantaneous forwarding may not be possible in practice, thereby leading to increased decoding complexity at the base station and a high detection probability at the adversary. Pointing at this drawback, we propose a delay-aware cooperative framework wherein the victim seeks assistance from a delay-aware FD helper to forward its messages to the base station within the latency constraints. In particular, we first model the processing delay at the helper based on its hardware architecture, and then propose two low-complexity mitigation schemes, wherein the victim and the helper share their uplink frequencies using appropriate energy-splitting factors. For both the schemes, we solve the optimization problems of computing the near-optimal energy-splitting factors that minimize the joint error rates at the base station. Finally, through rigorous analytical and simulation results, we show that the proposed schemes facilitate the victim in evading the jamming attack whilst deceiving the FDCA.

Finally, Chapter 6, concludes the works presented in Chapter 3, 4, and 5, and discuss the possible directions of the future research.

1.4 List of Publications

Proceedings

1. V. Chaudhary and J. Harshan, "Fast-Forward Relaying Scheme to Mitigate Jamming Attacks by Full-Duplex Radios," 2020 IEEE 31st Annual International Symposium on Personal, Indoor and Mobile Radio Communications, 2020, pp. 1-7, doi: 10.1109/PIMRC48278.2020.9217180.

2. V. Chaudhary and J. Harshan, "Non-Coherent Fast-Forward Relays for Full-Duplex Jamming Attack," 2021 IEEE Global Communications Conference (GLOBECOM), 2021, pp. 1-6, doi: 10.1109/GLOBECOM46510.2021.9685041.

3. V. Chaudhary and J. Harshan, "Whisper when under Attack: Delay Tolerant Fast-Forward Relays against Full-Duplex Jamming," 2022 14th International Conference on COMmunication Systems & NETworkS (COMSNETS), 2022, pp. 163-171, doi: 10.1109/COMSNETS53615.2022.9668596.

Journals

1. V. Chaudhary and H. Jagadeesh, “Fast-Forward Mitigation Schemes for Cognitive Adversary,” in IEEE Transactions on Cognitive Communications and Networking, vol. 7, no. 4, pp. 1304-1319, Dec. 2021, doi: 10.1109/TCCN.2021.3070582.

2. V. Chaudhary and H. Jagadeesh, “Constellation Design for Non-Coherent Fast-Forward Relays to Mitigate Full-Duplex Jamming Attacks,” in IEEE Transactions on Communications, vol. 70, no. 7, pp. 4755-4770, July 2022, doi: 10.1109/TCOMM.2022.3179412.

3. V. Chaudhary and H. Jagadeesh, “Low-Latency Communication using Delay-Aware Relays Against Reactive Adversaries,” (under review in IEEE Transactions on Communications).

CHAPTER 2

BACKGROUND

In this chapter, we discuss the background of the thesis, starting from a survey on jamming attacks on wireless communication in Sec. 2.1. We then introduce the basic working of the FD radios and the various Self-Interference Cancellation (SIC) techniques used to mitigate the Self-Interference (SI) in Sec. 2.2. Further, in Sec.2.3, we first discuss the working principle of Cognitive Radio (CRs) and then the need for FDCRs in the current wireless scenario. Finally, in Sec. 2.3.3, we discuss the notion of FDCA.

2.1 Wireless Jamming Attacks: A Survey

As already mentioned, the objective of a jamming adversary (also referred to as jammer) is to disrupt either the legitimate transmission or the reception (or both in some cases) by injecting unwanted noise using off-the-shelf radio devices. Thus, a jammer might continuously inject unwanted noise on a legitimate wireless link between two nodes to keep the link busy and degrade its performance. However, this jamming technique is energy inefficient from a jammer's viewpoint. However, the jammer can improve its energy efficiency by opportunistically pouring its jamming energy only when the target node transmits. Based on these attributes, a jammer can be categorised into five categories [41]:

1. Constant jammer;
2. Intermittent jammer;
3. Reactive jammer;
4. Adaptive jammer;
5. Intelligent jammer.

Here, the first four of the five jammers attack the physical layer of the protocol stack. In contrast, an intelligent jammer leverages the vulnerabilities in the higher layers of the protocol stack. In the subsequent sections, we will discuss these jamming attack models and their respective countermeasures in detail.

2.1.1 Constant Jammer

As already mentioned, a constant jammer continuously injects jamming noise on the legitimate link to reduce the SNR below the required threshold at the destination. Thus, requiring multiple retransmission from the sender node. Moreover, due to persistent jamming energy on the wireless link, a legitimate node always finds the link busy, thus, unable to access the link. Therefore, a constant jammer can degrade the communication between two legitimate nodes without specific channel information. However, due to constant injection of jamming energy, the constant jammer is energy inefficient.

In order to mitigate the constant jammer, one must first detect the presence of the jammer [41], [42]. There are several methods to detect the presence of a jammer, such as Received Signal Strength (RSS), Carrier Sensing Time (CST), and Packet Error Rate (PER). The RSS detector first collects several samples over a given observation period and computes the overall energy. The RSS detector then compares the cumulative energy to a predefined threshold. Since the received energy at the destination where the RSS detector is deployed is directly proportional to the jamming energy, the RSS detector decides the presence of the jammer when the cumulative energy is greater than the predefined threshold. Alternatively, one can also measure CST to determine the presence of a jammer. The basic idea behind CST measurement is that constant jamming energy keeps the channel busy, resulting in high CST. Additionally, one can also measure the number of unsuccessful packets decoded at the destination, denoted by PER. Generally, in the absence of jammer, PER is relatively low. Further, [43] showed that even in a very crowded network, PER greater that 0.2 is very unlikely. However, in the presence of the constant jammer, the receiver is overwhelmed by the jamming energy, resulting in PER close to one [43]. This serves as a detection mechanism at the destination.

On detecting the presence of the jammer, the legitimate nodes can deploy mitigation techniques to curb jamming. FH [18, 44, 45] is a well known technique to mitigate the jamming attack, wherein the victim node moves out of the jammed band and changes its carrier frequency based on a pseudo-random sequence, pre-shared between the victim and the destination.

2.1.2 Intermittent Jammer

Unlike the constant jammer, an intermittent jammer transmits the jamming signal in bursts [46]. Thus, an intermittent jammer transmits the jamming signal only for a specific time and keeps silent for the rest of the time. As a result, an intermittent jammer is more energy efficient than a constant jammer. Although this helps the jammer to save more energy, the jamming efficiency of the jammer degrades. Thus, from the jammer's viewpoint, it must choose an appropriate jamming duration that effectively degrades the performance of the legitimate nodes.

Similar to the constant jammer, one can use the RSS, CST, and PER-based techniques to detect the presence of the intermittent jammer. Further, one can again use FH to mitigate an intermittent jammer after the detection.

2.1.3 Reactive Jammer

A reactive jammer is an advanced version of the intermittent jammer as it first senses the transmission from the target node and then jams it [20,47]. Thus, unlike the intermittent jammer, which injects a jamming signal regardless of the transmission from the target node, a reactive jammer is more efficient in terms of energy and jamming. However, the jamming efficiency of the reactive adversary depends upon its sensing accuracy.

Detecting a reactive jammer is complex compared to the constant and the intermittent jammer. In particular, since the reactive jammer only transmits when it detects a transmission from the target node, the target node can still access the wireless channel. As a result, one cannot use CST-based techniques to detect the presence of the reactive jammer. However, RSS and PER-based techniques can still detect the presence of the reactive jammer.

One can use FH to effectively mitigate the reactive jammer, as discussed in the previous section. Besides FH, if the target node transmits its signal such that its communication is oblivious to the reactive jammer, the jammer will be unable to detect, thus, will be unable to jam the target node. DSSS [48] is a wideband transmission technique wherein the signal is transmitted such that its power spectral density is close to the noise floor. Thus, if the target node transmits its signal using DSSS, the reactive jammer cannot detect the signal transmission.

2.1.4 Adaptive Jammer

Adaptive jammers are an intelligent class of jamming adversaries that regulate their jamming energy based on the knowledge of RSS between the target node and the destination [19]. As a result, if the RSS between the target node and the destination is relatively good, the jammer pours more jamming energy to disrupt communication. However, when the link between the target node and the destination is in a deep fade, a small or zero jamming energy is required to jam the link. Thus, as compared to its previous counterparts, the adaptive jammer is more energy and jamming-efficient. Nevertheless, it is essential to note that, since obtaining RSS is challenging for the jammer, adaptive jamming models serve as a robust baseline attack model.

Detecting an adaptive adversary poses serious challenges as the jammer continuously changes its jamming energy based on RSS knowledge. Further, CST-based techniques are ineffective in detecting an adaptive jammer similar to the reactive jammer. However, [49] proposed a combination of RSS and PER-based detection technique. In this joint detection method, a high RSS and PER indicate an adaptive jammer's presence.

Towards mitigating an adaptive jammer, [19] proposed two mitigation schemes: i) channel surfing and ii) spatial retreating. Unlike FH, in the channel surfing method, the target node and the destination move to a completely different transmission band. However, in the target spatial retreating solution, the target node moves out of the jammed area to escape the jamming. This requires the target node to localize the jammer [50].

2.1.5 Intelligent Jammer

Intelligent jammer leverages on the vulnerabilities of the upper layers of the protocols to jam the control packets instead of the data packets. Thus, an intelligent jammer is much stronger than all the previous jammers. Further, an intelligent jammer is more energy-and jamming-efficient. Within the framework of intelligent jammers, there are various types of jammers depending upon the control packets they jam, such as Request To Send (RTS) jammer, Clear To Send (CTS) jammer, and Acknowledgement (ACK) jammer. These attacks can be detected by monitoring the abnormalities in RTS, CTS, or ACK frames at the destination. [51] proposed a protocol hopping approach based on the game-theoretic framework to evade the intelligent jamming attack.

Unlike the above jammers, this thesis introduces a new type of constant jammer with sophisticated radio devices that may take reactive measures against countermeasures. Thus, the jammer presented in this thesis lies in the intersection of the constant and reactive jammer. In this direction, in the following sections, we discuss two significant technological advancements in radio architecture, i.e., FD radio and CR, that might enable a jammer to execute more powerful jamming attacks soon.

2.2 Full-Duplex Radios

In-band FD is a promising technique that allows a radio device to simultaneously transmit and receive on the same frequency band during the same time. Thus, besides nearly doubling the throughput of the network at the physical layer, FD radios have the potential to solve other problems at the higher layers [52]. However, a major bottleneck in implementing FD radios is the SI, i.e., the interference from the transmitting antenna at its receiving antenna. Since in an FD radio, both transmitting and the receiving antennas are physically close, there exist a significant interference at the receiving antenna from the transmitting antenna [53]. Several researchers have proposed various SIC techniques in physical, analogue, and digital domains to reduce the level of SI close to the noise floor [52, 54–59]. Fig. 2.1 depicts the block diagram of FD transceiver with different of SIC at various stages.

As discussed above, the SIC modules employed by an FD radio are classified into

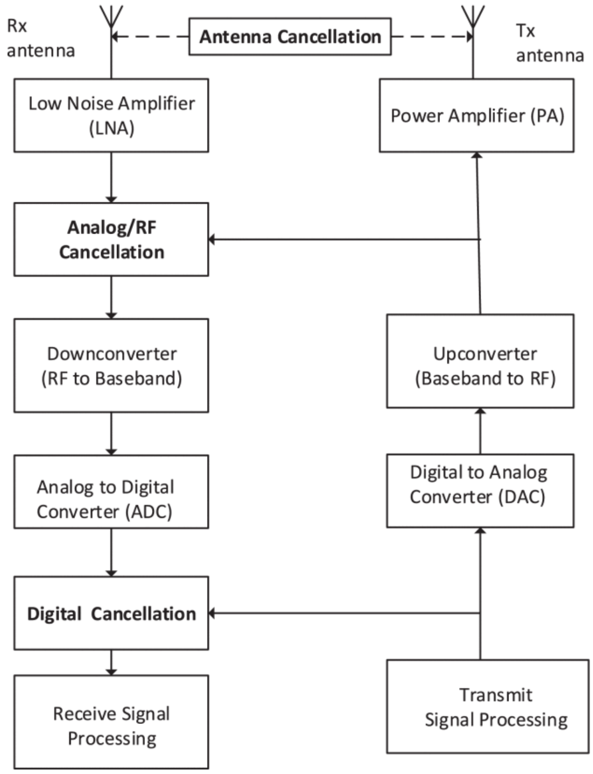

Figure 2.1: Block diagram of FD transceiver showing three types of SIC, as depicted in [1].

three categories,

1. Propagation domain cancellation,
2. Analogue domain cancellation,
3. Digital domain cancellation.

In the subsequent sections, we will discuss these cancellations in detail.

2.2.1 Propagation Domain Cancellation

Propagation domain cancellations aim at cancelling the SI signal before it enters the receive chain. The basic idea is to electromagnetically isolate the transmit and the received signals before the receive chain. Performing SIC at early stages reduces the need to use hardware with a huge dynamic range in the receiver chain. Propagation domain cancellation in separate antenna systems is achieved via a combination of cross-polarization [60, 61], path-loss [52, 53, 60, 62, 63] and antenna directionality [61]. Whereas in a shared antenna system, SIC is achieved using a circulator.

As enumerated in [52, 53, 60, 62, 63], increasing the *path loss* between the transmit and the receive antennas of FD radios results in decreased SI. Several methods increase the path loss, such as increasing the distance between the two antennas and placing an absorbing shield between the two antennas. However, increasing the path loss is governed by the device's form factor. Another method to achieve SIC is *cross-polarization*, wherein the transmit and receive antennas of the FD radio use different polarization methods for transmission and reception [60, 61]. Similarly, directional transmit and receive antennas are used such that their nulls are aligned [52, 58, 61, 62]. Although propagation domain cancellation cancel the dominant Line of Sight (LOS) component of the SI, the reflected SI from the nearby scatters still dominant. It is important to note that, due to the stochastic nature of the channel, it is difficult to cancel the reflected SI using propagation domain cancellation techniques. Therefore, propagation domain cancellation techniques are used with analogue and digital cancellation techniques.

2.2.2 Analogue Domain Cancellation

Analogue cancellation techniques are used to suppress the SI before the Analogue-to-Digital-Converter (ADC) of the receive chain. Analogue cancellation can be performed before the Low Noise Amplifier (LNA) or after the LNA (as shown in Fig. 2.1). If the cancellation is applied before the LNA, the outgoing signal from the transmit antenna is tapped, processed in the analogue domain, and finally subtracted from the received signal. As an alternate option, the outgoing signal can be tapped and processed in the digital domain and then converted back to the analogue domain. The converted signal is then used for interference cancellation [53, 64, 65]. Further, it is advantageous to tap the outgoing signal close to the transmit antenna as it captures the non-linearities of the high power amplifier distortion and the oscillator phase noise. Similarly, performing cancellation close to the receive antenna reduces the need for high dynamic range circuitry in the receive chain.

The SI channel between a transmit and receive antenna pair can be modelled for narrowband signals using a gain and a delay. For separate antenna systems, this gain and delay are used for cancellation. If the FD radio knows the channel, it will continuously tune the gain and the delay based on the reflection. However, when the FD radio is unaware of the channel knowledge, the adjustment is made once during the system design, or calibration [52, 53, 57, 60].

In the case of wideband signals, it is advisable to tap the transmit signal in the digital domain as it facilitates the use of adaptive digital filters and eliminates the need for an analogue filter for each transmit and receive-antenna pair of the FD radio [65]. Thus, to eliminate the SI for wideband signal, the signal has to be further processed in the digital domain, where adaptive Digital Signal Processing (DSP) techniques are implemented.

2.2.3 Digital Domain Cancellation

The digital domain cancellation module of the SIC is employed after the ADC, wherein we use sophisticated DSP techniques to cancel the residual SI after the propagation domain and analogue cancellation. The main advantage of using DSP techniques is their ease of implementation [66–69]. Towards cancelling the SI in the digital domain, a discrete-time baseband equivalent model capturing everything between the Digital-to-Analogue Converter (DAC) and the ADC, including the propagation domain and analogue domain cancellations, is created. These models also capture the inter-antenna and intra-antenna interferences [70, 71].

In digital domain cancellation, the FD radio first estimates the partially suppressed SI after the first two stages of the SIC. Using the knowledge of the transmit signal, it then creates an estimate of the interfering signal and subtracts it from the digital copy of the received signal [72]. However, a non-zero SI persists due to the channel estimation error and distortions due to the high power amplifier. Here, the nonlinearity due to the high power amplifier can be modelled as polynomial functions [73]. Further, estimating the polynomial parameters, some of these nonlinearities can be suppressed [57, 74, 75].

In addition to the above advancements in the SIC of the FD radios, [57] investigated SIC for WiFi protocols. Using a 80MHz WiFi 802.11ac signal with maximum transmit power of 20dBm, [57] demonstrated that their design cancels the SI close to the noise floor, such that the residual SI increased the noise floor by almost 1dB. In addition to this, [57] also showed that SI increases as the transmit power increases. Further, the FD radio achieved an throughput gain of $1.8\times$ compared to the standard HD mode.

Recently, [76] proposed a construct-and-forward FD relaying scheme to increase the network throughput and coverage. For WiFi Orthogonal Frequency Division Multiplexing (OFDM) symbols it was shown that the forwarded OFDM symbols and the reflected symbols do not interfere with each other as long as multipath reflections are within the duration of cyclic prefix, i.e., 400ns for WiFi symbols and 4.69μs for LTE.

Having discussed the basics of the FD radios, we discuss CR, another important radio technology, in the next section.

2.3 Full-Duplex Cognitive Radios: A Survey

Due to a large number of connected devices, the need to optimally utilize the licensed spectrum has gained a lot of attention from academia and industry. In the static spectrum access paradigm, each licensed user (also known as the Primary User (PU)) is allocated a dedicated channel, such that the unlicensed users (also known as the Secondary Users (SUs)) are prohibited to use these channels even if the PU is not using the channel. Thus, under the static spectrum access paradigm, the wireless spectrum is under utilised [2]. In order to accommodate the constantly increasing connected devices, it is imperative to optimally utilise the licensed spectrum. In the last decade, CR [77–79] have gained significant attention as a promising technology capable of replacing the static spectrum access with the dynamic spectrum access. In the subsequent sections, we first discuss CR in detail and then the need for FD-CR in the current regimes.

2.3.1 Cognitive Radios

First proposed in [80, 81], CRs are the devices that opportunistically use the under-utilised spectrum. An interconnection of CRs is referred to as the Cognitive Radio Network (CRN). The basic principle of CRs is to sense the empty spectrum bands, also referred to as *white spaces* or *spectrum holes*. Formally, a white space is a licensed band allocated to a PU at a geographical location at a given time, but not being used by it. Based on the idea of dynamic spectrum sharing using CRs, IEEE 802.22 was developed to facilitate sharing of the unused television spectrum at a geographical location [82,83].

Typically, CRs follow a four stage process to detect and utilize white spaces. The four stages of the white space exploitation cycle are as follows:

1. **Spectrum sensing:** During this stage, the SU monitors the activities of the PU while searching for the white spaces.

2. **Spectrum decision:** Based on various parameters, such as Quality of Service (QoS), the SU selects the best available channels [84].

3. **Spectrum mobility:** If the resource being used by the SU is required by the PU, the SU vacates the white space and starts using another white space. This ensures seamless connectivity of both, the PU and the SU.

4. **Spectrum sharing:** Since there could be multiple CRs in the network, coordination between the SUs is important in order to avoid collision. The spectrum sharing depends on the spectrum availability and the QoS requirements of the users.

Typically, CRNs are classified into three categories:

1. **Interweave network:** When the PU is ideal, the SU opportunistically transmit in the white spaces.
2. **Overlay network:** In this method, the SUs has the knowledge of the PU's messages and the encoder. This information is exploited to cancel the interference at the secondary receiver. Moreover, the SU can use a fraction of its power to relay the PU's messages.
3. **Underlay network:** In this paradigm, the SU transmits simultaneously along with the PU, such that the total interference level to the PU is bounded within acceptable limits.

2.3.2 Need for Full-Duplex Cognitive Radios

Existing CRNs deploy HD-CR for white space exploitation. However, it is known that HD systems operate on orthogonal time/frequency resources. Thus, in time-domain,

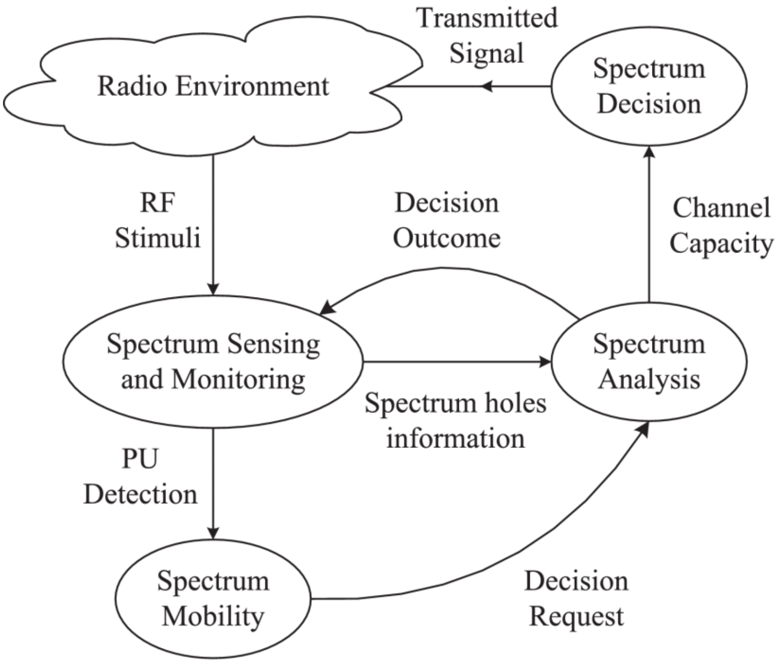

Figure 2.2: Dynamic spectrum management for an interweave network as depicted in [2,3].

HD-CR use two time slots. During the first time slot, they sense the white space and in the second time slot they access the spectrum. As a result, HD-CR waste a significant time in sensing the white spaces, leaving only a small fraction of time for its transmission. Along the similar lines, in frequency domain, HD-CR require two orthogonal frequency bands, one each for sensing and access. Further, during the transmission phase, the HD-CR cannot sense the white space, this increases the risk of interference to the PU.

Having listed the disadvantages of HD-CRs, we now highlight the advantages of using FD-CRs over HD-CRs.

1. Since FD-CRs can simultaneously sense and transmit on the same band at the same time, it can continuously monitor the transmission from the PU, thus, reducing the interference to the PU [85].

2. Due to in-band sensing and transmission, FD-CRs experience improved spectral efficiency as compared to HD-CRs.

3. The transmission operation in FD-CRs is not interrupted by the sensing operation. Therefore, SUs in FD-CRNs enjoy improved data-rates.

4. FD-CRs greatly reduce the collision between the SU and PU due to simultaneous transmission and sensing operation. However, in HD-CRs, the sensing operation

is halted during the transmission operation, thus increasing the probability of collision [86, 87].

5. The SUs in FD-CRs can harvest energy while sensing without interrupting the transmission operation [88]. Whereas, in HD-CRs, SU cannot harvest energy during sensing.

2.3.3 Full-Duplex Cognitive Radios as Adversaries: A Big Picture

The previous sections discuss FD radios from a legitimate user's viewpoint. In particular, FD radios are used to increase the network's range [76] and throughput [57]. Moreover, the advantages of FD-CRs have already been listed in the previous section. However, besides aiding the network, FD radios are also used to degrade the network's performance [89–91]. Thus, FDCA pose a significant threat to the next generation of wireless communication. Moreover, with advancements in the SIC cancellation models of the FD radios, the current state-of-art mitigation scheme might not be sufficient against FDCA. Thus, it becomes imperative to envisage new threats from an FDCA and propose corresponding countermeasures.

Consider a victim node with low-latency messages being jammed by a FDCA armed with an FD and a CR. In particular, the FDCA is such that, besides jamming a given frequency band of interest, it may also monitor the network for possible countermeasures based on existing techniques. Due to advancements in the radio architecture of the FD radios, it is indeed realistic to envisage the presence of an FDCA in next-generation networks. Since the adversary can observe the network, if the victim node deploys traditional jamming mitigation such as FH, it might detect the countermeasure owing to a significant drop in the energy levels on the victim's band. Consequently, this may compel the adversary to execute the jamming attack on another frequency band, guaranteeing degradation in the network performance, especially on crowded networks with no unused frequencies. Thus, using FD and cognitive radios at the jamming adversary opens up problems on how to design countermeasures that ensure that the victim's symbols reliably reach the destination within the deadline amidst an FDCA.

CHAPTER 3

Fast-Forward Mitigation Schemes for Reactive Adversaries for Slow-Fading Channels

3.1 Introduction

The discussions in Chapter 2 indicate that, in the presence of FDCA, if the victim node deploys traditional jamming mitigation such as FH, then it would create a *frequency hole* in the jammed band. Since the adversary has the capability to explicitly monitor the jammed band, it would detect an FH type of countermeasure owing to a significant drop in the energy levels. As a consequence, this may compel the adversary to execute the jamming attack on another frequency band thereby guaranteeing degradation in the network performance, especially on crowded networks that do not have any unused frequencies. Therefore, in order to mitigate this cognitive adversary, a new countermeasure is required to facilitate reliable communication of low-latency messages of the victim node, and to engage the adversary to the jammed frequency band. This implies that the countermeasure should force the adversary to measure the same energy levels in the jammed band thereby deceiving the adversary to believe that FH type of countermeasures have not been applied. If the countermeasure succeeds in achieving this objective, then it is considered as a covert scheme.

3.1.1 Contributions

The main contributions of this chapter are as follows:

1. In Sec. 3.2, we envisage a strong threat model on low-latency communication using a FDCA. A salient feature of the adversary is that it can jam a specific frequency band while simultaneously measuring the average energy level on the jammed band.

2. To mitigate this threat model, we propose a fast-forward framework wherein victim node forwards its messages to the base station with the help of an adjacent HD/FD helper node. Assuming slow-fading channel between the helper and the base station, and considering the jammer's distance from the helper node, we use Semi-Coherent Fast-Forward Half-Duplex (SC-F2HD) and Semi-Coherent Fast-Forward Full-Duplex (SC-F2FD) relaying scheme. In Sec. 3.3, we discuss the SC-F2HD relaying scheme, wherein the victim continues its transmission on the jammed band, whereas the helper node is asked to overhear the victim's frequency band to multiplex their information in its frequency band.

3. In Sec. 3.4, we discuss SC-F2FD relaying scheme, wherein the victim and the helper node use an energy-splitting factor $\alpha \in (0, 1)$ to cooperatively pour fraction of their energy on both frequency bands so as to reliably communicate their messages on the helper's frequency band. We present strong analytical results on the choice of α, that minimises the joint error performance of the victim and the helper node.

4. Through rigorous mathematical analysis and simulation results, we show the improvement in the victim's performance after implementing the scheme. Further, in Sec. 3.7, we also show that both schemes successfully engage the adversary on the jammed frequency band.

3.1.2 Related Works

The practical challenges in implementing FD radios are discussed in [92] and the references within. While SIC techniques are discussed in [52, 54, 72, 93], the problems related to modelling the residualSI after the interference cancellation process are discussed in [76, 94, 95]. Specifically, [64] experimentally showed that the SI channel is Rayleigh or Ricean fading distributed for different parts of the path. With respect to the use of FD radios for instantaneous manipulation, [76, 89, 90] studied the feasibility of using an FD radio as a fast-forward radio in order to modify the transmitted symbol of a source node. In particular, the results on instantaneous manipulation are experimentally proven in [76] using the OFDM framework. Several applications of FD radios are also studied in cognitive radio networks [84, 96] by [97–99], wherein the FD radios play the

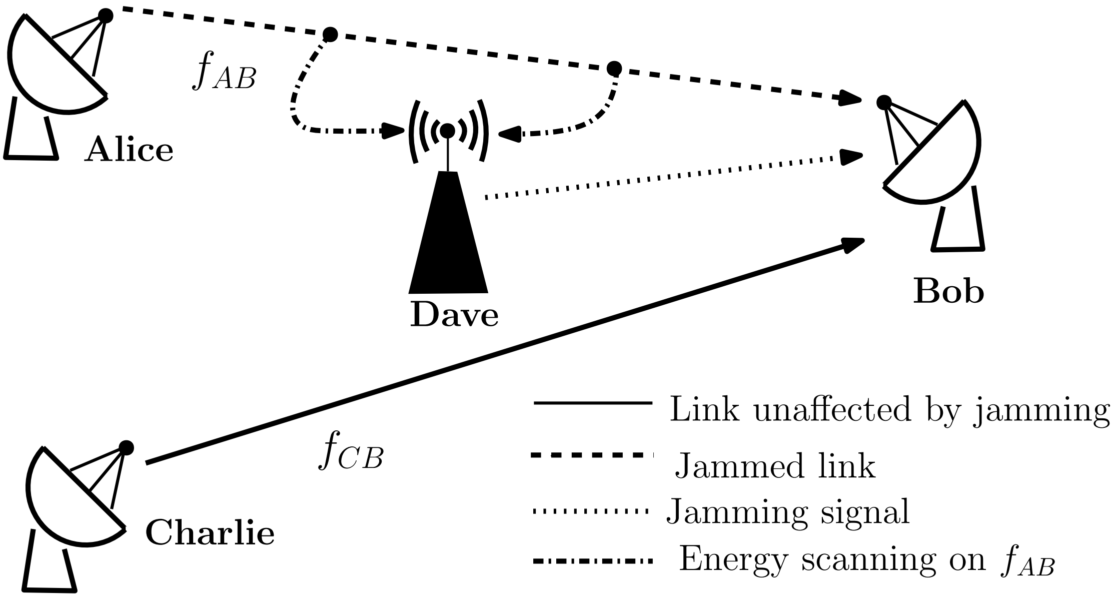

Figure 3.1: The network model for *cognitive* jamming, where Dave can *jam and measure*

role of secondary users by simultaneously transmitting signals and also scanning a wide range of frequency bands in the frequency-spectrum. In the literature, FD radios are also used in adversarial network models, wherein they aid the legitimate users in improving the secrecy capacity in presence of an eavesdropper [100–103]. Recently, [91] introduced an FD cognitive reactive jammer that jams multiple frequencies in the network with adaptive decision making capability. However, they use FH as a mitigation strategy owing to a number of unused frequencies in the network. As a result, fast-forward relay nodes are irrelevant in their set up.

3.2 System Model

Consider a *crowded* wireless network wherein a number of nodes intend to communicate with a base-station using a FDD mode. The network as crowded since all the available uplink frequencies have been used by the nodes, hence no unused frequencies are available. To capture an instantiation of this model, consider the network model as shown in Fig. 3.1, which comprises two nodes, namely Alice and Charlie, that communicate with the base-station, namely Bob, on two separate frequency bands f_{AB} and f_{CB}, respectively. Let the network requirements of Alice and Charlie are heterogeneous, i.e., Alice has low data-rate messages with strict latency constraints, whereas Charlie has arbitrary data-rate messages without low-latency constraints. Since low-latency constraints are usually accompanied with low data-rate messages (e.g., control channel messages (PUCCH) in 5G [104, Section 6.3.2]), Alice uses low-rate signalling. On the other hand, Charlie uses arbitrary data-rates with no latency constraints (e.g., shared channel messages (PUSCH) in 5G [104, Section 6.3.1]) since it has to tolerate acceptable degradation in its performance for cooperating with Alice. In this network, the communication between Alice and Bob is disrupted due to the presence of an FD *cognitive* adversary, Dave, who jams the uplink frequency of Alice-to-Bob link, i.e., f_{AB}, by injecting jamming energy, thereby making Bob unavailable to Alice. Specifically, due to the cognitive nature of Dave, he can also measure the average energy levels on f_{AB}. To incorporate a strong adversarial model, a perfect FD radio is assumed at Dave, as a result, he can explicitly measure the average energy contributed by Alice alone. Although FH is effective against DoS attacks, it cannot be used as a countermeasure in our network model since there are no unused frequencies. Furthermore, even if there are unused frequencies, when Alice hops out of f_{AB}, the average energy level on f_{AB} drops. As a result, since Dave is consistently monitoring the average energy levels on f_{AB}, he might suspect a countermeasure, and as a consequence, he may inject jamming energy on another frequency band thereby guaranteeing degradation of the network performance. Therefore, while Alice has to necessarily hop to a different frequency band in order to communicate her low-latency messages, she must also ensure that Dave does not experience a surge or dip in the average energy levels on f_{AB}.

To mitigate the cognitive adversary, we synthesize cooperative strategies that assist Alice in evading the jamming attack, and also forces Dave to measure the same energy levels. To facilitate this, we assume that Charlie is in the vicinity of Alice, and moreover, he is capable of operating in both HD as well as FD mode. Furthermore, we assume that the FD radio at Charlie is capable of instantaneous manipulation in a fast-forward mode [76]. In the following sections, we propose two strategies, namely: the Semi-Coherent Fast-Forward Half-Duplex (SC-F2HD) relying scheme and the Semi-Coherent Fast-Forward Full-Duplex (SC-F2FD) relaying scheme. We refer to our countermeasures as semi-coherent because Charlie decodes Alice's message using non-coherent detection as part of the decode-and-forward protocol in both the schemes. However, when decoding Alice's and Charlie's messages, Bob uses coherent detection in the SC-F2HD scheme, whereas a combination of coherent and non-coherent detection in the SC-F2FD scheme.

3.3 Semi-Coherent Fast-Forward Half-Duplex Relaying Scheme

In this scheme, Bob directs Alice to continue her transmission on f_{AB}. Since Charlie is in the vicinity of Alice, Bob directs Charlie to overhear Alice's transmitted symbol on f_{AB}, decode the transmitted bit, and then instantaneously embed the decoded bit in his transmission on f_{CB}. Since the Alice-to-Bob channel is under attack, we refrain the use of pilots on f_{AB} owing to a possible pilot contamination attack by Dave. Therefore, Alice uses non-coherent amplitude shift keying. Since Charlie embeds Alice's bit in his symbol, Bob receives a multiplexed symbol from Charlie, and then attempts to jointly decode the symbols of Alice and Charlie. It is worthwhile to note that, while Alice continues to communicate on f_{AB}, the corresponding received symbols are not utilized by Bob for decoding. However, the ongoing communication on f_{AB} compels Dave to measure the same average energy on f_{AB} even after the implementation of the SC-F2HD scheme. In the next section, we explain the baseband signal model for SC-F2HD.

3.3.1 Signal Model: SC-F2HD Relaying Scheme

In this scheme, Alice uses On-Off Keying (OOK) denoted by $\mathcal{S}_A = \{0, 1\}$, whereas Charlie uses PSK constellation $\mathcal{S}_C = \left\{ e^{\iota \frac{2\pi}{M}\left(j+\frac{1}{2}\right)} | j = 0, 1, 2, \ldots, M-1 \right\}$, where $\iota = \sqrt{-1}$, and M is the size of the PSK constellation. Among various constellations for non-coherent detection, we consider OOK since the rate requirements on the low-latency messages is usually low. However, for Charlie, since any pilot-assisted coherent modulation can be applied, we choose PSK for its circular structure. Let $x \in \mathcal{S}_A$ denote the information symbol transmitted by Alice, and let $r_{C,AB}$ denote the received symbol at Charlie on f_{AB}, given as, $r_{C,AB} = h_{AC}x + n_C$, where, h_{AC} is the baseband channel between Alice and Charlie distributed as $\mathcal{CN}(0, \sigma_{AC}^2)$ and $n_C \sim \mathcal{CN}(0, N_o)$ is the Additive White Gaussian Noise (AWGN) at Charlie. Using non-coherent energy detection, Charlie decides to transmit $y \in \mathcal{S}_C$, if $\hat{x} = 0$, or $e^{\iota \frac{\pi}{M}}y$, if $\hat{x} = 1$, where $\hat{x}$ is the decoded symbol at Charlie. Based on Charlie's transmitted symbol, the received symbol at Bob on f_{CB} is

$$r_B = \begin{cases} h_{CB}y + n_B, & \text{if } x = 0, \hat{x} = 0; \\ h_{CB}e^{\iota\frac{\pi}{M}}y + n_B, & \text{if } x = 0, \hat{x} = 1; \\ h_{CB}y + n_B, & \text{if } x = 1, \hat{x} = 0; \\ h_{CB}e^{\iota\frac{\pi}{M}}y + n_B, & \text{if } x = 1, \hat{x} = 1; \end{cases} \tag{3.1}$$

where $h_{CB} \sim \mathcal{CN}(0, \sigma_{CB}^2)$ is the channel between Charlie and Bob such that $\sigma_{CB}^2 = 1$, and $n_B \sim \mathcal{CN}(0, N_o)$ is the AWGN at Bob. Due to the proximity of Alice and Charlie, $\sigma_{AC}^2 > \sigma_{CB}^2$ to capture higher Signal-to-Noise Ratio (SNR) in the Alice-to-Charlie link compared to Charlie-to-Bob link. Also assume that Bob has the knowledge of h_{CB} owing to the use of pilots on f_{CB}.

3.3.2 Error Performance: SC-F2HD Relaying Scheme

Charlie uses non-coherent energy detection to decode Alice's symbols, where he compares the two likelihoods i.e., **f** $(r_{C,AB}|x = 0)$, and **f** $(r_{C,AB}|x = 1)$, where, **f**$(r_{C,AB}|x = i)$ is the Probability Density Function (PDF) of the received symbol $r_{C,AB}$ conditioned on $x \in \mathcal{S}_A$. Comparing the likelihoods, the optimal detection threshold is $\tau_{\text{HD}} \underset{0}{\overset{1}{\gtrless}} \frac{\Omega_{0,AB}\Omega_{1,AB}}{\Omega_{0,AB}-\Omega_{1,AB}} \ln\left(\frac{\Omega_{0,AB}}{\Omega_{1,AB}}\right)$, where $\Omega_{0,AB} = N_o$, and $\Omega_{1,AB} = N_o + \sigma_{AC}^2$, are the variance of the received symbols corresponding to $x = 0$ and $x = 1$, respectively. Using this decoding method, let $\Phi_{01,\text{HD}}$ and $\Phi_{10,\text{HD}}$ denote the probabilities with which Charlie decodes Alice's bit 0 as bit 1, and bit 1 as bit 0, respectively. Consequently, let $\Phi_{00,\text{HD}} = 1 - \Phi_{01,\text{HD}}$ and $\Phi_{11,\text{HD}} = 1 - \Phi_{10,\text{HD}}$, denote the probability of correctly decoding bit 0 and bit 1, respectively. The following proposition presents the expressions for the cross-over probabilities.

Proposition 1. $\Phi_{01,\text{HD}} = e^{-\frac{\tau_{\text{HD}}}{\Omega_{0,AB}}}$*, and* $\Phi_{10,\text{HD}} = 1 - e^{-\frac{\tau_{\text{HD}}}{\Omega_{1,AB}}}$.

Proof. Using non-coherent energy detection, $\Phi_{01,\text{HD}}$ is given by

$$\begin{aligned} \Phi_{01,\text{HD}} &= \Pr\left\{ \left. \frac{\frac{1}{\Omega_{0,AB}} e^{\frac{-|r_{C,AB}|^2}{\Omega_{0,AB}}}}{\frac{1}{\Omega_{1,AB}} e^{\frac{-|r_{C,AB}|^2}{\Omega_{1,AB}}}} < 1 \right| x = 0 \right\} \\ &= \Pr\left\{ |r_{C,AB}|^2 > \frac{\Omega_{0,AB}\Omega_{1,AB}}{\Omega_{0,AB} - \Omega_{1,AB}} \ln\left(\frac{\Omega_{0,AB}}{\Omega_{1,AB}}\right) \right\} = e^{-\frac{\tau_{\text{HD}}}{\Omega_{0,AB}}}. \end{aligned}$$

$$\mathbf{g}_{\text{HD}}\left(r_B\middle|\, x=0, y=e^{\iota\frac{2\pi}{M}\left(j+\frac{1}{2}\right)}, h_{CB}\right) = \Phi_{00,\text{HD}}\mathbf{f}_{0,\text{HD}}\left(r_B\middle|\, w=e^{\iota\frac{2\pi}{M}\left(j+\frac{1}{2}\right)}, h_{CB}\right) + \Phi_{01,\text{HD}}\mathbf{f}_{0,\text{HD}}\left(r_B\middle|\, w=e^{\iota\frac{2\pi}{M}\left(j+\frac{1}{2}\right)}e^{\iota\frac{\pi}{M}}, h_{CB}\right) \quad (3.3)$$

$$\mathbf{g}_{\text{HD}}\left(r_B\middle|\, x=1, y=e^{\iota\frac{2\pi}{M}\left(j+\frac{1}{2}\right)}, h_{CB}\right) = \Phi_{10,\text{HD}}\mathbf{f}_{1,\text{HD}}\left(r_B\middle|\, w=e^{\iota\frac{2\pi}{M}\left(j+\frac{1}{2}\right)}, h_{CB}\right) + \Phi_{11,\text{HD}}\mathbf{f}_{1,\text{HD}}\left(r_B\middle|\, w=e^{\iota\frac{2\pi}{M}\left(j+\frac{1}{2}\right)}e^{\iota\frac{\pi}{M}}, h_{CB}\right) \quad (3.4)$$

Similarly, it can shown that $\Phi_{10,\text{HD}} = 1 - e^{-\frac{\tau_{\text{HD}}}{\Omega_{1,AB}}}$. $\square$

To perform joint decoding of the multiplexed symbols of OOK and M-PSK, Bob uses a joint Maximum A Posteriori (MAP) decoder given as

$$\hat{i}, \hat{j} = \arg\max_{i,j} \mathbf{g}_{\text{HD}}\left(r_B\middle|\, x=i, y=e^{\iota\frac{2\pi}{M}\left(j+\frac{1}{2}\right)}, h_{CB}\right), \quad (3.2)$$

where $i \in \mathcal{S}_A$, and $j \in \{0, \ldots, M-1\}$, and $\mathbf{g}_{\text{HD}}(\cdot)$ for various realizations of i is given in (3.3) and (3.4), such that, $\mathbf{f}_{0,\text{HD}}\left(r_B\middle|\, w, h_{CB}\right) = (\pi N_o)^{-1}e^{-\frac{|r_B - h_{CB}w|^2}{N_o}}$, and $\mathbf{f}_{1,\text{HD}}\left(r_B\middle|\, w, h_{CB}\right) = (\pi N_o)^{-1}e^{-\frac{|r_B - h_{CB}w|^2}{N_o}}$.

With possible inclusion of error at Charlie, the likelihood function $\mathbf{g}_{\text{HD}}(\cdot)$ for each value of i is a Gaussian mixture, weighted by respective probabilities of correct and erroneous detection at Charlie. Using the above decoder, the simulation results showcasing the average error performance of Alice and Charlie before and after implementing SC-F2HD relaying scheme are presented. To present the results, we use 4-PSK at Charlie. Due to the vicinity of Alice and Charlie, we assume $\sigma_{AC}^2 = 4$, thereby providing a $10\log_{10}(\sigma_{AC}^2) \approx 6$ dB improvement in the SNR compared to that of Charlie-to-Bob channel. In general, it is intuitive to expect the performance of the SC-F2HD scheme to degrade as the channel quality between Alice and Charlie also degrades. This is because the proposed strategy relies on correct decoding of information symbols at Charlie with an overwhelming probability. We use SNR = $\frac{1}{N_o}$ to capture various values of the noise variance at Charlie and Bob. In Fig. 3.2, we present the error performance of Alice and Charlie before and after implementing SC-F2HD scheme. When implementing SC-F2HD scheme, we assume that the jamming energy injected by Dave introduces negligible interference at Charlie on f_{AB}. The plots show that the performance of Alice

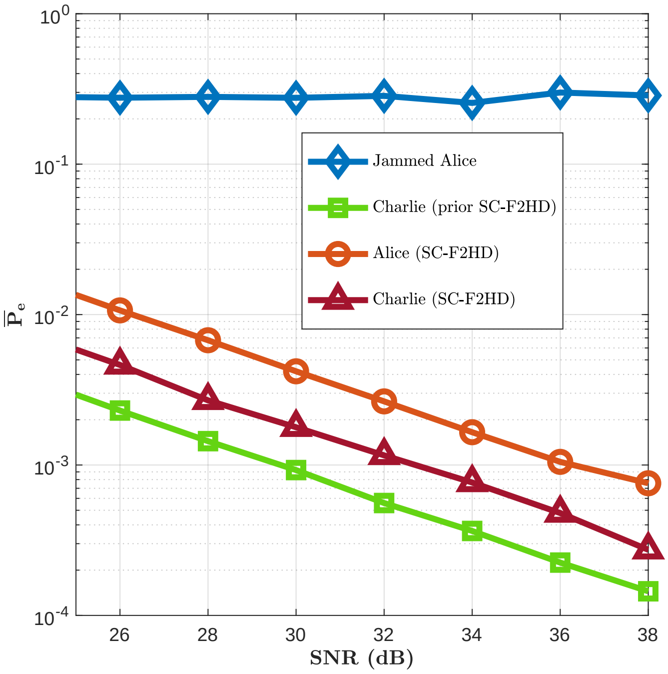

Figure 3.2: Average error performance of Alice and Charlie prior and after SC-F2HD relaying scheme for various SNR values.

improves substantially after implementing SC-F2HD scheme. In contrast, the error performance of Charlie degrades, and this is because Bob jointly decodes from an 8-PSK constellation instead of a 4-PSK constellation.

It is clear that SC-F2HD scheme allows Alice to overcome jamming without switching to a different frequency. However, since Dave's location is arbitrary, the assumption of zero leakage of Dave's jamming energy at Charlie will not hold in some cases. To explain this, in Fig. 3.3, we plot the error performance of Alice at Bob by incorporating non-zero interference from Dave at Charlie. With negligible interference from Dave, the performance of Alice is not affected. However, as the interference energy increases, Charlie starts introducing error in decoding bit 0 as bit 1, which in turn propagates to Bob. In particular, for some special values of interference from Dave, we observe that the error probability increases with SNR. This behaviour is attributed to the fact that probability of decoding bit 0 as bit 1 at Charlie increases with SNR since the threshold for energy detection does not account for interference. Overall, this limitation urges us to design a countermeasure such that the effect of jamming energy of Dave on its performance is inconsequential. In the next section, we propose the second mitigation scheme.

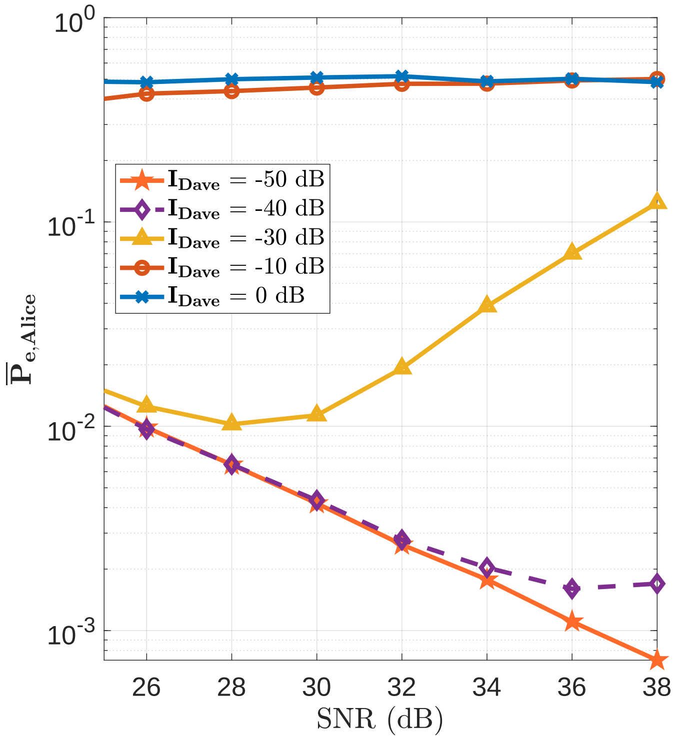

Figure 3.3: Average error performance of Alice in the SC-F2HD scheme with increasing interference (I_{Dave}) from Dave at Charlie.

3.4 Semi-Coherent Fast-Forward Full-Duplex Relaying Scheme

SC-F2FD is a cooperative strategy, akin to SC-F2HD, wherein Charlie instantaneously relays Alice's information to Bob by embedding them into his message. However, in contrast to SC-F2HD, Alice switches her frequency to f_{CB}, and therefore, Charlie need not listen to f_{AB}. While the relaying strategy is executed on f_{CB} by using a fraction of their energies, the residual fraction of their energies are used on f_{AB} in order to engage the attacker. Fig. 3.4 depicts the SC-F2FD relaying scheme wherein Bob directs Alice to transmit her OOK bit with energy levels $\{0, 1-\alpha\}$ in the uplink frequency of Charlie, i.e., f_{CB}, such that $\alpha \in (0, 1)$, whereas Charlie continues his communication on f_{CB}. Since Charlie has an FD radio, he is capable of in-band communication. Thus, Charlie non-coherently decodes Alice's OOK symbols. If the decoded bit is 0, Charlie transmits his original PSK symbol as it is, whereas if the decoded bit is 1, Charlie introduces a rotation to the PSK symbol and also scales the PSK symbol with $\sqrt{\alpha}$. As a result, Bob receives a multiplexed symbol on f_{CB} comprising information symbols of both Alice and Charlie. Due to the underlying multiple access channel (MAC) on f_{CB}, Bob receives a linear combination of the transmitted symbols from both Alice and Charlie.

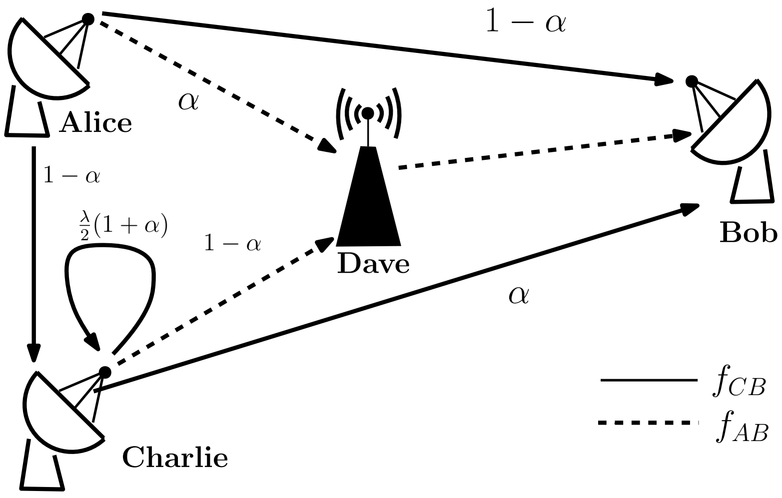

Figure 3.4: Network model depicting SC-F2FD relaying scheme. Alice and Charlie use $1-\alpha$ and α fractions of their energies on the frequency band f_{CB}, respectively. Concurrently, Alice and Charlie also pour α and $1-\alpha$ fraction of their energy on the frequency band f_{AB}, respectively. SI at Charlie is $\sim \mathcal{CN}\left(0, \lambda\frac{(1+\alpha)}{2}\right)$.

In the next section, we discuss the baseband signal model for the communication on f_{CB}.

3.4.1 Signal Model: SC-F2FD Relaying Scheme

When the network implements SC-F2FD, Charlie listens to the transmitted signal of Alice in the band f_{CB} while transmitting his signal to Bob in the same band. The underlying constellations used at Alice and Charlie are the same as discussed in Sec. 3.3.1. However, in this case, Alice transmits her bits with energy levels 0 and $1-\alpha$. Therefore, the received symbol at Charlie is $r_{C,CB} = \sqrt{1-\alpha}h_{AC}x + n_C + h_{CC}$, where h_{CC} is the SI channel at Charlie and h_{AC}, x, and n_C are already defined in Sec. 3.3.1. Upon switching to f_{CB}, Alice refrains from transmitting pilot symbols in order to satisfy low-latency constraints on her messages. As a result, using non-coherent energy detection, the decoded bit $\hat{x}$ at Charlie defines the outgoing symbol from Charlie, i.e., Charlie transmits $y \in \mathcal{S}_C$, when $\hat{x} = 0$, and $\sqrt{\alpha}e^{\iota\frac{\pi}{M}}y$, when $\hat{x} = 1$, where y is Charlie's PSK symbol. Thus, the symbol received at Bob is given as

$$r_B = \begin{cases} h_{CB}y + n_B, & \text{if } x = 0, \hat{x} = 0; \quad (3.5\text{a}) \\ \sqrt{\alpha}h_{CB}e^{\iota\frac{\pi}{M}}y + n_B, & \text{if } x = 0, \hat{x} = 1; \quad (3.5\text{b}) \\ \sqrt{1-\alpha}h_{AB} + h_{CB}y + n_B, & \text{if } x = 1, \hat{x} = 0; \quad (3.5\text{c}) \\ \sqrt{1-\alpha}h_{AB} + \sqrt{\alpha}h_{CB}e^{\iota\frac{\pi}{M}}y + n_B, & \text{if } x = 1, \hat{x} = 1; \quad (3.5\text{d}) \end{cases}$$

where $h_{AB} \sim \mathcal{CN}(0, 1)$ is the baseband channel from Alice to Bob on f_{CB}, whereas h_{CB} and n_B are as defined in the SC-F2HD relaying scheme. Unlike the case of SC-F2HD, in this scheme, Alice's information is embedded in Charlie's symbol using rotation as well as the scaling operation. In addition, Bob also receives the symbol transmitted by Alice superimposed with the symbol transmitted by Charlie.

With perfect knowledge of h_{CB}, Bob jointly decodes Alice's and Charlie's symbols in the band f_{CB}. Owing to the use of energy-splitting factor α and no knowledge of h_{AB}, Bob observes variation in the variance of the received symbol as well as the constellation used by Charlie. Specifically, from (3.5a) – (3.5d), we note that when Alice transmits bit 1, the noise variance of the received symbol is higher when compared to the case when bit 0 is transmitted, i.e., $N_{B1} > N_{B0}$, where $N_{B1} = N_o + (1 - \alpha)$ and $N_{B0} = N_o$. Therefore, this framework necessitates using a combination of non-coherent and coherent detection mechanism on f_{CB}. For example, consider a 4-PSK constellation used by Charlie, for which all possible multiplexed symbols received at Bob are shown in Fig. 3.5a. When Alice transmits bit 0, and Charlie transmits $y \in \mathcal{S}_C$ assuming he does not introduce a decoding error, then Bob receives a symbol with noise variance $N_{B0} = N_o$ centred around y. However, if Charlie makes a decoding error ($x \neq \hat{x}$), then Bob will receive a symbol centred around $\sqrt{\alpha}e^{\iota\frac{\pi}{M}}y$, but with the same noise variance N_{B0}. Similarly, the centres of symbols received at Bob when Alice transmits bit 1 are y and $\sqrt{\alpha}e^{\iota\frac{\pi}{M}}y$, for erroneous and non-erroneous decision at Charlie, respectively, wherein the corresponding noise variance is $N_{B1} = N_o + (1 - \alpha)$. Therefore, the received constellation at Bob is $\mathcal{S}_C \cup \sqrt{\alpha}e^{\iota\frac{\pi}{M}}\mathcal{S}_C \subset \mathbb{C}$. For example, for a 4-PSK constellation used by Charlie, Bob receives a 16 point constellation.

3.4.2 Error Performance at Charlie

In this section, we discuss the non-coherent decoding strategy at Charlie, which uses an FD radio, to instantaneously embed Alice's information symbol in its message. Given that a practical FD radio is limited by its SI, we use the well known first-order approximation [76], [105] by modelling the SI channel as Rayleigh distribution [106]. According to the SC-F2FD protocol, Charlie transmits a symbol with energy α, or energy 1 depending on the decoded bit from Alice. Therefore, with uniform distribution on the OOK symbols, the average outgoing energy from Charlie is $\frac{1+\alpha}{2}$. With

$\lambda \in (0,1)$ denoting the parameter of the SI cancellation technique, we model the SI channel at Charlie as $h_{CC} \sim \mathcal{CN}(0, \frac{(1+\alpha)\lambda}{2})$. Using the above probabilistic model on the SI, we are now ready to study the error performance of non-coherent detection at Charlie. Similar to the discussion in Sec. 3.3.2, we can derive the error performance at Charlie when using the SC-F2FD scheme. However, the major difference between the two schemes is that Charlie operates in the FD mode. Also, Alice transmits bit 1 with energy $1-\alpha$. Due to these differences, the threshold for energy detection changes as Charlie witnesses SI from his transmit antenna. Therefore, the new energy threshold at Charlie is $\tau_{\text{FD}} = \frac{\Omega_{0,CB}\Omega_{1,CB}}{\Omega_{0,CB}\Omega_{1,CB}}\ln\left(\frac{\Omega_{0,CB}}{\Omega_{1,CB}}\right)$, where, $\Omega_{0,CB} = N_o + \lambda\frac{(1+\alpha)}{2}$, and $\Omega_{1,CB} = N_o + \sigma_{AC}^2(1-\alpha) + \lambda\frac{(1+\alpha)}{2}$ are the effective noise variance of the received baseband symbol when Alice transmits bit 0 and bit 1, respectively. Using the non-coherent energy detection method, let $\Phi_{01,\text{FD}}$ and $\Phi_{10,\text{FD}}$ denote the probabilities with which Charlie decodes Alice's bit 0 as bit 1, and bit 1 as bit 0, respectively. Consequently, let $\Phi_{00,\text{FD}} = 1 - \Phi_{01,\text{FD}}$ and $\Phi_{11,\text{FD}} = 1 - \Phi_{10,\text{FD}}$, denote the probability of correctly decoding bit 0 and bit 1, respectively. The following proposition presents the expressions for the cross-over probabilities, which can be proved along the similar lines of Proposition 1.

Proposition 2. *$\Phi_{01,\text{FD}} = e^{-\frac{\tau_{\text{FD}}}{\Omega_{0,CB}}}$, and $\Phi_{10,\text{FD}} = 1 - e^{-\frac{\tau_{\text{FD}}}{\Omega_{1,CB}}}$.*

With $\flat \triangleq \frac{\Omega_{1,CB}}{\Omega_{0,CB}}$, it is straightforward to show that $\flat > 1$, and it is a decreasing function of α. In the rest of this section, we present results to analyse the behaviour of $\Phi_{00,\text{FD}}$, $\Phi_{01,\text{FD}}$, $\Phi_{10,\text{FD}}$, and $\Phi_{11,\text{FD}}$ as a function of α.

Lemma 1. *The error expressions at Charlie are such that $\Phi_{10,\text{FD}} < \Phi_{11,\text{FD}}$, for $\alpha \in (0,\nu)$, where $\nu = \frac{\sigma_{AC}^2 - N_o - \frac{\lambda}{2}}{\sigma_{AC}^2 + \frac{\lambda}{2}}$, and $\Phi_{00,\text{FD}} > \Phi_{01,\text{FD}}$ $\forall \alpha \in (0,1)$.*

Proof. For the first part, the ratio of $\Phi_{10,\text{FD}}$ and $\Phi_{11,\text{FD}}$ is $e^{\frac{\tau_{\text{FD}}}{\Omega_{1,CB}}} - 1 = (\flat)^{\frac{1}{\flat-1}} - 1$. For $\flat = 2$, $(\flat)^{\frac{1}{\flat-1}} - 1 = 1$, i.e., $\Phi_{10,\text{FD}} = \Phi_{11,\text{FD}}$. Further, for increasing values of $\flat$, $(\flat)^{\frac{1}{\flat-1}} - 1$ decreases. This implies that $\Phi_{10,\text{FD}} < \Phi_{11,\text{FD}}$ for $\flat > 2$. Finally, $\flat > 2$ implies that $\alpha < \nu \triangleq \frac{\sigma_{AC}^2 - N_o - \frac{\lambda}{2}}{\sigma_{AC}^2 + \frac{\lambda}{2}}$. This completes the first part of lemma.

Similarly, for the second part, the ratio of $\Phi_{00,\text{FD}}$ and $\Phi_{01,\text{FD}}$ is $e^{\frac{\tau_{\text{FD}}}{\Omega_{0,CB}}} - 1 = (\flat)^{\frac{\flat}{\flat-1}} - 1$. Since $\flat > 1$, it is straightforward to prove that $(\flat)^{\frac{\flat}{\flat-1}} - 1 > 1.71$ using the definition of e. Therefore, $\Phi_{00,\text{FD}} > \Phi_{01,\text{FD}}$. This completes the proof. □

$$\mathbf{g}_{\text{FD}}\left(r_B \middle| x=0, y=e^{\iota\frac{2\pi}{M}\left(j+\frac{1}{2}\right)}, h_{CB}\right) = \Phi_{00,\text{FD}}\mathbf{f}_{0,\text{FD}}\left(r_B \middle| t=e^{\iota\frac{2\pi}{M}\left(j+\frac{1}{2}\right)}, h_{CB}\right) + \Phi_{01,\text{FD}}\mathbf{f}_{0,\text{FD}}\left(r_B \middle| t=\sqrt{\alpha}e^{\iota\frac{2\pi}{M}\left(j+\frac{1}{2}\right)}e^{\iota\frac{\pi}{M}}, h_{CB}\right) \quad (3.7)$$

$$\mathbf{g}_{\text{FD}}\left(r_B \middle| x=1, y=e^{\iota\frac{2\pi}{M}\left(j+\frac{1}{2}\right)}, h_{CB}\right) = \Phi_{10,\text{FD}}\mathbf{f}_{1,\text{FD}}\left(r_B \middle| t=e^{\iota\frac{2\pi}{M}\left(j+\frac{1}{2}\right)}, h_{CB}\right) + \Phi_{11,\text{FD}}\mathbf{f}_{1,\text{FD}}\left(r_B \middle| t=\sqrt{\alpha}e^{\iota\frac{2\pi}{M}\left(j+\frac{1}{2}\right)}e^{\iota\frac{\pi}{M}}, h_{CB}\right) \quad (3.8)$$

Lemma 2. $\Phi_{10,\text{FD}} > \Phi_{01,\text{FD}}$, *for any* $0 < \alpha < 1$.

Proof. The ratio of $\Phi_{10,\text{FD}}$ and $\Phi_{01,\text{FD}}$ is $e^{\frac{\tau_{\text{FD}}}{\Omega_{0,CB}}} - \frac{\Omega_{1,CB}}{\Omega_{0,CB}} = (\flat)^{\frac{\flat}{\flat-1}} - \flat$. Since $\flat > 1$, we can prove $(\flat)^{\frac{\flat}{\flat-1}} - \flat > 1.71$ using the definition of e. Therefore, $\Phi_{10,\text{FD}} > \Phi_{01,\text{FD}}$. □

Lemma 3. $\Phi_{11,\text{FD}}$ *decreases with increasing* α *in the interval* $(0, 1)$.

Proof. $\Phi_{11,\text{FD}} = e^{-\frac{\tau_{\text{FD}}}{\Omega_{1,CB}}} = \left(\frac{1}{\flat}\right)^{\frac{1}{1-\flat}}$. As stated earlier, with increasing α, $\flat$ decreases. For decreasing $\flat$, $\left(\frac{1}{\flat}\right)^{\frac{1}{1-\flat}}$ also decreases. Therefore, $\Phi_{11,\text{FD}}$ decreases with α. This completes the proof. □

From the above lemma, we note that $\Phi_{10,\text{FD}}$ is an increasing function of $\alpha \in (0, 1)$. In the next subsection, we present the MAP decoding metric for the SC-F2FD scheme, and discuss the challenges in characterizing the error performance of the MAP decoder.

3.4.3 Error Performance at Bob

Similar to the SC-F2HD scheme, Bob uses a joint MAP decoder to decode Alice's and Charlie's symbols simultaneously. The joint MAP decoder for SC-F2FD relaying scheme is given as

$$\hat{i}, \hat{j} = \arg\max_{i,j} \mathbf{g}_{\text{FD}}\left(r_B \middle| x=i, y=e^{\iota\frac{2\pi}{M}\left(j+\frac{1}{2}\right)}, h_{CB}\right), \quad (3.6)$$

where $i \in \mathcal{S}_A$ and $j \in \{0, 1, \ldots, M-1\}$, and $\mathbf{g}_{\text{FD}}(\cdot)$ is the conditional PDF given by (3.7) and (3.8), such that $\mathbf{f}_{0,\text{FD}}\left(r_B \middle| t, h_{CB}\right) = (\pi N_{B0})^{-1}e^{-\frac{|r_B - h_{CB}t|^2}{N_{B0}}}$, where $N_{B0} = N_o$ and $\mathbf{f}_{1,\text{FD}}\left(r_B \middle| t, h_{CB}\right) = (\pi N_{B1})^{-1}e^{-\frac{|r_B - h_{CB}t|^2}{N_{B1}}}$, where $N_{B1} = N_o + (1-\alpha)$.

Using the joint MAP decoder defined in (3.6), one needs to compute the pairwise error events between the symbols (i, j), $\forall (i, j) \in \{0, 1\} \times \{0, 1, \ldots, M-1\}$, and then compute the average of each error event over h_{CB} to obtain an upper bound on the average error. However, note that $\mathbf{g}_{\text{FD}}(\cdot)$ is a Gaussian mixture, and therefore, computing the error events from the Gaussian mixture is non-trivial. To circumvent this problem, we propose an approximation of the joint MAP decoder that provides a near-optimal solution.

3.5 SC-F2FD Joint Dominant Decoder

Using [107], a joint MAP decoder can be approximated to obtain a Joint MAX (JMAX) decoder as

$$\hat{i}, \hat{j} = \arg\max_{i,j} \mathbf{g_m}\left(r_B \middle| \, x = i, y = e^{\iota \frac{2\pi}{M}\left(j+\frac{1}{2}\right)}, h_{CB} \right), \tag{3.9}$$

where the likelihood function $\mathbf{g_m}(\cdot)$, is such that it considers only the maximum of the two components in the Gaussian mixture. From Lemma 1, we have $\Phi_{10,\text{FD}} < \Phi_{11,\text{FD}}$ $\forall \alpha \in (0, \nu)$, and $\Phi_{01,\text{FD}} < \Phi_{00,\text{FD}}$ $\forall \alpha \in (0, 1)$. Therefore, we further approximate (3.9), for $\alpha \in (0, 1)$, to obtain the SC-F2FD Joint Dominant decoder.

Definition 1. *An approximation on* (3.9) *using Lemma 1, gives us the SC-F2FD JD decoder defined as*

$$\hat{i}, \hat{j} = \arg\max_{i,j} \mathbf{g_a}^{\psi}\left(r_B \middle| x = i, y = e^{\iota \frac{2\pi}{M}\left(j+\frac{1}{2}\right)} \right), \tag{3.10}$$

where, the conditional PDF $\mathbf{g_a}(\cdot)$ *is* $\frac{\Phi_{00,\text{FD}}}{\pi N_{B0}} e^{-\frac{|r_B - y \; h_{CB}|^2}{N_{B0}}}$ *and* $\frac{\Phi_{11,\text{FD}}}{\pi N_{B1}} e^{-\frac{|r_B - \sqrt{\alpha} y e^{\iota \frac{\pi}{M}} \; h_{CB}|^2}{N_{B1}}}$ *for* $x = 0$ *and* $x = 1$, *respectively.*

Due to this approximation, the decoder decodes to one of the 8 points shown in Fig. 3.5b instead of 16 points shown in Fig. 3.5a. In Fig. 3.5b, black dots are the symbols that occur with probability $\Phi_{00,\text{FD}}$, centred around $y \in \mathcal{S}_C$ with noise variance $N_{B0} = N_o$, whereas, the red diamonds are the symbols received with probability $\Phi_{11,\text{FD}}$ centred around $y' \in \sqrt{\alpha} e^{\iota \frac{\pi}{M}} \mathcal{S}_C$ with higher noise variance $N_{B1} = N_o + 1 - \alpha$. In the rest of the section, we compute the pairwise error probability expression using the decoder

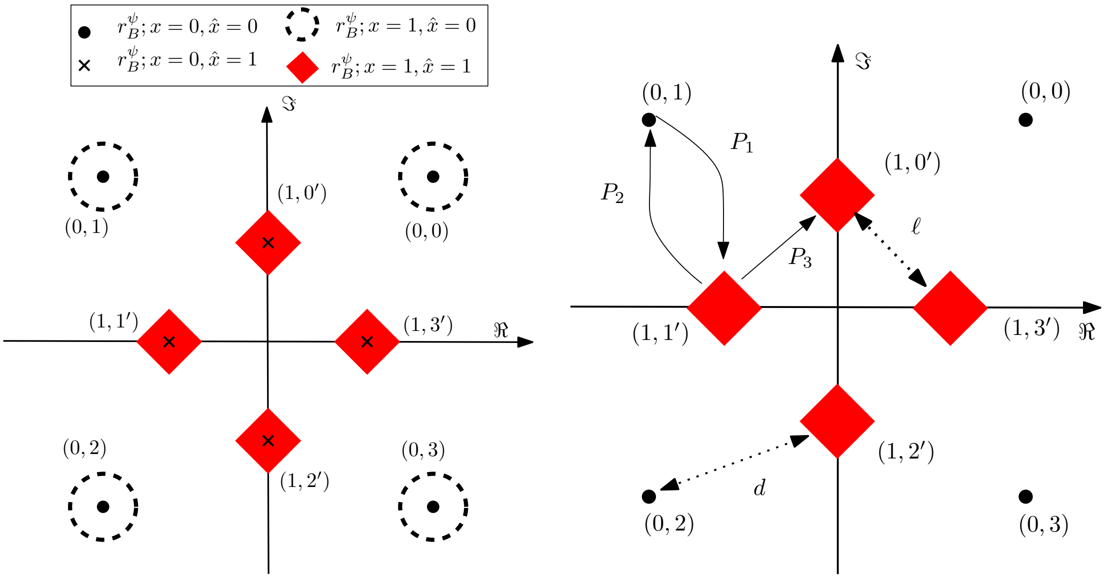

(a) Constellation diagram showing all possible symbols received ((3.5a) – (3.5d)) at Bob when 4-PSK is used at Charlie.

(b) Constellation diagram with dominant terms only, i.e., coefficients of $\Phi_{00,\mathrm{FD}}$ and $\Phi_{11,\mathrm{FD}}$ when 4-PSK scheme is used at Charlie.

Figure 3.5: Constellations diagrams in the SC-F2FD scheme.

in (3.10).

3.5.1 Probability of Error using SC-F2FD JD Decoder

Using the JD decoder defined in (3.10), a transmitted pair (i, j) can be decoded as $(\tilde{i}, \tilde{j})$, where $i \in \{0, 1\}$, and $j \in \{0, 1, \ldots, M-1\}$. Let $\nabla_{(i,j)\to(\tilde{i},\tilde{j})}$ be the event $(\tilde{i}, \tilde{j}) \neq (i, j)$, then a pair (i, j) is incorrectly decoded as $(\tilde{i}, \tilde{j})$ if

$$\nabla_{(i,j)\to(\tilde{i},\tilde{j}))} \triangleq \frac{\mathbf{g_a}\left(r_B | x = i, y = e^{\iota\frac{2\pi}{M}(j+\frac{1}{2})}, h_{CB}\right)}{\mathbf{g_a}\left(r_B | x = \tilde{i}, y = e^{\iota\frac{2\pi}{M}(\tilde{j}+\frac{1}{2})}, h_{CB}\right)} \leq 1. \tag{3.11}$$

Therefore, the probability of decoding a pair $(0, j)$ to $(\tilde{i}, \tilde{j})$ at Bob is given by

$$\begin{aligned}\Pr\left[(0, j) \to (\tilde{i}, \tilde{j})\right] = \Phi_{00,\mathrm{FD}} \Pr\left[\nabla_{(0,j)\to(\tilde{i},\tilde{j})} \leq 1 \middle| r_B = r_{00}^{\psi}\right] \\ + \Phi_{01,\mathrm{FD}} \Pr\left[\nabla_{(0,j)\to(\tilde{i},\tilde{j})} \leq 1 \middle| r_B = r_{01}^{\psi}\right],\end{aligned} \tag{3.12}$$

where r_{00}^{ψ} and r_{01}^{ψ} are r_B when $x = 0; \hat{x} = 0$, and $x = 0; \hat{x} = 1$, respectively in (3.5a) and (3.5b). Similarly, if Alice and Charlie choose a pair $(1, j)$, then the probability of decoding $(1,j)$ as $(\tilde{i},\tilde{j})$ is given as

$$\Pr\left[(1,j)\to(\tilde{i},\tilde{j})\right] = \Phi_{10,\mathrm{FD}}\Pr\left[\nabla_{(1,j)\to(\tilde{i},\tilde{j})}\leq 1\middle| r_B = r_{10}^{\psi}\right] + \Phi_{11,\mathrm{FD}}\Pr\left[\nabla_{(1,j)\to(\tilde{i},\tilde{j})}\leq 1\middle| r_B = r_{11}^{\psi}\right], \quad (3.13)$$

where r_{10}^{ψ}, and r_{11}^{ψ} are r_B when $x=1;\hat{x}=0$, and $x=1;\hat{x}=1$, respectively in (3.5c) and (3.5d). Therefore, the overall probability of error for $2M$ symbols conditioned on the knowledge of h_{CB} is given as

$$\Pr(error|h_{CB}) = \frac{1}{2M}\sum_{i,j}\Pr\left((\hat{i},\hat{j})\neq(i,j)\middle|(i,j)\right), \quad (3.14)$$

where $\Pr\left((\hat{i},\hat{j})\neq(i,j)\middle|(i,j)\right)$ is the conditional probability that Bob decodes a transmitted pair (i,j) as $(\tilde{i},\tilde{j})$. Furthermore, from the union bound in (3.12) and (3.13), we have $\Pr\left((\hat{i},\hat{j})\neq(i,j)\middle|(i,j)\right)\leq\sum_{(i,j)\neq(\tilde{i},\tilde{j})}\Pr\left((i,j)\to(\tilde{i},\tilde{j})\right)$. In the following theorem, we present a high SNR approximation for $\Pr(error|h_{CB})$.

Theorem 1. *For $N_o \ll 1$, the union bound on* (3.14) *is given by:*

$$\Pr(error|h_{CB}) \leq P_{e,Joint} = \Pr((0,1)\to(1,1)) + \Pr((1,1)\to(0,1)) + \Pr((1,1)\to(1,2)). \quad (3.15)$$

Proof. First, $\Pr\left((\hat{i},\hat{j})\neq(0,j)\middle|(0,j)\right)$ is upper bounded as, $\Pr\left((\hat{i},\hat{j})\neq(0,j)\middle|(0,j)\right)\leq 2\Pr((0,j)\to(1,j))$. Note that the pair $(0,1)$ has two nearest neighbours, i.e., $(1,1')$ or $(1,0')$, where $1'$ and $0'$ are the rotated and scaled version of symbol $j=1$ and $j=0$, respectively, as seen in Fig. 3.5b. Therefore, we have $2\Pr((0,j)\to(1,j))$. Due to symmetric constellation and the fact that the contribution of rest of terms is insignificant at high SNR, we apply the same bound on the rest of the terms to obtain

$$\sum_{j=0}^{M-1}\Pr\left((\hat{i},\hat{j})\neq(0,j)\middle|(0,j)\right)\leq 2M\left(\Pr((0,1)\to(1,1))\right). \quad (3.16)$$

Similarly, $\Pr\left((\hat{i},\hat{j})\neq(1,j)\middle|(1,j)\right)\leq 2\Pr((1,j)\to(0,j)) + 2\Pr((1,j)\to(1,\{j+1\}\text{ modulo }M))$. Again, neglecting the contribution of insignificant terms at high SNR and exploiting the symmetry of the constellation we have

$$\sum_{j=0}^{M-1} \Pr\left((\hat{\imath}, \hat{\jmath}) \neq (1, j) \middle| (1, j) \right) \leq 2M \left(\Pr((1,1) \to (0,1)) \right) + \\ 2M \left(\Pr((1,1) \to (1,2)) \right). \quad (3.17)$$

Finally, substituting (3.16) and (3.17) in (3.14), we get (3.15). □

Among the three terms in (3.15), the third term is the error between the intra-constellation symbols of $\sqrt{\alpha} e^{\iota \frac{\pi}{M}} \mathcal{S}_C$ (red diamond), where the minimum Euclidean distance is ℓ. In Fig. 3.5b, when α is small, ℓ is small, thus the error between intra-constellation points dominates (3.15). For larger value of α, ℓ is large but the inter-constellation distance d between $\mathcal{S}_C$ (black circles) and $\sqrt{\alpha} e^{\iota \frac{\pi}{M}} \mathcal{S}_C$ (red diamonds) reduces, and therefore, the first two terms of (3.15) dominate.

Towards deriving the expression for $P_{e,Joint}$, we use (3.12) to compute $\Pr((0,1) \to (1,1))$, and use (3.13) to compute $\Pr((1,1) \to (0,1))$ and $\Pr((1,1) \to (1,2))$. Specifically, (i) when computing $\Pr((0,1) \to (1,1))$ using (3.12), we define P_1 and P_1^c such that, $P_1 = \Pr\left[\nabla_{(0,1)\to(1,1)} \leq 1 \middle| r_B = r_{00}^{\psi} \right]$ and $P_1^c = \Pr\left[\nabla_{(0,1)\to(1,1)} \leq 1 \middle| r_B = r_{01}^{\psi} \right]$, (ii) when computing $\Pr((1,1) \to (0,1))$ using (3.13), we define, P_2 and P_2^c such that, $P_2 = \Pr\left[\nabla_{(1,1)\to(0,1)} \leq 1 \middle| r_B = r_{11}^{\psi} \right]$ and $P_2^c = \Pr\left[\nabla_{(1,1)\to(0,1)} \leq 1 \middle| r_B = r_{10}^{\psi} \right]$, and finally, (iii) when computing $\Pr((1,1) \to (1,2))$ using (3.13), we define P_3 and P_3^c such that, $P_3 = \Pr\left[\nabla_{(1,1)\to(1,2)} \leq 1 \middle| r_B = r_{11}^{\psi} \right]$ and $P_3^c = \Pr\left[\nabla_{(1,1)\to(1,2)} \leq 1 \middle| r_B = r_{10}^{\psi} \right]$. Furthermore, we notice that when computing P_1, P_1^c, P_2 and P_2^c, Marcum-Q functions will be needed, whereas when computing P_3 and P_3^c, regular Q functions will be needed. In the following propositions, we present the expressions for P_1, P_2 and P_3, and their counterparts P_1^c, P_2^c and P_3^c.

Proposition 3. *$P_1 = Q_1\left(\frac{|A|}{\sigma_0}, \frac{\sqrt{\eta}}{\sigma_0} \right)$ and $P_1^c = Q_1\left(\frac{|B|}{\sigma_0}, \frac{\sqrt{\eta}}{\sigma_0} \right)$, where $Q_1(\cdot, \cdot)$ is the standard Marcum-Q function, and the parameters η, A, B and σ_0 are as defined in the proof of this proposition.*

Proof. Using (3.11), we can write P_1 as

$$P_1 = \Pr\left\{ \frac{\frac{\Phi_{00,\mathrm{FD}}}{\pi N_{B0}} e^{-\frac{|r_B - y\ h_{CB}|^2}{N_{B0}}}}{\frac{\Phi_{11,\mathrm{FD}}}{\pi N_{B1}} e^{-\frac{|r_B - \sqrt{\alpha} e^{\iota \frac{\pi}{M}} y\ h_{CB}|^2}{N_{B1}}}} < 1 \middle| r_B = h_{CB} y + n_B \right\} = Q_1\left(\frac{|A|}{\sigma_0}, \frac{\sqrt{\eta}}{\sigma_0} \right),$$

where $\gamma = |h_{CB}|$, $d = \sqrt{1+\alpha-2\sqrt{\alpha}\cos\frac{\pi}{M}}$, $\sigma_0 = \sqrt{\frac{N_{B0}}{2}}$, $A = \frac{\gamma d N_{B0}}{N_{B0}-N_{B1}}$, and $\eta = \frac{N_{B0}N_{B1}}{N_{B0}-N_{B1}}\left[\ln\left(\frac{N_{B0}\Phi_{11,\text{FD}}}{N_{B1}\Phi_{00,\text{FD}}}\right)+\frac{\gamma^2 d^2}{N_{B0}-N_{B1}}\right]$. Similarly, using (3.11), we can write P_1^c as

$$\Pr\left\{ \frac{\frac{\Phi_{00,\text{FD}}}{\pi N_{B0}} e^{-\frac{|r_B - y\, h_{CB}|^2}{N_{B0}}}}{\frac{\Phi_{11,\text{FD}}}{\pi N_{B1}} e^{-\frac{|r_B - \sqrt{\alpha} e^{\iota\frac{\pi}{M}} y\, h_{CB}|^2}{N_{B1}}}} < 1 \,\middle|\, r_B = \sqrt{\alpha} h_{CB} e^{\iota\frac{\pi}{M}} y + n_B \right\}.$$

Thus, $P_1^c = Q_1\left(\frac{|B|}{\sigma_0}, \frac{\sqrt{\eta}}{\sigma_0}\right)$, where, $B = \frac{\gamma d N_{B1}}{N_{B0}-N_{B1}}$. ☐

Proposition 4. *$P_2 = 1 - Q_1\left(\frac{|B|}{\sigma_1}, \frac{\sqrt{\eta}}{\sigma_1}\right)$ and $P_2^c = 1 - Q_1\left(\frac{|A|}{\sigma_1}, \frac{\sqrt{\eta}}{\sigma_1}\right)$, where $\sigma_1 = \sqrt{\frac{N_{B1}}{2}}$, and η, A, B are as defined in Proposition 3.*

Proposition 5. *$P_3 = Q\left(\frac{\gamma \ell}{\sqrt{2N_{B1}}}\right)$ is the regular Q function, and $P_3^c = \frac{1}{2}$, where $\ell = 2\sqrt{\alpha}\sin\frac{\pi}{M}$ is the distance between two adjacent PSK symbols, and γ is defined in Proposition 3.*

Along the similar lines of the proof of Proposition 3, we can prove the above propositions using (3.11), and the definitions of P_2, P_2^c, P_3 and P_3^c. Substituting the results of the Proposition 3, Proposition 4, and Proposition 5 in (3.15), we obtain the closed form expression for $P_{e,Joint}$ as

$$P_{e,Joint} = \Phi_{00,\text{FD}}P_1 + \Phi_{01,\text{FD}}P_1^c + \Phi_{10,\text{FD}}P_2^c + \Phi_{11,\text{FD}}P_2 + \Phi_{10,\text{FD}}P_3^c + \Phi_{11,\text{FD}}P_3. \quad (3.18)$$

Further, averaging (3.18) over $|h_{CB}|^2$, we obtain $\overline{P}_{e,Joint} \triangleq \mathbb{E}_{|h_{CB}|^2}\left[P_{e,Joint}\right]$ given by

$$\begin{aligned}\overline{P}_{e,Joint} = {} & \Phi_{00,\text{FD}}\mathbb{E}_{|h_{CB}|^2}\left[P_1\right] + \Phi_{01,\text{FD}}\mathbb{E}_{|h_{CB}|^2}\left[P_1^c\right] + \Phi_{10,\text{FD}}\mathbb{E}_{|h_{CB}|^2}\left[P_2^c\right] \\ & + \Phi_{11,\text{FD}}\mathbb{E}_{|h_{CB}|^2}\left[P_2\right] + \Phi_{11,\text{FD}}\mathbb{E}_{|h_{CB}|^2}\left[P_3\right] + \Phi_{10,\text{FD}}\frac{1}{2}. \quad (3.19)\end{aligned}$$

The expression for $\overline{P}_{e,Joint}$ is a function of α, where α is the energy-splitting factor between Alice and Charlie. The value of α for which $\overline{P}_{e,Joint}$ is minimised is the optimal value of the energy-splitting factor. In the next section, we show that the optimal values of α corresponding to the Joint MAP (JMAP) decoder, the Joint MAX (JMAX) decoder, and the JD decoder are very close.

3.5.2 Validation of SC-F2FD JD Decoder

In this section, we simulate the average error performance of the JMAP decoder, the JMAX decoder, and the JD decoder given in (3.6), (3.9), and (3.10), respectively, w.r.t. α, to show that their error performance exhibit similar nature. For the simulations, we use the SI parameter $\lambda = 10^{-5}$ in addition to the system parameters defined in Sec. 3.3.1. In Fig. 3.6, for 4- and 8-PSK at 35 dB, the plots show that the joint error is high at extreme value of α. From $\alpha = 0$, with increasing values of α, Charlie pours more energy on his transmitted symbols, and thus Bob is less likely to introduce error in decoding Charlie's symbol, and at an intermediate value of α close to 1 the joint error of Alice and Charlie is minimum. We also empirically plot the expression $\overline{P}_{e,Joint}$ given in (3.19), shown as SC-F2FD JD decoder union bound (bottom right). We observe that the joint error of all the decoders have a global minima, and the values of α for which the decoders experience minima is towards larger values of α. Let $\alpha^{\dagger} \in (0, 1)$ minimise (3.19). Analytically computing $\alpha^{\dagger}$ requires computation of $\mathbb{E}_{|h_{CB}|^2}\left[P_l\right]$ and $\mathbb{E}_{|h_{CB}|^2}\left[P_l^c\right]$ for $l \in \{1, 2, 3\}$, and then setting the derivative of (3.19) w.r.t. α to 0. However, we note that P_l, and P_l^c, $l \in \{1, 2\}$ are Marcum-Q functions, and the exact expressions on the averages of these functions are intractable. Therefore, we exploit the dominance of error terms in (3.19) and compute an approximation to $\alpha^{\dagger}$ using an alternate method.

3.5.3 Dominant Error Events and a Near-Optimal Solution

We simplify the expression in (3.19) as

$$\overline{P}_{e,Joint} = \mathbb{E}_{|h_{CB}|^2}\left[P_1\right] + \Phi_{10,\mathrm{FD}}\mathbb{E}_{|h_{CB}|^2}\left[P_2^c\right] + \Phi_{11,\mathrm{FD}}\mathbb{E}_{|h_{CB}|^2}\left[P_2\right] + \\ \Phi_{10,\mathrm{FD}}\frac{1}{2} + \Phi_{11,\mathrm{FD}}\mathbb{E}_{|h_{CB}|^2}\left[P_3\right], \quad (3.20)$$

where we use Lemma 1 and Lemma 2 to apply $\Phi_{00,\mathrm{FD}}P_1 + \Phi_{01,\mathrm{FD}}P_1^c \approx P_1$.

Lemma 4. *For $N_o \ll 1$, an approximation for $\mathbb{E}_{|h_{CB}|^2}\left[P_3\right]$ is given by $\frac{2N_{B1}}{4N_{B1}+\ell^2}$ and an approximation on $\mathbb{E}_{|h_{CB}|^2}\left[P_1\right]$ is given by $\left(\frac{N_{B0}\Phi_{11,\mathrm{FD}}}{N_{B1}\Phi_{00,\mathrm{FD}}}\right)^{\frac{N_{B1}}{N_{B1}-N_{B0}}} \frac{(N_{B1}-N_{B0})^2}{(N_{B1}-N_{B0})^2+d^2N_{B1}}$.*

Proof. On observing the expression of P_1 in Proposition 3, the parameters of P_1 are such that $\frac{|A|}{\sigma_0} < \frac{\sqrt{\eta}}{\sigma_0}$. Further, due to unavailability of closed form expression on Marcum-

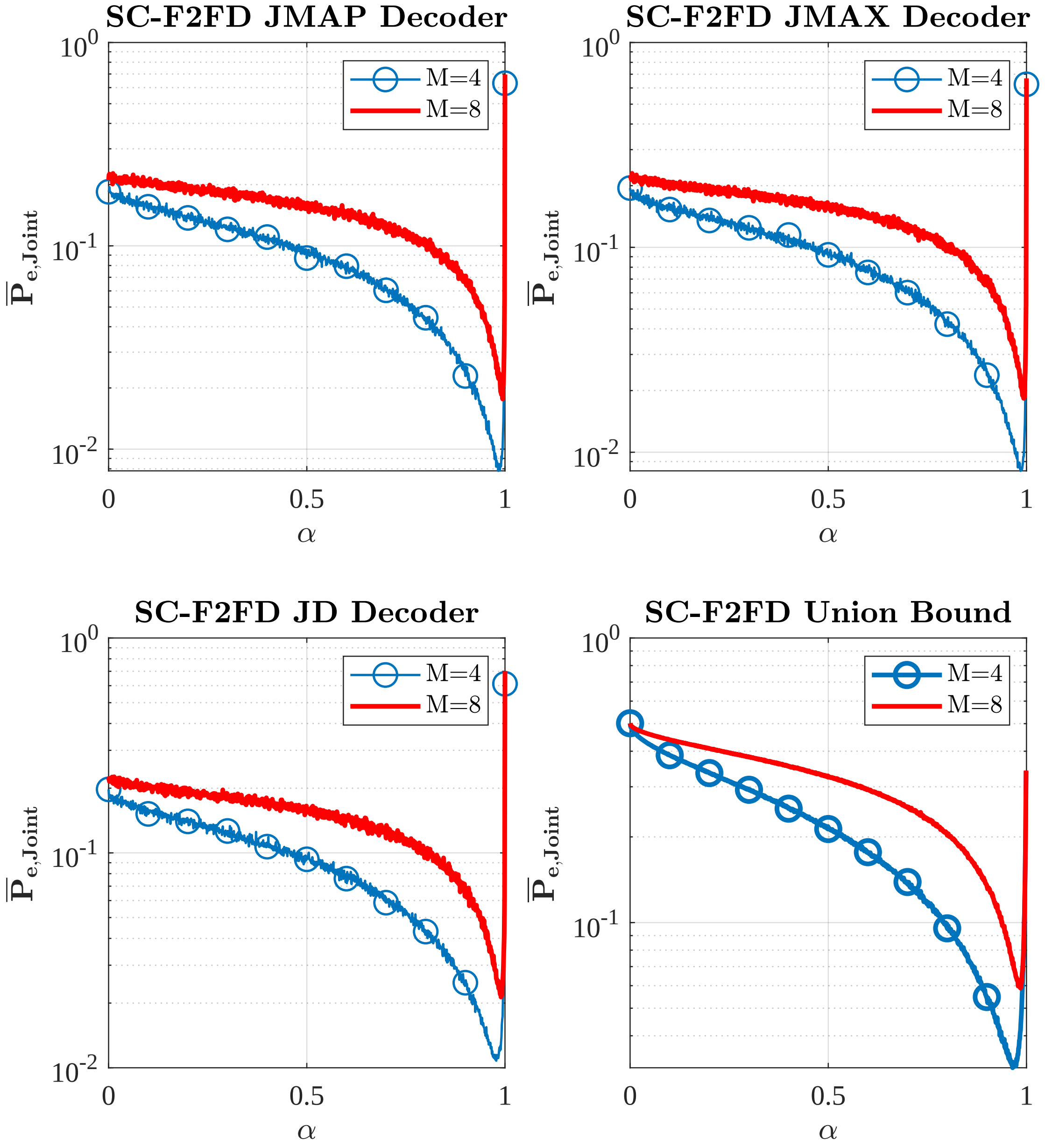

Figure 3.6: Average error performance of JMAP, JMAX, and JD decoder as a function of $\alpha \in (0, 1)$ at 35 dB for 4- and 8-PSK used by Charlie. Each decoder (along with the union bound in (3.18)) experiences a dip which is close to $\alpha = 1$.

Q function, we upper bound P_1 as $e^{\left(-\frac{1}{2}\left(\frac{\sqrt{\eta}}{\sigma_0}-\frac{|A|}{\sigma_0}\right)^2\right)}$ using results in [108]. The bound becomes tighter when we drop $\frac{|A|}{\sigma_0}$ from the exponent thus, $\mathbb{E}_{|h_{CB}|^2}\left[P_1\right] \leq e^{\left(-\frac{1}{2}\frac{\sqrt{\eta}}{\sigma_0}\right)^2}$. Averaging over $|h_{CB}|^2$, gives

$$P_{1,avg} \triangleq \left(\frac{N_{B0}\Phi_{11,\mathrm{FD}}}{N_{B1}\Phi_{00,\mathrm{FD}}}\right)^{\frac{N_{B1}}{N_{B1}-N_{B0}}} \frac{\left(N_{B1}-N_{B0}\right)^2}{\left(N_{B1}-N_{B0}\right)^2+d^2N_{B1}}.$$

To compute $\mathbb{E}_{|h_{CB}|^2}\left[P_3\right]$ we first use Chernoff bound on P_3, and then average it over $|h_{CB}|^2$. □

After obtaining the closed form expressions on an approximation of $\mathbb{E}_{|h_{CB}|^2}\left[P_1\right]$ denoted by, $P_{1,avg}$ and $\mathbb{E}_{|h_{CB}|^2}\left[P_3\right]$ denoted by $P_{3,avg}$, we can compare the two in the next theorem.

Theorem 2. *Let $\varsigma = \cos\frac{\pi}{M}$, where M is the size of PSK constellation such that $(1-\varsigma^2) = \mu N_o$, where $\mu \gg 1$, then we have the inequality $P_{1,avg} < \Phi_{11,\mathrm{FD}}P_{3,avg} + \Phi_{10,\mathrm{FD}}\frac{1}{2}$.*

Proof. We first prove that, $P_{1,avg} < P_{3,avg}$ or $\frac{2N_{B1}}{4N_{B1}+\ell^2} > \left(\frac{N_{B0}\Phi_{11,\mathrm{FD}}}{N_{B1}\Phi_{00,\mathrm{FD}}}\right)^{\frac{N_{B1}}{N_{B1}-N_{B0}}} \frac{(N_{B0}-N_{B1})^2}{(N_{B0}-N_{B1})^2+N_{B1}d^2}$. Further, we have an upper bound on $P_{1,avg}$ as, $P_{1,avg} \leq \left(\frac{N_{B0}\Phi_{11,\mathrm{FD}}}{\Phi_{00,\mathrm{FD}}}\right)^{\frac{N_{B1}}{N_{B1}-N_{B0}}} \frac{(1-\alpha)}{2-2\sqrt{\alpha}\cos\frac{\pi}{M}}$. Let $1-\alpha = \rho N_o$, then

$$P_{1,avg} < \left(\frac{\Phi_{11,\mathrm{FD}}}{(1+\rho)\Phi_{00,\mathrm{FD}}}\right)^{\frac{1+\rho}{\rho}} \frac{\rho N_o}{2-2\sqrt{1-\rho N_o}\cos\frac{\pi}{M}} \tag{3.21}$$

$$P_{1,avg} < (1+\rho)^{-\frac{1+\rho}{\rho}} \frac{\rho N_o}{2-2\sqrt{1-\rho N_o}\cos\frac{\pi}{M}} \tag{3.22}$$

where the second inequality is applicable from Lemma 2, $\Phi_{11,\mathrm{FD}} < \Phi_{00,\mathrm{FD}}, \forall\alpha$. Also, $P_{3,avg}$ is rewritten as

$$P_{3,avg} = \frac{(\rho+1)N_o}{N_o(2(1+\rho)-2\rho(1-\varsigma^2))+2(1-\varsigma^2)}, \tag{3.23}$$

where $\varsigma = \cos\frac{\pi}{M}$. In rest of the proof, we will prove that either (3.21), or (3.22) is less than (3.23) considering various values of ρ, i.e., $\rho = 1$, $\rho < 1$, and $\rho > 1$. For $\rho = 1$, (3.22) reduces to $\frac{1}{8}\frac{N_o}{1-\varsigma}$ by substituting $\rho = 1$ and upper bounding $(1-\rho N_o)$ by 1. Also (3.23) can be simplified as $\frac{N_o}{N_o(1+\varsigma^2)+(1-\varsigma^2)}$. Further, since, $1-\varsigma^2 = \mu N_o$, where $\mu >> 1$, $N_o(1+\varsigma^2) < 1-\varsigma^2$, (3.23) can be lower bounded as $\frac{N_o}{2(1-\varsigma^2)}$. Therefore, we can easily conclude that $\frac{1}{8}\frac{N_o}{1-\varsigma} < \frac{1}{2}\frac{N_o}{1-\varsigma^2}\ \forall\ 0 \leq \alpha \leq 1$.

For, $\rho < 1$, first term in (3.22) is upper bounded as $(1+\rho)^{-\frac{1+\rho}{\rho}} < e^{-1}$, therefore, (3.22) is upper bounded as $\frac{1}{5.42}\frac{\rho N_o}{1-\varsigma}$. Further, $\frac{1}{5.42}\frac{\rho N_o}{1-\varsigma} = \frac{\rho(1+\varsigma)}{5.42\mu} < \frac{2\rho}{5.42\mu}$. Also, in the first term in denominator of (3.23), we have the bound $N_o(2(1+\rho) - 2\rho(1-\varsigma^2)) < N_o(2(1+\rho)) < 4N_o$. Thus, (3.23) is lower bounded as $\frac{(\rho+1)}{2(2+\mu)}$. We can immediately infer that $\frac{(\rho+1)}{2(2+\mu)} > \frac{2\rho}{5.42\mu}$ when $\mu >> 1$ and for $\rho < 1$. This completes the case of $\rho < 1$. Finally, we split the case of $\rho > 1$ into two parts, namely, (i) $1 < \rho \leq 3$, and (ii) $\rho > 3$. For $1 < \rho \leq 3$, the first term of denominator of (3.23) is upper bounded as $8N_o$, and therefore, (3.23) is lower bounded as $\frac{\rho+1}{2(4+\mu)}$. Furthermore, upper bounding (3.22) on similar lines gives us $(1+\rho)^{-\frac{1+\rho}{\rho}}\frac{\rho(1+\varsigma)}{2\mu} < (1+\rho)^{-\frac{1+\rho}{\rho}}\frac{\rho}{\mu}$. From this discussion we can conclude that, $(1+\rho)^{-\frac{1+\rho}{\rho}}\frac{\rho}{\mu} < \frac{\rho+1}{2(4+\mu)}$. This inequality holds good because $(1+\rho)^{-\frac{1+\rho}{\rho}}$ is a decreasing function of ρ and is upper bounded by $\frac{1}{4}$.

For $\rho > 3$, $N_o(2(1+\rho) - 2\rho(1-\varsigma^2)) < 2(1-\varsigma^2)$, which lower bounds (3.23) $\frac{(\rho+1)N_o}{4(1-\varsigma^2)} = \frac{1+\rho}{4\mu}$, and (3.22) upper bounded as $(1+\rho)^{-\frac{1+\rho}{\rho}}\frac{\rho N_o}{2(1-\varsigma)}$,in which the term $(1+\rho)^{-\frac{1+\rho}{\rho}} < \left(\frac{1}{4}\right)^{\frac{4}{3}}$, and $\frac{\rho N_o}{2(1-\varsigma)} = \frac{\rho N_o(1+\varsigma)}{2(1-\varsigma^2)} < \frac{\rho}{\mu}$. It is now straightforward to prove that $\frac{0.157\rho}{\mu} < \frac{0.25(\rho+1)}{\mu}$, $\forall$, $0 < \varsigma < 1$, and $\rho > 3$. Additionally, for same $\rho > 3$, and $\rho \leq \mu$ but $N_o(2(1+\rho) - 2\rho(1-\varsigma^2)) > 2(1-\varsigma^2)$, then (3.23) is lower bounded as $\frac{(1+\rho)N_o}{2N_o[2(1+\rho)-2\rho(1-\varsigma^2)]} > \frac{(1+\rho)N_o}{4N_o(1+\rho)} = \frac{1}{4}$. Therefore, $\frac{0.157\rho}{\mu} < \frac{1}{4}$. Now for $\rho > 3$ and also, $\rho > \mu$, i.e., for larger values of ρ, $(1+\rho)^{-\frac{1+\rho}{\rho}} < (1+\rho)^{-1}$, and (3.22) is upper bounded by $\frac{1}{1+\rho}\frac{\rho}{\mu} < \frac{1}{\mu}$. We can clearly see that, $\frac{1}{\mu} < \frac{1}{4}$, because $\mu \gg 1$. $\square$

As a result of Theorem 2, we neglect the contribution of $\mathbb{E}_{|h_{CB}|^2}[P_1]$ in (3.20). Thus, we have an expression that only contains the dominant probability events, denoted by $\overline{P}_{e,dom}$ given as

$$\overline{P}_{e,dom} = \Phi_{11,\text{FD}}\left(\mathbb{E}_{|h_{CB}|^2}[P_2] + P_{3,avg}\right) + \Phi_{10,\text{FD}}\left(\mathbb{E}_{|h_{CB}|^2}[P_2^c] + \frac{1}{2}\right). \tag{3.24}$$

Towards optimizing (3.24), the problem in computing the average of Marcum-Q functions over $|h_{CB}|^2$ still persists as we have $\mathbb{E}_{|h_{CB}|^2}[P_2]$ and $\mathbb{E}_{|h_{CB}|^2}[P_2^c]$ in (3.24). Using numerical integration techniques we observed that $\Phi_{11,\text{FD}}\left(\mathbb{E}_{|h_{CB}|^2}[P_2] + P_{3,avg}\right)$ is a decreasing function of α, whereas $\Phi_{10,\text{FD}}\left(\mathbb{E}_{|h_{CB}|^2}[P_2^c] + \frac{1}{2}\right)$ is an increasing function of α. We also note that, the intersection of these terms was close to $\alpha^{\dagger}$. Furthermore, we observed that we can propose lower bounds on $\Phi_{11,\text{FD}}\left(\mathbb{E}_{|h_{CB}|^2}[P_2] + P_{3,avg}\right)$ and $\Phi_{10,\text{FD}}\left(\mathbb{E}_{|h_{CB}|^2}[P_2^c] + \frac{1}{2}\right)$ that also intersected close to $\alpha^{\dagger}$ while retaining their increasing and decreasing nature, respectively. With this key insight and the fact that the exact expressions of $\mathbb{E}_{|h_{CB}|^2}\left[P_2\right]$ and $\mathbb{E}_{|h_{CB}|^2}\left[P_2^c\right]$ are unavailable, we propose lower bounds on the terms, $\Phi_{11,\mathrm{FD}}\left(\mathbb{E}_{|h_{CB}|^2}\left[P_2\right]+P_{3,avg}\right)$ and $\Phi_{10,\mathrm{FD}}\left(\mathbb{E}_{|h_{CB}|^2}\left[P_2^c\right]+\frac{1}{2}\right)$, and then prove that the lower bounds are also decreasing and increasing functions of α, respectively. Subsequently, we prove that the lower bounds on $\Phi_{11,\mathrm{FD}}\left(\mathbb{E}_{|h_{CB}|^2}\left[P_2\right]+P_{3,avg}\right)$ and $\Phi_{10,\mathrm{FD}}\left(\mathbb{E}_{|h_{CB}|^2}\left[P_2^c\right]+\frac{1}{2}\right)$ have a unique intersection. We denote the intersection of the lower bounds as α^*. In that direction, first, we provide a lower bound on $\mathbb{E}_{|h_{CB}|^2}\left[P_2^c\right]$.

Proposition 6. *The term $\mathbb{E}_{|h_{CB}|^2}\left[P_2^c\right]$ is lower bounded as $\mathbb{E}_{|h_{CB}|^2}\left[P_2^c\right] > P_{2,avg}^c$, such that $P_{2,avg}^c = \frac{4d^2(N_{B0})^2}{4d^2(N_{B0})^2+N_{B1}(N_{B0}-N_{B1})^2}$.*

Proof. Using the results in [108], we lower bound P_2^c by upper bounding the Marcum-Q function. Therefore, $P_2^c \geq 1-e^{-\frac{1}{2}\left(\frac{\sqrt{\eta}}{\sigma_1}-\frac{|A|}{\sigma_1}\right)^2}$. Further, we can show that $\frac{\sqrt{\eta}}{\sigma_1} > 3\frac{|A|}{\sigma_1}$, therefore, we bound P_2^c more tightly as $P_2^c \geq 1-e^{-2\left(\frac{|A|}{\sigma_1}\right)^2}$. Lastly, to compute the $\mathbb{E}_{|h_{CB}|^2}\left[P_2^c\right]$, we average the obtained bound over $|h_{CB}|^2$. □

Furthermore, a straightforward lower bound on the coefficient of $\Phi_{11,\mathrm{FD}}$ in (3.24) is given by $\mathbb{E}_{|h_{CB}|^2}\left[P_2\right]+P_{3,avg} \geq P_{3,avg}$. In Lemma 5 we prove that $P_{3,avg}$ is a decreasing function of α. Similarly, in Lemma 6 we prove that the lower bound on $\Phi_{10,\mathrm{FD}}\left(\mathbb{E}_{|h_{CB}|^2}\left[P_2^c\right]+\frac{1}{2}\right)$ is an increasing function of α.

Lemma 5. *The expression for $P_{3,avg}$ is a decreasing function of α.*

Proof. From Lemma 4 we have $P_{3,avg}$, and differentiating $P_{3,avg}$ w.r.t. α gives us

$$\frac{1}{2}\frac{\left[-N_o-1+\alpha\left(1-\sin^2\frac{\pi}{M}\right)\right]+\left[\left(N_o+1-\alpha\right)\left(1-\sin^2\frac{\pi}{M}\right)\right]}{\left[N_o+1-\alpha\left(1-\sin^2\frac{\pi}{M}\right)\right]^2}$$

The denominator of $\frac{dP_{3,avg}}{d\alpha}$ is always positive. Furthermore, the numerator of $\frac{dP_{3,avg}}{d\alpha}$ simplifies to $-(N_o+1)\sin^2\frac{\pi}{M}$. Therefore, we conclude that $\frac{dP_{3,avg}}{d\alpha}$ is always negative and thus, $P_{3,avg}$ is a decreasing function. □

Remark 1. *From Lemma 3, $\Phi_{11,\mathrm{FD}}$ is a decreasing function, therefore, $\Phi_{11,\mathrm{FD}}P_{3,avg}$ is a decreasing function.*

Lemma 6. *Let $\varsigma = \cos(\frac{\pi}{M})$, where M is the size of the PSK constellation such that $(1-\varsigma^2) = \mu N_o$, where $\mu \gg 1$. When $\alpha \in (\varsigma^2, 1)$, $P_{2,avg}^c$ is an increasing function of α, and when $\alpha \in (0, \varsigma^2)$, we have $P_{2,avg}^c + 0.5 \approx 0.5$.*

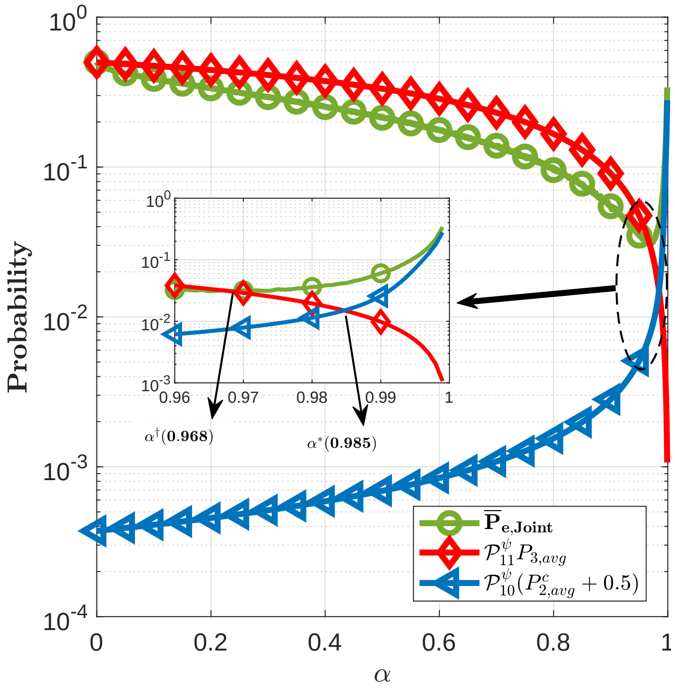

Figure 3.7: The intersection of $\Phi_{11,\mathrm{FD}}P_{3,avg}$ and $\Phi_{10,\mathrm{FD}}\left(P^{c}_{2,avg}+0.5\right)$ and the actual minima of (3.18) at 35 dB.

Proof. When $\alpha \in (\varsigma^2, 1)$, we note that d^2 is an increasing function of α. Also, the term $P^{c}_{2,avg}$ can be rewritten as, $\frac{4N_o^2}{4N_o^2+\frac{(N_o+(1-\alpha))(1-\alpha)^2}{d^2}}$. Since d^2 is an increasing function in $\alpha \in (\varsigma^2, 1)$, and the term $(N_o + (1-\alpha))(1-\alpha)^2$ is a decreasing function of $\alpha \in (0, 1)$, the fraction $\frac{(N_o+(1-\alpha))(1-\alpha)^2}{d^2}$ is a decreasing function of α in the range $\alpha \in (\varsigma^2, 1)$. This completes the proof that $P^{c}_{2,avg}$ is an increasing function of α when $\alpha \in (\varsigma^2, 1)$. For the second part, the term $P^{c}_{2,avg}$ is upper bounded as $\frac{4d^2N_o^2}{(N_o+(1-\alpha))(1-\alpha)^2+4\mu N_o^3}$. By using the lower bound $d^2 \geq 1-\varsigma^2 = \mu N_o$ in the second term of the denominator. Furthermore, we can upper bound d^2 in the numerator by $1-\alpha$ by using the lower bound $\varsigma > \sqrt{\alpha}$ in the range $\alpha \in (0, \varsigma^2)$. Let us also denote $(1-\alpha) = \rho N_o$, where $\rho > 0$. With that the upper bound can be written as, $\frac{4\rho N_o^3}{N_o^3(\rho^3+\rho^2)+4\mu N_o^3} = \frac{4\rho}{(\rho^3+\rho^2+4\mu)}$, where $\rho \geq \mu$ since $\alpha \leq \varsigma^2$ and $1-\varsigma^2 = \mu N_o$. Finally, since $\rho \geq \mu >> 1$, $\frac{4\rho}{(\rho^3+\rho^2+4\mu)}$ is negligible, and therefore, $P^{c}_{2,avg} + 0.5 \approx 0.5$. $\square$

From Lemma 5, 6, we have shown that $\Phi_{11,\mathrm{FD}}P_{3,avg}$ and $\Phi_{10,\mathrm{FD}}\left(P^{c}_{2,avg}+\frac{1}{2}\right)$ are indeed decreasing and increasing functions of α, respectively. While we aim to find the intersection of these functions, it is essential to prove that they intersect at only one point, that is denoted by α^*.

Theorem 3. *Let* $\beta(\alpha) = \beta_1(\alpha) - \beta_2(\alpha)$, *where* $\beta_1(\alpha) = \Phi_{11,\mathrm{FD}}P_{3,avg}$ *and* $\beta_2(\alpha) = \Phi_{10,\mathrm{FD}}\left(P^{c}_{2,avg}+\frac{1}{2}\right)$, *then* $\beta(\alpha)$ *has a unique root.*

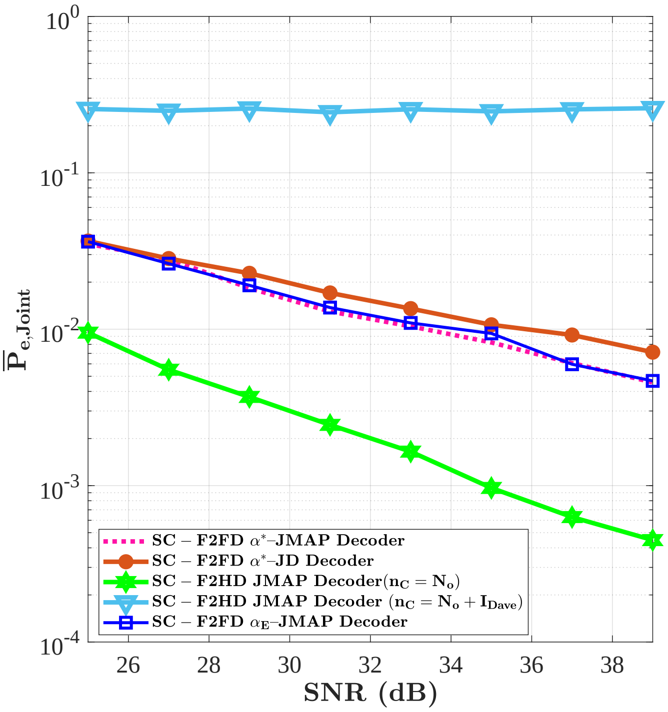

Figure 3.8: Comparison of average error performance of JMAP and JD decoder for SC-F2FD and JMAP decoder for SC-F2HD, at high SNRs.

Proof. We can evaluate that, $\beta_1(\alpha = 0) = \Phi_{11,\text{FD}}(\alpha = 0)P_{3,avg}(\alpha = 0) = \frac{1}{2}$ and $\beta_2(\alpha = 0) = \Phi_{10,\text{FD}}(\alpha = 0)\left(P^c_{2,avg}(\alpha = 0) + \frac{1}{2}\right) < \frac{1}{2}$, where the second inequality is because, $\Phi_{01,\text{FD}}(\alpha = 0) \ll 1$, and from Lemma 6, $P^c_{2,avg} + \frac{1}{2} \approx \frac{1}{2}$ for $\alpha = 0$. Similarly, $\beta_1(\alpha = 1) = \Phi_{11,\text{FD}}(\alpha = 1)P_{3,avg}(\alpha = 1) = N_o e^{-1}$ and $\beta_2(\alpha = 1) = \Phi_{10,\text{FD}}(\alpha = 1)\left(P^c_{2,avg}(\alpha = 1) + \frac{1}{2}\right) \approx \frac{3}{2}(1 - e^{-1})$. Thus, $\beta(\alpha = 0) = \beta_1(\alpha = 0) - \beta_2(\alpha = 0) > 0$, and $\beta(\alpha = 1) = \beta_1(\alpha = 1) - \beta_1(\alpha = 1) < 0$. Finally, it is also evident that $\beta(\alpha)$ is a decreasing function of α, and therefore, it has a unique root. $\square$

Finally, we compute α^* using Newton-Raphson (NR) algorithm [109]. We present the simulation results for the SC-F2FD JD decoder in the next section.

3.6 Simulation Results on the Performance of SC-F2FD Relaying Scheme

We present simulation results on the SC-F2FD relaying scheme, and showcase its efficacy in combating the cognitive adversary. We use the system model discussed in Sec. 3.4.1, and use the simulation parameters as in Sec. 3.3. Further, we assume that Charlie uses 4-PSK constellation and the SI parameter at his receiving antenna

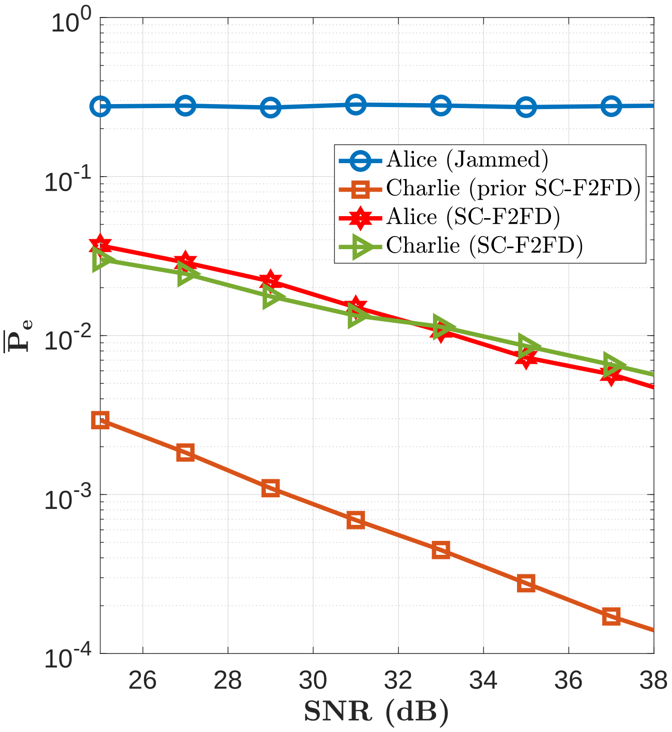

Figure 3.9: Individual performance using α^* as energy-splitting factor: Charlie uses 4-PSK constellation and has $\lambda = 10^{-5}$ as residual SI.

is $\lambda = 10^{-5}$. We first show the accuracy in computing the energy-splitting factor explained in Sec. 3.5.3. In Fig. 3.7, we plot the expression of $\overline{P}_{e,Joint}$ given in (3.19) as a function of α at 35 dB. The plot shows that $\overline{P}_{e,Joint}$ experiences a minima when $\alpha = \alpha^{\dagger}$. We also plot the lower bounds obtained in Lemma 5 and Lemma 6 to show that the intersection point (denoted by α^*) evaluated via NR algorithm, is close to $\alpha^{\dagger}$. It is evident that difference between $\alpha^{\dagger}$ and α^* is very small. In the next set of results, we show that this difference does not have a considerable impact on the overall error performance.

In Fig. 3.8, we plot the error performance of the SC-F2FD α^*-JMAP decoder given in (3.2) and the SC-F2FD α^*-JD decoder given in (3.10). Here the prefix α^* denotes that these decoders are implemented when α^*, obtained from the NR algorithm, is used for the SC-F2FD scheme. We also plot α_E-JMAP decoder, wherein α_E minimises the joint error of the JMAP decoder. We obtain the value of α using an exhaustive search that minimises (3.18). The search resolution for α_E is 0.001 for $0 < \alpha < 1$. The plots show that the performances of the α_E-JMAP decoder and the α^*-JMAP decoder almost overlaps, thus showing the accuracy of α^*. We also plot the performance of the α^*-JD decoder, and as expected, it is clear that the JD decoder provides a suboptimal, yet a near-optimal solution. Finally, we also compare the performance of the SC-F2HD and

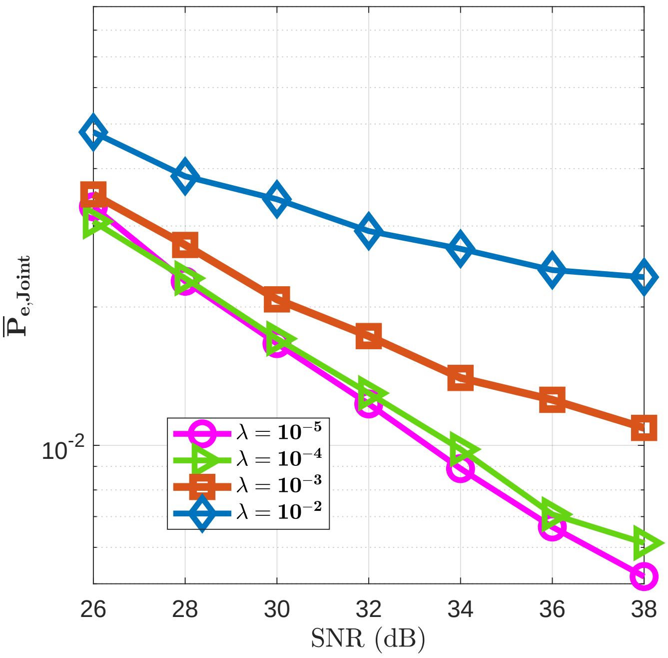

Figure 3.10: Joint error performance at Bob using α^*-JMAP decoder for various degree of residual SI at Charlie.

the SC-F2FD relaying schemes. For SC-F2HD, when the interference from Dave at Charlie is negligible, SC-F2HD vastly outperforms SC-F2FD relaying scheme. However, when the interference from Dave is significant, error floor is observed at Bob. In contrast, SC-F2FD scheme is invariant to the effect of interference from Dave as both Alice and Charlie operate on f_{CB}.

We also use α^*-JMAP decoder to plot the individual error performances of Alice and Charlie at Bob. In Fig. 3.9, we observe that when Dave jams Alice to prior to countermeasure, Bob observes an error floor while decoding Alice's bits. However, after implementing SC-F2FD, the error performance of Alice drastically improves. On the contrary, the performance of Charlie degrades after he helps Alice. Therefore, a trade-off exists between the error performance of the victim node and the helper node. In the last part of this section, we present simulation results on SC-F2FD when practical FD radios with non-negligible SI is used. In Fig. 3.10, we plot the average error performance of Alice and Charlie at Bob when using the α^*-JMAP decoder for various levels of SI cancellation. It is evident from Fig. 3.10 that, for lower values of λ, which captures low residual SI, the joint error performance is relatively good. However, for large λ, Charlie introduces decoding errors at his end, which in turn propagates to Bob. For instance, the plots in Fig. 3.11, show the individual performance of Alice and Charlie for $\lambda = 10^{-3}$ using α^*-JMAP decoder. It is noticed that the performance of

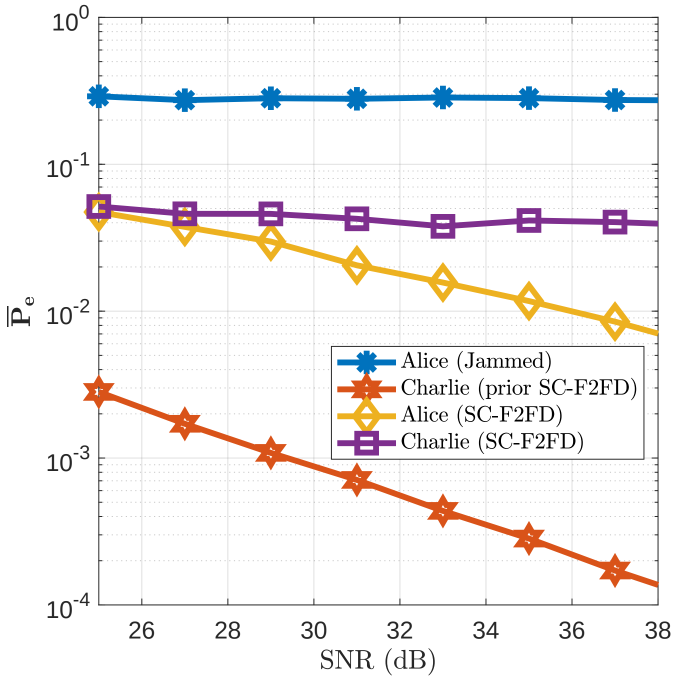

Figure 3.11: Plots showcasing the effect on the average error performance of Alice and Charlie when FD radio at Charlie has large residual SI ($\lambda = 10^{-3}$).

Alice improves, however, the performance of Charlie degrades. The reason for such a behaviour is attributed to large SI, because of which Charlie introduces error in decoding Alice's bit. Therefore, Alice has to increase her transmission energy which in turn forces Charlie to operate at lower value of α^*.

3.7 Covertness Analysis of the Relaying Schemes

In this section, we show that the proposed countermeasures are effective in engaging the cognitive attacker on f_{AB} while facilitating Alice to reliably communicate with Bob on f_{CB}. As a cognitive adversary, Dave uses energy-sensing on f_{AB} to detect a countermeasure. To model a strong adversary, we assume that the FD radio at Dave offers perfect SI cancellation. When no countermeasure is used, let $\mathcal{E}_n = \frac{1}{n}\sum_{k=1}^{n} |r_{D,k}|^2$ be the average received energy measured at Dave using a frame containing n symbols, where $r_{D,k}$ is the k^{th} baseband received symbol at Dave, given by $r_{D,k} = h_{AD,k}x_k + n_{D,k}$, where $x_k \in \mathcal{S}_A$, $n_{D,k}$ is the AWGN distributed as $\mathcal{CN}(0, N_o)$, and $h_{AD,k}$ is the Alice-to-Dave channel distributed as $\mathcal{CN}(0,1)$. Note that from weak law of large number, we have $\frac{1}{n}\sum_{k=1}^{n} |r_{D,k}|^2 \rightarrow \mathcal{E}_{AB}$ in probability, where $\mathcal{E}_{AB} = N_o + \frac{1}{2}$ follows from the statistics of the channel, the variance of AWGN, and uniform distribution on the

$$r_{D,k}^{\text{FD}} = \begin{cases} n_{D,k}, & \text{if } x_k = 0, \hat{x}_k = 0; \quad (3.25a) \\ \sqrt{1-\alpha^*}h_{CD,k}y_k + n_{D,k}, & \text{if } x_k = 0, \hat{x}_k = 1; \quad (3.25b) \\ \sqrt{\alpha^*}h_{AD,k} + n_{D,k}, & \text{if } x_k = 1, \hat{x}_k = 0; \quad (3.25c) \\ \sqrt{\alpha^*}h_{AD,k} + \sqrt{1-\alpha^*}h_{CD,k}y_k + n_{D,k}, & \text{if } x_k = 1, \hat{x}_k = 1; \quad (3.25d) \end{cases}$$

---

symbols of the OOK scheme, and the assumption that $r_{D,k}$ are statistically independent across the index k. Due to the enhanced capabilities of Dave, Alice and Charlie are interested in maintaining the average energy of $\mathcal{E}_{AB}$ on the jammed band f_{AB} when using the countermeasure. In the SC-F2HD scheme, Alice does not leave f_{AB}, and Charlie instantaneously embeds Alice's symbol in his symbol, and forwards the same to Bob on f_{CB}. Thus, after implementing SC-F2HD scheme, Dave continues to measure the average received energy $\mathcal{E}_{AB}$, and therefore SC-F2HD scheme successfully mitigates the cognitive adversary. In the next section, we discuss the covertness of SC-F2FD scheme.

3.7.1 Covertness of SC-F2FD Relaying Scheme

The covertness analysis for SC-F2FD is non-trivial because Alice and Charlie cooperatively pour energy in the band f_{AB} and f_{CB} as shown in Fig. 3.4. We assume that the SC-F2FD scheme uses the energy-splitting factor of α^* that minimizes the error performance of the joint decoder. In addition to the SC-F2FD cooperative strategy employed on f_{CB}, Alice and Charlie use the following strategy on f_{AB}. Whenever Alice transmits bit 1 in the band f_{CB} with energy $1-\alpha^*$, she transmits a symbol of energy α^* in the band f_{AB}. However, when Alice transmits bit 0 in the band f_{CB}, no energy is poured in the band f_{AB} as well. Meanwhile, on f_{AB}, Charlie does not pour any energy when he decodes bit 0, however, if Charlie decodes bit 1, then he sends any arbitrary $y \in \sqrt{1-\alpha^*}\mathcal{S}_C$. This way, Alice and Charlie cooperatively synthesize a sequence of OOK symbols on f_{AB}. Based on this strategy, after incorporating errors at Charlie, the received symbol at Dave is given by (3.25a)-(3.25d), where $\hat{x}_k$ is the decoded bit by Charlie on the k-th received symbol, $h_{AD,k}$ is Alice-to-Dave link distributed as $\mathcal{CN}(0,1)$, and $h_{CD,k}$ is the Charlie-to-Dave link distributed as $\sim \mathcal{CN}(0, 1+\partial)$, where the parameter ∂ captures the difference in the variance of Charlie-to-Dave link with respect to the Alice-to-Dave link. We introduce this differential variance in order to capture the difference in the physical distance between Alice-to-Dave, and Charlie-to-

$$\mathbf{P}_{FA}\approx 1+\frac{1}{2^n}\sum_{k=1}^{n}\binom{n}{k}\left[\sum_{d=0}^{k-1}\frac{\left(\mathcal{E}_{AB}+\epsilon\right)^d}{d!}e^{-\left(\mathcal{E}_{AB}+\epsilon\right)}-\sum_{d=0}^{k-1}\frac{\left(\mathcal{E}_{AB}-\epsilon\right)^d}{d!}e^{-\left(\mathcal{E}_{AB}-\epsilon\right)}\right] \tag{3.26}$$

$$\mathbf{P}_{MD}\approx\frac{1}{2^n}\sum_{k=1}^{n}\binom{n}{k}\left[1-\sum_{d=0}^{k-1}\frac{\left(\left(1+\partial\right)\left(1-\alpha^*\right)+\alpha^*\right)^{-d}\left(\mathcal{E}_{AB}+\epsilon\right)^d}{d!}e^{-\frac{\left(\mathcal{E}_{AB}+\epsilon\right)}{\left(\left(1+\partial\right)\left(1-\alpha^*\right)+\alpha^*\right)}}\right]-$$
$$\frac{1}{2^n}\sum_{k=1}^{n}\binom{n}{k}\left[1-\sum_{d=0}^{k-1}\frac{\left(\left(1+\partial\right)\left(1-\alpha^*\right)+\alpha^*\right)^{-d}\left(\mathcal{E}_{AB}-\epsilon\right)^d}{d!}e^{-\frac{\left(\mathcal{E}_{AB}-\epsilon\right)}{\left(\left(1+\partial\right)\left(1-\alpha^*\right)+\alpha^*\right)}}\right]. \tag{3.27}$$

Dave. Finally, $n_{D,k}$ is the complex AWGN at Dave with zero mean and variance N_o.

When implementing the SC-F2FD scheme, using the received signal $\{r_{D,k}^{\mathrm{FD}} \mid k = 1,2,\ldots,n\}$, the average measured energy across n symbols at Dave is given by $\mathcal{E}_n = \frac{1}{n}\sum_{k=1}^{n}\left|r_{D,k}^{\mathrm{FD}}\right|^2$. Let $\mathcal{H}_0$ and $\mathcal{H}_1$ be the hypothesis that no countermeasure is used and SC-F2FD is used, respectively. Since n can be small, we immediately observe that $\mathcal{E}_n$, which is a random variable, need not be equal to $\mathcal{E}_{AB}$ with probability one. Thus, given that $\mathcal{H}_0$ is true, false-alarm event is the event when the measured energy at Dave is away from $\mathcal{E}_{AB}$ by an amount ϵ, where the threshold ϵ is Dave's choice. Similarly, miss-detection event is the event when the measured energy at Dave is away from $\mathcal{E}_{AB}$ by an amount ϵ given that $\mathcal{H}_1$ is true. Formally, the probabilities of false-alarm and miss-detection are defined below.

Definition 2. *For a given $\epsilon > 0$, the probability of false-alarm and probability of miss-detection are defined as $\mathbf{P}_{FA} = \Pr\left(\left|\mathcal{E}_n - \mathcal{E}_{AB}\right| > \epsilon\right)$, and $\mathbf{P}_{MD} = \Pr\left(\left|\mathcal{E}_n - \mathcal{E}_{AB}\right| < \epsilon\right)$, respectively, where $\mathcal{E}_n$ and $\mathcal{E}_n$ is the average measured energy when hypothesis $\mathcal{H}_0$ is true and $\mathcal{H}_1$ is true, respectively.*

We now compute $\mathbf{P}_{FA}$ and $\mathbf{P}_{MD}$ in Theorem 4 and Theorem 5

Theorem 4. *For hypothesis $\mathcal{H}_0$ and $N_o \ll 1$, the PDF of the received energy of n symbols is approximated as $\tilde{p}^{*n}\left(z\right) \approx \frac{1}{2^n}\left(\delta(z) + \sum_{k=1}^{n}\binom{n}{k}G(k,1)\right)$, and hence $\mathbf{P}_{FA}$ is approximated as* (3.26)*, where $\mathcal{E}_{AB}$ is the average energy expected by Dave, $G(\cdot,\cdot)$ denotes the PDF of Gamma distribution.*

Proof. Let $p_{Z,X}\left(z,x\right)$ be the joint PDF of random variable Z and X on the k^{th} symbol received at Dave. Here, Z refers to the energy received at Dave, X is a discrete

Bernoulli random variable corresponding to the transmitted symbol of Alice distributed as $X \sim Bernoulli\left(\frac{1}{2}\right)$. Then the marginal distribution of Z is $p(z) = p\left(x=0\right) p\left(z \middle| x=0\right) + p\left(x=1\right) p\left(z \middle| x=1\right)$.

Since $p\left(z \middle| \cdot\right)$ is an exponential distribution with parameters $\frac{1}{N_o}$, and $\frac{1}{N_o+1}$, for $x=0$ and $x=1$, respectively, $p(z)$ is an exponential mixture. We assume $N_o \ll 1$, therefore, $p\left(z\right) \approx \tilde{p}\left(z\right) = \frac{1}{2}\left[\delta\left(z\right) + Exp\left(1\right)\right]$, where, $\delta(\cdot)$ is the Dirac-delta function, and $Exp(\phi) = \phi e^{-\phi a}$, is the PDF of exponential distribution with parameter ϕ over support interval $a \in [0, \infty)$. Note that Dave receives n i.i.d. symbols to compute the average. Let $\tilde{p}^{*n}\left(z\right)$ be the PDF of the average received energy of n i.i.d. symbols, then computing $\tilde{p}^{*n}\left(z\right)$ is equivalent to computing n-fold convolution of $\tilde{p}\left(z\right)$. Therefore, the approximation on the PDF of the measured average energy is given as

$$\begin{aligned} \tilde{p}^{*n}\left(z\right) = \left(\frac{1}{2}\left(\delta\left(z\right) + e^{-z}\right)\right)^{*n} &= \frac{1}{2^n}\left(\delta(z) + \sum_{k=1}^{n}\binom{n}{k}\left(e^{-z}\right)^{*k}\right) \\ &= \frac{1}{2^n}\left(\delta(z) + \sum_{k=1}^{n}\binom{n}{k} G(k,1)\right). \end{aligned} \tag{3.28}$$

This completes the first part of the proof. For the second part, we compute the tail of $\tilde{p}^{*n}\left(z\right)$ to obtain $\mathbf{P}_{FA}$ by using the tail distribution of standard Gamma distributions.

$\square$

Theorem 5. *For the hypothesis* $\mathcal{H}_1$*, when* $N_o \ll 1$ *and* $\alpha^* \rightarrow 1$*, then PDF of the average received energy of* n *symbols given is upper bounded by* $\tilde{q}^{*n}$*, such that* $\tilde{q}^{*n}\left(z^{\psi}\right) = \frac{1}{2^n}\left(\delta(z^{\psi}) + \sum_{k=1}^{n}\binom{n}{k} G\left(k, \left(\left(1+\partial\right)\left(1-\alpha^*\right) + \alpha^*\right)\right)\right)$*. Furthermore,* $\mathbf{P}_{MD}$ *is approximated as* (3.27).

Proof. Let Z^{ψ} be the random variable for the instantaneous received energy of k^{th} symbol at Dave. Further, since the transmitted symbol of Alice along with the flipping probabilities at Charlie dictate the energy measured in f_{AB}, the marginal PDF of Z^{ψ} is $q\left(z^{\psi}\right) = \sum_{x=0}^{1}\sum_{\hat{x}=0}^{1} p\left(x, \hat{x}\right) q\left(z^{\psi} \middle| x, \hat{x}\right)$, where $p\left(x, \hat{x}\right) = \frac{1}{2} P_{x\hat{x}}^{\psi}$ is the probability that x is transmitted by Alice and $\hat{x}$ is decoded at Charlie, such that $x, \hat{x} \in \{0, 1\}$, $q\left(z^{\psi} \middle| x, \hat{x}\right)$ is the distribution on the energy of symbols given in (3.25a) - (3.25d), and z^{ψ} is the realization of Z^{ψ}. Substituting the respective values in $q\left(z^{\psi}\right)$, yields us an exponential mixture given by

$$\begin{aligned}q\left(z^{\psi}\right)=\frac{1}{2}\Bigg\{&Exp\left(\frac{1}{N_o+\alpha^*+(1+\partial)(1-\alpha^*)}\right)+Exp\left(\frac{1}{N_o}\right)+\\&\Phi_{01,\mathrm{FD}}\left[Exp\left(\frac{1}{N_o+(1+\partial)(1-\alpha^*)}\right)-Exp\left(\frac{1}{N_o}\right)\right]+\\&\Phi_{10,\mathrm{FD}}\left[Exp\left(\frac{1}{N_o+\alpha^*}\right)-Exp\left(\frac{1}{N_o+\alpha^*+(1+\partial)(1-\alpha^*)}\right)\right]\Bigg\}.\end{aligned}$$

For $N_o \ll 1$ and $\alpha^* \to 1$ we have

$$\begin{aligned}\Phi_{01,\mathrm{FD}}&\left[Exp\left(\frac{1}{N_o+(1+\partial)(1-\alpha^*)}\right)-Exp\left(\frac{1}{N_o}\right)\right]+\\&\Phi_{10,\mathrm{FD}}\left[Exp\left(\frac{1}{N_o+\alpha^*}\right)-Exp\left(\frac{1}{N_o+\alpha^*+(1+\partial)(1-\alpha^*)}\right)\right].\end{aligned}$$

We can approximate above expression to 0. Thus, an approximation on $q\left(z^{\psi}\right)$ is given as, $q\left(z^{\psi}\right) \approx \tilde{q}\left(z^{\psi}\right)=\frac{1}{2}\left\{\delta\left(z^{\psi}\right)+Exp\left(\frac{1}{\alpha^*+(1+\partial)(1-\alpha^*)}\right)\right\}$. Now, similar to computation of $\mathbf{P}_{FA}$, the n-fold convolution of $\tilde{q}\left(z^{\psi}\right)$ is given as

$$\begin{aligned}\tilde{q}^{*n}\left(z^{\psi}\right)&=\left(\frac{1}{2}\left\{\delta\left(z^{\psi}\right)+Exp\left(\frac{1}{\alpha^*+(1+\partial)(1-\alpha^*)}\right)\right\}\right)^{*n}\\&=\frac{1}{2^n}\left(\delta(z^{\psi})+\sum_{k=1}^{n}\binom{n}{k}G\left(k,((1+\partial)(1-\alpha^*)+\alpha^*)\right)\right).\end{aligned}$$

This completes the first part of the proof. Finally, we compute the tail of $\tilde{q}^{*n}\left(z^{\psi}\right)$ to obtain $\mathbf{P}_{MD}$ by using the tail of standard Gamma functions. □

The main objective of our countermeasure is to force Dave to measure an average energy between $\mathcal{E}_{AB}-\epsilon$ and $\mathcal{E}_{AB}+\epsilon$ with high probability in the band f_{AB}, no matter which hypothesis is true. This implies that it is desired to have $\mathbf{P}_{FA}=1-\mathbf{P}_{MD}$. Therefore, for SC-F2FD relaying scheme, we maximise $\mathbf{P}_{FA}+\mathbf{P}_{MD}$, and preferably drive it to one for any threshold ϵ chosen by Dave. The following proposition proves that under special conditions, the SC-F2FD scheme maximizes the covertness metric.

Proposition 7. *Let the Alice-to-Dave channel and Charlie-to-Dave channel be such that* $\partial=0$. *Further, for any arbitrary values of* n *and* ϵ, *under the condition that*

$N_o \ll 1$ and $\alpha^* \to 1$, we have $\mathbf{P}_{FA} + \mathbf{P}_{MD} \approx 1$.

Proof. From Theorem 4 and Theorem 5, it is clear that condition $N_o \ll 1$ and $\alpha^* \to 1$ provides an approximation on $\mathbf{P}_{FA} + \mathbf{P}_{MD}$. By substituting the value $\partial = 0$, we can verify that the approximation evaluates to one. Thus, we have $\mathbf{P}_{FA} + \mathbf{P}_{MD} \approx 1$. This completes the proof. $\square$

Although the above result provides theoretical guarantees on the covertness under specific constraints, we present simulation results to understand the covertness for arbitrary values of ∂ and λ.

3.7.2 Simulation Results on Covertness

In this section, we validate the covertness of the proposed SC-F2FD scheme through simulations. To generate the results, we assume that Alice and Charlie use the energy-splitting factor α^*, which is obtained in Sec. 3.5. Furthermore, we assume Dave's position is such that the relative variance in the channels between Alice-to-Dave and Charlie-to-Dave takes the values $\partial \in [0, 0.5]$. Note that larger values of ∂ are irrelevant to the SC-F2FD scheme as it implies that Charlie is not in Alice's vicinity. Thus, we assume that $h_{AD} \sim \mathcal{CN}(0, 1)$, whereas $h_{CD} \sim \mathcal{CN}(0, \sigma_{CD}^2)$ with $\sigma_{CD}^2 \in [1, 1.5]$. Furthermore, due to the low-latency constraint on Alice, SC-F2FD scheme is employed only for a short frame, constituting n channel uses. As a result, to detect the countermeasure, Dave must measure average energy levels using one frame.

When Dave measures average energy on n samples, then the computed values of $\mathbf{P}_{FA} + \mathbf{P}_{MD}$ is expected to vary around 1 since the simulation process involves an ensemble of random channel realizations. The same behaviour is also captured in Fig. 3.12, wherein we plot $\mathbf{P}_{FA} + \mathbf{P}_{MD}$ as a function of n at SNR = 35 dB. To generate the plots, we used $\mathcal{E}_{AB} = \frac{1}{2} + N_o$, where $N_o = 10^{-3.5}$, and the threshold margin $\epsilon = 10^{-3}$. Furthermore, when plotting the results, we considered FD radios with different values of λ at Charlie, which in turn yields different values of α^* using the NR algorithm. With a combination of these simulation parameters, the plots show that $\mathbf{P}_{FA} + \mathbf{P}_{MD}$, has a variation which is within $\pm 0.4\%$ around 1. This implies that, even when Dave witnesses asymmetric channel variance between Alice and Charlie (with

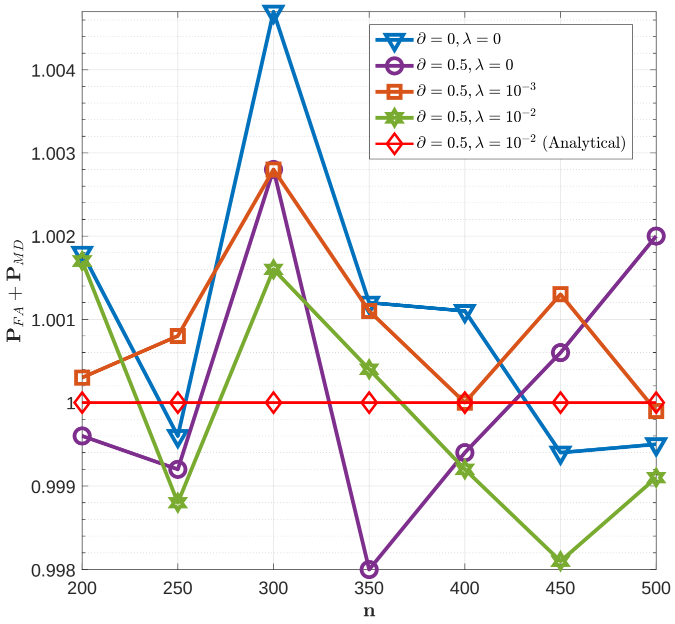

Figure 3.12: $\mathbf{P}_{FA} + \mathbf{P}_{MD}$ as a function of n at 35 dB for simulation as well as analytical expression (from approximation) for various combinations of ∂ and λ.

$\partial = 0.5$), and when Charlie operates with an FD radio of parameter $\lambda = 10^{-2}$, Dave is unable to detect SC-F2FD with high probability. In the same figure, we also plot the approximation on $\mathbf{P}_{FA} + \mathbf{P}_{MD}$ from Theorem 4 and 5, when $\partial = 0.5$ and $\lambda = 10^{-2}$. From the plots, we observe a difference between the approximation and the simulated results because the approximation on $\mathbf{P}_{MD}$ is applicable when α^* is close to one; however, with $\lambda = 10^{-2}$, the corresponding value of α^* is away from one. Finally, in Fig. 3.13, we also plot $\mathbf{P}_{FA} + \mathbf{P}_{MD}$ with varying ∂ for a fixed $n = 250$ and various levels of residual SI at Charlie. For each λ, we obtain the corresponding α^* using NR algorithm, and for the obtained α^*, we observe from the plots that $\mathbf{P}_{FA} + \mathbf{P}_{MD}$ is approximately 1 for all ∂. Thus, the SC-F2FD scheme ensures that Dave's measured average energy is within $(\mathcal{E}_{AB} - \epsilon, \mathcal{E}_{AB} + \epsilon)$ with high probability.

3.8 Chapter Summary

This chapter addressed a DoS attack on low-latency communication between Alice and Bob in a crowded network with no unused frequencies. To execute this attack, Dave was armed with a perfect FD radio, wherein he was also able to measure the average energy on the jammed frequency band. As countermeasures, SC-F2HD and SC-F2FD relaying schemes were proposed. It was shown that SC-F2HD performs well when

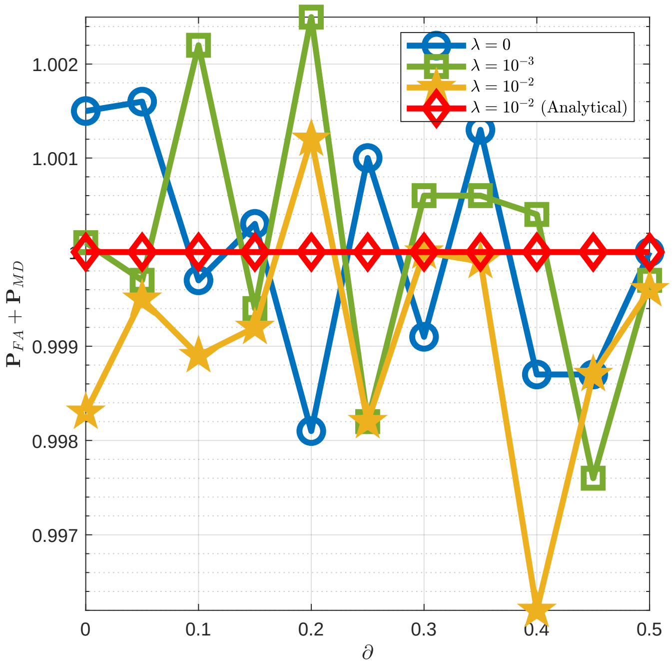

Figure 3.13: $\mathbf{P}_{FA} + \mathbf{P}_{MD}$ as a function of ∂ for $n = 250$ and SNR = 35 dB. For $\lambda = 10^{-2}$, analytical result is approximately 1, the simulated sum fluctuates around 1.

Table 3.1: Comparison between the proposed SC-F2HD and SC-F2FD relaying schemes

Features	SC-F2HD	SC-F2FD
Individual performance ($I_{Dave} = 0$ at Charlie)	Alice's performance improves but Charlie's performance degrades	Alice's performance improves but Charlie's performance degrades.
Individual performance ($I_{Dave} \neq 0$ at Charlie)	Alice's performance degrades, whereas Charlie's performance is unaffected (same as $I_{Dave} = 0$).	Alice's and Charlie's performance improves with increasing SNR; Unaffected by presence of Dave.
Implementation Complexity	No FD radios thus relatively simple implementation; No energy-splitting computation; No change in communicating frequency of cooperating nodes.	Complex implementation due to FD radio; Involves computation of energy-splitting factor; Cooperating nodes communicate on f_{AB} and f_{CB} simultaneously.
Covertness	Implicitly covert. No analysis required.	Analysis required. Covertness proved through simulations and analytical results.

Dave is far from Charlie, however the error performance at Bob deteriorates as Dave moves closer to Charlie. In contrast, SC-F2FD scheme is invariant to the location of Dave with respect to Charlie. Unlike the SC-F2HD scheme, we showed that the SC-F2FD scheme requires Alice and Charlie to cooperatively pour energies in the frequency bands f_{AB} and f_{CB} using an appropriate energy-splitting factor α^{*}. Upper bounding the probability of error using the joint dominant decoder, a rigorous analysis to compute α^{*} was proposed. The proposed schemes provide near-optimal error performance, and successfully engages Dave on the jammed frequency. A thorough comparison of the proposed relaying schemes is also presented in Table 3.1.

CHAPTER 4

Fast-Forward Mitigation Schemes for Reactive Adversaries for Fast-Fading Channels

4.1 Introduction

The discussions in Chapter 3 indicate that FDCRs can also scan multiple frequencies while executing a *jam-and-measure* attack on the victim's frequency. Subsequently, this can allow the adversary to compute a correlation measure between the symbols on the victim's frequency and other frequencies thereby detecting repetition coding across frequencies, such as the FFFD based countermeasures in Chapter 3. Thus, new countermeasures must be designed to mitigate adversaries which can scan multiple frequencies, in addition to monitoring the energy level on the jammed frequency band. This chapter points out that the modulation techniques designed as part of the countermeasures depend on the wireless environment. For instance, in slow-fading channels, coherent modulation based countermeasures must be designed by allowing the receiver to learn the Channel State Information (CSI) through pilots. However, acquiring CSI using pilots is difficult when channel conditions vary rapidly over time. As a result, non-coherent modulation based countermeasures must be designed when jam-and-measure attacks are executed in fast-fading channels, thereby allowing the receiver to decode the information symbols without instantaneous CSI. From the above discussion, we identify that the countermeasures proposed in Chapter 3 are not applicable for fast-fading channels, thereby opening up new problem statements in designing non-coherent modulation based countermeasures.

4.1.1 Contributions

In this chapter, we design non-coherent modulation based countermeasures to mitigate jamming attacks by FDCAs. Amongst various non-coherent modulation techniques, we use energy detection based Amplitude Shift Keying (ASK) due to its higher spectral efficiency. Towards this end, we summarize the contribution of this chapter as follows:

1. We envisage an attack model wherein the adversary uses an FDCA to jam a victim that has low-latency symbols to communicate with the base station. The salient feature of the adversary is that it can scan multiple frequencies in the network while executing a jamming attack on the victim's frequency. In particular, the adversary uses an Energy Detector (ED) and a Correlation Detector (CD) to detect the state-of-art countermeasures. (See Sec. 4.2)

2. As a countermeasure against the proposed threat, we propose a Non-Coherent FFFD (NC-FFFD) relaying scheme, wherein an FFFD helper assists the victim by instantaneously fast-forwarding victim's message along with its message to the base station. The proposed NC-FFFD scheme also uses a Gold-sequence based scrambler to cooperatively pour energy on the victim's frequency in order to evade detection by ED and CD. With On-Off Keying (OOK) at the victim and $M-$ary ASK at the helper, we propose an approximate joint maximum a posteriori decoder to compute the closed-form expression of symbol error probability for the NC-FFFD scheme. We then formulate an optimization problem of minimizing the SEP over the victim's and the helper's energy levels, subject to a modified average energy constraint at the helper. Subsequently, we solve the optimization problem for $M = 2$ and then generalise it for $M > 2$. (See Sec. 4.3, 4.4)

3. We also consider the case when fast-forwarding at the helper is not instantaneous, i.e., imperfect fast-forwarding. Here, we propose Delay Tolerant NC-FFFD (DT NC-FFFD) scheme, where we solve the optimization problem similar to $M \geq 2$ by upper bounding the energy contributed by the victim by a small number. We show that the error performance of DT NC-FFFD scheme is independent of the delays introduced due to imperfect fast-forwarding. For all the cases, we provide strong analytical results and based on these results, we provide a family of algorithms to obtain near-optimal solutions to the optimization problem. (See Sec. 4.5)

4. Finally, through various analytical and simulation results, we show that despite having robust detectors, the adversary cannot detect the proposed mitigating scheme with high probability. (See Sec. 4.6)

4.1.2 Related Work and Novelty

FD radios have found their applications in aiding [34,35,76,101–103] as well as degrading [34, 35, 89–91] a network's performance. Along the lines of [34] and [35], we also use FD radios at both the adversary and the helper node. However, in contrast, the threat model of this chapter is stronger than the one in [34] and [35] as it can scan multiple frequencies to measure correlation between symbols on different frequencies. Furthermore, the FD radio at the helper in this chapter implements non-coherent modulation as against coherent modulation in [34] and [35]. This chapter deals with the constellation design problem for a NC-FFFD strategy. In literature, [110–115] address the problem of constellation design for point-to-point Single-Input Multiple-Output (SIMO) non-coherent systems. Further, [116], [117] study the constellation design for non-coherent Multiple Access Channel (MAC). However, due to distributed setting, our work cannot be viewed as a direct extension of [110–117]. Some preliminary results on the NC-FFFD scheme have been presented by us in [37], where we compute the optimal energy levels at the victim and the helper for $M = 2$. In addition, the results of this chapter are generalisable for $M \geq 2$. Further, we provide solutions for imperfect fast-forwarding at the helper and also present an extensive analysis on the covertness of the proposed schemes.

4.2 System Model

We consider a *crowded* network wherein multiple nodes communicate with a base station on orthogonal frequencies. In the context of this chapter, crowded network implies that all the nodes use orthogonal frequency bands to communicate with the base station such that the number of frequency bands is equal to the number of nodes in the network. Fig. 4.1 captures one simple instantiation of the network where two nearby nodes, Alice and Charlie communicate with a multi-antenna base station, Bob. The uplink frequencies of Alice and Charlie are centred around f_{AB} and f_{CB}, respectively. Alice is a single-antenna transmitter that has low-rate and low-latency messages to communicate with Bob. In contrast, Charlie, which is a Fast-Forward Full-Duplex (FFFD) node with N_C receive-antennas and a single transmit-antenna, has arbitrary data-rate messages to communicate with no latency constraints. Here, fast-forwarding [76] refers to Charlie's

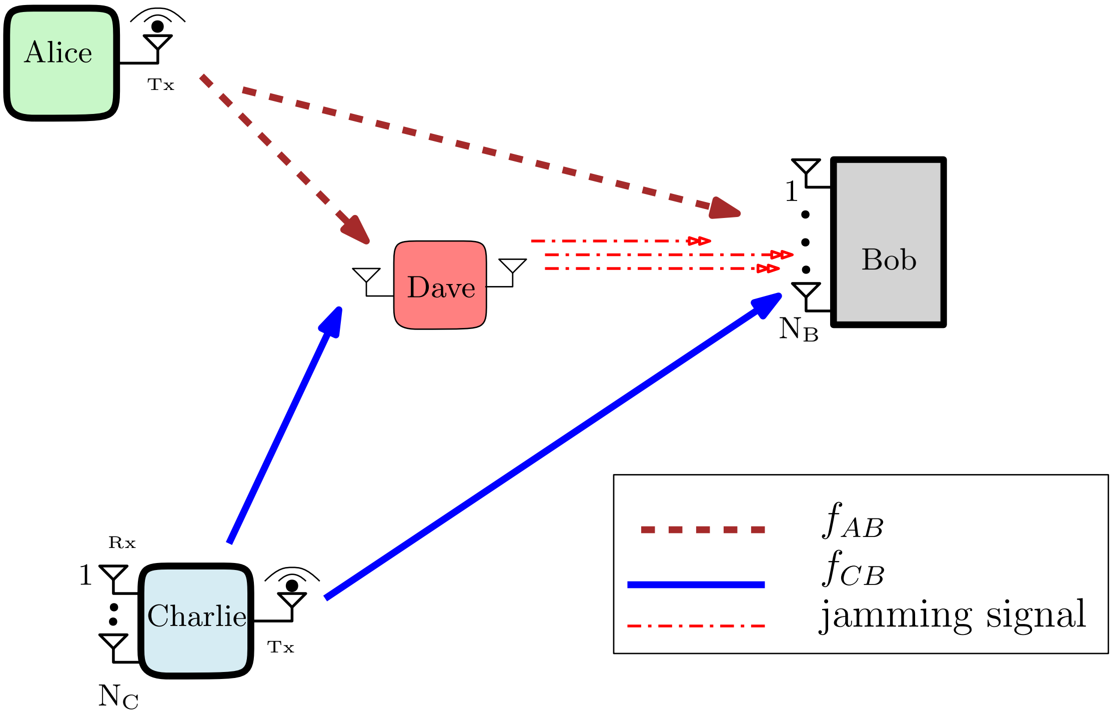

Figure 4.1: A network model consisting legitimate nodes Alice and Charlie communicating with Bob, on f_{AB}, and f_{CB}, respectively. Dave is the FD cognitive adversary, jamming f_{AB}. He also measures the energy level on f_{AB} and computes the correlation between the symbols on f_{AB} and f_{CB}.

capability to instantaneously manipulate the received symbols on its uplink frequency and then multiplex them along with its information symbols to the base station. The mobility conditions of the network are such that the wireless channels from Alice to Bob, and from Charlie to Bob experience fast-fading with a coherence-interval of one symbol duration. Therefore, both Alice and Charlie use non-coherent Amplitude Shift Keying (ASK) for uplink communication. In particular, since Alice has low data-rate messages, she uses the On-Off Keying (OOK) scheme. On the other hand, since Charlie transmits at arbitrary data-rates, he uses an M-ary ASK scheme, for some $M = 2^m$, with $m \geq 1$.

Within the same network, we also consider an adversary, named Dave, who is a cognitive jamming adversary equipped with an FD radio that constantly jams f_{AB} and also monitors it to detect any countermeasures. We assume that Dave can learn Alice's frequency band by listening to the radio resource assignment information broadcast from the base station [118]. To monitor f_{AB} for any possible countermeasures, Dave uses an Energy Detector (ED), which measures the average energy level on f_{AB}. Furthermore, assuming that Dave does not have the knowledge of helper's frequency band, he uses a Correlation Detector (CD) that estimates the correlation between the symbols on

f_{AB} and all other frequencies in the network. To envision a practical adversarial model, we assume that Dave's FD radio experiences residual SI. From the above threat model, we note that Alice cannot use frequency hopping to evade the jamming attack due to two reasons: (i) the absence of vacant frequency bands in the uplink, and moreover, (ii) an ED at Dave restricts Alice to completely switch her operating frequency. This is because, if Alice switches her operating frequency, Dave measures a significant dip in the energy level of f_{AB}, thereby detecting a countermeasure. Other than frequency hopping, if Alice implements repetition coding using frequency-diversity techniques, where she replicates her messages on f_{AB} and another frequency (say f_{CB}), simultaneously, then the CD at Dave detects a high correlation between the symbols on both the frequencies. Subsequently, a detection by either ED or CD compels Dave to jam f_{CB} thereby degrading the network's performance. Therefore, Alice must use a countermeasure that helps her to communicate reliably with Bob while deceiving ED and CD at Dave.

For ease of understanding, in Table 4.1, we have provided the notations that appear in the rest of the chapter. In the next section, we present a communication setting wherein Alice seeks assistance from Charlie to evade the jamming attack whilst deceiving the ED and the CD at Dave.

Table 4.1: FREQUENTLY OCCURRING NOTATIONS

N_C	Receive antennas at Charlie
N_B	Receive antennas at Bob
M	Charlie's constellation size
E_A	Alice's OOK symbol
E_C	Charlie's multiplexed symbol
$\mathbf{r}_C$	$N_C \times 1$ receive vector at Charlie
Ω_i	Energy received at Charlie corresponding to Alice's i^{th} symbol
$\mathbf{r}_B$	$N_B \times 1$ receive vector at Bob
$\mathbf{0}_{N_C}$	$N_C \times 1$ vector of zeros
$\mathbf{I}_{N_C}$	$N_C \times N_C$ Identity matrix
S_ℓ	Sum energy received at Bob on f_{CB}
ν	Detection threshold at Charlie

$\rho_{\ell\ell^*}$	Detection threshold between S_ℓ and S_{ℓ^*}
λ	Residual self-interference
α	Energy splitting factor
L	Number of symbols received at Dave
$E_{C,f_{AB}}$	Avg. transmit energy of Charlie on f_{CB}
$E_{D,f_{AB}}$	Avg. receive energy of Dave on f_{AB}
$r_{D,l}$	l^{th} symbol received at Dave
$\mathbf{P}_{FA}$	Probability of false-alarm at Dave before implementing the countermeasure.
$\mathbf{P}_D$	Probability of detection at Dave after implementing the countermeasure.

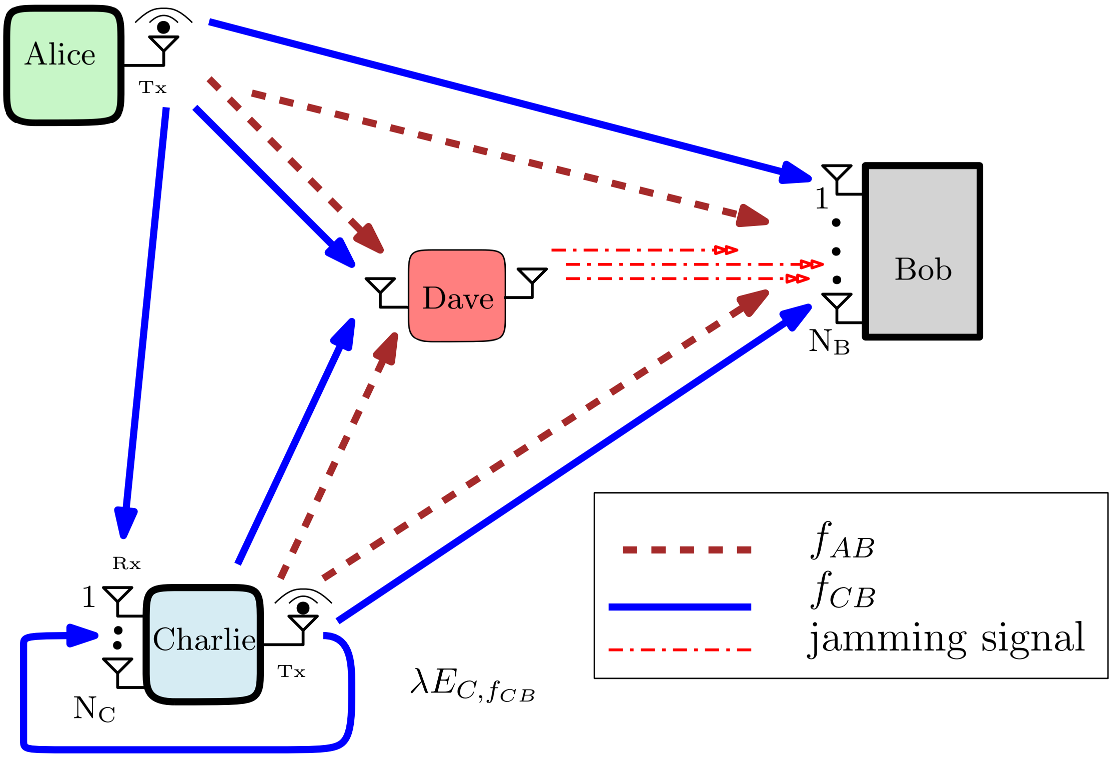

Figure 4.2: System model of NC-FFFD relaying scheme.

4.3 Non-Coherent Fast-Forward Full-Duplex Relaying Scheme

In order to help Alice evade the jamming attack, we propose a Non-Coherent Fast-Forward Full-Duplex (NC-FFFD) relaying scheme, described as follows: Bob directs Alice to broadcast her OOK symbols on f_{CB} with $(1-\alpha)$ fraction of her energy, where $\alpha \in (0,1)$ is a design parameter. Since Charlie also has symbols to communicate to Bob, he uses his in-band FD radio to receive Alice's symbols on f_{CB}, decodes them, multiplexes them to his symbols, and then *fast-forwards* them on f_{CB}, such that the average energy of the multiplexed symbols is $(1+\alpha)/2$ fraction of his original average energy. As a result, Bob observes a MAC on f_{CB}, and attempts to decode Alice's and Charlie's symbols jointly. To deceive the ED at Dave, the average energy level on f_{AB} needs to be the same as before implementing the countermeasure. Therefore, Alice and Charlie use a Gold sequence-based scrambler as a pre-shared key to cooperatively transmit dummy OOK symbols on f_{AB} by using residual $\alpha/2$ and $(1-\alpha)/2$ fractions of their average energies, respectively. Note that the use of dummy OOK symbols on f_{AB} assists in deceiving the CD at Dave. In the next section, we discuss the signal model of the NC-FFFD scheme on f_{CB} so as to focus on reliable communication of Alice's symbols with the help of Charlie.

4.3.1 NC-FFFD: Signal Model

Before implementing the NC-FFFD relaying scheme, Alice transmits her OOK symbols with energy $E_A \in \{0, 1\}$, such that $E_A = 0$ and $E_A = 1$ correspond to symbols $i = 0$ and $i = 1$, respectively. Similarly, Charlie transmits his symbols using an $M-$ary ASK scheme with average energy 1. When implementing the NC-FFFD relaying scheme, as illustrated in Fig. 4.2, Alice transmits her OOK symbols with energy $(1 - \alpha)E_A$, for some $\alpha \in (0, 1)$ on f_{CB}. With this modification, the average transmit energy of Alice on f_{CB}, denoted by $\mathrm{E}_{A,f_{CB}}$, is $\mathrm{E}_{A,f_{CB}} = (1 - \alpha)/2$. Since Charlie is an in-band FD radio, the received baseband vector at Charlie on f_{CB} is

$$\mathbf{r}_C = \mathbf{h}_{AC}\sqrt{(1 - \alpha)E_A} + \mathbf{h}_{CC} + \mathbf{n}_C, \tag{4.1}$$

where $\mathbf{h}_{AC} \sim \mathcal{CN}\left(\mathbf{0}_{N_C}, \sigma_{AC}^2\mathbf{I}_{N_C}\right)$ is $N_C \times 1$ channel vector. Further, the SI channel of the FD radio at Charlie [35] is denoted by $\mathbf{h}_{CC} \sim \mathcal{CN}\left(\mathbf{0}_{N_C}, \lambda\mathrm{E}_{C,f_{CB}}\mathbf{I}_{N_C}\right)$ and $\mathbf{n}_C \sim \mathcal{CN}\left(\mathbf{0}_{N_C}, N_o\mathbf{I}_{N_C}\right)$ is the $N_C \times 1$ Additive White Gaussian Noise (AWGN) vector.

As a salient feature of the NC-FFFD scheme, Charlie uses $\mathbf{r}_C$ to instantaneously decode Alice's information symbol, and then transmits an energy level E_C on f_{CB}, which is a function of Alice's decoded symbol and its information symbol. If $\hat{i}_C$ and $j \in \{1, \cdots, M\}$ denote Alice's decoded symbol and Charlie's information symbol, respectively, then the energy level, E_C is given by

$$E_C = \begin{cases} \epsilon_j & \text{if } \hat{i}_C = 0, \\ \eta_j & \text{if } \hat{i}_C = 1. \end{cases} \tag{4.2}$$

Here $\{\epsilon_j, \eta_j \mid j = 1, \cdots, M\}$, which represent the set of energy levels corresponding to different combinations of $\hat{i}_C$ and j, are the parameters under design consideration. Note that Charlie transmits M energy levels corresponding to each value of $\hat{i}_C$. Towards designing $\{\epsilon_j, \eta_j\}$, the energy levels are such that, $0 \leq \epsilon_1 < \cdots < \epsilon_M$, $0 \leq \eta_1 < \cdots < \eta_M$, and $\epsilon_j < \eta_j$, if j is odd and $\epsilon_j > \eta_j$, if j is even.

Given that Alice contributes an average energy of $(1 - \alpha)/2$ on f_{CB}, Charlie is constrained to transmit his multiplexed symbols with an average energy of $(1+\alpha)/2$ so that the average energy on f_{CB} continues to be unity. Thus, the average energy constraint on Charlie, denoted by $\mathrm{E}_{C,f_{CB}}$ is

$$\mathrm{E}_{C,f_{CB}} = \frac{1}{2M}\sum_{j=1}^{M}(\epsilon_j + \eta_j) = \frac{1+\alpha}{2}. \tag{4.3}$$

Finally, upon transmission of the energy level E_C from Charlie, Bob observes a multiple access channel on f_{CB} from Alice and Charlie. Thus, the $N_B \times 1$ receive vector at Bob is

$$\mathbf{r}_B = \mathbf{h}_{AB}\sqrt{(1-\alpha)E_A} + \mathbf{h}_{CB}\sqrt{E_C} + \mathbf{n}_B, \tag{4.4}$$

where $\mathbf{h}_{AB} \sim \mathcal{CN}\left(\mathbf{0}_{N_B}, \sigma_{AB}^2\mathbf{I}_{N_B}\right)$ and $\mathbf{h}_{CB} \sim \mathcal{CN}\left(\mathbf{0}_{N_B}, \sigma_{CB}^2\mathbf{I}_{N_B}\right)$ are the Alice-to-Bob link and Charlie-to-Bob link, respectively. Further, $\mathbf{n}_B \sim \mathcal{CN}\left(\mathbf{0}_{N_B}, N_o\mathbf{I}_{N_B}\right)$ is the AWGN vector at Bob. We assume that all the channel realizations and noise samples are statistically independent. We also assume that only the channel statistics and not the instantaneous realizations of $\mathbf{h}_{AB}$ and $\mathbf{h}_{CB}$ are known to Bob. Similarly, only the channel statistics and not the instantaneous realizations of $\mathbf{h}_{AC}$ are known to Charlie. Further, due to the proximity of Alice and Charlie, we assume $\sigma_{AC}^2 > \sigma_{AB}^2$ to capture higher Signal-to-Noise Ratio (SNR) in the Alice-to-Charlie link compared to Charlie-to-Bob link. Henceforth, throughout the chapter, various noise variance at Charlie and Bob are given by SNR $= N_o^{-1}$ and $\sigma_{AB}^2 = \sigma_{CB}^2 = 1$.

Given that Alice-to-Bob and Charlie-to-Bob channels are non-coherent, Bob must use $\mathbf{r}_B$ in (4.4) to jointly decode the information symbols of both Alice and Charlie. Towards that direction, in the next section, we study the distribution on $\mathbf{r}_B$ conditioned on their information symbols.

4.3.2 The Complementary Energy Levels and Distribution of $\mathbf{r}_B$

Based on the MAC in (4.4), $\mathbf{r}_B$ is sampled from an underlying multi-dimensional Gaussian distribution whose parameters depend on i, j, and $\hat{i}_C$. If e denotes the error event at Charlie, then, $e = 0$, if $i = \hat{i}_C$ and $e = 1$, if $i \neq \hat{i}_C$. Recall that for a given j, Charlie transmits ϵ_j or η_j corresponding to $\hat{i}_C = 0$ and $\hat{i}_C = 1$, respectively. Therefore, Bob receives $\mathbf{r}_B$ sampled from two different sets with $2M$ multi-dimensional Gaussian distributions corresponding to $e = 0$ and $e = 1$. For example, assume that Alice transmits symbol $i = 1$, and it gets decoded as $\hat{i}_C = 0$ at Charlie. According to (4.2), Charlie transmits the energy level ϵ_j, and as a result, each component of $\mathbf{r}_B$ is sampled from a circularly symmetric complex Gaussian distribution with mean zero and variance $1 - \alpha + \epsilon_j + N_o$. On the other hand, if Charlie had decoded the symbol correctly, each component of $\mathbf{r}_B$ would be sampled from a circularly symmetric complex Gaussian distribution with mean zero and variance $1 - \alpha + \eta_j + N_o$. To obtain these variance values, we have used the fact that $\mathbf{h}_{AB} \sim \mathcal{CN}\left(\mathbf{0}_{N_B}, \mathbf{I}_{N_B}\right)$, $\mathbf{h}_{CB} \sim \mathcal{CN}\left(\mathbf{0}_{N_B}, \mathbf{I}_{N_B}\right)$, and $\mathbf{n}_B \sim \mathcal{CN}\left(\mathbf{0}_{N_B}, N_o\mathbf{I}_{N_B}\right)$. Overall, using (4.4), the distribution of $\mathbf{r}_B$ is given as

$$\mathbf{r}_B \sim \begin{cases} \mathcal{CN}\left(\mathbf{0}_{N_B}, (\epsilon_j + N_o)\mathbf{I}_{N_B}\right) & \text{if } i = 0, e = 0, \\ \mathcal{CN}\left(\mathbf{0}_{N_B}, (\eta_j + N_o)\mathbf{I}_{N_B}\right) & \text{if } i = 0, e = 1, \\ \mathcal{CN}\left(\mathbf{0}_{N_B}, (1 - \alpha + \eta_j + N_o)\mathbf{I}_{N_B}\right) & \text{if } i = 1, e = 0, \\ \mathcal{CN}\left(\mathbf{0}_{N_B}, (1 - \alpha + \epsilon_j + N_o)\mathbf{I}_{N_B}\right) & \text{if } i = 1, e = 1, \end{cases} \tag{4.5}$$

where we have substituted $E_A = 0$ and $E_A = 1$, for $i = 0$ and $i = 1$, respectively, and $\sigma_{AB}^2 = \sigma_{CB}^2 = 1$ in (4.4). From (4.5), it is clear that the sum of the energy levels transmitted by Alice and Charlie characterizes all the possible distributions from which $\mathbf{r}_B$ is sampled.

We now define an index ℓ that is a one-to-one function of the transmit pair (i, j), such that

$$\ell = \frac{1}{2}\left[(-1)^{ij}\left(4j(1-i) + 4i(-1)^j + (-1)^{j+i} - 1\right)\right]. \tag{4.6}$$

Since $(i, j) \in \{0, 1\} \times \{1, \cdots, M\}$, we have $\ell \in \{1, \cdots, 2M\}$. We also define two sets of energy levels, denoted by $\mathcal{S} = \{S_\ell \mid \ell = 1, \cdots, 2M\}$ and $\overline{\mathcal{S}} = \{\overline{S}_\ell \mid \ell = 1, \cdots, 2M\}$ that correspond to the sum of energy levels jointly contributed by Alice and Charlie, and the AWGN at Bob when $e = 0$ and $e = 1$, respectively. In particular, the ℓ^{th} element of $\mathcal{S}$ and $\overline{\mathcal{S}}$ are given by

$$S_\ell \triangleq (1 - \alpha + \eta_j)\, i + \epsilon_j(1 - i) + N_o \text{ and } \overline{S}_\ell \triangleq (1 - \alpha + \epsilon_j)\, i + \eta_j(1 - i) + N_o. \tag{4.7}$$

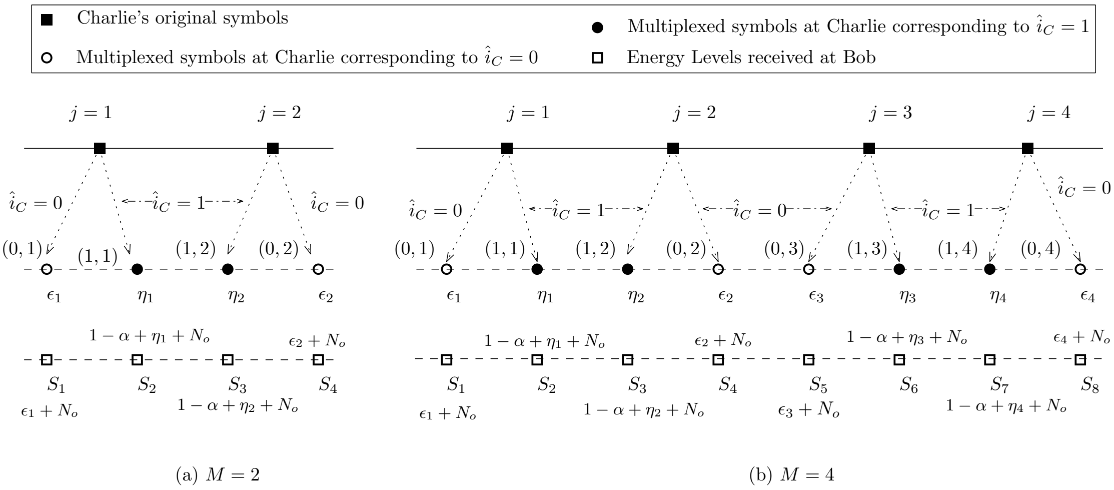

(a) $M = 2$ (b) $M = 4$

Figure 4.3: Illustration of multiplexing at Charlie and corresponding energy levels received at Bob.

Since $\overline{\mathcal{S}}$, corresponds to the sum of energy levels when $e = 1$, we refer to $\overline{\mathcal{S}}$ as the set of complementary energy levels. Note that there is one-to-one correspondence between the elements of $\mathcal{S}$ and $\overline{\mathcal{S}}$, and the distributions in (4.5) corresponding to $e = 0$ and $e = 1$, respectively. Also, note that $\mathcal{S}$ is such that $S_1 < S_2 < \cdots < S_{2M-1} < S_{2M}$. To exemplify the sum of energy levels that characterises $\mathbf{r}_B$ at Bob, in Fig. 4.3, we present the elements of $\mathcal{S}$ and $\overline{\mathcal{S}}$ for $M = 2, 4$.

4.3.3 Joint Maximum A Posteriori (JMAP) decoder for NC-FFFD Relaying Scheme

Due to the decode-multiplex-and-forward nature of the NC-FFFD scheme, we first compute the error-rates introduced by Charlie while decoding Alice's symbols, and then compute the joint error-rates at Bob. Since Alice-to-Charlie link is non-coherent, Charlie uses energy detection to decode Alice's symbols. If $f\left(\mathbf{r}_C|i\right)$ is the PDF of $\mathbf{r}_C$ conditioned on the Alice's symbol, i, then the Maximum Likelihood (ML) decision rule for detection is

$$\hat{i}_C = \arg\max_{i\in\{0,1\}} \ln\left\{f\left(\mathbf{r}_C|i\right)\right\} = \arg\min_{i\in\{0,1\}} N_C \ln(\pi\Omega_i) + \frac{\mathbf{r}_C^H\mathbf{r}_C}{\Omega_i}, \tag{4.8}$$

where $(\mathbf{r}_C|i) \sim \mathcal{CN}\left(\mathbf{0}_{N_C}, \Omega_i\mathbf{I}_{N_C}\right)$, such that $\Omega_0 = \left(\lambda\frac{(1+\alpha)}{2} + N_o\right)$ is the variance of the received symbol when $i = 0$ and $\Omega_1 = \left(\sigma_{AC}^2(1-\alpha) + \lambda\frac{(1+\alpha)}{2} + N_o\right)$ is the variance of the received symbol, when $i = 1$. Here, $(\cdot)^H$ denotes the Hermitian operator. Using the first principles, the energy detection threshold at Charlie, denoted by ν, is given as, $N_C\frac{\Omega_0\Omega_1}{\Omega_0-\Omega_1}\ln\left(\frac{\Omega_0}{\Omega_1}\right)$. Using ν, it is straightforward to prove the next theorem that presents the probability of error at Charlie in decoding Alice's symbols.

Theorem 6. *If P_{ik} denotes the probability of decoding symbol i as symbol k, for $i, k = 0, 1$, then $\Phi_{01} = \frac{\Gamma\left(N_C, \frac{\nu}{\Omega_0}\right)}{\Gamma(N_C)}$ and $\Phi_{10} = \frac{\gamma\left(N_C, \frac{\nu}{\Omega_1}\right)}{\Gamma(N_C)}$, where $\gamma(\cdot,\cdot)$, $\Gamma(\cdot,\cdot)$, and $\Gamma(\cdot)$ are incomplete lower, incomplete upper, and complete Gamma functions, respectively.*

Proof. If Alice transmits symbol 0, then $\Phi_{01} = \Pr\left(e = 1|i = 0\right) = \Pr\left(\mathbf{r}_C^H\mathbf{r}_C > \nu|i = 0\right)$. Since $\mathbf{r}_C^H\mathbf{r}_C$ is gamma distributed, it is straightforward to get Φ_{01}.

Similarly, when Alice transmits symbol 1, we have $\Phi_{10} = \Pr\left(e = 1|i = 1\right) = \Pr\left(\mathbf{r}_C^H\mathbf{r}_C \leq \nu|i = 1\right)$. Thus, we get the expression of Φ_{10}. ☐

Lemma 7. *The terms Φ_{01} and Φ_{10} are increasing functions of α for a given SNR, N_C, and λ.*

Proof. Consider the expression of Φ_{10} as given in Theorem 6. The ratio, ν/Ω_1 can be rewritten as, $\frac{\nu}{\Omega_1} = N_C\frac{\ln(1+\theta)}{\theta}$, where $\theta = \frac{(\Omega_1-\Omega_0)}{\Omega_0}$. Differentiating θ w.r.t. α, we get, $-\frac{N_o\sigma_{AC}^2}{\left(N_o+\lambda\frac{1+\alpha}{2}\right)^2}$. Since $\frac{d\theta}{d\alpha} < 0$, as α increases θ decreases. Further, when θ decreases, $N_C\frac{\ln(1+\theta)}{\theta}$ increases. Therefore, $\frac{\nu}{\Omega_1}$ is an increasing function of α. Finally, since $\gamma\left(N_C, \frac{\nu}{\Omega_1}\right)$ is an increasing function of $\frac{\nu}{\Omega_1}$, Φ_{10} is an increasing function of α. Using similar argument, we can prove that Φ_{01} is also an increasing function of α. ☐

Along the similar lines of Lemma 7, the following lemma is also straightforward to prove.

Lemma 8. *The terms Φ_{01} and Φ_{10} are decreasing functions of N_C for a fixed SNR, α, and λ.*

Using Φ_{01} and Φ_{10} at Charlie, we study the performance of non-coherent decoder at Bob. With $i \in \{0, 1\}$ and $j \in \{1, 2, \ldots, M\}$ denoting Alice's and Charlie's information symbols, respectively, we define a transmit pair as the two-tuple (i, j). Based on $\mathbf{r}_B$ in (4.4), the JMAP decoder at Bob is

$$\hat{i}, \hat{j} = \arg\max_{i\in\{0,1\}, j\in\{1,\cdots,M\}} g\left(\mathbf{r}_B|(i, j)\right), \tag{4.9}$$

where $g\left(\mathbf{r}_B|(i,j)\right)$ is the PDF of $\mathbf{r}_B$, conditioned on i and j. However, note that due to errors introduced by Charlie in decoding Alice's symbols, $g(\cdot)$ is a Gaussian mixture for each realization of i. The conditional PDF of $g\left(\mathbf{r}_B|(i,j)\right)$ for $i=0,1$ is

$$g\left(\mathbf{r}_B|(i,j)\right) = P_{ii} g\left(\mathbf{r}_B|(i,j), e=0\right) + P_{i\bar{i}} g\left(\mathbf{r}_B|(i,j), e=1\right), \tag{4.10}$$

where $g\left(\mathbf{r}_B|(i,j), e=0\right)$ and $g\left(\mathbf{r}_B|(i,j), e=1\right)$ are the PDFs given in (4.5) and $\bar{i}$ is the complement of i. Since solving the error performance of the JMAP decoder using the Gaussian mixtures in (4.10) is non-trivial, we approximate the JMAP decoder by only considering the dominant terms in the summation of (4.10) [35] to obtain

$$\hat{i}, \hat{j} = \arg \max_{i \in \{0,1\}, j \in \{1, \cdots, M\}} \tilde{g}\left(\mathbf{r}_B|(i,j), e=0\right), \tag{4.11}$$

where $\tilde{g}\left(\mathbf{r}_B|(i,j), e=0\right)$ is the first term on the RHS of (4.10). Henceforth, we refer to the above decoder as the Joint Dominant (JD) decoder. To showcase the accuracy of the approximation in (4.11), we tabulate the error-rates for arbitrary energy levels and α for JMAP and JD decoders in Table 4.2. We compute the relative-error between error-rates of JMAP and JD decoder as, $\left|\frac{P_{\text{JMAP}} - P_{\text{JD}}}{P_{\text{JMAP}}}\right|$ and show that the maximum relative error is within 5.55%. Therefore, in the next section, we discuss the error analysis using JD decoder.

Table 4.2: ERROR-RATES AT BOB WHEN USING JMAP DECODER AND JD DECODER FOR $M=2$

$N_C = 1$, $N_B = 8$				
SNR	$\{\epsilon_1, \epsilon_2, \eta_1, \eta_2, \alpha\}$	P_{JMAP}	P_{JD}	rel. error
5 dB	$\{0, 1\text{e}^{-6}, 0.3052, 2.6421, 0.4736\}$	3.06×10^{-1}	3.23×10^{-1}	5.55×10^{-2}
14 dB	$\{0, 1\text{e}^{-6}, 0.5554, 3.0750, 0.8152\}$	8.32×10^{-2}	8.42×10^{-2}	1.20×10^{-2}
25 dB	$\{0, 1\text{e}^{-6}, 0.4382, 3.4008, 0.9195\}$	1.88×10^{-2}	1.90×10^{-2}	1.06×10^{-2}
$N_C = 2$, $N_B = 4$				
SNR	$\{\epsilon_1, \epsilon_2, \eta_1, \eta_2, \alpha\}$	P_{JMAP}	P_{JD}	rel. error
5 dB	$\{0, 1\text{e}^{-6}, 0.4334, 2.7135, 0.5734\}$	3.735×10^{-1}	3.782×10^{-1}	1.25×10^{-2}
14 dB	$\{0, 1\text{e}^{-6}, 0.5353, 3.1645, 0.8499\}$	1.32×10^{-1}	1.33×10^{-1}	7.57×10^{-4}
25 dB	$\{0, 1\text{e}^{-6}, 0.3228, 3.6082, 0.9655\}$	2.43×10^{-2}	2.47×10^{-2}	1.64×10^{-2}

4.3.4 Joint Dominant (JD) Decoder for NC-FFFD Relaying Scheme

From (4.6), we observe that there exist a one-to-one correspondence between (i, j) and ℓ. Thus, the JD decoder in (4.11) can be rewritten as, $\hat{\ell} = \arg \max\limits_{\ell \in \{1,\ldots,2M\}} \tilde{g}\left(\mathbf{r}_B | \ell, e = 0\right)$. Henceforth, a transmit pair jointly chosen by Alice and Charlie will be denoted by the index $\ell \in \{1, 2, \ldots, 2M\}$. As a consequence, the JD decoder only considers the likelihood functions corresponding to the $2M$ dominant energy levels in $\mathcal{S}$ with the assumption that no decoding error is introduced by Charlie. Let $\triangle_{\substack{\ell \to \ell^* \\ \ell \neq \ell^*}}$ denotes the event when Bob incorrectly decodes an index ℓ to ℓ^* such that $\ell \neq \ell^*$. Then, $\Pr\left(\triangle_{\substack{\ell \to \ell^* \\ \ell \neq \ell^*}}\right) = \Pr\left(\tilde{g}\left(\mathbf{r}_B | \ell, e = 0\right) \leq \tilde{g}\left(\mathbf{r}_B | \ell^*, e = 0\right)\right)$. To characterize $\Pr\left(\triangle_{\substack{\ell \to \ell^* \\ \ell \neq \ell^*}}\right)$, one should determine the energy detection threshold between the energy levels corresponding to ℓ and ℓ^*. Towards this direction, we use the following lemma that computes the energy detection threshold between S_ℓ and S_{ℓ^*}.

Lemma 9. *If S_ℓ denotes the energy level jointly contributed by Alice and Charlie corresponding to the transmitted index ℓ and S_{ℓ^*} denotes the energy level corresponding to the decoded index ℓ^* such that $\ell \neq \ell^*$, then the probability of the event $\triangle_{\substack{\ell \to \ell^* \\ \ell \neq \ell^*}}$ is given by $\Pr\left(\triangle_{\substack{\ell \to \ell^* \\ \ell \neq \ell^*}}\right) = \Pr(\mathbf{r}_B^H \mathbf{r}_B \geq \rho_{\ell,\ell^*})$, where the threshold ρ_{ℓ,ℓ^*} is given by, $\rho_{\ell,\ell^*} \approx N_B \frac{S_\ell S_{\ell^*}}{S_{\ell^*} - S_\ell} \ln\left(\frac{S_{\ell^*}}{S_\ell}\right)$.*

Proof. Bob uses JD decoder and compares the conditional PDF of $\mathbf{r}_B$ conditioned on ℓ and ℓ^* as

$$\Pr\left(\triangle_{\substack{\ell \to \ell^* \\ \ell \neq \ell^*}}\right) = \Pr\left(\frac{\tilde{g}\left(\mathbf{r}_B | \ell^*, e = 0\right)}{\tilde{g}\left(\mathbf{r}_B | \ell, e = 0\right)} \leq 1\right) = \Pr\left(\frac{\dfrac{P_{i^*i^*}}{\left(\pi S_{\ell^*}\right)^{N_B}} \exp\left(-\frac{\mathbf{r}_B^H \mathbf{r}_B}{S_{\ell^*}}\right)}{\dfrac{P_{ii}}{\left(\pi S_{\ell}\right)^{N_B}} \exp\left(-\frac{\mathbf{r}_B^H \mathbf{r}_B}{S_{\ell}}\right)} \leq 1\right)$$
$$= \Pr\left(\mathbf{r}_B^H \mathbf{r}_B \geq \rho_{\ell,\ell^*}\right),$$

where $\rho_{\ell,\ell^*} = \frac{S_\ell S_{\ell^*}}{S_{\ell^*} - S_\ell}\left(N_B \ln\left(\frac{S_{\ell^*}}{S_\ell}\right) + \ln\left(\frac{P_{ii}}{P_{i^*i^*}}\right)\right)$ and P_{ii} and $P_{i^*i^*}$ are a priori probabilities of index ℓ and ℓ^*, respectively. It is straightforward that when $i = i^*$, $\ln\left(\frac{P_{ii}}{P_{i^*i^*}}\right) = 0$. Further, since $\ln\left(\frac{\Phi_{00}}{\Phi_{11}}\right) \approx 0$ for $N \geq 1$, when $i \neq i^*$, we have $\ln\left(\frac{P_{ii}}{P_{i^*i^*}}\right) = \ln\left(\frac{\Phi_{00}}{\Phi_{11}}\right) \approx 0$ and $\ln\left(\frac{P_{ii}}{P_{i^*i^*}}\right) = \ln\left(\frac{\Phi_{11}}{\Phi_{00}}\right) \approx 0$, for $i = 0$ and $i = 1$, respectively. Thus, $\rho_{\ell,\ell^*} \approx N_B \frac{S_\ell S_{\ell^*}}{S_{\ell^*} - S_\ell} \ln\left(\frac{S_{\ell^*}}{S_\ell}\right)$. □

Since $S_1 < S_2 \cdots < S_{2M-1} < S_{2M}$, the set of relevant thresholds for the JD decoder are $\{\rho_{\ell,\ell+1}, \ell = 1, 2, \ldots, 2M-1\}$. Therefore, based on the received energy $\mathbf{r}_B^H \mathbf{r}_B$, the JD decoder for detecting $\hat{\ell}$ can be realized using an energy detector as, $\hat{\ell} = \ell$, if $\rho_{\ell-1,\ell} < \mathbf{r}_B^H \mathbf{r}_B \leq \rho_{\ell,\ell+1}$, where $\rho_{0,1} = 0$ and $\rho_{2M,\infty} = \infty$.

Using $\hat{\ell}$, the average Symbol Error Probability (SEP), denoted by P_e, is given by, $P_e = \frac{1}{2M} \sum_{\ell=1}^{2M} P_{e,\ell}$, where $P_{e,\ell} = \Pr(\ell \neq \ell^*)$ is the probability that Bob decodes a transmitted index ℓ as ℓ^*, where $\ell \neq \ell^*$. Since, the decision of the energy detector is based on the received energies at Bob, we notice that sum energy levels can be from $\mathcal{S}$, when $e = 0$ or $\overline{\mathcal{S}}$, when $e = 1$. Therefore, $P_{e,\ell} = \Pr(e = 0) \Pr(\ell \neq \ell^* | e = 0) + \Pr(e = 1) \Pr(\ell \neq \ell^* | e = 1)$. Thus, we have

$$P_{e,\ell} = \begin{cases} \Phi_{00} P_{e,S_\ell} + \Phi_{01} P_{e,\overline{S}_\ell} & \text{if } \ell (\mathrm{mod} 4) \leq 1, \\ \Phi_{11} P_{e,S_\ell} + \Phi_{10} P_{e,\overline{S}_\ell} & \text{if otherwise,} \end{cases} \tag{4.12}$$

where P_{e,S_ℓ} and $P_{e,\overline{S}_\ell}$ are the terms associated with erroneous decision in decoding ℓ, when $e = 0$ and $e = 1$, respectively. Since $\mathbf{r}_B^H \mathbf{r}_B$ is gamma distributed, we get P_{e,S_ℓ} as given in (4.13).

$$P_{e,S_\ell} = \begin{cases} \dfrac{\Gamma\left(N_B, \frac{\rho_{1,2}}{S_1}\right)}{\Gamma(N_B)} & \text{for } \ell = 1, \\ \dfrac{\gamma\left(N_B, \frac{\rho_{\ell-1,\ell}}{S_\ell}\right)}{\Gamma(N_B)} + \dfrac{\Gamma\left(N_B, \frac{\rho_{\ell,\ell+1}}{S_\ell}\right)}{\Gamma(N_B)} & \text{for } 2 \leq \ell \leq 2M-1, \\ \dfrac{\gamma\left(N_B, \frac{\rho_{2M-1,2M}}{S_{2M}}\right)}{\Gamma(N_B)} & \text{for } \ell = 2M. \end{cases} \tag{4.13}$$

Since Bob uses the same thresholds to compute $P_{e,\overline{S}_\ell}$, we obtain the expression of $P_{e,\overline{S}_\ell}$, by replacing S_ℓ by $\overline{S}_\ell$ in (4.13). Finally, substituting (4.12), (4.13), and corresponding $P_{e,\overline{S}_\ell}$ in P_e, we get

$$\begin{aligned} P_e = \frac{1}{2M} \Bigg[\sum_{\ell_1=1}^{M} \Phi_{00} P_{e,S_{\frac{1}{2}\left(4\ell_1 + (-1)^{\ell_1} - 1\right)}} + \Phi_{11} P_{e,S_{\frac{1}{2}\left((-1)^{\ell_1}\left(4(-1)^{\ell_1}\ell_1 + (-1)^{\ell_1+1} - 1\right)\right)}} + \\ \Phi_{01} P_{e,\overline{S}_{\frac{1}{2}\left(4\ell_1 + (-1)^{\ell_1} - 1\right)}} + \Phi_{10} P_{e,\overline{S}_{\frac{1}{2}\left((-1)^{\ell_1}\left(4(-1)^{\ell_1}\ell_1 + (-1)^{\ell_1+1} - 1\right)\right)}} \Bigg]. \end{aligned} \tag{4.14}$$

4.4 Optimization of Energy Levels

In this section, we formulate an optimization problem in order to compute the optimal energy levels at Alice and Charlie. In particular, as given in (4.15), we fix N_C and N_B and then optimise the energy levels, $\{\epsilon_j, \eta_j\}$, and α so as to minimise the SEP subject to the energy constraint in (4.3).

$$\begin{aligned} \min_{\epsilon_1,\cdots,\epsilon_M,\eta_1,\cdots,\eta_M,\alpha} \quad & P_e \\ \text{subject to:} \quad & \sum_{j=1}^{M}(\epsilon_j+\eta_j) = M(1+\alpha), \\ & \epsilon_1 < \cdots < \epsilon_M, \eta_1 < \cdots < \eta_M, 0 < \alpha < 1, \\ & \epsilon_j < \eta_j \text{ for } j \in \{1,3,\cdots,2M-1\}, \\ & \epsilon_j > \eta_j \text{ for } j \in \{2,4,\cdots,2M\}. \end{aligned} \tag{4.15}$$

One can solve the above optimization problem by first formulating the Lagrangian and then solving the system of $2M+2$ non-linear equations. Since solving a system of non-linear equations is complex in general, we use an alternate approach for minimising P_e using its analytical structure, as discussed in the next section. We first discuss the optimization of energy levels for $M = 2$ and then propose a generalised approach of $M = 2^m$ such that $m > 1$.

4.4.1 Optimization of Energy Levels for $M = 2$

The expression of SEP in (4.14) when $M = 2$ is given as

$$P_e = \frac{1}{4}\left(\Phi_{00}\left(P_{e,S_1}+P_{e,S_4}\right)+\Phi_{11}\left(P_{e,S_2}+P_{e,S_3}\right)+\Phi_{01}\left(P_{e,\overline{S}_1}+P_{e,\overline{S}_4}\right)+\Phi_{10}\left(P_{e,\overline{S}_2}+P_{e,\overline{S}_3}\right)\right). \tag{4.16}$$

Instead of using P_e for optimization problem, we use an upper-bound on P_e, where we upper-bound $P_{e,\overline{S}_1} \leq P_{e,\overline{S}_4} \leq P_{e,\overline{S}_2} \leq P_{e,\overline{S}_3} \leq 1$, such that

$$P_e \leq P_e' \triangleq \frac{1}{4}\left(\Phi_{00}\left(P_{e,S_1}+P_{e,S_4}\right)+\Phi_{11}\left(P_{e,S_2}+P_{e,S_3}\right)+2\left(\Phi_{01}+\Phi_{10}\right)\right). \tag{4.17}$$

Henceforth, we optimise the energy levels, ϵ_1, ϵ_2, η_1, and η_2 and α so as to minimise P_e'.[1] Thus, the modified optimization problem when $M = 2$ is

$$\begin{aligned} \min_{\epsilon_1,\epsilon_2,\eta_1,\eta_2,\alpha} \quad & P_e' \\ \text{subject to:} \quad & \epsilon_1+\epsilon_2+\eta_1+\eta_2 = 2(1+\alpha), \\ & \epsilon_1 < \epsilon_2, \eta_1 < \eta_2, 0 < \alpha < 1, \\ & \epsilon_1 < \eta_1 < \eta_2 < \epsilon_2. \end{aligned} \tag{4.18}$$

In order to minimise P_e', it is clear that we must minimise each P_{e,S_ℓ}, for $\ell = 1, \cdots, 4$ in (4.18). Towards this direction, in the next lemma, we show that when $\epsilon_1 = 0$, P_{e,S_1} is minimum.

Lemma 10. *The expression* $P_{e,S_1} = \dfrac{\Gamma\left(N_B, \frac{\rho_{1,2}}{S_1}\right)}{\Gamma(N_B)}$ *is minimum when* $\epsilon_1 = 0$.

Proof. The expression of P_{e,S_1} is an upper incomplete Gamma function. Since upper incomplete Gamma function is a decreasing function of the second parameter, $\Gamma\left(N_B, \frac{\rho_{1,2}}{S_1}\right)$ is a decreasing function of $\frac{\rho_{1,2}}{S_1}$. Therefore, P_{e,S_1} is minimum when $\frac{\rho_{1,2}}{S_1}$ is maximum and $\frac{\rho_{1,2}}{S_1}$ is maximum when S_1 is minimum. Since $S_1 = \epsilon_1 + N_o$, S_1 is minimum when $\epsilon_1 = 0$. This completes the proof. □

Lemma 11. *At high SNR,* $P_{e,S_1} \ll 1$ *and* $P_{e,S_2} \approx \dfrac{\Gamma\left(N_B, \frac{\rho_{2,3}}{S_2}\right)}{\Gamma(N_B)}$.

Proof. We first prove that $P_{e,S_1} \ll 1$. We have $P_{e,S_1} = \frac{\Gamma\left(N_B, \frac{\rho_{1,2}}{S_1}\right)}{\Gamma(N_B)}$. The ratio $\frac{\rho_{1,2}}{S_1}$ is expressed as, $N_B \frac{\ln(1+\kappa_1)}{\kappa_1}$, where $\kappa_1 = (S_1 - S_2)/S_2$. Further. since $S_1 < S_2$, $-1 < \kappa_1 < 0$. Also, the ratio $\frac{\ln(1+\kappa_1)}{\kappa_1}$ follows the inequalities, $\frac{2}{2+\kappa_1} \leq \frac{\ln(1+\kappa_1)}{\kappa_1} \leq \frac{2+\kappa_1}{2+2\kappa_1}$, for $\kappa > -1$. Therefore, $\frac{\Gamma\left(N_B, \frac{2N_B}{2+\kappa_1}\right)}{\Gamma(N_B)} \geq \frac{\Gamma\left(N_B, \frac{\rho_{1,2}}{S_1}\right)}{\Gamma(N_B)} \geq \frac{\Gamma\left(N_B, N_B\frac{2+\kappa_1}{2+2\kappa_1}\right)}{\Gamma(N_B)}$, where the second inequality is because $\Gamma\left(N_B, \frac{\rho_{1,2}}{S_1}\right)$ is a decreasing function of $\frac{\rho_{1,2}}{S_1}$. Thus, $\frac{\Gamma\left(N_B, \frac{\rho_{1,2}}{S_1}\right)}{\Gamma(N_B)} \leq \frac{\Gamma\left(N_B, \frac{2N_B}{2+\kappa_1}\right)}{\Gamma(N_B)} = \frac{\Gamma(N_B, 2N_B)}{\Gamma(N_B)} \ll 1$. Since $S_1 \approx 0$ at high SNR, $2/(2+\kappa_1) = 2S_2/(S_1+S_2) \approx 2$ and therefore, we have the second inequality. This proves the first part of Lemma. On similar lines, we can prove that at high SNR, the term $\frac{\gamma\left(N_B, \frac{\rho_{1,2}}{S_2}\right)}{\Gamma(N_B)} \leq \frac{\gamma\left(N_B, \frac{N_B}{2}\right)}{\Gamma(N_B)}$, thus, $\frac{\gamma\left(N_B, \frac{N_B}{2}\right)}{\Gamma(N_B)} \ll 1$ and therefore, we have $P_{e,S_2} \approx \frac{\Gamma\left(N_B, \frac{\rho_{2,3}}{S_2}\right)}{\Gamma(N_B)}$. □

---

[1] Later through simulation results, we show that, optimizing (4.17) gives us near-optimal results.

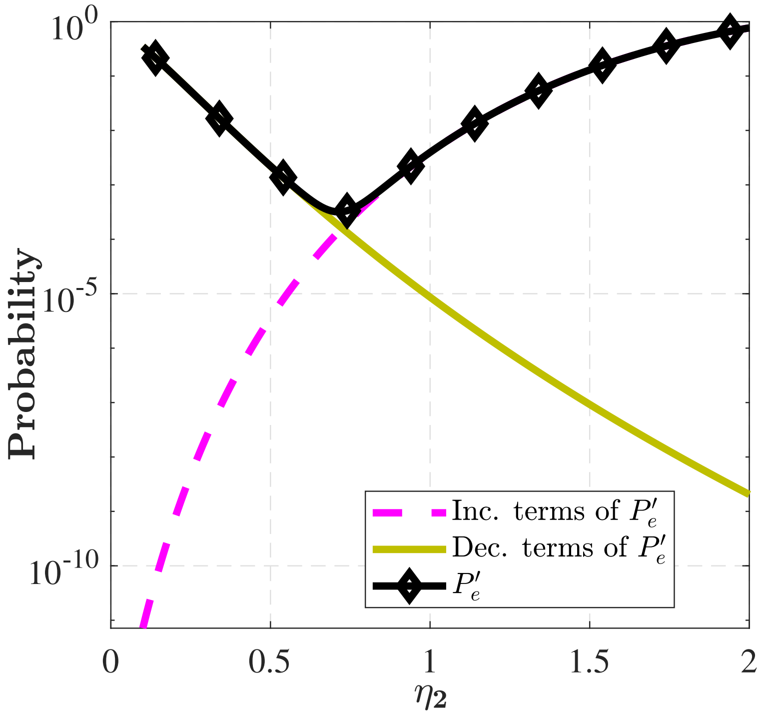

Figure 4.4: Variation of P_e', its increasing and decreasing terms as a function of η_2, when η_1 and α are fixed.

Using the results of Lemma 11, the expression of P_e' is approximated as

$$P_e' \approx \frac{1}{4}\left(\Phi_{00}P_{e,S_4}+\Phi_{11}\left(P_{e,S_2}+P_{e,S_3}\right)+2\left(\Phi_{01}+\Phi_{10}\right)\right). \tag{4.19}$$

From (4.18) we have 5 variables, resulting in a 5-dimensional search space to find the optimal set $\{\epsilon_1, \epsilon_2, \eta_1, \eta_2, \alpha\}$. Using the result of Lemma 10, we have $\epsilon_1 = 0$. Further, rearranging the sum energy constraint, we express ϵ_2 as a function of η_1, η_2, and α, therefore, $\epsilon_2 = 2(1+\alpha)-(\eta_1+\eta_2)$. Thus, the search space is reduced to 3 dimensions. Through simulations we observe that, when we fix η_1 and α, P_e' exhibits unimodal nature w.r.t. η_2. Similarly, P_e' is unimodal w.r.t. α, when we fix η_1 and η_2. The variation of P_e', the increasing terms of P_e', and the decreasing terms of P_e', w.r.t. η_2 and α are shown in Fig. 4.4 and Fig. 4.5, respectively. Further, we also observe that the unique mode in both the cases is very close to the intersection of increasing and decreasing terms of P_e'. Therefore, in the next two theorems, we prove that the increasing and decreasing terms of P_e' w.r.t. η_2 and α, have a unique intersection that is close to the local minima of P_e'.

Theorem 7. *For a given η_1 and α, the increasing and decreasing terms in P_e' intersect only once for $\eta_2 \in (\eta_1, 1+\alpha-0.5\eta_1)$.*

Proof. We first determine the increasing and decreasing terms of P'_e. Towards this direction, we first analyse the behaviour of each term in (4.19), i.e., P_{e,S_2}, P_{c,S_3}, and P_{e,S_4} as a function of η_2, where

$$P_{e,B2} = \frac{\Gamma\left(N_B, \frac{\rho_{2,3}}{S_2}\right)}{\Gamma\left(N_B\right)}, \quad P_{e,S_3} = \frac{\Gamma\left(N_B, \frac{\rho_{3,4}}{S_3}\right)}{\Gamma\left(N_B\right)} + \frac{\gamma\left(N_B, \frac{\rho_{2,3}}{S_3}\right)}{\Gamma\left(N_B\right)}, \quad P_{c,S_4} = \frac{\gamma\left(N_B, \frac{\rho_{3,4}}{S_4}\right)}{\Gamma\left(N_B\right)}.$$

Consider the term P_{e,S_2}, where the ratio $\frac{\rho_{2,3}}{S_2}$ is given by, $N_B\frac{\ln(1+\kappa_3)}{\kappa_3}$, where $\kappa_3 = (S_2 - S_3)/S_3$. Since $S_2 < S_3$, $\kappa_3 < 0$. Differentiating κ_3 w.r.t. η_2 we get $-S_1/S_2^2$. Therefore, as η_2 increases, κ_3 decreases. Since $\ln(1+\kappa_3)/\kappa_3$ is a decreasing function of κ_3, as κ_3 decreases, $N_B \ln(1+\kappa_3)/\kappa_3$ increases. Finally, since $\frac{\Gamma\left(N_B, \frac{\rho_{2,3}}{S_2}\right)}{/}\Gamma\left(N_B\right)$ is a decreasing function of $\rho_{2,3}/S_2$, $P_{e,B2}$ decreases with increasing $\ln(1+\kappa_3)/\kappa_3$. Therefore, P_{e,S_4} is a decreasing function of η_2.

On similar lines, we can prove that $\frac{\gamma\left(N_B, \frac{\rho_{2,3}}{S_3}\right)}{\Gamma(N_B)}$ is also a decreasing function of η_2. In contrast, the terms, $\frac{\Gamma\left(N_B, \frac{\rho_{3,4}}{S_3}\right)}{\Gamma(N_B)}$ and $\frac{\gamma\left(N_B, \frac{\rho_{3,4}}{S_4}\right)}{\Gamma(N_B)}$ are increasing functions of η_2.

To prove that the increasing and decreasing terms intersect only once, we can prove that the order of increasing and decreasing terms reverses at extreme values of $\eta_2 \in (\eta_1, (1 + \alpha - 0.5\eta_1))$. Thus, we evaluate the sum of decreasing terms at left extreme, i.e., $\eta_2 \to \eta_1$ and right extreme, i.e., $\eta_2 \to (1 + \alpha - 0.5\eta_1)$

$$\lim_{\eta_2 \to \eta_1} \frac{\Gamma\left(N_B, \frac{\rho_{2,3}}{S_2}\right)}{\Gamma\left(N_B\right)} + \frac{\Gamma\left(N_B, \frac{\rho_{2,3}}{S_3}\right)}{\Gamma\left(N_B\right)} = 1$$
$$\lim_{\eta_2 \to (1+\alpha-0.5\eta_1)} \frac{\Gamma\left(N_B, \frac{\rho_{2,3}}{S_2}\right)}{\Gamma\left(N_B\right)} + \frac{\Gamma\left(N_B, \frac{\rho_{2,3}}{S_3}\right)}{\Gamma\left(N_B\right)} \ll 1.$$

Similarly, we evaluate the sum of increasing terms at left extreme and right extremes of η_1

$$\lim_{\eta_2 \to \eta_1} \frac{\Gamma\left(N_B, \frac{\rho_{3,4}}{S_3}\right)}{\Gamma\left(N_B\right)} + \frac{\gamma\left(N_B, \frac{\rho_{3,4}}{S_4}\right)}{\Gamma\left(N_B\right)} \ll 1$$
$$\lim_{\eta_2 \to (1+\alpha-0.5\eta_1)} \frac{\Gamma\left(N_B, \frac{\rho_{3,4}}{S_3}\right)}{\Gamma\left(N_B\right)} + \frac{\gamma\left(N_B, \frac{\rho_{3,4}}{S_4}\right)}{\Gamma\left(N_B\right)} = 1.$$

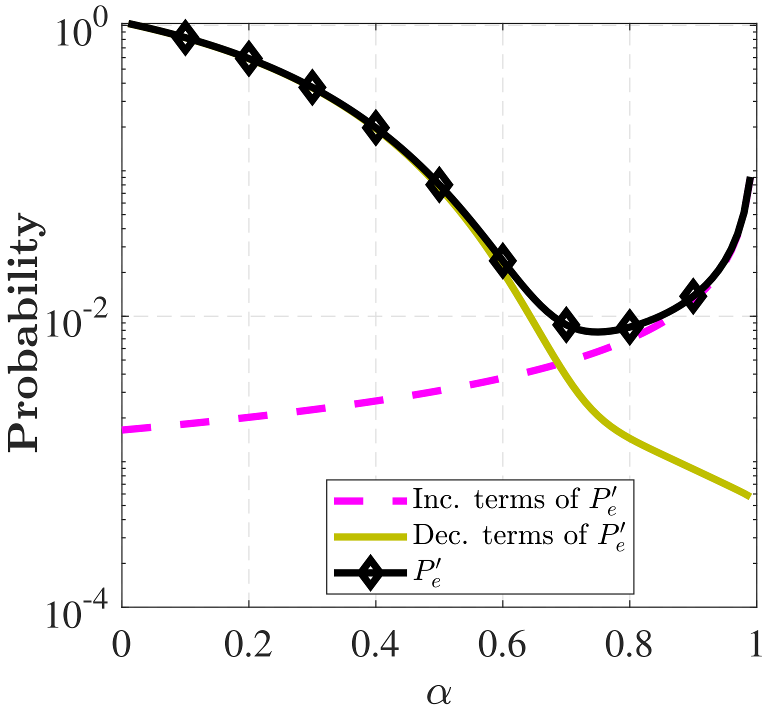

Figure 4.5: Variation of P_e', its increasing and decreasing terms as a function of α, when η_1 and η_2 are fixed.

The above discussion is summarised as

$$\begin{array}{ll}\frac{\Gamma\left(N_B,\frac{\rho_{2,3}}{S_2}\right)}{\Gamma\left(N_B\right)}+\frac{\Gamma\left(N_B,\frac{\rho_{2,3}}{S_3}\right)}{\Gamma\left(N_B\right)}>\frac{\Gamma\left(N_B,\frac{\rho_{3,4}}{S_3}\right)}{\Gamma\left(N_B\right)}+\frac{\gamma\left(N_B,\frac{\rho_{3,4}}{S_4}\right)}{\Gamma\left(N_B\right)}, & \text{if } \eta_2\rightarrow\eta_1\\ \frac{\Gamma\left(N_B,\frac{\rho_{2,3}}{S_2}\right)}{\Gamma\left(N_B\right)}+\frac{\Gamma\left(N_B,\frac{\rho_{2,3}}{S_3}\right)}{\Gamma\left(N_B\right)}<\frac{\Gamma\left(N_B,\frac{\rho_{3,4}}{S_3}\right)}{\Gamma\left(N_B\right)}+\frac{\gamma\left(N_B,\frac{\rho_{3,4}}{S_4}\right)}{\Gamma\left(N_B\right)}, & \text{if } \eta_2\rightarrow(1+\alpha-0.5\eta_1).\end{array}$$

□

Theorem 8. *For a given η_1 and η_2, the increasing and decreasing terms in P_e' intersect only once for $\alpha \in (0,1)$.*

Proof. Since α is variable, we recall Lemma 7 to show that Φ_{01} and Φ_{10} are decreasing function of α. Further, since Φ_{01} and Φ_{10} are decreasing functions of α, Φ_{00} and Φ_{11} are decreasing functions of α. In addition to these 4 probabilities, P_{e,S_2}, P_{e,S_3}, and P_{e,S_4} are also functions of α in (4.19). On similar lines of Theorem 7, we prove that, P_{e,S_2}, P_{e,S_3}, and P_{e,S_4} are decreasing function of α. Therefore, we observe that $\Phi_{00}P_{e,S_4} + \Phi_{11}\left(P_{e,S_2} + P_{e,S_3}\right)$ is a decreasing function of α and since $\Phi_{00} = \Phi_{11} \approx 0$, when $\alpha \rightarrow 1$, $\Phi_{00}P_{e,S_4} + \Phi_{11}\left(P_{e,S_2} + P_{e,S_3}\right) \approx 0$, when $\alpha \rightarrow 1$. Further, $2(\Phi_{01} + \Phi_{10})$ is an increasing function of α such that, $2(\Phi_{01} + \Phi_{10}) \approx 0$, when $\alpha \rightarrow 0$ and $2(\Phi_{01} + \Phi_{10}) \approx 2$, when

$\alpha \to 1$. Therefore, it is straightforward to observe that the increasing and decreasing terms of P_e' reverse their orders at extreme values of α. Thus, they have a unique intersection point. $\square$

In the next section, we use Theorem 7 and Theorem 8 to present a low-complexity algorithm to solve the optimization problem in (4.18). Using this algorithm, we obtain a local minima over the variables η_2 and α for a given η_1.

Two-Layer Greedy Descent (TLGD) Algorithm

Algorithm 1. Two-Layer Greedy Descent Algorithm

```
Input: $P_e'$ from (4.19), $\delta_{P_e'} > 0$, $\delta_{\eta_1} > 0$, $\epsilon_1 = 0$
Outpuut: $\{\eta_1^\star, \eta_2^\star, \alpha^\star\}$
Initialize: $\eta_1 \leftarrow 0$, $\eta_2 \leftarrow \eta_2^o$, $\alpha \leftarrow \alpha^o$
$P_e^o \leftarrow P_e'(\alpha, \eta_1, \eta_2)$
while true do
    while true do
        Compute $\eta_2^i$ using Theorem 7 and obtain $P_e^{\eta_2} \leftarrow P_e'(\eta_1, \eta_2^i, \alpha)$
        Compute $\alpha^i$ using Theorem 8 and obtain $P_e^{\alpha} \leftarrow P_e'(\eta_1, \eta_2, \alpha^i)$
        if $P_e^{\alpha} - P_e^{\eta_2} \geq \delta_{P_e'}$ then
            $\eta_2 \leftarrow \eta_2^i$; continue
        else if $P_e^{\alpha} - P_e^{\eta_2} \leq -\delta_{P_e'}$ then
            $\alpha \leftarrow \alpha^i$; continue
        else
            $|P_e^{\alpha} - P_e^{\eta_2}| < \delta_{P_e'}$
        end
        $P_e^{\iota} = \min(P_e^{\alpha}, P_e^{\eta_2})$; break
    end
    if $(P_e^{\iota} - P_e^o) \leq -\delta_{P_e'}$ then
        $\eta_1 \leftarrow \eta_1 + \delta_{\eta_1}$, $P_e^o \leftarrow P_e^{\iota}$; $\alpha^* \leftarrow \alpha$, $\eta_2^* \leftarrow \eta_2$
    else if $(P_e^{\iota} - P_e^o) \geq \delta_{P_e'}$ then
        $\eta_1^\star \leftarrow \eta_1 - \delta_{\eta_1}$, $\eta_2^\star \leftarrow \eta_2^*$, $\alpha^\star \leftarrow \alpha^*$; break
    else
        $|P_e^{\iota} - P_e^o| < \delta_{P_e'}$
    end
    $\eta_1^\star \leftarrow \eta_1$, $\eta_2^\star \leftarrow \eta_2^i$, $\alpha^\star \leftarrow \alpha^i$; break
end
```

In this section, we present Two-Layer Greedy Descent (TLGD) algorithm, as presented in Algorithm 1. It first fixes N_C, N_B, and SNR and then initialise $\eta_1 = 0$, and η_2 and α with arbitrary values η_2^o and α^o, respectively. Using the initial values, it computes P_e^o using (4.19) and then obtains η_2^i and α^i using Theorem 7 and Theorem 8, respectively. It then evaluates $P_e^{\eta_2}$, i.e., P_e' at $\{\eta_1, \eta_2^i, \alpha\}$ and P_e^{α}, i.e., P_e' at $\{\eta_1, \eta_2, \alpha^i\}$. If for a given η_1, $|P_e^{\alpha} - P_e^{\eta_2}| < \delta_{P_e'}$, for some $\delta_{P_e'} > 0$, then the algorithm exits the inner while-loop with P_e^{ι} such that $P_e^{\iota} = \min(P_e^{\alpha}, P_e^{\eta_2})$ else, the algorithm iteratively

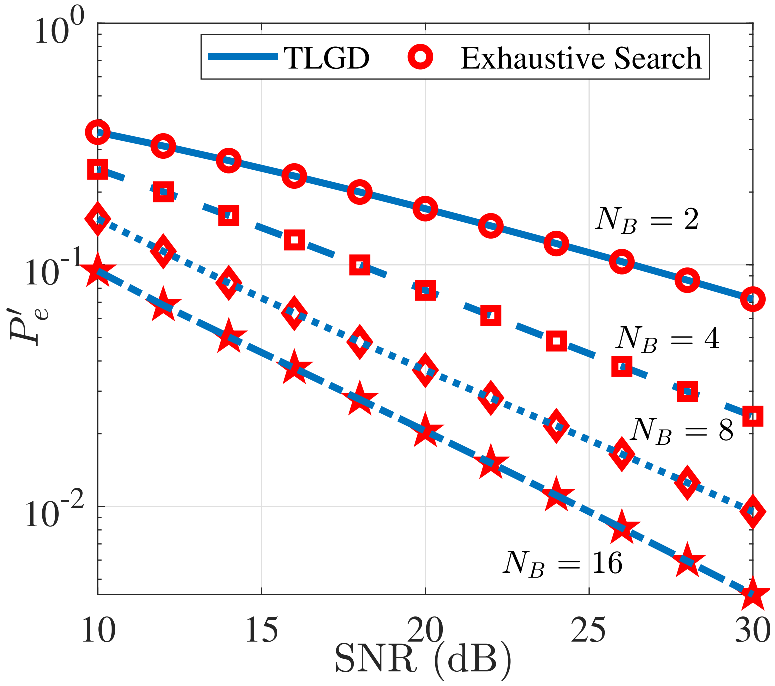

Figure 4.6: Performance of NC-FFFD using energy levels obtained using TLGD and the exhaustive search.

descents in the steepest direction with new values of η_2 and α. After traversing several values of η_1, TLGD finally stops when for a given η_1, the obtained P_e^{ι} is within $\delta_{P_e'}$, resolution of the previously computed value. The points at which P_e' is minimum as computed by TLGD are given by $\eta_1^\star$, $\eta_2^\star$ and $\alpha^\star$. We rearrange the constraint in (4.18) to obtain $\epsilon_2^\star = 2(1+\alpha^\star)-(\eta_1^\star+\eta_2^\star)$. Further, from Lemma 10, we have $\epsilon_1 = 0$, therefore, $\epsilon_1^\star = 0$. Thus, TLGD computes all the 5 variables, i.e., $\epsilon_1^\star$, $\epsilon_2^\star$, $\eta_1^\star$, $\eta_2^\star$, and $\alpha^\star$.

In Fig. 4.6, we plot the error performance of NC-FFFD scheme as a function of SNR and N_B using Monte-Carlo simulations. We assume, $\sigma_{AB}^2 = \sigma_{CB}^2 = 1$, $\lambda = -50$ dB, and $N_C = 1$. Further, due to vicinity of Alice and Charlie, we assume $\sigma_{AC}^2 = 4$, thus, providing 6 dB improvement in SNR on Alice-to-Charlie link as compared to Alice-to-Bob link. We compute the error-rates when the optimal energy levels and α are obtained using exhaustive search on (4.16). We also compute the error-rates using the proposed algorithm. For both the scenarios, we observe that the error curves approximately overlap, indicating the efficacy of the proposed algorithm, as well as our approach of using (4.18) instead of (4.16).

Further, in Fig 4.7, for same parameters and $N_B = 8$, we plot the error performance of ND-FFFD scheme as a function of SNR for various values of N_C. We observe that, the error performance of NC-FFFD scheme improves as a function of N_C. Finally,

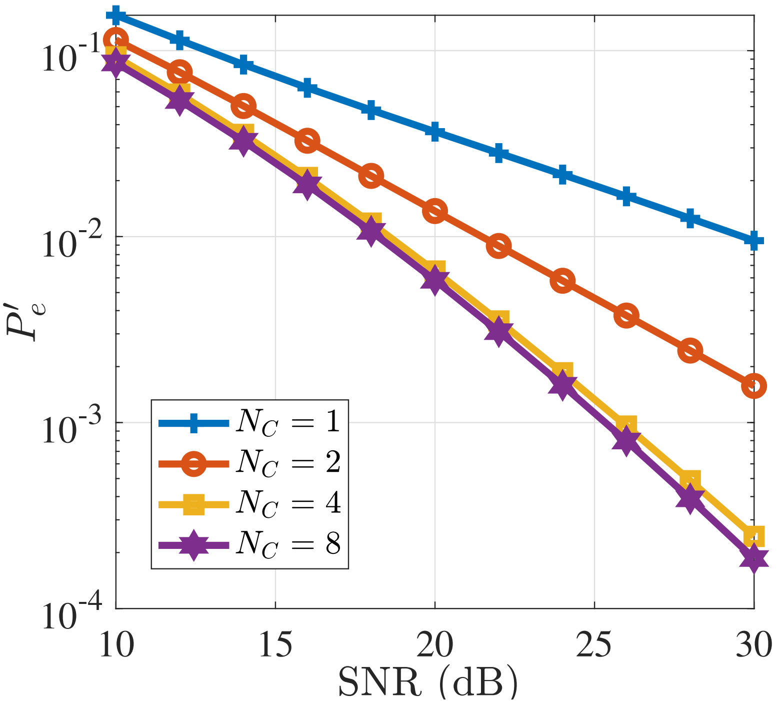

Figure 4.7: Performance of NC-FFFD for fixed $N_B = 8$ and varying N_C.

for the same parameters and $N_B = 8$, in Fig. 4.8, we show the improvement in Alice's performance when using NC-FFFD relaying scheme. In terms of feasibility of implementation, the complexity analysis of TLGD algorithm has been discussed in the conference proceedings of this work [37].

4.4.2 Optimization of Energy Levels for $M \geq 2$

In this section, we provide a solution that computes the optimal energy levels, $\{\epsilon_j, \eta_j\}$, and the factor α, when $M \geq 2$. Since the average transmit energy of Charlie is constrained to $\mathrm{E}_{C,f_{CB}}$, increasing the data-rate at Charlie results in degraded joint error performance as compared to $M = 2$. One way to improve the error performance is by using a large number of receive antennas at Bob. Despite this improvement, it is important to note that the joint error performance is also a function of the SNR of Alice-to-Charlie link. Therefore, an improved Alice-to-Charlie link can help to improve the overall performance of the scheme. This is also evident from Fig. 4.7, where we observe that the error performance of the scheme improves as a function of N_C. This motivates us to solve P_e in (4.15) for optimal $\{\epsilon_j, \eta_j\}$, and α under the assumption that Charlie has a sufficiently large number of receive-antennas. In this section, we take a similar approach as that of Sec. 4.4.1, by upper bounding the complementary error terms by 1

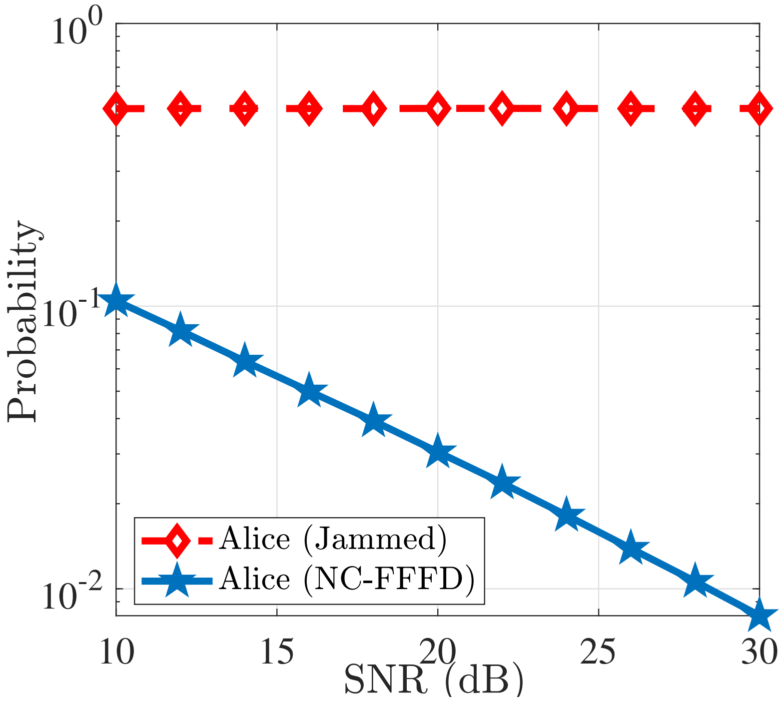

Figure 4.8: Alice's performance when using NC-FFFD scheme for $N_C = 1$ and $N_B = 8$.

to obtain an upper bound on P_e given by

$$P_e \leq P'_e \triangleq \frac{1}{2M}\left[\sum_{\ell_1=1}^{M}\Phi_{00}P_{e,S_{\frac{1}{2}\left(4\ell_1+(-1)^{\ell_1}-1\right)}}+\sum_{\ell_2=1}^{M}\Phi_{11}P_{e,S_{\frac{1}{2}\left((-1)^{\ell_2}\left(4(-1)^{\ell_2}\ell_2+(-1)^{\ell_2+1}-1\right)\right)}}+\right.$$
$$\left. M\left(\Phi_{01}+\Phi_{10}\right)\right]. \quad (4.20)$$

Since P'_e is a function of S_ℓ and α, besides N_C, N_B, and SNR, in the next theorem, we compute the optimal value of $\alpha \in (0, 1)$, that minimises P'_e, when $S_1, \cdots, S_{2M}$, N_C, N_B, and SNR are fixed.

Theorem 9. *When $S_1, \cdots, S_{2M}$ are fixed, such that $S_2 < 1$, the optimal value of $\alpha \in (0, 1)$ that minimises P'_e in* (4.20) *is given by, $\alpha^\dagger = 1 - S_2$.*

Proof. We will first show that P'_e in (4.20) is an increasing function of α. Then, we compute a lower bound on α considering the feasible energy levels jointly contributed by Alice and Charlie.

The expression of P'_e in (4.20) is a convex combination of Φ_{00}, Φ_{01}, Φ_{10}, and Φ_{11}. Further, we notice that Φ_{00} and Φ_{11} are decreasing functions of α (Lemma 7). However, since $S_1, \cdots, S_{2M}$ are fixed, the coefficients of Φ_{00} and Φ_{11} are independent of α, such that, $\sum_{\ell_1=1}^{M} P_{e,S_{\frac{1}{2}\left(4\ell_1+(-1)^{\ell_1}-1\right)}} \leq M$ and $\sum_{\ell_2=1}^{M} P_{e,S_{\frac{1}{2}\left((-1)^{\ell_2}\left(4(-1)^{\ell_2}\ell_2+(-1)^{\ell_2+1}-1\right)\right)}} \leq M$.

Further, since Φ_{01} and Φ_{10} are increasing functions of α, it is straightforward that, P_e' is an increasing function of α. This completes the first part of the proof.

Although, we upper bound the energy levels $\overline{S}_\ell$ by 1, in practice, Bob receives these energy levels when $e = 1$ at Charlie. From (4.7), we have, $\overline{S}_{\frac{1}{2}\left(4\ell_1+(-1)^{\ell_1}-1\right)} = S_{\frac{1}{2}\left((-1)^{\ell_1}\left(4(-1)^{\ell_1}+(-1)^{\ell_1+1}-1\right)\right)} - (1-\alpha)$. It is important to note that, $\overline{S}_{\frac{1}{2}\left(4\ell_1+(-1)^{\ell_1}-1\right)} < 0$, if $S_{\frac{1}{2}\left((-1)^{\ell_1}\left(4(-1)^{\ell_1}+(-1)^{\ell_1+1}-1\right)\right)} < 1 - \alpha$. However, since $\overline{S}_\ell \in \overline{\mathcal{S}}$ are energy levels, $\overline{S}_\ell \geq 0$. Therefore, to achieve $\overline{S}_{\frac{1}{2}\left(4\ell_1+(-1)^{\ell_1}-1\right)} \geq 0$, we must have $\alpha \geq 1 - S_{\frac{1}{2}\left((-1)^{\ell_1}\left(4(-1)^{\ell_1}+(-1)^{\ell_1+1}-1\right)\right)}$. Therefore, $\alpha \geq \max\left\{1 - S_{\frac{1}{2}\left((-1)^{\ell_1}\left(4(-1)^{\ell_1}+(-1)^{\ell_1+1}-1\right)\right)}\right\}$, where $\ell_1 = 1, \cdots, M$. However, we know that, $S_1 < \cdots < S_{2M}$, thus, we have $\alpha \geq 1 - S_2$.

Finally, since P_e' in (4.20) is an increasing function of α and $\alpha \geq 1 - S_2$, P_e' is minimised when $\alpha = \alpha^\dagger = 1 - S_2$. $\square$

The result of Lemma 8 indicates that Φ_{01} and Φ_{10} are decreasing functions of N_C. Further, S_ℓ, $\ell = 1, \cdots, 2M$ are independent of N_C, as a result, each convex combination in (4.20) decreases as N_C increases. Therefore, it is straightforward to prove that P_e' is a decreasing function of N_C.

Proposition 8. *For a fixed* $\alpha \in (0, 1)$*, when* $N_C \to \infty$*, we have* $\Phi_{01} = \Phi_{10} \approx 0$ *and* $\Phi_{00} = \Phi_{11} \approx 1$*, we have the following lower bound on* P_e'

$$P_e' \geq P_{e,approx} = \frac{1}{2M}\left[\sum_{\ell_1=1}^{M} P_{e,S_{\frac{1}{2}\left(4\ell_1+(-1)^{\ell_1}-1\right)}} + \sum_{\ell_2=1}^{M} P_{e,S_{\frac{1}{2}\left((-1)^{\ell_2}\left(4(-1)^{\ell_2}\ell_2+(-1)^{\ell_2+1}-1\right)\right)}}\right].$$

Motivated by the result of Proposition 8, instead of solving (4.15) for a sufficiently large N_C using the first principles, we take an alternate approach, where we first compute $S_1, \cdots, S_{2M}$ that minimises $P_{e,approx}$ and then compute the respective $\{\epsilon_j, \eta_j\}$, and α using the relation in (4.7).

Towards computing the optimal $S_1, \cdots, S_{2M}$, we observe that since an energy level S_ℓ corresponds to the sum of energies contributed by Alice, Charlie, and the AWGN at Bob on f_{CB}, the sum energies contributed by Alice and Charlie will be $S_\ell - N_o$. Furthermore, since the average energy on f_{CB} is 1, we have the following constraint of

S_ℓ:

$$\frac{1}{2M}\sum_{\ell=1}^{2M}(S_\ell - N_o) = 1. \tag{4.21}$$

Finally, we formulate the following optimization problem of computing optimal S_ℓ so as to minimise $P_{e,approx}$, subject to (4.21).

$$\begin{aligned} S_1^\star, \cdots, S_{2M}^\star = \arg \min_{S_1,\cdots,S_{2M}} \quad & P_{e,approx} \\ \text{subject to:} \quad & \frac{1}{2M}\sum_{\ell=1}^{2M}(S_\ell - N_o) = 1, S_1 < \cdots < S_{2M}. \end{aligned} \tag{4.22}$$

While (4.22) can be solved using the first principles, [110] provides a near-optimal solution for (4.22). Therefore, we use the results of [110] to compute $S_1^\star, \cdots, S_{2M}^\star$. In the next lemma, we prove that, when we use $S_1, \cdots, S_{2M}$ to obtain $\{\epsilon_j, \eta_j\}$, such that $S_1, \cdots, S_{2M}$ follows (4.21), $\{\epsilon_j, \eta_j\}$ satisfies (4.3).

Lemma 12. *If* $S_1, \cdots, S_{2M}$ *are fixed such that* (4.21) *is satisfied, then the average transmit energy of Charlie is given by* (4.3).

Proof. From (4.7), $S_{\frac{1}{2}\left(4\ell_1+(-1)^{\ell_1}-1\right)} = \epsilon_{\ell_1} + N_o$, and $S_{\frac{1}{2}\left((-1)^{\ell_1}\left(4(-1)^{\ell_1}+(-1)^{\ell_1+1}-1\right)\right)} = 1-\alpha+\eta_{\ell_1}+N_o$ for $i = 0, 1$, respectively, where $\ell_1 = 1, \cdots, M$. Rearranging and adding both the equations, we get, $\sum_{\ell=1}^{2M}(S_\ell - N_o) = \sum_{\ell_1=1}^{M}\left(\epsilon_{\ell_1} + \eta_{\ell_1} + (1-\alpha)\right)$. Dividing both sides by $2M$ and rearranging, we get (4.3). □

In the next section, we propose the energy backtracking algorithm, where we first solve (4.22) using [110] to obtain $S_1^\star, \cdots, S_{2M}^\star$ and then compute corresponding $\{\epsilon_j, \eta_j | j = 1, \cdots, M\}$, and α. It is important to note that, since Charlie cannot have $N_C \to \infty$, we must bound the number of receive-antennas at Charlie. Thus, we use a parameter $0 < \Delta_{RE} \ll 1$ to bound N_C. Therefore, we compute the minimum number of receive-antennas at Charlie, such that the relative error between $P_{e,approx}^\star$ and $P_{e,eval}$ is within Δ_{RE}, where $P_{e,approx}^\star$ is $P_{e,approx}$ evaluated at $S_1^\star, \cdots, S_{2M}^\star$ and $P_{e,eval}$ is P_e evaluated at optimal $\{\epsilon_j, \eta_j | j = 1, \cdots, M\}$, and α.

Algorithm 2. Energy Backtracking Algorithm

```
Input: $P_e$ (4.14), $P_{e,approx}$, $\Delta_{RE} > 0$, $M$, $N_B$, $N_o$
Outpuut: $\epsilon_1^\dagger, \cdots, \epsilon_M^\dagger$, $\eta_1^\dagger, \cdots, \eta_M^\dagger$, $N_C^\dagger$, $\alpha^\dagger$
Compute $S_1^\star, \cdots, S_{2M}^\star$ using [110] and evaluate $P^\star_{e,approx}$.
$\alpha^\dagger = 1 - S_2^\star$
; $\epsilon_j^\dagger = S^\star_{\frac{1}{2}(4j+(-1)^j-1)} - N_o$;
  $\eta_j^\dagger = S^\star_{\frac{1}{2}((-1)^j(4(-1)^j+(-1)^{j+1}-1))} - (1-\alpha^\dagger) - N_o,\ j = 1, \cdots, M$
Set: $N_C = 1$, $P_{e,eval} = 1$
while $\left|\dfrac{P^\star_{e,approx} - P_{e,eval}}{P^\star_{e,approx}}\right| \geq \Delta_{RE}$ do
    Substitute $S_1^\star, \cdots, S_{2M}^\star$, $\alpha^\dagger$, $N_C$, and $N_B$ in (4.14) and obtain $P_{e,eval}$
    if $\left|\dfrac{P^\star_{e,approx} - P_{e,eval}}{P^\star_{e,approx}}\right| > \Delta_{RE}$ then
        $N_C = N_C + 1$; continue
    else
        $N_C^\dagger = N_C$; break
    end
end
```

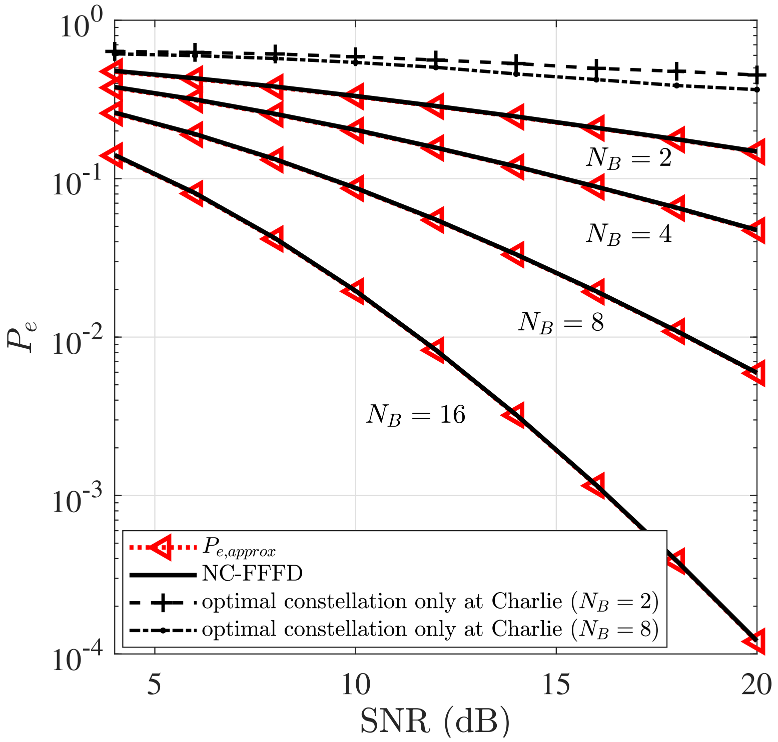

Figure 4.9: Error performance of NC-FFFD when energy levels are computed using EB algorithm for $M = 2$.

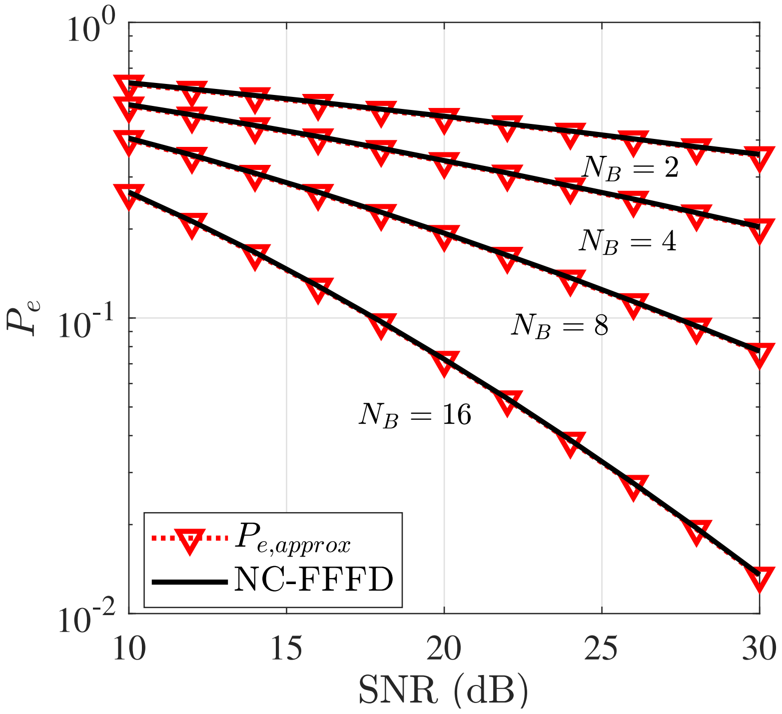

Figure 4.10: Error performance of NC-FFFD when energy levels are computed using EB algorithm for $M = 4$.

4.4.3 Energy Backtracking (EB) Algorithm

The Energy Backtracking (EB) Algorithm, first computes energy levels $S_1^\star, \cdots, S_{2M}^\star$ using the semi-analytical results of [110]. It then computes $\alpha^\dagger$, and $\epsilon_j^\dagger$ and $\eta_j^\dagger$ based on Theorem 9 and the relation in (4.7), respectively. It then sets $N_C = 1$ and computes $P_{e,eval}$, i.e., P_e at $\alpha^\dagger$, $\epsilon_j^\dagger$, $\eta_j^\dagger$ for the given N_B. The algorithm increments N_C until relative error between the $P_{e,approx}^\star$ and $P_{e,eval}$ is within Δ_{RE}. The algorithm exits the while-loop when the relative error is less than or equal to Δ_{RE}. The pseudo-code for the proposed EB algorithm is given in Algorithm 2.

In Fig. 4.9 and Fig. 4.10, we plot the error performance of NC-FFFD relaying scheme when using the EB Algorithm for $M = 2$ and $M = 4$ for various values of N_B. In addition to the simulation parameters assumed above, we assume $\Delta_{RE} = 10^{-2}$ for both the cases. For both the cases, we observe that the error performance improves as a function of SNR. In Fig. 4.9, we also plot the performance of NC-FFFD scheme when Charlie uses optimal energy levels for point-to-point communication obtained using [110] for $N_B = 2, 8$. From the plot it is clear that, although Charlie is using optimal energy levels for point-to-point communication, the corresponding error performance of NC-FFFD is poor. This reinforces that to minimise P_e, energy levels at both the

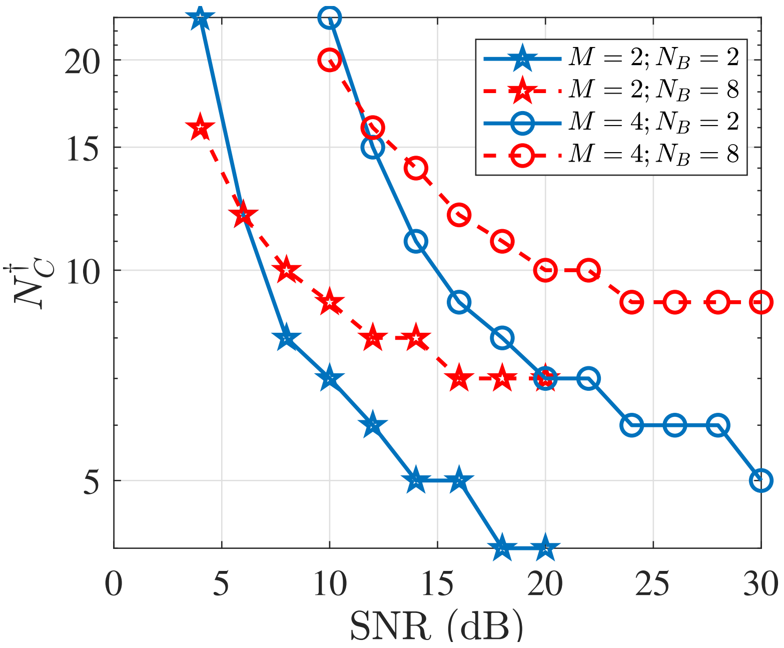

Figure 4.11: $N_C^\dagger$ as a function of SNR for $M=2$ and $M=4$.

users must be jointly optimised as proposed in Algorithm 2. Finally, in Fig. 4.11, we also plot $N_C^\dagger$ as a function of SNR, for various combinations of M and N_B and observe that with only tens of antennas at the helper, we can achieve the performance close to its large-antenna counterpart.

If NC-FFFD scheme provides performance close to $P^\star_{e,approx}$, it assumes that fast-forwarding at Charlie is perfect. Therefore, the symbols on the direct link, i.e., Alice-to-Bob link and relayed link, i.e., Charlie-to-Bob link, arrive during the same time instant, thereby resulting in the signal model in (4.4). In the next section, we discuss the case when fast-forwarding at Charlie is imperfect. In particular, we discuss the consequences related to this problem and a possible solution.

4.5 Delay-Tolerant NC-FFFD (DT NC-FFFD) Relaying Scheme

If nT denotes the delay on the relayed link w.r.t. the direct link, such that $n \geq 0$ and T is the symbol duration, then $nT = 0$, when fast-forwarding is perfect. However, when fast-forwarding is imperfect, $nT \neq 0$ and $\mathbf{r}_B$ must be a function of nT. In particular, when $nT \neq 0$, the symbol received at Bob is a function of Alice's current symbol, Charlie's current symbol, and Alice's symbol delayed by nT. Although, Charlie's cur-

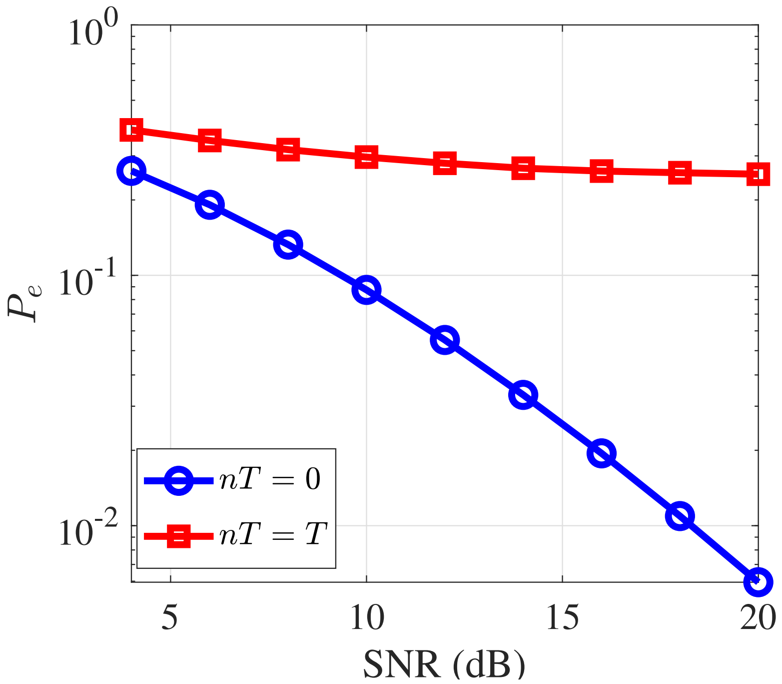

Figure 4.12: Error performance for $nT = 0$ and $nT = T$.

rent symbol and Alice's symbol delayed by nT are captured by E_C, the current symbol of Alice creates an interference in the symbol decoding, thereby degrading the error performance. To illustrate this behaviour, we plot the error performance of NC-FFFD scheme in Fig. 4.12, when the symbols on the relayed link arrive one symbol period after the symbols on the direct link. The plot shows that, the error performance degrades as the energy on the direct link interferes when Bob tries to decode symbols using the relayed link.

Towards computing the optimal energy levels at Alice and Charlie when $nT \neq 0$, one can formulate a new signal model, where $\mathbf{r}_B$ is a function of nT and then compute the optimal energy levels using the first principles. However, we note that, Alice contributes *zero* and $1-\alpha$ energies on the direct link, when she transmits symbol 0 and symbol 1, respectively. Thus, in order to reduce the interference from the direct link, we must reduce the term $1-\alpha$. Therefore, if we upper bound the contribution $1-\alpha$ by small value, then we can continue to use the same signal model on $\mathbf{r}_B$ as given in (4.4), thereby making NC-FFFD scheme *Delay Tolerant*. To this end, we propose an upper bound on $1-\alpha$ as, $1-\alpha \leq \Delta_{\text{DT}} N_o$, where $0 < \Delta_{\text{DT}} \ll 1$ is the design parameter. Since $1-\alpha \leq \Delta_{\text{DT}} N_o$, we have the relation $\alpha \geq 1 - \Delta_{\text{DT}} N_o$. Further, the result of Theorem 9 shows that P_e' is an increasing function of α, therefore, the optimal choice of α would be, $\alpha = 1 - \Delta_{\text{DT}} N_o$. However, since $\Delta_{\text{DT}} \ll 1$, $1 - S_2 < 1 - \Delta_{\text{DT}} N_o$ and

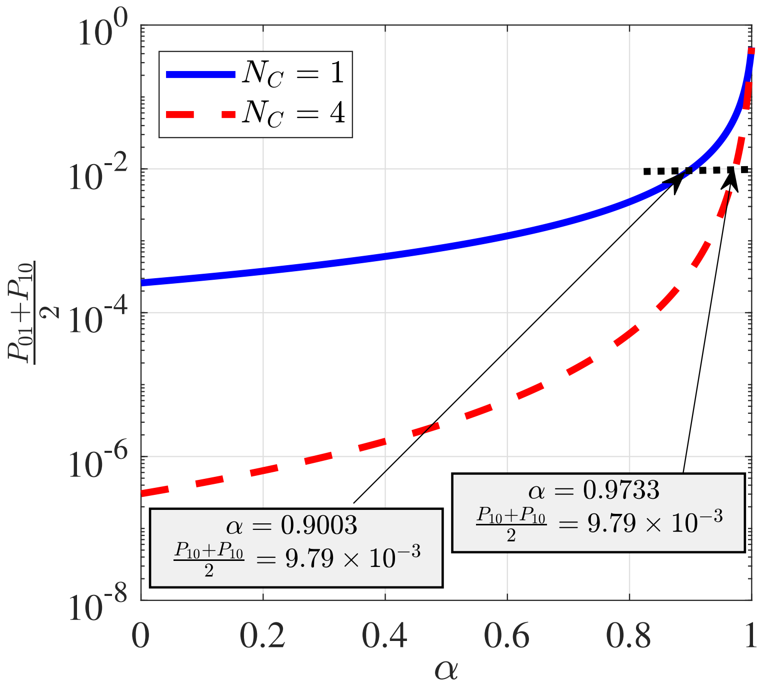

Figure 4.13: Variation of $\frac{\Phi_{01}+\Phi_{10}}{2}$ as a function of N_C and α.

therefore, using $\alpha = 1 - \Delta_{\text{DT}} N_o$ will degrade the error performance. In the following discussion, we show that we can achieve the same error performance at $\alpha = 1 - \Delta_{\text{DT}} N_o$ as achieved in Sec. 4.4.2 at $\alpha = 1 - S_2$, by increasing the receive-diversity at Charlie.

Since the terms Φ_{00}, Φ_{01}, Φ_{10}, and Φ_{11} are functions of α and N_C in P'_e, we show that one can achieve the same Φ_{00}, Φ_{01}, Φ_{10}, and Φ_{11} at different combinations of α and N_C. The results of Lemma 7 show that for a fixed N_C, Φ_{01} and Φ_{10} are increasing functions of α. Subsequently, from Lemma 8, for a fixed α, Φ_{01} and Φ_{10} are decreasing functions of N_C. In Fig. 4.13, we plot $\frac{\Phi_{01}+\Phi_{10}}{2}$ as a function of α for various N_C at 25 dB and observe that, for $N_C = 1$ and $\alpha = 0.9003$, the average probability of error of Alice-to-Charlie link is 9.79×10^{-3}. However, to obtain the same error performance at larger α, i.e., $\alpha = 0.9733$, we must use $N_C = 4$.

Based on the above discussion, in the next section, we propose a variant of EB algorithm, where we bound the interference from the direct link by $\Delta_{\text{DT}} N_o$ and obtain $\{\epsilon_j, \eta_j\}$ and the minimum N_C, such that the error performance is close to $P_{e,approx}$.

4.5.1 Delay Tolerant Energy Backtracking (DT-EB) Algorithm

In the Delay Tolerant Energy Backtracking (DT-EB) algorithm, we obtain the optimal energy levels at Alice and Charlie, such that the energy level on the direct link is

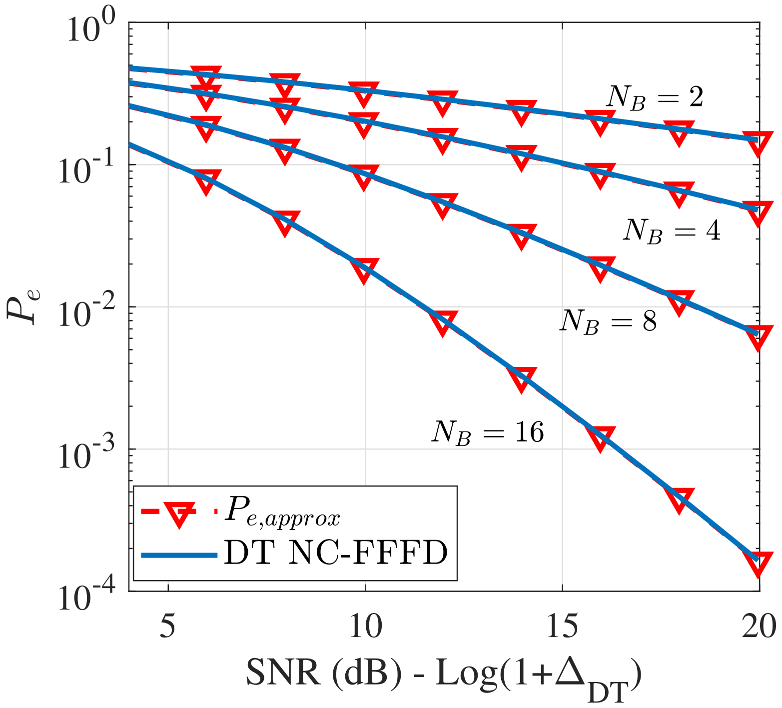

Figure 4.14: Performance of DT NC-FFFD when energy levels are computed using DT-EB algorithm for $M = 2$.

bounded by $\Delta_{\rm DT} N_o$. To facilitate this, we use the EB algorithm with two variations, i) we set $\alpha = 1 - \Delta_{\rm DT} N_o$, instead of $\alpha = 1 - S_2^\star$, ii) the effective SNR to compute $S_1^\star, \cdots, S_{2M}^\star$ is $(N_o + \Delta_{\rm DT} N_o)^{-1}$.

We now demonstrate the performance of DT NC-FFFD scheme. For all simulation purposes, we assume $\Delta_{RE} = 10^{-2}$, and $\Delta_{\rm DT} = 10^{-1}$, in addition to simulation parameters considered in the previous sections. Further, the effective SNR at Bob, denoted by SNR_{eff}, is given by SNR_{eff} (dB) = SNR (dB) $- \log(1 + \Delta_{\rm DT})$. In Fig. 4.14 and Fig. 4.15, we plot the error performance of DT NC-FFFD scheme as a function of SNR_{eff} for $M = 2$ and $M = 4$, respectively, when $N_B = 2, 4, 8, 16$. From these plots, we show that the error performance of DT NC-FFFD improves as a function of SNR_{eff}. However, to achieve this performance Charlie must use more receive-antennas as compared to its NC-FFFD counterpart.

In Fig. 4.16, we plot the optimal receive-antennas at Charlie, denoted by $N_C^\ddagger$, as a function of SNR for various combinations of M and N_B, and observe that since α is a function of N_o, the number of receive-antennas required by Charlie is an increasing function of SNR. Further, it is clear from the plot that we need to mount more receive-antennas at Charlie for DT NC-FFFD scheme as compared to NC-FFFD scheme. Furthermore, we also plot the error performances of NC-FFFD and DT NC-FFFD schemes

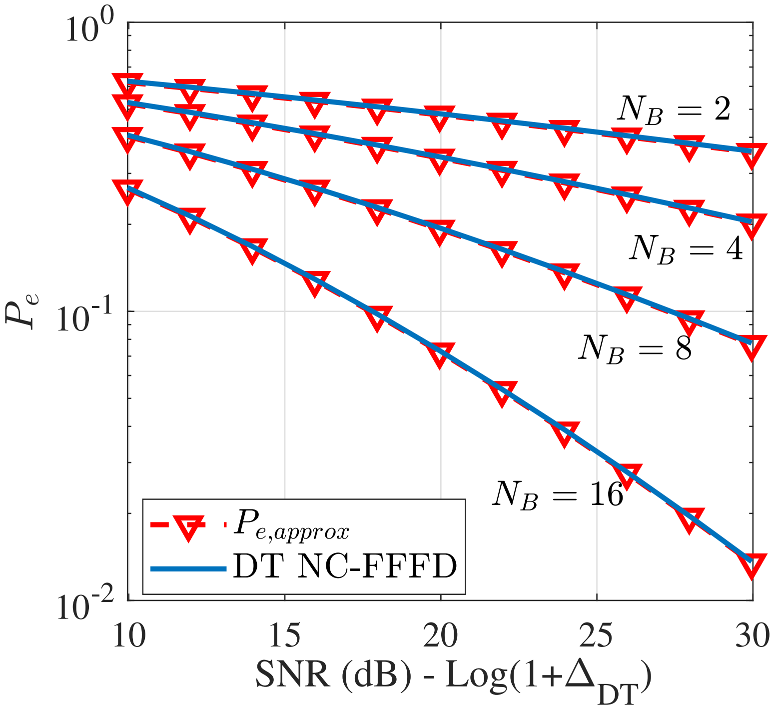

Figure 4.15: Performance of DT NC-FFFD when energy levels are computed using DT-EB algorithm for $M = 4$.

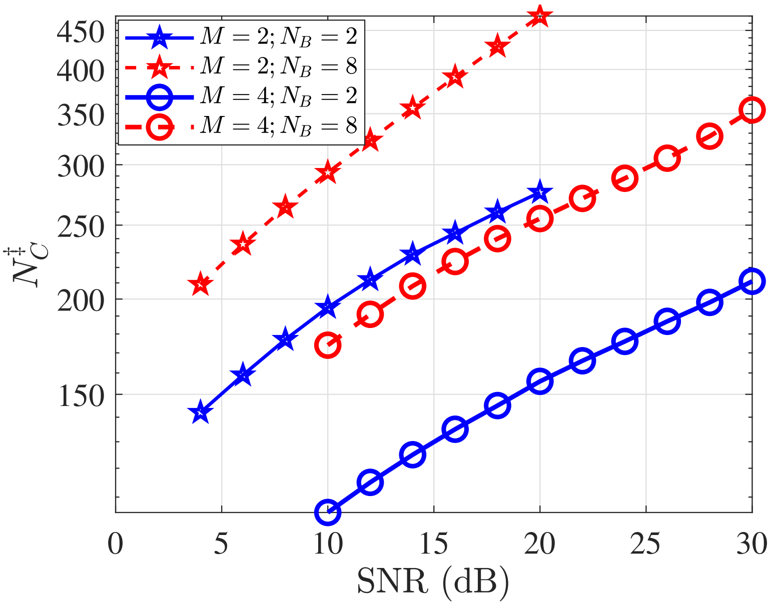

Figure 4.16: $N_C^\ddagger$ as a function of SNR for $M = 2$ and $M = 4$.

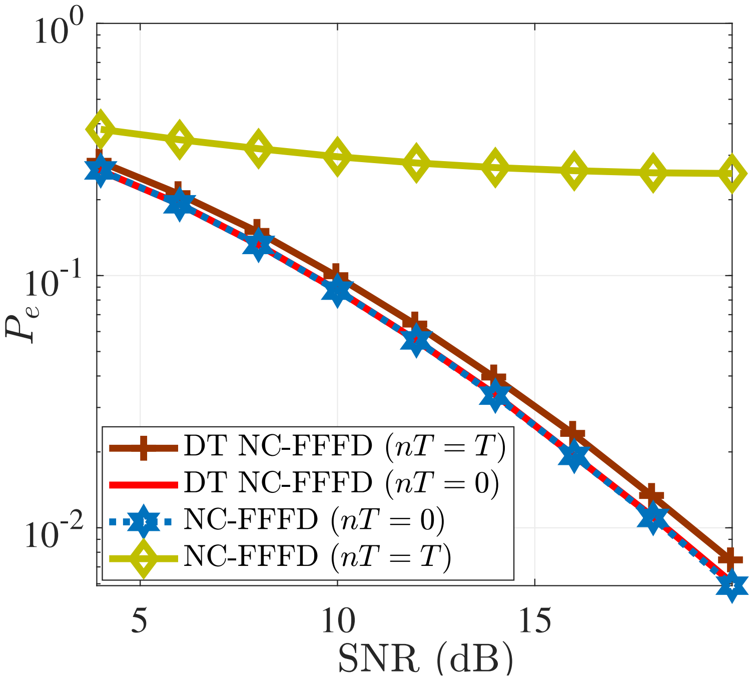

Figure 4.17: DT NC-FFFD scheme, when $nT = 0$ and $nT = T$ for $M = 2$, $N_B = 8$, $\Delta_{RE} = 10^{-2}$, and $\Delta_{\text{DT}} = 10^{-1}$.

in Fig 4.17, for the case when $nT = 0$ and $nT = T$, when $M = 2$ and $N_B = 8$. From the plots, we find that, when $nT = 0$, the error performance of NC-FFFD and DT NC-FFFD exactly overlaps. However, when $nT = T$, the error-rates of DT NC-FFFD are better than the error-rates of NC-FFFD scheme. We also notice a marginal degradation in the performance of DT NC-FFFD when $nT = T$ compared to $nT = 0$ due to lower effective SINR in the former case.

4.6 Covertness Analysis of NC-FFFD Relaying Scheme

When communicating in the presence of a reactive jamming adversary, it becomes imperative that the communication is covert. In the context of this chapter, covertness is the ability of Alice and Charlie to communicate without getting detected by Dave's ED or CD. Henceforth, we discuss Dave's capability to detect the proposed countermeasures by focusing on the communication over f_{AB}.

4.6.1 Energy Detector (ED)

After executing the jamming attack, Dave collects a frame of L symbols on f_{AB} and computes their average energy. A countermeasure is detected when the difference between the computed average energy (after the jamming attack) and the average energy (before the jamming attack) is greater than the tolerance limit τ_{ED}, where $\tau_{\text{ED}} \geq 0$ is a small number of Dave's choice.

When no countermeasure is implemented, Dave receives symbols from Alice on f_{AB}. Since Dave has single receive-antenna, the l^{th} symbol received by Dave on f_{AB} is, $r_{D,l} = h_{AD,l}x_l + n_{D,l},\ l = 1, \cdots, L$, where, $h_{AD,l} \sim \mathcal{CN}(0, 1)$ is the fading channel on the l^{th} symbol on Alice-to-Dave link, $n_{D,l} \sim \mathcal{CN}\left(0, \tilde{N}_o\right)$ is the effective AWGN at Dave, such that $\tilde{N}_o = N_o + \sigma_{DD}^2$, where σ_{DD}^2 is the variance of the residual SI at Dave and N_o is the variance of the AWGN at Dave. Further, the scalar $x_l \in \{0, 1\}$ is the l^{th} symbol transmitted by Alice. Due to uncoded communication over fast-fading channel, $r_{D,l}$ is statistically independent over l. The average energy received by Dave on f_{AB} corresponding to $r_{D,l},\ l \in \{1, \cdots, L\}$ is given by, $E_{D,f_{AB}}$, where $E_{D,f_{AB}} = \frac{1}{L}\sum_{l=1}^{L} |r_{D,l}|^2$. Since $h_{AD,l}$ and the AWGN $n_{D,l}$ are Random Variables (RV), $E_{D,f_{AB}}$ is also a RV. Using weak law of large numbers, $\frac{1}{L}\sum_{l=1}^{L} |r_{D,l}|^2 \to \mathcal{E}_{AB}$ in probability, where, $\mathcal{E}_{AB} = \tilde{N}_o + 0.5$ denotes the expected energy of $r_{D,l}$ on f_{AB}, before the jamming attack. Since low-latency messages typically have short packet-length, Dave cannot collect a large number of observation samples. Therefore, L is generally small, and with probability 1, $E_{D,f_{AB}} \neq \mathcal{E}_{AB}$. If $\mathcal{H}_0$ and $\mathcal{H}_1$ denote the hypothesis of no countermeasure and countermeasure, respectively, then, given $\mathcal{H}_0$ is true, false-alarm is an event when $E_{D,f_{AB}}$ deviates from $\mathcal{E}_{AB}$ by an amount greater than τ_{ED}. We now formally define the probability of false-alarm.

Definition 3. *For any $\tau_{\text{ED}} > 0$, the probability of false-alarm denoted by, $\mathbf{P}_{FA}$ is given as,* $\Pr\left(|E_{D,f_{AB}} - \mathcal{E}_{AB}| > \tau_{\text{ED}} |\, \mathcal{H}_0\right)$.

If u_l denotes the energy of l^{th} symbol on f_{AB} without any countermeasure, then the RV corresponding to the average energy of L symbols is denoted by, $\mathcal{U}_L = \frac{1}{L}\sum_{l=1}^{L} u_l$. In order to compute $\mathbf{P}_{FA}$, first we compute the distribution of $\mathcal{U}_L$ in the next theorem.

Theorem 10. *Given $\mathcal{H}_0$ is true, if $\tilde{N}_o << 1$, then the PDF of $\mathcal{U}_L$, i.e., $p_{\mathcal{U}_L}(\varsigma)$ is* $\left(\frac{1}{2}\right)^L \sum_{l=0}^{L} \binom{L}{l} \frac{L^l e^{-L\varsigma} \varsigma^{l-1}}{\Gamma(l)}$, *$\varsigma > 0$. [35, Theorem 5]*

From Definition 3, $\mathbf{P}_{FA} = \Pr\left(E_{D,f_{AB}} > \mathcal{E}_{AB} + \tau_{\text{ED}}\right) + \Pr\left(E_{D,f_{AB}} \leq \mathcal{E}_{AB} - \tau_{\text{ED}}\right)$. Therefore, using the PDF of $\mathcal{U}_L$ from Theorem 10, the closed-form expression of $\mathbf{P}_{FA}$ is given by

$$\mathbf{P}_{FA} = \frac{1}{2^L} \sum_{l=0}^{L} \binom{L}{l} \frac{\Gamma\left(l, L(\mathcal{E}_{AB} + \tau_{\text{ED}})\right)}{\Gamma(l)} + \frac{\gamma\left(l, L(\mathcal{E}_{AB} - \tau_{\text{ED}})\right)}{\Gamma(l)}. \tag{4.23}$$

When using NC-FFFD relaying scheme, at the l^{th} symbol instant, Alice and Charlie synchronously transmit dummy OOK bit $b_l \in \{0, 1\}$ with energies α and $1 - \alpha$, respectively, on f_{AB}, where b_l is the least significant bit of the pre-shared Gold sequence. The baseband symbol received at Dave is, $r_{D,l} = h_{AD,l}\sqrt{\alpha}b_l + h_{CD,l}\sqrt{1-\alpha}b_l + n_{D,l}$, where, for l^{th} symbol, $h_{AD,l} \sim \mathcal{CN}(0, 1)$ and $h_{CD,l} \sim \mathcal{CN}(0, (1 + \partial))$ are Rayleigh fading channels for Alice-to-Dave and Charlie-to-Dave links, respectively. Since the location of Dave can be arbitrary, the variances of Alice-to-Dave and Charlie-to-Dave links are not identical. Thus, ∂ captures the relative difference in the variance. If $E_{D,f_{AB}}^{FF}$ denotes the average energy received at Dave, when Alice and Charlie use NC-FFFD scheme, then due to change in the signal model, $E_{D,f_{AB}}^{FF} \neq E_{D,f_{AB}}$. Along the similar lines of $\mathbf{P}_{FA}$, we now formally define the probability of detection at Dave when NC-FFFD scheme is implemented.

Definition 4. *If $\mathbf{P}_D$ denotes the probability of detection at Dave when $\mathcal{H}_1$ true, then for any $\tau_{\text{ED}} > 0$, $\mathbf{P}_D = \Pr\left(\left|E_{D,f_{AB}}^{FF} - \mathcal{E}_{AB}\right| > \tau_{\text{ED}} \middle| \mathcal{H}_1\right)$.*

Further, if v_l denotes the energy of l^{th} received symbol when using the countermeasure, then $\mathcal{V}_L$ denotes the average energy of L symbols, where, $\mathcal{V}_L = \frac{1}{L}\sum_{l=1}^{L} v_l$. We provide the closed-form expression of PDF of v_l and $\mathcal{V}_L$ in the next theorem.

Theorem 11. *When $\tilde{N}_o << 1$ and $\mathcal{H}_1$ is true, the PDF of $\mathcal{V}_L$, i.e., $p_{\mathcal{V}_L}(\varsigma)$, is given by*

$$\left(\frac{1}{2}\right)^L \sum_{l=0}^{L} \binom{L}{l} \frac{\left(\frac{L}{\mathcal{A}}\right)^l e^{-\frac{L}{\mathcal{A}}\varsigma} \varsigma^{l-1}}{\Gamma(l)}, \tag{4.24}$$

where $\varsigma > 0$ and $\mathcal{A} = \alpha + (1 - \alpha)(1 + \partial)$.

Proof. When $\mathcal{H}_1$ is true, the received symbol at Dave on f_{AB} is given as, $r_{D,l} = h_{AD,l}\sqrt{\alpha}b_l + h_{CD,l}\sqrt{1-\alpha}b_l + n_{D,l}$. Thus, using $r_{D,l}$, the PDF of v_l is given as, $p_{v_l}(\varsigma) = \frac{1}{2}\left(\frac{1}{\tilde{N}_o}e^{-\frac{\varsigma}{\tilde{N}_o}} + \frac{1}{\tilde{N}_o + \mathcal{A}}e^{-\frac{\varsigma}{\tilde{N}_o + \mathcal{A}}}\right)$, where $\mathcal{A} = \alpha + (1 - \alpha)(1 + \partial)$. Computing $\mathcal{V}_M$ requires us to sum L independent v_l random variables each scaled by L, i.e., sum of L independent v_m/M random variables. Therefore,

$$p_{v_l/L}(\varsigma) = \frac{1}{2}\left(\frac{1}{\tilde{N}_o}e^{-\frac{L\varsigma}{\tilde{N}_o}} + \frac{L}{\tilde{N}_o+\mathcal{A}}e^{-\frac{L\varsigma}{\tilde{N}_o+\mathcal{A}}}\right) \approx \frac{1}{2}\left(\delta(\varsigma) + \frac{L}{\mathcal{A}}e^{-\frac{L}{\mathcal{A}}\varsigma}\right),$$

where, the approximation is because $\tilde{N}_o << 1$. The pdf of $\mathcal{V}_L$ is equivalent to computing L-fold convolution $(*L)$ of $p_{v_l/L}(\varsigma)$. For simplification, we use the properties of Laplace transform $(\mathscr{L}[\cdot])$ and inverse Laplace transform $(\mathscr{L}^{-1}[\cdot])$ to compute the pdf of $\mathcal{V}_L$ as

$$p_{\mathcal{V}_L}(\varsigma) = \left(p_{v_l/L}(\varsigma)\right)^{*L} = \mathscr{L}^{-1}\left[\left(\mathscr{L}\left[p_{v_l/L}(\varsigma)\right]\right)^L\right] = \mathscr{L}^{-1}\left[\left(\frac{1}{2}\right)^L\left[1+\frac{L/\mathcal{A}}{(s+L/\mathcal{A})}\right]^L\right].$$

Using binomial expansion we expand $\left[1+\frac{L/\mathcal{A}}{(s+L/\mathcal{A})}\right]^L$ and substitute in above to obtain (4.24). □

Overall, from Definition 4, the probability of detection at Dave is given as, $\mathbf{P}_D = \Pr\left(E^{FF}_{D,f_{AB}} > \mathcal{E}_{AB}+\tau_{\text{ED}}\right) + \Pr\left(E^{FF}_{D,f_{AB}} \leq \mathcal{E}_{AB}-\tau_{\text{ED}}\right)$. Thus, the probability of miss-detection, $\mathbf{P}_{MD}$ is given by $1-\mathbf{P}_D$. From the result of Theorem 11,

$$\mathbf{P}_{MD} = 1 - \frac{1}{2^L}\sum_{l=0}^{L}\binom{L}{l}\frac{\Gamma\left(l, \frac{L}{\mathcal{A}}(\mathcal{E}_{AB}+\tau_{\text{ED}})\right)}{\Gamma(l)} - \frac{\gamma\left(l, \frac{L}{\mathcal{A}}(\mathcal{E}_{AB}-\tau_{\text{ED}})\right)}{\Gamma(l)}. \quad (4.25)$$

Ideally, a low $\mathbf{P}_{FA}$ and a high $\mathbf{P}_D$ allows Dave to detect a countermeasure. However, the legitimate nodes would like to drive the sum $\mathbf{P}_{FA}+\mathbf{P}_{MD}$ close to 1 for any value of τ_{ED}.

Remark 2. *If* $\partial = 0$ *in* (4.25)*, then* $\mathbf{P}_{FA}+\mathbf{P}_{MD} = 1$*, for all* $\alpha \in (0,1)$ *and arbitrary* M *and* τ_{ED}.

Although, the above result theoretically guarantees $\mathbf{P}_{FA}+\mathbf{P}_{MD} = 1$ for specific value of ∂, Fig. 4.18 shows the simulation results for $\partial = 0.1$ and $\partial = 0.4$. Since Alice and Charlie transmit b_l, with energy α and $1-\alpha$, respectively, the communication on f_{AB} is independent of $\{\epsilon_j, \eta_j | j = 1, \cdots, M\}$ and only depends on the value of α. In the previous sections, we have computed the values of α using TLGD algorithm, EB algorithm, and DT-EB algorithm. Therefore, in Fig. 4.18, we plot the sum $\mathbf{P}_{FA}+\mathbf{P}_{MD}$ at Dave as a function of L, when the optimal value of α is computed using TLGD, EB, and DT-EB algorithm. For SNR $= 25$ dB, $N_B = 8$, and $\Delta_{\text{DT}} = 0.1$, we observe that the

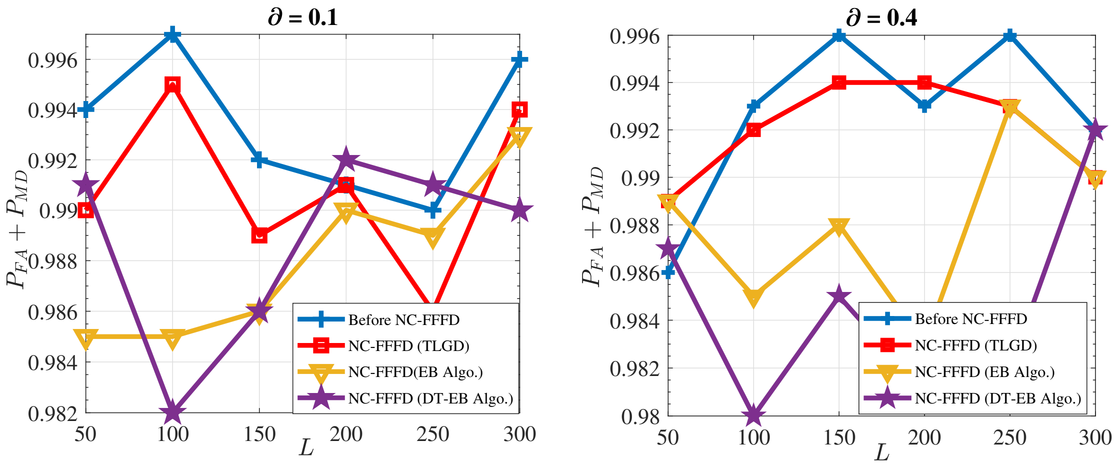

Figure 4.18: $\mathbf{P}_{FA}$+$\mathbf{P}_{MD}$ as a function of L and ∂ at 25 dB (including the residual SI), $N_B = 8$, and $\Delta_{\text{DT}} = 0.1$.

sum $\mathbf{P}_{FA} + \mathbf{P}_{MD} \approx 1$, despite a large number of samples at Dave. These simulation results indicate that the ED at Dave is oblivious to the countermeasures implemented by Alice and Charlie.

4.6.2 Correlation Detector (CD)

In order to prevent Alice and Charlie from using repetitive coding across the frequencies [34] and [35], Dave deploys a CD to capture the correlation between the symbols on the jammed frequency and other frequencies in the network. Amongst several methods to estimate the correlation, Dave uses a CD that estimates the correlation in terms of Mutual Information (MI) to capture both, linear as well as non-linear correlation between the samples. However, estimating MI requires estimating the underlying marginal and joint PDFs, which is hard in general. Therefore, Dave needs a non-parametric method of MI estimation that does not require him to know the underlying joint and marginal PDFs. KSG estimators [119] based on **k**-nearest neighbours (**k**-NN) are well known for non-parametric MI estimation for their ease of implementation. Thus, Dave uses a KSG estimator to detect the proposed countermeasures. Since the information symbols on the frequency bands other than f_{CB} are implicitly independent of symbols on f_{AB}, we only focus on estimating the correlation between the symbols on f_{AB} and f_{CB} as f_{CB} is the helper's frequency band. In the context of this chapter, Dave estimates the MI between the energies of the samples on f_{AB} and f_{CB}.

We will first show the effect of transmitting dummy OOK bit $b \in \{0, 1\}$ on f_{AB},

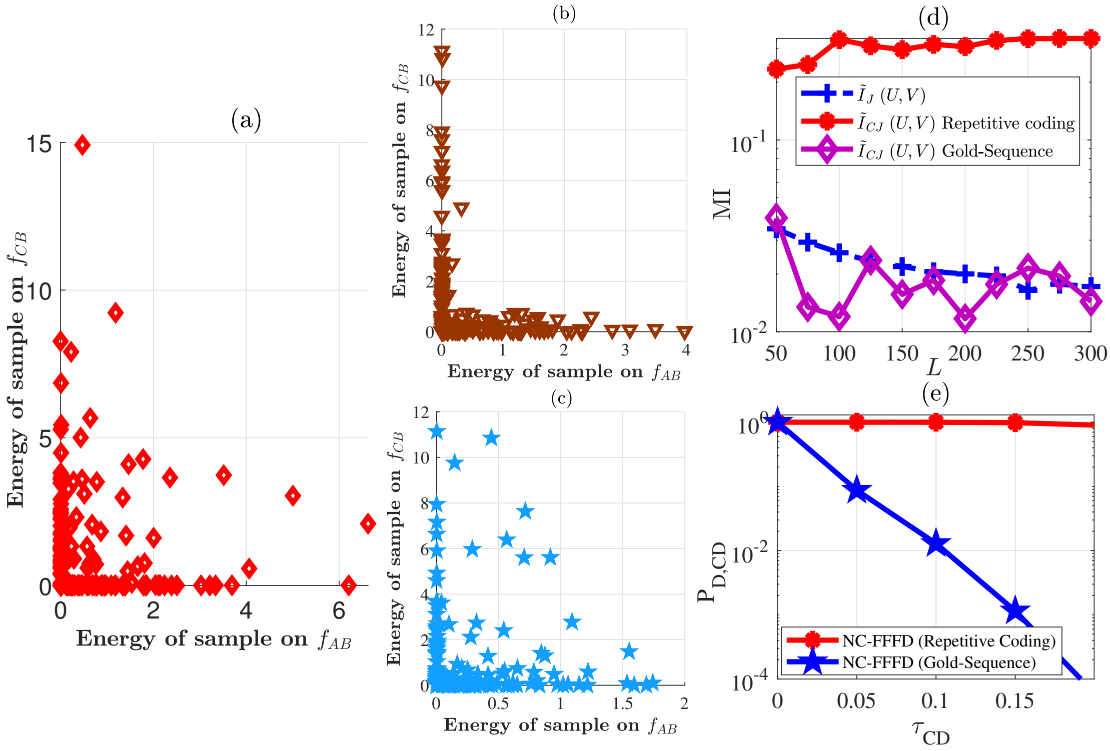

Figure 4.19: Scatter-plots representing the energy pairs received at Dave for SNR = 25 dB, $N_B = 8$, $L = 50$, when (a) Dave is not jamming. (b)Alice and Charlie use repetitive coding across f_{AB} and f_{CB}. (c) Alice and Charlie cooperatively use Gold-sequence. (d) MI before jamming and after using NC-FFFD with Gold-sequence and with Repetitive coding as a function of L at SNR = 25 dB, $\mathbf{k} = 2$, and $N_B = 8$. (e) $\mathbf{P}_{\text{D,CD}}$ when NC-FFFD is implemented with repetitive coding and with Gold-sequence, for $L = 150$ at 25 dB, $N_B = 8$, and $\mathbf{k} = 2$.

from the pre-shared Gold sequence. When no countermeasure is used, and Alice and Charlie transmit independent symbols on f_{AB} and f_{CB}, respectively, the energy scatter-plot is as shown in Fig. 4.19 (a). If Alice and Charlie use repetitive coding across the frequencies, the energy samples are clustered only around few centres as shown in Fig.4.19 (b). Further, when Alice and Charlie cooperatively use Gold-sequence bits, the scatter-plot is as shown in Fig. 4.19 (c). It can be observed that the scatter-plot in Fig 4.19 (a) and Fig 4.19 (c) are more randomised as compared to Fig. 4.19 (b). This suggests that, when Alice and Charlie transmits bits from a Gold-sequence based scrambler on f_{AB}, the observations at Dave are similar to when they were transmitting independent symbols.

To formally measure the correlation, let U and V denote the RVs corresponding to the energy of samples on f_{AB} and f_{CB}, respectively. Before the jamming attack, since Alice and Charlie transmit independent symbols, the MI estimate denoted by, $\tilde{I}(U, V)$, should be zero. However, due to small number of samples, i.e., L, $\tilde{I}(U, V)$ is a small non-zero value which approaches zero as the number of samples increases. In Fig. 4.19 (d), for 25 dB, $N_B = 8$, and $\mathbf{k} = 2$, we plot the estimated MI at Dave, before the jamming attack, and after implementing NC-FFFD scheme with repetitive coding and Gold-sequence. We use 10^3 iterations for each value of L to compute $\tilde{I}(U, V)$ before the jamming attack because Dave wants to have a good estimate of MI. However, after the jamming attack, Dave cannot use multiple iterations for estimating $\tilde{I}(U, V)$ for a given L. From Fig. 4.19 (d), it is clear that the estimated MI for NC-FFFD is high and an increasing function of L when repetitive coding is used. In contrast, when Gold-sequence is used, the estimated MI oscillates near the MI estimate before the jamming attack.

If τ_{CD} denotes the resolution of Dave's CD, then probability of detection denoted by, $\mathbf{P}_{\text{D,CD}}$ is given as, $\mathbf{P}_{\text{D,CD}} = \Pr\left(\left|\mathbb{E}\left[\tilde{I}_{\text{J}}(U, V)\right] - \tilde{I}_{\text{CJ}}(U, V)\right| \geq \tau_{\text{CD}} \middle| \mathcal{H}_1\right)$, where, $\mathbb{E}\left[\tilde{I}_{\text{J}}(U, V)\right]$ denotes the long term estimate of MI before the jamming attack and $\tilde{I}_{\text{CJ}}(U, V)$ denotes the estimate of MI after implementing NC-FFFD with pre-shared Gold-sequence bits. In Fig. 4.19 (e), we plot $\mathbf{P}_{\text{D,CD}}$ at SNR = 25 dB, $N_B = 8$, and $L = 150$ samples, where the optimal value of α is computed using the EB algorithm. Since τ_{CD} determines the accuracy of the CD, we assume $0 \leq \tau_{\text{CD}} \leq 0.20$, because a very large resolution results in poor detection. When NC-FFFD is implemented and Alice uses repetitive coding, $\mathbf{P}_{\text{D,CD}}$ is close to 1 for the given range of τ_{CD}. However, when NC-FFFD is implemented using Gold-sequence bits b, $\mathbf{P}_{\text{D,CD}}$ reduces as a function of τ_{CD}. Thus, when Alice and Charlie use Gold-sequence bits to transmit on f_{AB}, the probability of detecting the countermeasure at Dave is small, as the symbols on f_{AB} and f_{CB} are independent by design.

4.7 Chapter Summary

This chapter envisaged a strong FD adversary who injects jamming energy on the low-latency messages of the victim in a fast-fading environment. Unlike the reactive adversaries in the literature, the adversary in this chapter uses an energy detector and a correlation detector to prevent the use of any pre-existing countermeasures. Against this threat model, we have proposed NC-FFFD relaying scheme, where the victim seeks help from a helper to fast-forward its symbols to the base station. Based on the helper's data-rate we have derived analytical results on the joint error performance, and then have proposed a family of algorithms to compute the near-optimal energy levels at the victim and the helper nodes. Further, it was also shown that, with high probability, the proposed scheme successfully engages the reactive adversary to the jammed frequency. Overall, this is the first work of its kind to address security threats from a reactive adversary in a fast-fading environment.

CHAPTER 5

Delay-Aware Full-Duplex Relaying Scheme Against Reactive Jammers

5.1 Introduction

In the countermeasures proposed in Chapter 3 and 4, it is assumed that the processing delay at the helper in forwarding the victim's symbols is negligible. Thus, the victim's symbols and the multiplexed symbols from the helper reach the destination during the same time slot. However, when using practical FD radios, the forwarding process may not be instantaneous, and the processing delay at the helper can be of the order of several symbol durations. In such cases, the symbols on the two links reach the destination during different time slots, thereby yieliding a signal model different from that of Chapter 3 and 4. Moreover, if the helper decides to use multiple receive-antennas to improve the diversity order, the processing delay further increases due to additional delay contributed by the self-interfernce cancellation (SIC) blocks of the FD radios [120]. Thus, using practical FD radios to combat reactive adversaries has the following three consequences: (i) The existing analysis of Chapter 3 and 4 does not hold as the symbols on the Victim-to-Destination and the Helper-to-Destination links are observed at the destination in an asynchronous fashion, (ii) Due to the processing delay, a few multiplexed symbols reach the destination after the deadline, thereby violating the low-latency constraint, and (iii) The symbols on the victim's and the helper's frequencies are uncoordinated in energy, resulting in fluctuations in the average energy level of both the frequencies, thereby increasing the probability of detection by the energy detector. *Thus, these limitations of the existing countermeasures motivate us to design new countermeasures that consider the helper's practical limitations in facilitating reliable and low-latency communication of the victim's symbols.*

5.1.1 Contributions

1. To facilitate reliable communication between the victim and the destination, we propose a framework wherein the victim seeks assistance from an FD helper to multiplex-and-forward its symbols to the destination in an asynchronous manner, such that the victim and the helper share the helper's uplink frequency using an energy-splitting factor $\alpha \in (0, 1)$. We first model the processing delay at the helper using the parameter Θ which is a function of the number of receive-antennas at the helper and then propose a strategy so that the victim and the helper cooperatively use their bands to reliably communicate and still not get detected by the adversary. Since this framework incorporates the delay parameter at the helper, we refer to this framework as the Delay-Aware Semi-Coherent Multiplex-and-Forward (DASC-MF) mitigation scheme. With On-Off Keying (OOK) at the victim and $M-$PSK at the helper, we highlight that due to the processing delay, the symbols received across several time slots at the destination are correlated. Thus, the decoding complexity of the optimal decoder is $\mathcal{O}(4M^2)$, which makes its implementation challenging. We also show that the symbols received at the destination from the victim and the helper are still uncoordinated in energy, thereby, making the proposed countermeasure susceptible to detection by the adversary. To circumvent these challenges, we propose 3ϕ DASC-MF scheme, which falls under the framework of DASC-MF as a special case. (See Sec. 5.3)

2. In the 3ϕ DASC-MF scheme, we divide the frame structure into three parts, parameterized by the processing delay, Θ, such that, $\Theta \leq \frac{L}{2}$, where L denotes the number of symbols transmitted in a frame by the victim. The novel idea of this strategy is to use two energy-splitting factors, $\alpha \in (0, 1)$ and $\beta \in (0, 1)$ at different portions of the frame. Through an appropriate choice of α, we show that the correlation across the symbols can be minimized thereby ensuring that symbols at different time slots can be independently decoded and also show improved energy coordination when compared to the vanilla DASC-MF scheme. For this strategy, we provide strong analytical results on the error performance, and based on these results, we provide a near-optimal solution on α and β to the optimization problem of minimizing the error-rates. We also show that 3ϕ DASC-MF is

less complex than DASC-MF, and a majority of the symbols transmitted during 3ϕ DASC-MF scheme are coordinated in energy. (See Sec. 5.4)

3. When $\Theta > \frac{L}{2}$, we propose a new countermeasure, referred to as the semi-coherent multiple access channel (SC-MAC) scheme. As a salient feature of this scheme, the helper does not decode the victim's symbols, instead, the victim and the helper transmit their symbols synchronously to the destination on the helper's frequency using an energy-splitting factor, $\varepsilon \in (0, 1)$, thereby, eliminating the need of an FD radio at the helper. For SC-MAC, we first derive a closed-form expression on the error-rates and then, formulate an optimization problem of finding near-optimal values on ε that minimizes the error-rates at the destination. (See Sec. 5.5)
4. Finally, through various analytical and simulation results, we show that our schemes are covert when the adversary measures energy on the victim's and the helper's frequencies. (See Sec. 5.6)

5.1.2 Related Work and Novelty

Although, FD radios have been studied from a legitimate user's view point [76, 101–103] and from an adversarial view point [89–91], [34, 35, 37, 39, 40], this work studies FD radios from both the viewpoints. The main novelty of this work is the use of delay-aware FD radios, which has not been addressed in the literature hitherto.

5.2 System Model

We consider a network model, where all the uplink frequencies to the destination are occupied by the legitimate nodes of the network. As a result, there are no vacant frequencies in the network. Let Alice and Charlie be two legitimate nodes of the network who communicate with the destination, Bob using orthogonal frequencies. Alice is a single-antenna transmitter which uses a frequency band centred around f_{AB} to communicate her low data-rate symbols with strict low-latency constraints (e.g., PUCCH in 5G [104]) to Bob. In contrast, Charlie uses a frequency band centred around f_{CB} to communicate his symbols to Bob. A salient feature of Charlie is that he is equipped with a full-duplex (FD) radio with N_C receive-antennas and a single transmit-antenna,

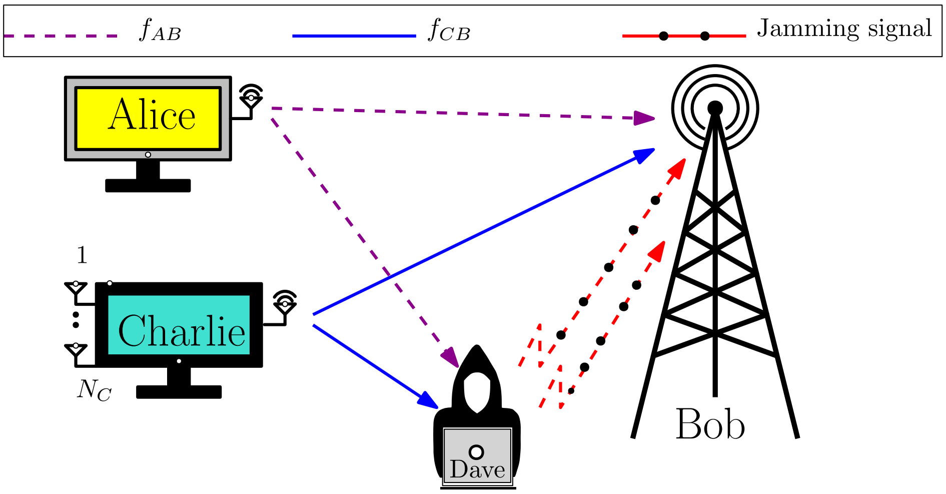

Figure 5.1: A network model depicting legitimate nodes, Alice and Charlie, and the reactive adversary, Dave.

thus, enabling him to implement FD communication on f_{CB}. Further, Charlie transmits symbols with arbitrary data-rate and relaxed latency constraints. An instantiation of the network is as shown in Fig. 5.1. In this network, we also assume the presence of a jammer, Dave. Unlike traditional jammers, Dave is an FD reactive jammer who intends to jam Alice's uplink symbols on f_{AB} [16] and monitors all the frequencies (including f_{AB}) for possible countermeasures by the legitimate nodes. In context of this chapter, Dave uses an energy detector (ED) to measure the average energy level of all the frequencies in the network before and after jamming. Thus, if ED measures a significant fluctuation in the average energy level on any band, it raises the flag. This in turn forbids Alice from using traditional mitigation techniques, such as FH. Subsequently, a raised flag by ED compels Dave to jam other frequencies, thereby degrading the network's performance. Thus, in the next section, we propose a framework wherein Charlie assists Alice to reliably communicate her messages to Bob without getting detected by ED on any frequency band.

5.3 Delay-Aware Semi-Coherent Multiplex-and-Forward Relaying Scheme

As shown in Fig. 5.3, let Alice has a frame of L symbols to communicate with Bob within T seconds from the generation of the first symbol, where $T = L/W$, such that W is the bandwidth of communication. Since f_{AB} is jammed by Dave, Alice seeks

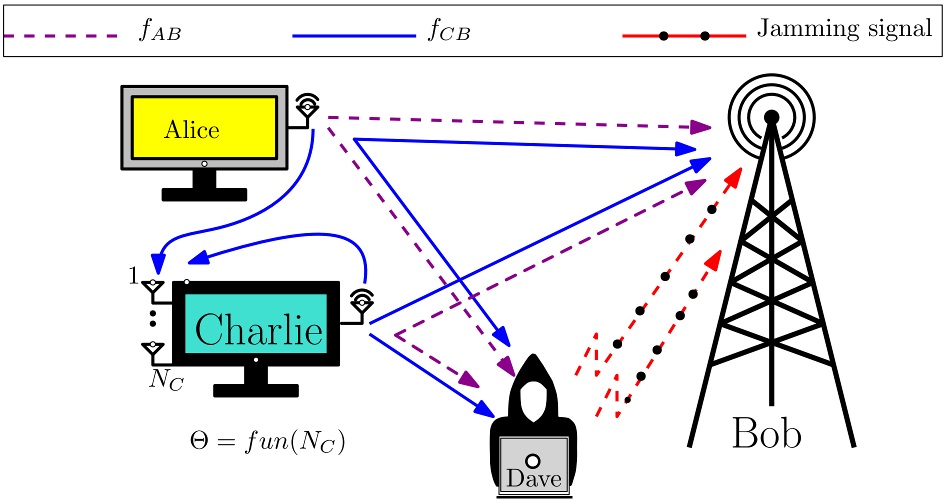

Figure 5.2: System model for DASC-MF scheme, where Charlie takes Θ symbols to multiplex-and-forward Alice's symbols to Bob.

help from Charlie. As part of the protocol, Alice broadcasts her symbols on f_{CB}. Then, Charlie, uses his FD radio to forward Alice's symbols to Bob on f_{CB}. Since Charlie is a legitimate node in the network, he also has symbols to communicate with Bob. Therefore, he decodes Alice's symbols, multiplexes her symbols to his symbols, and forwards them to Bob. However, the time taken by Charlie for this process depends on his receiver architecture. In particular, this *delay* is directly proportional to the time taken by him to cancel his self-interference (SI), which in turn is directly proportional to the number of receiving antennas, N_C. Therefore, we assume that Charlie requires a time duration equivalent to that of Θ symbols to decode, multiplex, and forward Alice's symbols, where Θ is governed by the SIC architecture of Charlie. The top two frames in Fig. 5.3 show the symbols transmitted simultaneously by Alice and Charlie on f_{CB}. The received symbols at Bob, denoted by $r_{B,n}$ are captured by the bottom frame, where n denotes the time slot index for communication. Further, x_n denotes Alice's symbol, and y_n, for $1 \leq n \leq \Theta$ and t_n, for $\Theta + 1 \leq n \leq L + \Theta$ denote the unmultiplexed and multiplexed symbols transmitted by Charlie, respectively. Due to delay of Θ symbols, $r_{B,n}$ is a function of x_n and y_n, for $1 \leq n \leq \Theta$. In addition, $r_{B,n}$ is a function of $x_{n-\Theta}$, x_n, and y_n, for $\Theta + 1 \leq n \leq L$. Note that, since the multiplexed symbols, t_n, for $L + 1 \leq n \leq L + \Theta$ are received after the deadline of T seconds, Bob cannot use these symbols for decoding Alice's symbols due to latency constraints. Therefore, Bob only uses the first L symbols received on f_{CB} after implementing the proposed countermeasure to jointly decode Alice's and Charlie's symbols.[1]

---

[1] During implementation, Charlie may decide not to multiplex after the L-th time slot since Alice's symbols are no longer used for decoding from $r_{B,n}$ for $n > L$

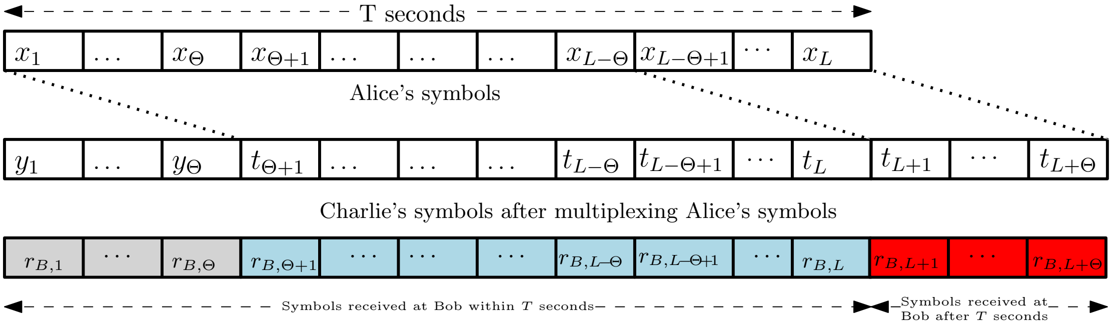

Figure 5.3: Illustration of symbol transmission in DASC-MF scheme.

Although the above scheme ensures that Alice's symbols reach Bob within the deadline, Dave observes a significant drop in the energy level on f_{AB}, provided Alice uses her entire energy to communicate on f_{CB}. Therefore, to avoid getting detected by Dave, Alice and Charlie use $1-\alpha$ and α fractions of their energies, respectively, to communicate their messages on f_{CB}, where $\alpha \in (0,1)$ is the design parameter under consideration. Subsequently, Alice and Charlie also use α and $1-\alpha$ fractions of their energies, respectively, to cooperatively transmit dummy OOK symbols on f_{AB}. The dummy OOK symbols are sampled from a pre-shared Gold sequence, thus, ensuring that the average energy level on f_{AB} is the same as it was before implementing the countermeasure. We highlight that the use of dummy OOK symbols also ensures that the symbols on f_{AB} and f_{CB} are uncorrelated. Fig. 5.2 illustrates the transmission strategy by Alice and Charlie on both f_{AB} and f_{CB}.

Due to low-latency constraints, Alice avoids the use of pilots for assisting channel estimation on f_{CB}, as a result, the communication on the links Alice-to-Charlie and Alice-to-Bob are inherently non-coherent. Further, since Alice has low data-rate symbols, she uses OOK signalling scheme. In contrast, since f_{CB} is not under attack, Charlie uses a coherent signalling scheme. In particular, Charlie uses $M-$ary PSK to communicate with Bob. As a result, the proposed scheme is a combination of coherent and non-coherent communication under a multiple access channel setup. Further, since this scheme takes into account the delay in processing Alice's symbols at Charlie, we refer to the proposed scheme as Delay-Aware Semi-Coherent Multiplex-and-Forward (DASC-MF) scheme.

In the next section, we discuss the signal model of DASC-MF scheme on f_{CB}. A detailed description of communication on f_{AB} and the analysis on the energy detectors will be discussed in Sec. 5.6.

5.3.1 Signal Model

In the DASC-MF scheme, Alice transmits $x_n \in \{0,1\}$ scaled by $\sqrt{1-\alpha}$ throughout the entire frame. Since Charlie is equipped with an FD radio with N_C receive-antennas, the $N_C \times 1$ received vector at Charlie is given by

$$\mathbf{r}_{C,n} = \sqrt{1-\alpha}\mathbf{h}_{AC,n}x_n + \mathbf{h}_{CC,n} + \mathbf{w}_{C,n}, \quad 1 \leq n \leq L, \tag{5.1}$$

where $\mathbf{h}_{AC,n} \sim \mathcal{CN}\left(\mathbf{0}_{N_C}, \sigma_{AC}^2 \mathbf{I}_{N_C}\right)$ and $\mathbf{h}_{CC,n} \sim \mathcal{CN}\left(\mathbf{0}_{N_C}, \lambda\frac{1+\alpha}{2}\mathbf{I}_{N_C}\right)$ are the $N_C \times 1$ vectors of fading channel coefficients of Alice-to-Charlie's link, residual SI of Charlie's FD radio, respectively, such that such that $\mathbf{0}_{N_C}$ is the $N_C \times 1$ vector of zeros and $\mathbf{I}_{N_C}$ is the $N_C \times N_C$ Identity matrix. Further, $\mathbf{w}_{C,n} \sim \mathcal{CN}\left(\mathbf{0}_{N_C}, N_o\mathbf{I}_{N_C}\right)$ is the Additive White Gaussian Noise (AWGN) vector at Charlie. Further, $\lambda \in [0,1]$ denotes the level of residual SI after the active and passive cancellations at Charlie. Finally, $N_o = \text{SNR}^{-1}$ is the variance of each element of the AWGN vector.

Charlie first uses non-coherent energy detection to decode x_n as $\hat{x}_n$ using the received vector, $\mathbf{r}_{C,n}$ and then multiplexes the decoded symbol, $\hat{x}_n$ to his symbol. However, due to the use of multiple receive-antennas, Charlie introduces a delay equivalent to Θ symbols to decode and multiplex $\hat{x}_n$ to his current symbol after SIC. Therefore, a symbol received at Charlie from Alice during the n^{th} time slot is multiplexed and forwarded to Bob during the $(n+\Theta)^{th}$ time slot. As a result, for all $1 \leq n \leq \Theta$, if $y_n \in \mathcal{S}_C$ denotes the original PSK symbol of Charlie to be transmitted at n^{th} time slot, such that $\mathcal{S}_C = \left\{ e^{\iota\frac{\pi}{M}(2m+1)} \middle| \, m = 0, \ldots, M-1 \right\}$, Charlie transmits $\sqrt{\alpha}y_n$. Subsequently, for all $n \geq \Theta + 1$, Charlie transmits the multiplexed symbol, t_n, such that

$$t_n = \begin{cases} y_n, & \text{if } \hat{x}_{n-\Theta} = 0, & (5.2\text{a}) \\ \sqrt{\alpha}e^{\iota\frac{\pi}{M}}y_n, & \text{if } \hat{x}_{n-\Theta} = 1. & (5.2\text{b}) \end{cases}$$

With this transmission strategy, Bob observes a multiple access channel on f_{CB} from Alice and Charlie. We note that Alice's symbol transmitted during the n^{th} time slot is observed at Bob during n^{th} time symbol on Alice-to-Bob link on $r_{B,n}$ and is again observed as multiplexed symbol from Charlie at $(n+\Theta)^{th}$ time symbol on Charlie-to-Bob link on $r_{B,n+\Theta}$, thus, introducing correlation between $r_{B,n}$ and $r_{B,n+\Theta}$. Overall, the received symbol at Bob during n^{th} time slot is given as

$$r_{B,n} = \begin{cases} \sqrt{1-\alpha}h_{AB,n}x_n + \sqrt{\alpha}h_{CB,n}y_n + w_{B,n}, & \text{if } 1 \leq n \leq \Theta, \qquad (5.3a) \\ \sqrt{1-\alpha}h_{AB,n}x_n + h_{CB,n}t_n + w_{B,n}, & \text{if } \Theta + 1 \leq n \leq L, \qquad (5.3b) \end{cases}$$

where $h_{AB,n} \sim \mathcal{CN}(0, \sigma_{AB}^2)$ and $h_{CB,n} \sim \mathcal{CN}(0, \sigma_{CB}^2)$ are the channel coefficients of Alice-to-Bob and Charlie-to-Bob links, respectively. Further, $w_{B,n} \sim \mathcal{CN}(0, N_o)$ is the AWGN at Bob during the n^{th} time slot. For the decoding process, we assume that Bob has the knowledge of $h_{CB,n}$. Further, since Charlie is in the vicinity of Alice, we assume $\sigma_{AC}^2 > \sigma_{AB}^2$, thus achieving a higher SNR on Alice-to-Charlie link as compared to Alice-to-Bob link. We also assume that all channels and noise realizations are statistically independent. Finally, for error analysis in the rest of the chapter, we use $\sigma_{AB}^2 = \sigma_{CB}^2 = 1$.

5.3.2 Error Analysis at Bob

Since Charlie decodes and multiplexes Alice's symbols to Bob, in this section, we first characterise the error introduced by Charlie in decoding Alice's symbols. We then compute the joint error-rates at Bob in decoding Alice's and Charlie's symbols.

Based on (5.1), the maximum likelihood (ML) decoder for detection of Alice's symbols at Charlie is

$$\hat{x}_n = \arg \max_{i \in \{0,1\}} g\left(\mathbf{r}_{C,n} | x_n = i\right) = \arg \min_{i \in \{0,1\}} N_C \ln(\pi \Omega_i) + \frac{\mathbf{r}_{C,n}^H \mathbf{r}_{C,n}}{\Omega_i}, \tag{5.4}$$

where $g\left(\mathbf{r}_{C,n} | x_n\right)$ is the probability density function (PDF) of $\mathbf{r}_{C,n}$ conditioned on x_n and $\Omega_i = \sigma_{AC}^2(1-\alpha)i + \lambda\frac{(1+\alpha)}{2} + N_o$. Based on (5.4), the threshold for energy detection is given by $\tau = N_C \frac{\Omega_0 \Omega_1}{\Omega_0 - \Omega_1} \ln\left(\frac{\Omega_0}{\Omega_1}\right)$. Finally, using τ, it is straightforward to prove the next theorem that presents the probability of error at Charlie in decoding Alice's symbols.

Theorem 12. *If $\Phi_{i\bar{i}}$ denotes the probability of decoding symbol i as $\bar{i}$, for $i, \bar{i} = \{0,1\}$, then $\Phi_{01} = \frac{\Gamma\left(N_C, \frac{\tau}{\Omega_0}\right)}{\Gamma(N_C)}$ and $\Phi_{10} = \frac{\gamma\left(N_C, \frac{\tau}{\Omega_1}\right)}{\Gamma(N_C)}$, where $\Gamma(\cdot,\cdot)$ and $\gamma(\cdot,\cdot)$ denote the lower and upper incomplete gamma functions, respectively, and $\Gamma(\cdot)$ denotes the complete gamma function.*

From Theorem 12, we immediately observe the following two remarks.

Remark 3. *The terms* Φ_{01} *and* Φ_{10} *are increasing functions of* α *for a given* N_C*,* SNR*, and* λ*.*

Remark 4. *The terms* Φ_{01} *and* Φ_{10} *are decreasing functions of* N_C*, for a given* α*,* SNR*, and* λ*.*

Based on (5.3a) and (5.3b), the joint maximum a posteriori (MAP) decoder for DASC-MF scheme is

$$\hat{i}, \hat{j}, \hat{k}, \hat{l} = \arg\max_{i,j,k,l} g_B\Big(r_{B,n}, r_{B,n-\Theta} | x_n = i, x_{n-\Theta} = j, y_n = e^{\iota\frac{\pi}{M}(2l+1)}, \\ y_{n-\Theta} = e^{\iota\frac{\pi}{M}(2k+1)}, h_{CB,n}, h_{CB,n-\Theta}\Big), \quad (5.5)$$

where $i, j \in \{0, 1\}$, $k, l \in \{0, M-1\}$ and $g_B(.)$ is the joint PDF of $r_{B,n}$ and $r_{B,n-\Theta}$ conditioned on x_n and y_n for $1 \leq n \leq \Theta$ and x_n, $x_{n-\Theta}$, $y_{n-\Theta}$, and y_n, for $\Theta + 1 \leq n \leq L$.

Towards decoding Alice's and Charlie's symbols, the implementation of the decoder in (5.5) is complex due to the correlation between the symbols received Θ symbols apart. In particular, the complexity of the proposed decoder is $\mathcal{O}(4M^2)$ as Bob has to jointly decode two OOK and two PSK symbols. Further, we note that, at any instant the symbols transmitted by Alice and Charlie are uncoordinated in their energies. For instance, when Alice transmits bit-0, Alice and Charlie contribute zero and α energies, respectively. Thus, the resultant sum energy on f_{CB} is α. As a result, Dave's ED that is monitoring f_{CB} may observe a dip in the average energy level on f_{CB}. Therefore, to circumvent the above problems, in the next section, we propose a variation of DASC-MF scheme, such that the new scheme is amenable to lower-decoding complexity at Bob. Further, the new scheme also ensures that despite uncoordinated transmission from Alice and Charlie, the duration for which Dave's ED observes a dip in the average energy level on f_{CB} is small as compared to its previous counterpart.

5.4 3ϕ Delay-Tolerant Semi-Coherent Multiplex-and-Forward Relaying Scheme

From the discussions in the previous section, we note that Alice's information symbol, x_n, $1 \leq n \leq L - \Theta$ is observed twice at Bob during the interval of T seconds: once during the time slot $1 \leq n \leq L-\Theta$ on the Alice-to-Bob link of the MAC and again after Θ symbols as t_n, for $\Theta+1 \leq n \leq L$ on the Charlie-to-Bob link of the MAC. Therefore, if Bob discards Alice's symbols on Alice-to-Bob link of the MAC for $1 \leq n \leq L - \Theta$ and treat these symbols as interference, he can still recover these symbols using the multiplexed symbols t_n, $\Theta + 1 \leq n \leq L$. Furthermore, if the interference caused from Alice's symbols on the time slots $1 \leq n \leq L - \Theta$ are somehow suppressed, then the correlation between $r_{B,n}$ and $r_{B,n+\Theta}$ can be minimized, thereby ensuring that Charlie's symbols on $r_{B,n}$ are decoded independent of Charlie's multiplexed symbols on the other time slots. Subsequently this would facilitate reduced decoding complexity at Bob. To facilitate interference suppression, we propose a method of choosing α for the time slots $1 \leq n \leq L - \Theta$, such that Charlie would continue to reliably recover Alice's symbols for multiplexing process. We note that, since the Alice-to-Bob link of the MAC is non-coherent, Alice contributes $1 - \alpha$ and zero energies on this link for $x_n = 1$ and $x_n = 0$, respectively. As a result, the variance of the effective noise at Bob is utmost $N_o + 1 - \alpha$ and N_o for $x_n = 1$ and $x_n = 0$, respectively. Since $N_o + 1 - \alpha$ is a decreasing function of α, if we increase α close to 1, we can suppress the interference on Alice-to-Bob link of the MAC, when $x_n = 1$ is sent from Alice. In particular, if $1 - \alpha = \Delta N_o$, such that $0 < \Delta \ll 1$, where Δ is the design parameter, then, $N_o + 1 - \alpha = N_o(1 + \Delta) \approx N_o$. However, we must note that, when α is close to 1, Charlie requires a large N_C to reliably decode Alice's symbols (Remark 3). Therefore, if we indefinitely reduce Δ to a very small value to increase α close to 1, N_C increases which in turn increases the latency at Charlie. Thus, in our proposed scheme, interference suppression at Bob comes at a cost of large N_C.

From the above discussion, the transmission scheme for the time slots, $1 \leq n \leq L$ at Alice and Charlie can be divided into three phases. During Phase-I, $1 \leq n \leq \Theta$, Alice and Charlie transmit their symbols scaled by $1 - \alpha$ and α fractions of their energies, respectively. Subsequently, during Phase-II, $\Theta + 1 \leq n \leq L - \Theta$, Alice continues to transmit her symbols scaled by $1-\alpha$ fraction of her energy, however, Charlie scales the multiplexed symbol by α fraction of his energy as given in (5.2a) - (5.2b). Further, due to processing delay of Θ symbols at Charlie, the multiplexed symbols corresponding to x_n, $L-\Theta+1 \leq n \leq L$, reach Bob after the deadline i.e., after T seconds. Therefore, these symbols cannot be decoded using the multiplexed symbols and instead must be decoded using the symbols on Alice-to-Bob link of the MAC. Thus, for $L-\Theta+1 \leq n \leq L$, Bob must jointly decode three symbols, i.e., Alice's current symbol, x_n, Charlie's current symbol, y_n, and multiplexed Alice's symbol, $x_{n-\Theta}$. Since these symbols are transmitted via combination of coherent and non-coherent modulation schemes, Bob needs distinguishable energy levels for detection when $x_n = 0$ and $x_n = 1$ is sent. As a consequence, for $L-\Theta+1 \leq n \leq L$, we cannot use $\alpha = 1 - \Delta N_o$ and instead use a different energy-splitting factor, $\beta \in (0, 1)$. Therefore, we refer to the time slots $L-\Theta+1 \leq n \leq L$ as Phase-III, wherein, Alice and Charlie transmit their symbols scaled by $1-\beta$ and β fraction of their energies, respectively. Here, Charlie only rotates his PSK symbol by $e^{\iota\frac{\pi}{M}}$ when he decodes symbol 1 from Alice. It is evident from the discussions that the maximum delay tolerated by the proposed 3ϕ DASC-MF scheme is $\frac{L}{2}$, i.e., $\Theta \leq \frac{L}{2}$. This is because, for $\Theta > \frac{L}{2}$, only a fraction of Alice's symbols are recoverable using Charlie's multiplexed symbols and a majority of the multiplexed symbols are received after the deadline, thus, violating the deadline constraint.

Overall, the symbols received at Bob during each phase are tabulated in Table 5.1. Further, in Fig. 5.4, the top two frames depict the symbols transmitted by Alice and Charlie when using the 3ϕ DASC-MF scheme. The bottom frame depicts the corresponding symbols received at Bob during each phase. Furthermore, assuming Charlie transmits symbols using $4-$PSK signalling, the constellation diagrams jointly contributed by Alice and Charlie during each phase at Bob are shown in Fig. 5.5, 5.6, 5.7.

From the above discussions, it is clear that, the decoding complexities during Phase-I, Phase-II and Phase-III are $\mathcal{O}(M)$, $\mathcal{O}(2M)$, and $\mathcal{O}(4M)$, respectively. Hence, unlike DASC-MF scheme, the worst-case complexity of 3ϕ DASC-MF is linear in M. Further, since α is close to 1, for $1 \leq n \leq L-\Theta$, the energy level on f_{CB} is solely controlled by Charlie and only the last Θ symbols out of the L symbols received at Bob are uncoordinated in energy. In particular, in 3ϕ DASC-MF scheme, $\frac{\Theta}{L}$ fraction of symbols are uncoordinated in energy, whereas, in traditional DASC-MF scheme, the entire frame of

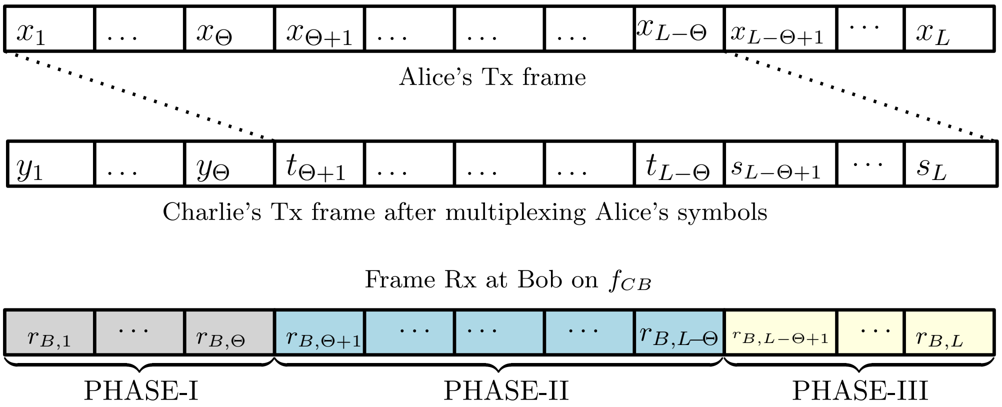

Figure 5.4: Frame model for the 3ϕ DASC-MF scheme.

Table 5.1: SYMBOLS TRANSMITTED IN EACH PHASE

	Alice-to-Bob link	Charlie-to-Bob link
Phase-I	$\sqrt{1-\alpha}x_n$	$\sqrt{\alpha}y_n$
Phase-II	$\sqrt{1-\alpha}x_n$	$t_n = \begin{cases} y_n & \text{if } \hat{x}_{n-\Theta} = 0, \\ \sqrt{\alpha}e^{\iota\frac{\pi}{M}}y_n & \text{if } \hat{x}_{n-\Theta} = 1. \end{cases}$
Phase-III	$\sqrt{1-\beta}x_n$	$s_n = \begin{cases} \sqrt{\beta}y_n & \text{if } \hat{x}_{n-\Theta} = 0, \\ \sqrt{\beta}e^{\iota\frac{\pi}{M}}y_n & \text{if } \hat{x}_{n-\Theta} = 1. \end{cases}$

L symbols are uncoordinated in energy. Hence, 3ϕ DASC-MF scheme helps reduce the decoding complexity and reduce the fraction of symbols over which the energy is uncoordinated. Towards characterising the error performance of the 3ϕ DASC-MF scheme, if $P_{e,3\phi}$ denotes the average probability of error across all the three phases, then

$$P_{e,3\phi} = \frac{\Theta}{L}P_{I,avg} + \frac{(L-2\Theta)}{L}P_{II,avg} + \frac{\Theta}{L}P_{III,avg}, \tag{5.6}$$

where $P_{I,avg}$ denotes the average probability of error in decoding y_n, $1 \leq n \leq \Theta$, during Phase-I, $P_{II,avg}$ denotes the average probability of error in jointly decoding y_n and $x_{n-\Theta}$, $\Theta + 1 \leq n \leq L - \Theta$, during Phase-II, and $P_{III,avg}$ denotes the average probability of error in jointly decoding x_n, y_n, $x_{n-\Theta}$, $L - \Theta + 1 \leq n \leq L$, during Phase-III. All the error terms in (5.6) are averaged over $h_{CB,n}$, $1 \leq n \leq L$. Note that, here, $P_{I,avg}$ is a function of α, $P_{II,avg}$ is a function of N_C and α, and $P_{III,avg}$ is a function of N_C and β. Since $\alpha = 1 - \Delta N_o$ is fixed for a given choice of Δ and SNR, the parameters of interest are N_C and β. Therefore, in (5.7) we formulate an optimization problem to compute the optimal values of N_C and β for a given L, Δ and SNR.

$$N_C^{\star}, \beta^{\star} = \arg\min_{N_C, \beta} \quad P_{e,3\phi}; \text{ s.t.: } N_C > 1, 0 < \beta < 1. \tag{5.7}$$

In the subsequent sections, we discuss the signal model for all the three phases in detail and compute $P_{I,avg}$, $P_{II,avg}$, and $P_{III,avg}$, so as to obtain $P_{e,3\phi}$.

5.4.1 Signal Model and Error Analysis of Phase-I

During Phase-I, Bob receives the first Θ symbols of Alice on Alice-to-Bob link of the MAC scaled by the factor $\sqrt{1-\alpha}$ and the unmultiplexed symbols of Charlie scaled by the factor $\sqrt{\alpha}$ on Charlie-to-Bob link of the MAC. However, according to the protocol of 3ϕ DASC-MF scheme, Bob treats the incoming symbols from Alice on the Alice-to-Bob link of the MAC as interference. Thus, the n^{th} baseband symbol received at Bob during Phase-I is given as $r_{B,n} = h_{CB,n}\sqrt{\alpha}y_n + \tilde{w}_{B,n}$, for $1 \leq n \leq \Theta$, where $\tilde{w}_{B,n} = \sqrt{1-\alpha}h_{AB,n}x_n + w_{B,n}$ denotes the effective noise at Bob, such that $N_{o\alpha} = N_o + 1 - \alpha$ is its worst case effective variance. Given that α is close to 1, we assume that $\tilde{w}_{B,n} \sim \mathcal{CN}(0, N_{o\alpha})$. For $4-$PSK signalling scheme, the constellation diagram during Phase-I at Bob is as shown in Fig. 5.5, where m denotes the index of the PSK symbol transmitted by Charlie. Owing to the Gaussian statistics of $\tilde{w}_{B,n}$ and $h_{CB,n}$, $r_{B,n}|_{y_n,h_{CB,n}} \sim \mathcal{CN}\left(\sqrt{\alpha}h_{CB,n}y_n, N_{o\alpha}\right)$. Since the symbols received at Bob during Phase-I only contains Charlie's symbols, based on $r_{B,n}$, the Maximum A Posteriori (MAP) decoder for Phase-I is

$$\hat{m} = \arg\max_{m} g_I\left(r_{B,n}|y_n = e^{\iota\frac{\pi}{M}(2m+1)}, h_{CB,n}\right), \tag{5.8}$$

where $m \in \{0, \ldots, M-1\}$ and $g_I(\cdot)$ is the PDF of $r_{B,n}$ conditioned on $h_{CB,n}$ and y_n. Further, $\hat{m}$ denotes the decoded PSK index. Using (5.8), in the following theorem, we characterise the average probability of error over all the realizations of $h_{CB,n}$, denoted by $P_{1,avg}$.

Theorem 13. *At high SNR, a union bound on the probability of error during Phase-I is approximated as* $2Q\left(\frac{|h_{CB,n}|d_{\mathrm{I}}}{\sqrt{2N_{o\alpha}}}\right)$, *where* $Q(\cdot)$ *denotes the Q-function. Further, we first use Chernoff bound to upper bound the error expression and then average it over all*

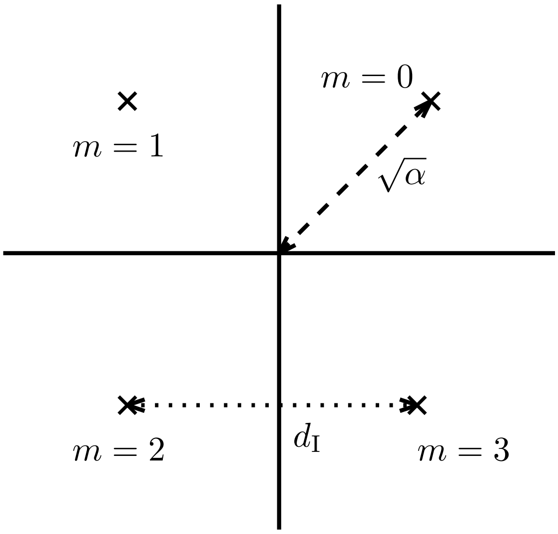

Figure 5.5: Constellation diagram jointly contributed by Alice and Charlie during Phase-I

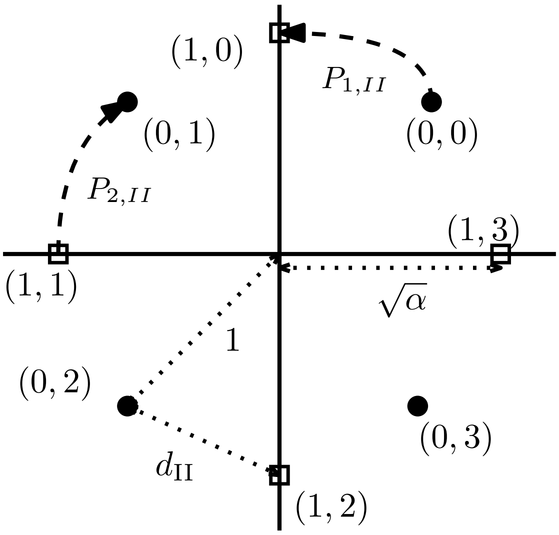

Figure 5.6: Constellation diagram jointly contributed by Alice and Charlie during Phase-II

the realizations of $h_{CB,n}$ *to obtain* $\mathcal{P}_1$*, such that* $\mathcal{P}_I = \frac{4N_{o\alpha}}{4N_{o\alpha} + d_{\mathrm{I}}^2}$*. [121]*

5.4.2 Signal Model and Error Analysis of Phase-II

During Phase-II, Alice continues to transmit her OOK symbol, x_n, with $1 - \alpha$ fraction of her energy and Charlie transmits the multiplexed symbol t_n, which is a function of y_n and $x_{n-\Theta}$. Thus, Bob receives Alice's symbols on the Alice-to-Bob link of the MAC and Charlie's multiplexed symbols on the Charlie-to-Bob link of the MAC. However, he considers Alice's symbols as interference and jointly decodes y_n and $x_{n-\Theta}$. The n^{th} baseband symbol received during Phase-II at Bob is given as $r_{B,n} = h_{CB,n}t_n + \tilde{w}_{B,n}$, for $\Theta + 1 \leq n \leq L - \Theta$, where t_n is as given in Table 5.1 and $\tilde{w}_{B,n}$ is the effective noise at Bob. Fig. 5.6 depicts the constellation received at Bob during Phase-II. If Alice and Charlie choose to transmit $x_{n-\Theta} = j$ and $y_n = e^{\iota\frac{\pi}{M}(2m+1)}$, then the transmit pair is denoted by (j, m). It can be observed that for $4-$PSK used by Charlie, Bob can receive one out of the 8 symbols. In general, when Charlie uses $M-$PSK constellation, Bob receives one out of the $2M$ constellation points. Therefore, the distribution of $r_{B,n}$ conditioned on $x_{n-\Theta}$, y_n, and $h_{CB,n}$ is

$$\begin{cases} \mathcal{CN}(h_{CB,n}y_n, N_{o\alpha}) & \begin{array}{l}\text{if } x_{n-\Theta} = 0 \text{ and } \hat{x}_{n-\Theta} = x_{n-\Theta} \\ \text{or } x_{n-\Theta} = 1 \text{ and } \hat{x}_{n-\Theta} \neq x_{n-\Theta},\end{array} \quad (5.9a) \\ \mathcal{CN}(\sqrt{\alpha}h_{CB,n}e^{\iota\frac{\pi}{M}}y_n, N_{o\alpha}) & \begin{array}{l}\text{if } x_{n-\Theta} = 0 \text{ and } \hat{x}_{n-\Theta} \neq x_{n-\Theta} \\ \text{or } x_{n-\Theta} = 1 \text{ and } \hat{x}_{n-\Theta} = x_{n-\Theta}.\end{array} \quad (5.9b) \end{cases}$$

Using (5.9a) – (5.9b), the joint MAP decoder for Phase-II is given by

$$\hat{j}, \hat{m} = \arg\max_{j,m} g_{II}\left(r_{B,n} | x_{n-\Theta} = j, y_n = e^{\iota\frac{\pi}{M}(2m+1)}, h_{CB,n}\right), \tag{5.10}$$

where $j \in \{0, 1\}$ and $m \in \{0, \ldots, M-1\}$. Further, $g_{II}(\cdot)$ is the conditional PDF of $r_{B,n}$ conditioned on $x_{n-\Theta}$, y_n, and $h_{CB,n}$. Note that due to errors introduced by Charlie in decoding Alice's symbols, the distribution of $g_{II}(\cdot)$ is a Gaussian mixture. In particular, the distribution of $g_{II}(\cdot)$ is a convex combination of $g_{II}\left(r_{B,n}|y_n, h_{CB,n}, x_{n-\Theta} = \hat{x}_{n-\Theta}\right)$ and $g_{II}\left(r_{B,n}|e^{\iota\frac{\pi}{M}}y_n, h_{CB,n}, x_{n-\Theta} \neq \hat{x}_{n-\Theta}\right)$, when $x_{n-\Theta} = 0$ and $x_{n-\Theta} = 1$. The distribution of $g_{II}(\cdot)$ for different realizations of $x_{n-\Theta}$ is as given in (5.11).

$$\begin{aligned} g_{II}\left(r_{B,n}|x_{n-\Theta} = j, y_n, h_{CB,n}\right) = \Phi_{jj} g_{II}\left(r_{B,n}|y_n, h_{CB,n}, x_{n-\Theta} = \hat{x}_{n-\Theta}\right) + \\ \Phi_{j\bar{j}} g_{II}\left(r_{B,n}|e^{\iota\frac{\pi}{M}}y_n, h_{CB,n}, x_{n-\Theta} \neq \hat{x}_{n-\Theta}\right), \end{aligned} \tag{5.11}$$

where $\bar{j}$ is the complement of j and $\Phi_{00} = 1 - \Phi_{01}$ and $\Phi_{11} = 1 - \Phi_{10}$ are the probabilities of correct detection of bit-0 and bit-1 at Charlie, respectively. Further, $g_{II}\left(r_{B,n}|e^{\iota\frac{\pi}{M}}y_n, h_{CB,n}, x_{n-\Theta} \neq \hat{x}_{n-\Theta}\right)$ is the conditional PDF of the symbol received at Bob when Charlie makes an error in decoding Alice's symbol. Since solving the error-performance of the joint MAP decoder using the Gaussian mixtures is non-trivial, we propose an approximation on (5.10), where we only consider the dominant term in (5.11) for error computation, for each realization of j. Along the similar lines of [35], we observe that Φ_{00} is dominant over Φ_{01} when $x_{n-\Theta} = 0$ and Φ_{11} is dominant over

Φ_{10}, when $x_{n-\Theta} = 1$. Therefore, we approximate the joint MAP decoder in (5.10) by a Joint Dominant Decoder (JDD), by retaining the first term in the RHS of (5.11). The expression of JDD is given as

$$\hat{j}, \hat{m} = \arg\max_{j,m} \tilde{g}_{II}\left(r_{B,n} | x_{n-\Theta} = j, y_n = e^{\iota \frac{\pi}{M}(2m+1)}, h_{CB,n}\right), \tag{5.12}$$

where $j \in \{0, 1\}$ and $m \in \{0, \ldots, M-1\}$. Further, $\tilde{g}_{II}(\cdot)$ is an approximation on $g_{II}(\cdot)$ when considering the first term in the RHS of (5.11). In the next theorem, we derive a union bound on the probability of error in jointly decoding Alice's and Charlie's symbols during Phase-II.

Theorem 14. *At high SNR, the probability of error for Phase-II, denoted by $P_{e,II}$, is upper bounded by $\Phi_{00}P_{1,II} + \Phi_{01}P_{\bar{1},II} + \Phi_{11}P_{2,II} + \Phi_{10}P_{\bar{2},II}$, where $P_{1,II} = P_{2,II}$ and $P_{\bar{1},II} = P_{\bar{2},II} = 1 - P_{1,II}$, such that $P_{1,II} \approx Q\left(\frac{|h_{CB,n}|d_{\text{II}}}{\sqrt{2N_{o\alpha}}}\right)$. Further, the minimum Euclidean distance between the constellation points transmitted by Charlie during Phase-II is denoted by $d_{\text{II}} = \sqrt{1 + \alpha - 2\sqrt{\alpha}\cos\left(\frac{\pi}{M}\right)}$.*

Proof. Let a transmit pair corresponding to $x_{n-\Theta}$ and y_n is denoted by (j, m), such that y_n denotes the PSK symbol transmitted by Charlie corresponding to the index m. Let $\nabla_{(j,m)\to(j',m')}$ be the event $(j', m') \neq (j, m)$, then a pair (j, m) is incorrectly decoded as (j', m') if

$$\nabla_{(j,m)\to(j',m')} \triangleq \frac{\tilde{g}_{II}\left(r_{B,n} | x_{n-\Theta} = j, y_n = e^{\iota \frac{\pi}{M}(2m+1)}, h_{CB,n}\right)}{\tilde{g}_{II}\left(r_{B,n} | x_{n-\Theta} = j', y_n = e^{\iota \frac{\pi}{M}(2m'+1)}, h_{CB,n}\right)} \leq 1.$$

Therefore, the probabilities of decoding a pair $(0, m)$ as (j', m') and $(1, m)$ as (j', m') at Bob is

$$\Pr\left((0, m) \to (j', m')\right) = \Phi_{00} \Pr\left(\nabla_{(0,m)\to(j',m')} \leq 1 | \hat{x}_{n-\Theta} = x_{n-\Theta}\right) + \Phi_{01} \Pr\left(\nabla_{(0,m)\to(j',m')} \leq 1 | \hat{x}_{n-\Theta} \neq x_{n-\Theta}\right), \tag{5.13}$$

$$\Pr\left((1, m) \to (j', m')\right) = \Phi_{11} \Pr\left(\nabla_{(1,m)\to(j',m')} \leq 1 | \hat{x}_{n-\Theta} = x_{n-\Theta}\right) + \Phi_{10} \Pr\left(\nabla_{(1,m)\to(j',m')} \leq 1 | \hat{x}_{n-\Theta} \neq x_{n-\Theta}\right). \tag{5.14}$$

Combining (5.13) and (5.14), the probability of error in decoding a transmit pair

(j, m) as (j', m') is

$$\Pr((j,m) \to (j',m')) = \Phi_{jj} \Pr\left(\nabla_{(j,m)\to(j',m')} \leq 1 | \hat{x}_{n-\Theta} = x_{n-\Theta}\right) + \\ \Phi_{j\bar{j}} \Pr\left(\nabla_{(j,m)\to(j',m')} \leq 1 | \hat{x}_{n-\Theta} \neq x_{n-\Theta}\right). \quad (5.15)$$

Therefore, if the overall probability of error in decoding a transmit pair (j, m) is denoted by $\Pr\left((\hat{j}, \hat{m}) \neq (j, m)\right)$, then an upper bound on the overall expression is

$$\Pr\left((\hat{j}, \hat{m} \neq (j, m)\right) \leq \sum_{j'=0}^{1} \sum_{\substack{m'=0 \\ (j',m') \neq (j,m)}}^{M-1} \Pr((j,m) \to (j',m')). \quad (5.16)$$

As discussed earlier, Bob receives one out of the $2M-$PSK symbols corresponding to the $M-$PSK constellation used by Charlie. Finally, if $P_{e,II}$ denotes the average probability of error over $2M$ symbols, then using (5.13) - (5.16), it is straightforward to compute an upper bound on $P_{e,II}$ as $P_{e,II} \leq \frac{1}{2M} \sum_{j=0}^{1} \sum_{m=0}^{M-1} M \Pr\left((\hat{j}, \hat{m}) \neq (j, m)\right) \approx \Phi_{00} P_{1,II} + \Phi_{01} P_{\bar{1},II} + \Phi_{11} P_{2,II} + \Phi_{10} P_{\bar{2},II}$. Here, we only considered the nearest-neighbours at high SNR to approximate the upper bound. The pairwise probability terms in $P_{e,II}$ are depicted in Fig. 5.6. When evaluating the various error terms in the upper bound, we observe that $P_{1,II} = P_{2,II}$ and $P_{\bar{1},II} = P_{\bar{2},II} = 1 - P_{1,II}$, such that $P_{1,II} \approx Q\left(\frac{|h_{CB,n}| d_{\mathrm{II}}}{\sqrt{2N_{o\alpha}}}\right)$. Here, $d_{\mathrm{II}} = \sqrt{1 + \alpha - 2\sqrt{\alpha}\cos\left(\frac{\pi}{M}\right)}$ denotes the minimum Euclidean distance between the constellation points transmitted by Charlie during Phase-II. $\square$

Corollary 1. *If* $P_{II,avg} = \mathbb{E}_{h_{CB,n}}[P_{e,II}]$ *denotes the average probability of error over all the realizations of* $h_{CB,n}$, *then, using the Chernoff bound,* $P_{II,avg}$ *is upper bounded as* $P_{II,avg} \leq \mathcal{P}_{II} \triangleq \dfrac{2N_{o\alpha}}{4N_{o\alpha} + d_{\mathrm{II}}^2} (\Phi_{00} + \Phi_{11}) + (\Phi_{01} + \Phi_{10})$, *where we have used* $P_{\bar{1},II} \leq 1$, $P_{\bar{2},II} \leq 1$ *in the upper bound given in Theorem 14.*

5.4.3 Signal Model and Error Analysis of Phase-III

During Phase-III, Bob observes the symbols on both the links, i.e., the Alice-to-Bob link of the MAC and the Charlie-to-Bob of the MAC to decode x_n, y_n, and $x_{n-\Theta}$, for $L - \Theta + 1 \leq n \leq L$. Unlike Phase-I and Phase-II, Alice and Charlie use the energy-splitting factor, $\beta \in (0, 1)$ to transmit their respective symbols. In particular, Charlie

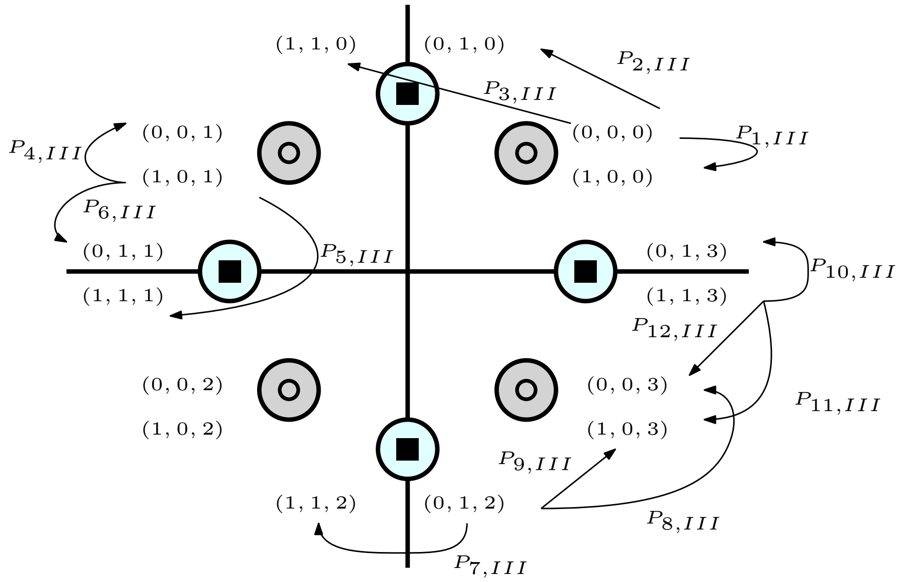

Figure 5.7: Constellation diagram jointly contributed by Alice and Charlie during Phase-III

scales his PSK symbols with $\sqrt{\beta}$, irrespective of $\hat{x}_{n-\Theta} = 0$ or $\hat{x}_{n-\Theta} = 1$. Further, Alice transmits her OOK symbols with $1 - \beta$ fraction of her energy. With this modification, the n^{th} baseband symbol received at Bob during Phase-III is given as

$$r_{B,n} = h_{AB,n}\sqrt{1-\beta}x_n + h_{CB,n}\sqrt{\beta}s_n + w_{B,n}, \quad L - \Theta + 1 \leq n \leq L, \quad (5.17)$$

where s_n is defined in Table 5.1 and $w_{B,n} \sim \mathcal{CN}(0, N_o)$ is the AWGN at Bob. Owing to the non-coherent nature of Alice-to-Bob link of the MAC, the variance of the effective noise is $N_o + 1 - \beta$ and N_o, when $x_n = 1$ and $x_n = 0$, respectively.

Fig. 5.7) depicts the received constellation symbols at Bob during Phase-III, when Charlie uses $4-$PSK signalling. If Alice's current symbol, $x_n = i$, Alice's multiplexed symbol, $x_{n-\Theta} = j$, and Charlie's current symbol, $y_n = e^{\iota \frac{\pi}{M}(2m+1)}$, then a transmit triplet is denoted by (i, j, m). The variance of the effective noise corresponding to $i = 0$ is N_o (small disk and solid squares), whereas, the variance of the effective noise corresponding to $i = 1$ is $N_o + 1 - \beta$ (blue and grey disks). We highlight that, Bob receives one out of the $16-$PSK symbols corresponding to $4-$PSK used by Charlie. In general, when Charlie uses $M-$PSK constellation, Bob is likely to receive one out of the $4M-$PSK symbols, out of which, $2M-$ PSK symbols are received with variance N_o and the rest $2M-$ PSK symbols are received with variance $N_o + 1 - \beta$. The distribution of $r_{B,n}$ as a function of x_n, $x_{n-\Theta}$, y_n, and $h_{CB,n}$ is $r_{B,n}|_{x_n,x_{n-\Theta},y_n,h_{CB,n}} \sim \mathcal{CN}(\sqrt{\beta}h_{CB,n}s_n, N_o)$, if $x_n = 0$ and $r_{B,n}|_{x_n,x_{n-\Theta},y_n,h_{CB,n}} \sim \mathcal{CN}(\sqrt{\beta}h_{CB,n}s_n, N_{o\beta})$, if

$x_n = 1$. Thus, using the distribution of $r_{B,n}$, the joint MAP decoder for Phase-III is

$$\hat{i}, \hat{j}, \hat{m} = \arg\max_{i,j,m} g_{III}\left(r_{B,n} | x_n = i, x_{n-\Theta} = j, y_n = e^{\iota \frac{\pi}{M}(2m+1)}, h_{CB,n}\right), \quad (5.18)$$

where $i \in \{0, 1\}$, $j \in \{0, 1\}$, and $m \in \{0, \ldots, M-1\}$. Further, $g_{III}(\cdot)$ is the conditional PDF of $r_{B,n}$, conditioned on $x_{n-\Theta}$, x_n, y_n, and $h_{CB,n}$. Along the similar lines of Phase-II, we note that $g_{III}(\cdot)$ in (5.18) is also a Gaussian mixture for various realizations of $x_{n-\Theta}$. Therefore, we approximate $g_{III}(\cdot)$ as $\tilde{g}_{III}(\cdot)$, where we retain the dominant terms from the Gaussian mixture, for $x_{n-\Theta} = 0$ and $x_{n-\Theta} = 1$, respectively. The JDD for Phase-III of 3ϕ DASC-MF is

$$\hat{i}, \hat{j}, \hat{m} = \arg\max_{i,j,m} \tilde{g}_{III}\left(r_{B,n} | x_n = i, x_{n-\Theta} = j, y_n = e^{\iota \frac{\pi}{M}(2m+1)}, h_{CB,n}\right), \quad (5.19)$$

where $i, j \in \{0, 1\}$ and $m \in \{0, \ldots, M-1\}$. In the next theorem, we compute a union bound on the probability of error in jointly decoding x_n, $x_{n-\Theta}$, and y_n, when using the JDD presented in (5.19).

Table 5.2: ERROR TERMS FOR PHASE-III AS GIVEN IN THEOREM 15

$P_{1,III} = \quad e^{\frac{-\varrho}{N_o}}$	$P_{2,III} = \quad Q\left(\frac{\lvert h_{CB,n}\rvert d_{\text{III}}}{\sqrt{2N_o}}\right)$	$P_{3,III} = \quad Q_1\left(\frac{\lvert A\rvert}{\sqrt{N_o/2}}, \frac{\sqrt{\xi_1}}{\sqrt{N_o/2}}\right)$
$P_{4,III} = \quad 1 - e^{\frac{-\varrho}{N_{o\beta}}}$	$P_{5,III} = \quad Q\left(\frac{\lvert h_{CB,n}\rvert d_{\text{III}}}{\sqrt{2N_{o\beta}}}\right)$	$P_{6,III} = \quad 1 - Q_1\left(\frac{\lvert B\rvert}{\sqrt{N_{o\beta}/2}}, \frac{\sqrt{\xi_2}}{\sqrt{N_{o\beta}/2}}\right)$
$P_{9,III} = \quad Q_1\left(\frac{\lvert A\rvert}{\sqrt{N_o/2}}, \frac{\sqrt{\xi_2}}{\sqrt{N_o/2}}\right)$	$P_{12,III} = \quad 1 - Q_1\left(\frac{\lvert B\rvert}{\sqrt{N_{o\beta}/2}}, \frac{\sqrt{\xi_1}}{\sqrt{N_{o\beta}/2}}\right)$	$P_{\overline{3},III} = \quad Q_1\left(\frac{\lvert B\rvert}{\sqrt{N_o/2}}, \frac{\sqrt{\xi_1}}{\sqrt{N_o/2}}\right)$
$P_{\overline{6},III} = \quad 1 - Q_1\left(\frac{\lvert A\rvert}{\sqrt{N_{o\beta}/2}}, \frac{\sqrt{\xi_2}}{\sqrt{N_{o\beta}/2}}\right)$	$P_{\overline{9},III} = \quad Q_1\left(\frac{\lvert B\rvert}{\sqrt{N_o/2}}, \frac{\sqrt{\xi_2}}{\sqrt{N_o/2}}\right)$	$P_{\overline{12},III} = \quad 1 - Q_1\left(\frac{\lvert A\rvert}{\sqrt{N_{o\beta}/2}}, \frac{\sqrt{\xi_1}}{\sqrt{N_{o\beta}/2}}\right)$

Theorem 15. *At high SNR, the error probability for Phase-III, denoted by* $P_{e,III}$*, is upper bounded by*

$$\begin{aligned}\frac{1}{4}\Bigg[&\Phi_{00}\left(P_{1,III} + 2P_{2,III} + 2P_{3,III} + P_{4,III} + 2P_{5,III} + 2P_{6,III}\right) + \\ &\Phi_{01}\left(P_{\overline{1},III} + 2P_{\overline{2},III} + 2P_{\overline{3},III} + P_{\overline{4},III} + 2P_{\overline{5},III} + 2P_{\overline{6},III}\right) + \\ &\Phi_{11}\left(P_{7,III} + 2P_{8,III} + 2P_{9,III} + P_{10,III} + 2P_{11,III} + 2P_{12,III}\right) + \\ &\Phi_{10}\left(P_{\overline{7},III} + 2P_{\overline{8},III} + 2P_{\overline{9},III} + P_{\overline{10},III} + 2P_{\overline{11},III} + 2P_{\overline{12},III}\right)\Bigg],\end{aligned} \quad (5.20)$$

where the various error terms in (5.20) *are tabulated in Table 5.2, such that,* $P_{4,III} = P_{10,III} = P_{\overline{4},III} = P_{\overline{10},III}$*;* $P_{5,III} = P_{11,III} = 1 - P_{\overline{5},III} = 1 - P_{\overline{11},III}$*;* $P_{1,III} = P_{7,III} = P_{\overline{1},III} = P_{\overline{7},III}$*;* $P_{2,III} = P_{8,III} = 1 - P_{\overline{2},III} = 1 - P_{\overline{8},III}$*.*

Proof. Let a triplet corresponding to x_n, $x_{n-\Theta}$, and y_n is denoted by (i,j,m). Let $\nabla_{(i,j,m)\rightarrow(i',j',m')}$ be the event $(i,j,m) \neq (i',j',m')$, then a triplet (i,j,m) is incorrectly decoded as (i',j',m') if

$$\nabla_{(i,j,m)\rightarrow(i',j',m')} \triangleq \frac{\tilde{g}_{III}\left(r_{B,n}|x_n = i, x_{n-\Theta} = j, y_n = e^{\iota\frac{\pi}{M}(2m+1)}, h_{CB,n}\right)}{\tilde{g}_{III}\left(r_{B,n}|x_n = i', x_{n-\Theta} = j', y_n = e^{\iota\frac{\pi}{M}(2m'+1)}, h_{CB,n}\right)} \leq 1.$$

Therefore, the probability of decoding $(i,0,m)$ as (i',j',m') and $(i,1,m)$ as (i',j',m') at Bob are

$$\begin{aligned}\Pr((i,0,m)\rightarrow(i',j',m')) = \Phi_{00}\Pr(\nabla_{(i,0,m)\rightarrow(i',j',m')} \leq 1|\hat{x}_{n-\Theta} = x_{n-\Theta}) + \\ \Phi_{01}\Pr(\nabla_{(i,0,m)\rightarrow(i',j',m')} \leq 1|\hat{x}_{n-\Theta} \neq x_{n-\Theta}), \quad (5.21)\end{aligned}$$

$$\begin{aligned}\Pr((i,1,m)\rightarrow(i',j',m')) = \Phi_{11}\Pr(\nabla_{(i,1,m)\rightarrow(i',j',m')} \leq 1|\hat{x}_{n-\Theta} = x_{n-\Theta}) + \\ \Phi_{10}\Pr(\nabla_{(i,1,m)\rightarrow(i',j',m')} \leq 1|\hat{x}_{n-\Theta} \neq x_{n-\Theta}). \quad (5.22)\end{aligned}$$

Thus, if probability of error in decoding (i,j,m) is denoted by $\Pr\left((\hat{i},\hat{j},\hat{m} \neq (i,j,m))\right)$, then $\Pr\left((\hat{i},\hat{j},\hat{m} \neq (i,j,m))\right)$ is upper bounded as

$$\begin{aligned}\Pr\left((\hat{i},\hat{j},\hat{m} \neq (i,j,m))\right) \leq \sum_{\substack{i'=0 \\ (i,j,m)\neq(i',j',m')}}^{1}\sum_{j'=0}^{1}\sum_{m'=0}^{M-1} \Phi_{jj}\Pr\left(\nabla_{(i,j,m)\rightarrow(i',j',m')}|\hat{x}_{n-\Theta} = x_{n-\Theta}\right) + \\ \Phi_{j\bar{j}}\Pr\left(\nabla_{(i,j,m)\rightarrow(i',j',m')}|\hat{x}_{n-\Theta} \neq x_{n-\Theta}\right).\end{aligned}$$

As discussed earlier, Bob receives $4M$ constellation symbols corresponding to $M-$PSK used by Charlie. Thus, if $P_{e,III}$ denotes the overall probability of error for $4M$ symbols, then $P_{e,III} \leq \frac{1}{4M}\sum_{i=0}^{1}\sum_{j=0}^{1}\sum_{m=0}^{M-1} M\Pr\left((\hat{i},\hat{j},\hat{m}) \neq (i,j,m)\right)$. Finally, considering the nearest-neighbours at high SNR and solving $P_{e,III}$ using the first principles we get (5.20). The various error terms in (5.20) are tabulated in Table 5.2. □

In addition to the terms defined in Table 5.2, $\varrho = \frac{N_o N_{o\beta}}{N_o - N_{o\beta}}\ln\left(\frac{N_o}{N_{o\beta}}\right)$ is the threshold for non-coherent energy detection at Bob between $(0,j,m)$ and $(1,j,m)$, $A =$

$\frac{|h_{CB,n}|d_{\mathrm{III}}N_o}{N_o-N_{o\beta}}$, $B = \frac{|h_{CB,n}|d_{\mathrm{III}}N_{o\beta}}{N_o-N_{o\beta}}$, $\xi_1 = \frac{N_oN_{o\beta}}{N_o-N_{o\beta}}\left[\ln\left(\frac{N_o\Phi_{11}}{N_{o\beta}\Phi_{00}}\right)+\frac{|h_{CB,n}|^2d_{\mathrm{III}}^2}{N_o-N_{o\beta}}\right]$, and $\xi_2 = \frac{N_oN_{o\beta}}{N_o-N_{o\beta}}\left[\ln\left(\frac{N_o\Phi_{00}}{N_{o\beta}\Phi_{11}}\right)+\frac{|h_{CB,n}|^2d_{\mathrm{III}}^2}{N_o-N_{o\beta}}\right]$ are the parameters of the respective Marcum-Q functions ($Q_1(\cdot,\cdot)$), where $d_{\mathrm{III}} = 2\sqrt{\beta}\sin\frac{\pi}{2M}$ is the minimum Euclidean distance between the constellation symbols received during Phase-III.

For $M = 4$, the various error terms in (5.20) are depicted in Fig. 5.7. We note that the upper bound on $P_{e,III}$ in (5.20) contains exponential functions, Q-functions, and Marcum-Q functions. Although it is straightforward to compute the average of Q-functions over various realizations of $h_{CB,n}$ in closed-form, averaging Marcum-Q functions over various realizations of $h_{CB,n}$ is non-tractable for certain cases. Therefore, in the next lemma, we directly provide an upper bound on the Marcum-Q function averaged over the realizations of $h_{CB,n}$ to simplify the analysis.

Lemma 13. *The term* $\mathbb{E}_{h_{CB,n}}\left[P_{3,III}\right]$ *is upper bounded by* $P_{1,III}$*, for all* $0<\beta<1$.

Proof. Along the similar lines of [35]

$$\mathbb{E}_{h_{CB,n}}\left[P_{3,III}\right] = \left(\frac{N_o\Phi_{11}}{N_{o\beta}\Phi_{00}}\right)^{\frac{N_{o\beta}}{N_{o\beta}-N_o}}\frac{\left(N_{o\beta}-N_o\right)^2}{\left(N_{o\beta}-N_o\right)^2+d_{\mathrm{III}}^2N_{o\beta}}.$$

From the expression of Φ_{00} and Φ_{11}, we have $\Phi_{00}\geq\Phi_{11}$, thus, $\frac{\mathbb{E}_{h_{CB,n}}\left[P_{3,III}\right]}{P_{1,III}}\leq 1$. □

In addition to the above result, for moderate and high SNRs, we observe that, $\mathbb{E}_{h_{CB,n}}\left[P_{3,III}\right]\ll P_{1,III}$. Therefore, we use the upper bound $\mathbb{E}_{h_{CB,n}}[2P_{3,III}]\leq P_{1,III}$. Along the similar lines, the following inequalities also hold good: $\mathbb{E}_{h_{CB,n}}[2P_{6,III}]\leq P_{4,III}$, $\mathbb{E}_{h_{CB,n}}[2P_{9,III}]\leq P_{7,III}$, and $\mathbb{E}_{h_{CB,n}}[2P_{12,III}]\leq P_{10,III}$. Furthermore, we also upper bound all the error terms that are the coefficients of Φ_{01} and Φ_{10} in (5.20) by 1, thereby circumventing the non-tractable issue of Marcum-Q functions.

Corollary 2. *If* $P_{III,avg}=\mathbb{E}_{h_{CB,n}}[P_{e,III}]$ *denotes the average probability of error over all the realizations of* $h_{CB,n}$*, then an upper bound on* $P_{III,avg}$ *is given as*

$$\mathcal{P}_{III}\triangleq\frac{1}{2}\Big(\Phi_{00}\left(P_{1,III}+P_{2,III}^{\star}+P_{4,III}+P_{5,III}^{\star}\right)+5\left(\Phi_{01}+\Phi_{10}\right)+$$
$$\Phi_{11}\left(P_{7,III}+P_{8,III}^{\star}+P_{10,III}+P_{11,III}^{\star}\right)\Big),$$

where $P_{2,III}^{\star}=P_{8,III}^{\star}=\frac{2N_o}{4N_o+d_{\mathrm{III}}^2}$, $P_{5,III}^{\star}=P_{11,III}^{\star}=\frac{2N_{o\beta}}{4N_{o\beta}+d_{\mathrm{III}}^2}$.

5.4.4 Optimization of N_C and β for 3ϕ DASC-MF Relaying Scheme

Substituting $\mathcal{P}_I$, $\mathcal{P}_{III}$, and $\mathcal{P}_{III}$ from Theorem 13, Corollary 1, and Corollary 2, respectively in (5.6), we obtain an upper bound on the average probability of error of 3ϕ DASC-MF, denoted by $\mathcal{P}_{e,3\phi}$ as

$$P_{e,3\phi} \leq \mathcal{P}_{e,3\phi} \triangleq \frac{\Theta}{L}\mathcal{P}_I + \frac{(L-2\Theta)}{L}\mathcal{P}_{II} + \frac{\Theta}{L}\mathcal{P}_{III}. \tag{5.23}$$

Therefore, instead of solving (5.7), we solve an alternate optimization problem of minimising $\mathcal{P}_{e,3\phi}$ over the variables on interest, N_C and β. Thus, the modified optimization problem is given as

$$N_C^{\dagger}, \beta^{\dagger} = \arg\min_{N_C, \beta} \quad \mathcal{P}_{e,3\phi}; \text{ s.t.: } N_C > 1, 0 < \beta < 1. \tag{5.24}$$

Unlike Phase-I and Phase-II, decoding in Phase-III is a combination of coherent and non-coherent detection. As a result, for a given N_C, β, and SNR, the error-rates for Phase-III dominates Phase-I and Phase-II, and thus, dominates $\mathcal{P}_{e,3\phi}$. Although, we can achieve improved error-rates during Phase-III by increasing N_C, we cannot indefinitely increase N_C, because Θ is an increasing function of N_C and for large values of N_C, the fraction of symbols decoded during Phase-III increases, which in turn increases $\mathcal{P}_{e,3\phi}$. Therefore, we must use an appropriate N_C that solves (5.24). Towards solving (5.24), we observe that proving unimodality of $\mathcal{P}_{e,3\phi}$ as a function of N_C and β is challenging due to the presence of the upper and the lower Gamma functions in the expressions of $\mathcal{P}_{II}$ and $\mathcal{P}_{III}$. Therefore, in this section, we first fix N_C to analyse $\mathcal{P}_{e,3\phi}$ as a function of β and then propose a low-complexity algorithm to obtain the near-optimal values of N_C and β that minimizes $\mathcal{P}_{e,3\phi}$.

Towards minimising $\mathcal{P}_{e,3\phi}$, we observe that when we fix N_C and vary β, $\mathcal{P}_{e,3\phi}$ has a unique dip, for $\beta \in (0, 1)$. This is due to the fact that, when we fix $\alpha = 1 - \Delta N_o$ and N_C, $\mathcal{P}_I$ and $\mathcal{P}_{II}$ are independent of β, but $\mathcal{P}_{III}$ has a unique dip for $\beta \in (0, 1)$. Further, we also observe that, the unique dip of $\mathcal{P}_{III}$ is close to the intersection of the increasing and decreasing terms of $\mathcal{P}_{III}$. The above observation is exemplified in Fig. 5.8 for $\Theta = \lceil 10 \log_{10}(N_C) \rceil$ at SNR = 25 dB and $\Delta = 0.1$. Therefore, in the next lemma, we fix N_C and identify the increasing and decreasing terms in $\mathcal{P}_{III}$ as a function of β.

Subsequently, in Theorem 16, we show that the increasing and decreasing terms in $\mathcal{P}_{III}$ intersect only once for $\beta \in (0,1)$.

Lemma 14. *For a fixed α and N_C, if P_+ and P_- denote the increasing and decreasing terms in $\mathcal{P}_{III}$, respectively, w.r.t. β, then, $P_+ = \Phi_{00}\left(P_{1,III} + P_{4,III}\right) + \Phi_{11}\left(P_{7,III} + P_{10,III}\right)$ and $P_- = \Phi_{00}\left(P^\star_{2,III} + P^\star_{5,III}\right) + \Phi_{11}\left(P^\star_{8,III} + P^\star_{11,III}\right)$.*

Proof. Along the similar lines of Remark 3, we can prove that the terms $P_{1,III}$, $P_{4,III}$, $P_{7,III}$, and $P_{10,III}$ are increasing functions of β. Further, since Φ_{00} and Φ_{11} are independent of β, $P_+ = \Phi_{00}(P_{1,III} + P_{4,III}) + \Phi_{11}(P_{7,III} + P_{10,III})$ is an increasing function of β.

Further, the expressions of $P^\star_{2,III}$, $P^\star_{5,III}$, $P^\star_{8,III}$, and $P^\star_{11,III}$ are such that, $P^\star_{2,III} = P^\star_{8,III} = \frac{2N_o}{4N_o + d^2_{\text{III}}}$ and $P^\star_{5,III} = P^\star_{11,III} = \frac{2N_{o\beta}}{4N_{o\beta} + d^2_{\text{III}}}$. Differentiating $P^\star_{2,III}$ w.r.t. β we get, $-\frac{2N_o}{(4N_o + d^2_{\text{III}})^2} \sin^2 \frac{\pi}{2M}$. Therefore, $P^\star_{2,III}$ and $P^\star_{8,III}$ are decreasing functions of β. Along similar lines, we can prove that $P^\star_{5,III}$ and $P^\star_{11,III}$ are decreasing functions of β. Thus, we have $P_- = \Phi_{00}\left(P^\star_{2,III} + P^\star_{5,III}\right) + \Phi_{11}\left(P^\star_{8,III} + P^\star_{11,III}\right)$. $\square$

Theorem 16. *For a fixed α and N_C, P_+ and P_- intersect only once for $\beta \in (0,1)$.*

Proof. To prove that the increasing and decreasing terms of $\mathcal{P}_{III}$ intersect only once for $\beta \in (0,1)$, we show that the order of these terms reverses at $\beta \to 0$ and $\beta \to 1$. From Table 5.2, we have, $P_{1,III} = P_{7,III} = e^{-\frac{\varrho}{N_o}}$ and $P_{4,III} = P_{10,III} = 1 - e^{-\frac{\varrho}{N_{o\beta}}}$. Therefore, $\lim_{\beta \to 0} P_+ = 2\Phi_{00} N_o + 2\Phi_{11}\left(1 - N_o^{N_o}\right)$ and $\lim_{\beta \to 1} P_+ = 2\Phi_{00} e^{-1} + 2\Phi_{11}\left(1 - e^{-1}\right)$.

Similarly, $P^\star_{2,III} = P^\star_{8,III} = \frac{2N_o}{4N_o + d^2_{\text{III}}}$, $P^\star_{5,III} = P^\star_{11,III} = \frac{2N_{o\beta}}{4N_{o\beta} + d^2_{\text{III}}}$. Evaluating $P^\star_{2,III}$, $P^\star_{8,III}$, $P^\star_{5,III}$, and $P^\star_{11,III}$ at extreme values of β, we get, $\lim_{\beta \to 0} P_- = \Phi_{00} + \Phi_{11}$ and $\lim_{\beta \to 1} P_- = (\Phi_{00} + \Phi_{11}) \frac{N_o}{N_o + \sin^2 \frac{\pi}{2M}}$. From the above discussion it is straightforward that, $\lim_{\beta \to 0} P_- > \lim_{\beta \to 0} P_+$ and $\lim_{\beta \to 1} P_- < \lim_{\beta \to 1} P_+$. Thus, P_+ and P_- reverse their order at extreme values of β. Finally, from the results of Lemma 14, we know that P_+ and P_- are increasing and decreasing functions of β, respectively. Thus, we conclude that the increasing and decreasing functions of $\mathcal{P}_{III}$ intersect at a unique point. $\square$

Remark 5. *The unique intersection of P_+ and P_- can be computed using the Newton-Raphson (NR) algorithm.*

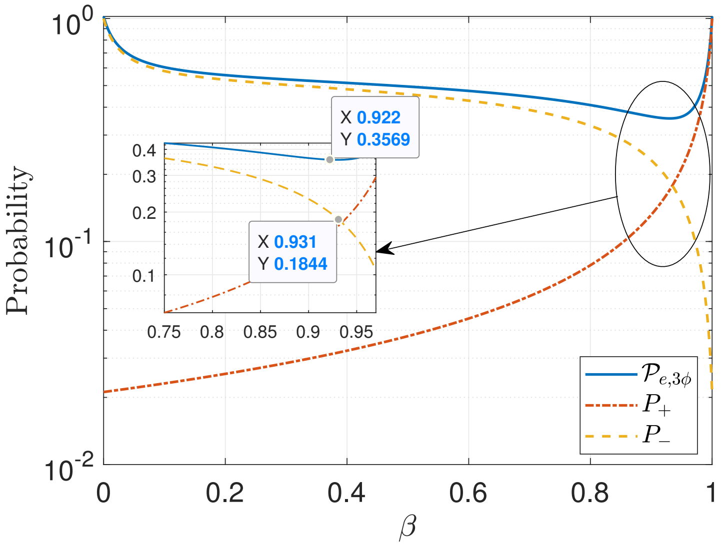

Figure 5.8: Variation of $\mathcal{P}_{e,3\phi}$ and its increasing and decreasing terms as a function of β at 25 dB.

Using the insights of Lemma 14 and Theorem 16, we now present a low-complexity algorithm in Algorithm 3, referred to as the N_C-β Optimization algorithm, which provides a local minima of $\mathcal{P}_{e,3\phi}$ over the variables, N_C and β.

We start the algorithm with $N_C = 1$, an initial estimate of $\mathcal{P}_{e,3\phi}$, denoted by P_o, and an initial estimate of the intersection of P_+ and P_-, denoted by β_o. We use the NR algorithm to compute the intersection of P_+ and P_- as β_{int} and evaluate P_{eval} by substituting N_C and β_{int} in $\mathcal{P}_{e,3\phi}$. We iteratively compute β_{int} by incrementing N_C in steps of 1 until the absolute value of the difference between P_{eval} and P_o is less than the tolerance value, δ_{tol}. When $|P_o - P_{eval}| < \delta_{tol}$, we exit the while-loop with the near-optimal values of N_C and β, denoted by $N_C^\dagger$ and $\beta^\dagger$, respectively.

In the next section, we present the simulation results showing the efficacy of the proposed scheme for various models on Θ.

5.4.5 Simulation Results for 3ϕ DASC-MF Relaying Scheme

For all simulation purposes, we assume $\Delta = 0.1$, $L = 200$, and $\sigma_{AB}^2 = \sigma_{CB}^2 = 1$. Further, we also assume $\sigma_{AC}^2 = 4$, thus providing 6 dB improvement in SNR on Alice-to-Charlie link as compared to Alice-to-Bob link of the MAC. Using these parameters, we use the N_C-β Optimization algorithm to obtain $N_C^\dagger$ and $\beta^\dagger$ at various SNRs. To generate the simulation results, we have used four delay models, i.e., $\Theta = \lceil 10 \log N_C^\dagger \rceil$,

Algorithm 3. N_C-β Optimization

```
Input: $\mathcal{P}_{e,3\phi}$, $P_+$, $P_-$, $\triangle$, $SNR$, $\delta_{tol}$
Outpuut: $N_C^\dagger$, $\beta^\dagger$
$\beta \leftarrow \beta_o$;
$N_C \leftarrow 1$;
$P_o = 0.5$;
while true do
    Use NR algorithm to compute intersection of $P_+$ and $P_-$, denoted by $\beta_{int}$;
    Substitute $\beta_{int}$ in $\mathcal{P}_{e,3\phi}$ and compute $P_{eval}$;
    if $|P_o - P_{eval}| > \delta_{tol}$ then
        $N_C \leftarrow N_C + 1$;
        $\beta_o \leftarrow \beta_{int}$;
        $P_o \leftarrow P_{eval}$
    else
        $N_C^\dagger = N_C$;
        $\beta^\dagger = \beta_{int}$
    end
end
```

Table 5.3: VALUES OF EXACT AND APPROXIMATE (N_C, β) FOR VARIOUS Θ

$\downarrow \Theta \setminus$ SNR $\rightarrow$	21 dB		25 dB		29 dB	
	$(N_C^\dagger, \beta^\dagger)_{Exact}$	$(N_C^\dagger, \beta^\dagger)_{Int}$	$(N_C^\dagger, \beta^\dagger)_{Exact}$	$(N_C^\dagger, \beta^\dagger)_{Int}$	$(N_C^\dagger, \beta^\dagger)_{Exact}$	$(N_C^\dagger, \beta^\dagger)_{Int}$
$\lceil 10 \log_{10} N_C \rceil$	(125,0.8730)	(125, 0.9020)	(127,0.9220)	(127,0.9310)	(129, 0.9580)	(129, 0.9570)
$\lceil \log_2 N_C \rceil$	(126,0.8730)	(126, 0.9020)	(128,0.9220)	(128,0.9310)	(130, 0.9580)	(130, 0.9570)
$\lceil \sqrt{N_C} \rceil$	(122,0.8730)	(122, 0.9020)	(127,0.9220)	(127,0.9310)	(129, 0.9580)	(129, 0.9570)

$\Theta = \lceil \log_2 N_C^\dagger \rceil$, $\Theta = \lceil \sqrt{N_C^\dagger} \rceil$, and $\Theta = \lceil \frac{L}{2} \rceil$. Since, Θ is a function of the FD architecture of Charlie, similar results can be generated for any model on Θ, as long as, $\Theta \leq \frac{L}{2}$.

Using the above parameters, we exhaustively compute the pair (N_C, β), that minimizes $\mathcal{P}_{e,3\phi}$ and denote the pair as $(N_C^\dagger, \beta^\dagger)_{Exact}$. Here, we start with $N_C = 1$ and increment it in the steps of 1 whereas, the resolution of β is 10^{-3}. We then tabulate $(N_C^\dagger, \beta^\dagger)_{Exact}$ in Table 5.3 for various combinations of Θ and SNR. For the same Θ and SNR, we also tabulate the pair (N_C, β) obtained by N_C-β Optimization algorithm and denote the pair by $(N_C^\dagger, \beta^\dagger)_{Int}$, and observe that while the obtained values of N_C for both the cases are exactly identical, the values of β are close. Further, in Fig. 5.9, for $M = 4$, we plot the joint error performance at Bob when using the 3ϕ DASC-MF scheme, for various models on Θ, as a function of SNR. It is evident from the plots that the error performance of 3ϕ DASC-MF scheme improves as a function of SNR. Further, we also note that amongst the four models, the error performance is best when

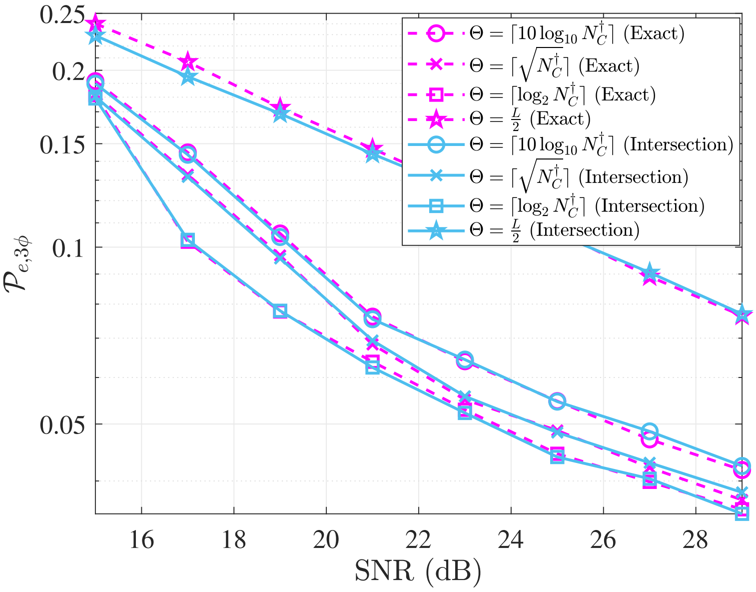

Figure 5.9: Joint error-performance when using 3ϕ DASC-MF.

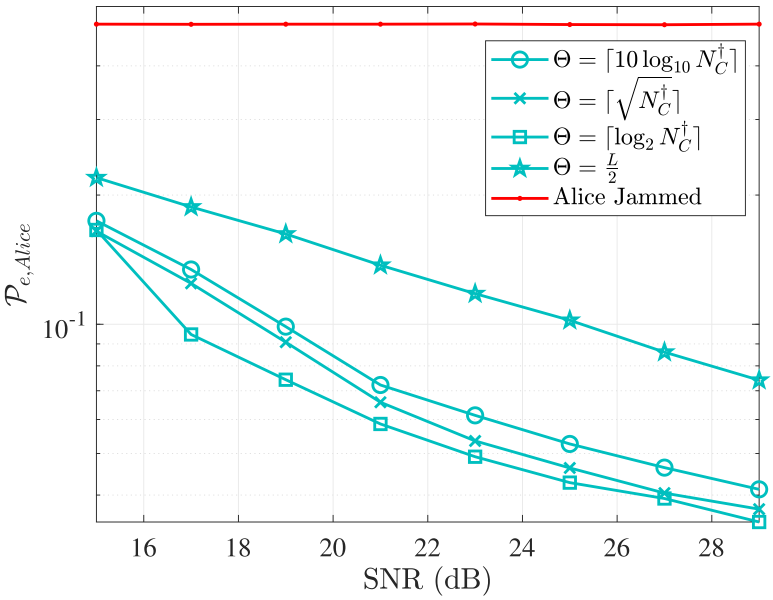

Figure 5.10: Improvement in Alice's performance when using 3ϕ DASC-MF.

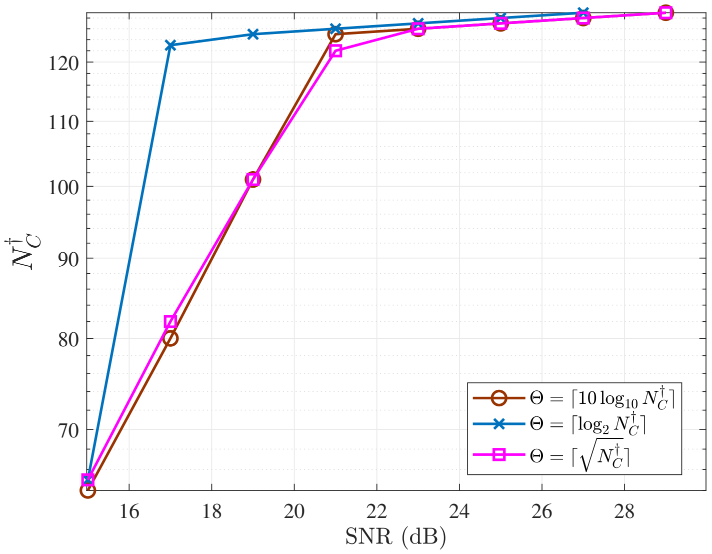

Figure 5.11: Optimal N_C versus SNR for Phase-III of 3ϕ DASC-MF.

$\Theta = \lceil \log_2 N_C^\dagger \rceil$ as $\frac{\Theta}{L}$ is minimum when $\Theta = \lceil \log_2 N_C^\dagger \rceil$, thereby reducing the fraction of symbols decoded during Phase-III. Further, in Fig. 5.10, we also plot the improvement in Alice's error performance before the jamming attack and after implementing 3ϕ DASC-MF scheme, and observe that when she uses 3ϕ DASC-MF scheme, she is able to reliably communicate her symbols to Bob within the deadline of T seconds. Finally, in Fig. 5.11, we plot $N_C^\dagger$ as a function of SNR and notice that $N_C^\dagger$ increases with SNR. This is due to the fact that, although we have upper bounded the interference from Alice on Alice-to-Bob link of the MAC by ΔN_o, Charlie uses the same energy, ΔN_o to decode Alice's symbols. Therefore, as SNR increases, N_o decreases, and Charlie requires more receive-antennas to faithfully decode Alice's symbols.

5.5 Semi-Coherent Multiple Access Channel Scheme

A major limitation of the 3ϕ DASC-MF scheme proposed in the previous section is that when $\Theta > \frac{L}{2}$, only a fraction of Alice's symbols can be recovered using the multiplexed symbols within the deadline and a majority of the multiplexed symbols are received at Bob after the deadline, resulting in violation of the latency constraint. As a result, when $\Theta > \frac{L}{2}$, Alice and Charlie must resort to uncoordinated multiple access communication, wherein Alice and Charlie transmit their symbols using $1-\varepsilon$ and ε fractions of their energies, respectively, on f_{CB} over the MAC, where $\varepsilon \in (0,1)$ is the design parameter under consideration. Here, Charlie does not decode Alice's symbol and only transmits his $M-$PSK symbols. Subsequently, Bob uses the received symbols to jointly decode Alice's and Charlie's symbols. A major distinction between the 3ϕ DASC-MF scheme and SC-MAC is that due to no knowledge of Alice's symbols, Charlie always scales his constellation by energy ε. This phenomenon is similar to Phase-III 3ϕ DASC-MF scheme. Furthermore, since the Alice-to-Bob link of the MAC is non-coherent and Charlie-to-Bob link of the MAC is coherent, we refer to this scheme as the Semi-Coherent Multiple Access Channel (SC-MAC). Subsequently, similar to the 3ϕ DASC-MF scheme, Alice and Charlie transmit dummy OOK symbols from a Gold-sequence based scrambler with ε and $1-\varepsilon$ fractions of their energies, respectively, on f_{AB} to evade the ED.

5.5.1 Error Analysis of SC-MAC

If $x_n \in \{0,1\}$ and $y_n \in \mathcal{S}_C$ denote the OOK and $M-$PSK symbols of Alice and Charlie, respectively, then the received symbol at Bob, assuming symbol level synchronization, is given by

$$r_{B,n} = \sqrt{1-\varepsilon} h_{AB,n} x_n + \sqrt{\varepsilon} h_{CB,n} y_n + w_{B,n}, \quad 1 \leq n \leq L, \tag{5.25}$$

where $h_{AB,n}$, $h_{CB,n}$, and $w_{B,n}$ are as defined in previous sections. Unlike 3ϕ DASC-MF, $r_{B,n}$ in SC-MAC are independent across time, therefore, we drop the subscript n from the variables during the error analysis of SC-MAC. Owing to the non-coherent nature of Alice-to-Bob link of the MAC and coherent nature of the Charlie-to-Bob link of the MAC, and the Gaussian statistics of the channels and the noise, the distribution of r_B conditioned on x and y as $r_B|_{x,y,h_{CB}} \sim \mathcal{CN}\left(\sqrt{\varepsilon} h_{CB} y, N_o\right)$, if $x = 0$ and $r_B|_{x,y,h_{CB}} \sim \mathcal{CN}\left(\sqrt{\varepsilon} h_{CB} y, N_{o\varepsilon}\right)$, if $x = 1$. Using the distribution of r_B, the joint MAP decoder for SC-MAC is

$$\hat{i}, \hat{m} = \arg\max_{i,m} g_{MAC}\left(r_B | x = i, y = e^{\iota \frac{\pi}{M}(2m+1)}, h_{CB}\right), \tag{5.26}$$

where $i \in \{0,1\}$ and $m \in \{0,\ldots,M-1\}$ and g_{MAC} is the PDF of r_B conditioned on x, y, and h_{CB}. If Alice and Charlie transmit OOK and $M-$PSK, then a transmitted pair is denoted by (i,m). Fig. 5.12 depicts the constellation diagram at Bob jointly contributed by Alice and Charlie when using SC-MAC scheme with $M = 4$. When

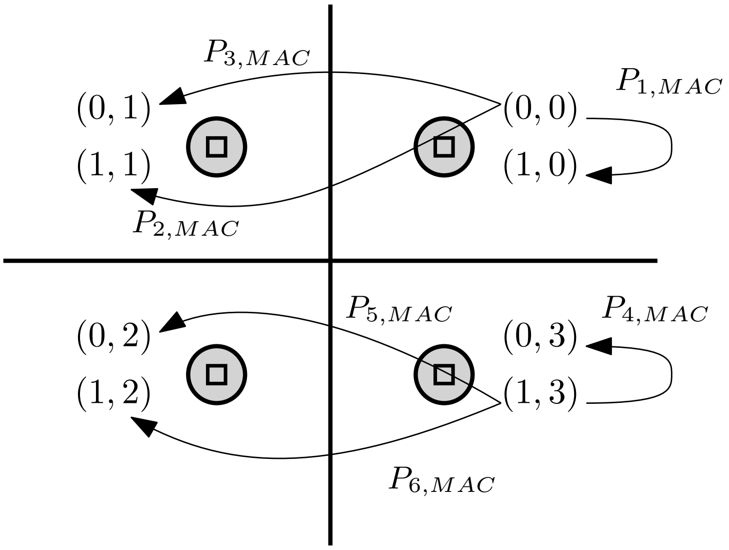

Figure 5.12: Constellation diagram jointly contributed by Alice and Charlie when using SC-MAC.

$x_n = 1$ and $x_n = 0$, the effective variance of the noise at Bob is $N_o + 1 - \varepsilon$ and N_o, respectively. The *square box* denotes the symbols with variance N_o and *circular disks* represent the symbols with variance $N_{o\varepsilon} = N_o + 1 - \varepsilon$. In the next section, we discuss the error analysis of the SC-MAC scheme.

Table 5.4: ERROR TERMS FOR SC-MAC AS GIVEN IN THEOREM 17

$P_{1,MAC} = \quad 1 - e^{\frac{-\psi}{N_o}}$	$P_{2,MAC} = \quad Q_1\left(\frac{\lvert C\rvert}{\sqrt{N_o/2}}, \frac{\sqrt{\eta}}{\sqrt{N_o/2}}\right)$	$P_{3,MAC} = \quad Q\left(\frac{\lvert h_{CB,n}\rvert d}{\sqrt{2N_o}}\right)$
$P_{4,MAC} = \quad e^{\frac{-\psi}{N_{o\varepsilon}}}$	$P_{5,MAC} = \quad 1 - Q_1\left(\frac{\lvert D\rvert}{\sqrt{N_{o\varepsilon}/2}}, \frac{\sqrt{\eta}}{\sqrt{N_{o\varepsilon}/2}}\right)$	$P_{6,MAC} = \quad Q\left(\frac{\lvert h_{CB,n}\rvert d}{\sqrt{2N_{o\varepsilon}}}\right)$

Theorem 17. *At high SNR, a union bound on probability of error for SC-MAC is approximated as*

$$\frac{1}{2}\left(P_{1,MAC} + 2P_{2,MAC} + 2P_{3,MAC} + P_{4,MAC} + 2P_{5,MAC} + 2P_{6,MAC}\right), \quad (5.27)$$

where the various error terms in (5.27) *are tabulated in Table 5.4. Further,* $\psi = \frac{N_o N_{o\varepsilon}}{N_o - N_{o\varepsilon}} \ln\left(\frac{N_o}{N_{o\varepsilon}}\right)$, $C = \frac{|h_{CB,n}| d N_o}{N_o - N_{o,\varepsilon}}$, $D = \frac{|h_{CB,n}| d N_{o\varepsilon}}{N_o - N_{o,\varepsilon}}$, *and* $\eta = \frac{N_o N_{o\varepsilon}}{N_o - N_{o\varepsilon}}\left[\ln\left(\frac{N_o}{N_{o\varepsilon}}\right) + \frac{|h_{CB,n}|^2 d^2}{N_o - N_{o\varepsilon}}\right]$ *are the parameters of the Marcum-Q function, where,* $\mathrm{d} = 2\sqrt{\varepsilon}\sin\frac{\pi}{M}$ *denotes the minimum Euclidean distance between the constellation points received at Bob.*

Proof. Let a pair corresponding to the symbols x and y be denoted by (i,m). Let $\nabla_{(i,m)\rightarrow(i',m')}$ be the event $(i,m) \neq (i',m')$, then a transmitted pair (i,m) is incorrectly decoded as (i', m') if

$$\nabla_{(i,m)\rightarrow(i',m')} \triangleq \frac{g_{MAC}\left(r_B | x = i, y = e^{\iota \frac{\pi}{M}(2m+1)}, h_{CB}\right)}{g_{MAC}\left(r_B | x = i', y = e^{\iota \frac{\pi}{M}(2m'+1)}, h_{CB}\right)} \leq 1. \tag{5.28}$$

Therefore, the probability of decoding a transmitted pair (i, m) as (i', m') is given as $\Pr((i, m) \rightarrow (i', m')) = \Pr\left(\nabla_{(i,m)\rightarrow(i',m')} \leq 1\right)$. If $\Pr\left((\hat{i}, \hat{m}) \neq (i, m)\right)$ denotes the overall probability of error in decoding a transmit pair (i, m), then $\Pr\left((\hat{i}, \hat{m}) \neq (i, m)\right)$ is upper bounded as

$$\Pr\left((\hat{i}, \hat{m}) \neq (i, m)\right) \leq \sum_{\substack{i'=0 \\ (i,m)\neq(i',m')}}^{1} \sum_{m'=0}^{M-1} \Pr\left(\nabla_{(i,m)\rightarrow(i',m')}\right), \tag{5.29}$$

where $(\hat{i}, \hat{m})$ is the decoded pair at Bob, corresponding to the transmitted pair (i, m). Note that Bob receives $2M-$PSK symbols corresponding to $M-$PSK used by Charlie, where M symbols out of the $2M$ symbols are received with variance N_o. Subsequently, the rest of the M symbols are received with variance $N_o + 1 - \varepsilon$. Thus, if $P_{e,MAC}$ denotes the overall probability of error for $2M$ symbols, then $P_{e,MAC}$ is upper bounded as $P_{e,MAC} \leq \frac{1}{2M}\sum_{i=0}^{1}\sum_{m=0}^{M-1} M \Pr((\hat{i}, \hat{m}) \neq (i, m))$. Finally, considering the nearest-neighbours at high SNR, $P_{e,MAC}$ is approximated as (5.27), where the various error terms in (5.27) are tabulated in Table 5.4. Furthermore, these terms are also depicted in Fig. 5.12 for $4-$PSK used by Charlie. □

Corollary 3. *Using the results of Lemma 13, we upper bound* $P_{2,MAC}$ *and* $P_{3,MAC}$ *as* $2P_{2,MAC} \leq P_{1,MAC}$ *and* $2P_{3,MAC} \leq P_{4,MAC}$*. Further, using the Chernoff bound on the Q-functions and averaging* $P_{e,MAC}$ *over the realisations of* h_{CB}*, we get* $\mathbb{E}_{h_{CB}}[P_{e,MAC}] \leq \mathcal{P}_{MAC} \triangleq P_{1,MAC} + P^{\star}_{3,MAC} + P_{4,MAC} + P^{\star}_{6,MAC}$*, where* $P^{\star}_{3,MAC} = \frac{2N_o}{4N_o + d^2}$ *and* $P^{\star}_{6,MAC} = \frac{2N_{o\varepsilon}}{4N_{o\varepsilon} + d^2}$.

While observing (5.25), we notice that when $\varepsilon \rightarrow 1$, Alice's symbols are transmitted with lower energy, whereas Charlie transmits his symbols with higher energy. However, when $\varepsilon \rightarrow 0$, Alice's symbols are transmitted with higher energy as compared to Charlie. Thus, in the extreme range, the joint error-rates at Bob are expected to be high and therefore, Alice and Charlie must use a value of ε that minimizes the error-rates at Bob. Towards minimizing $\mathcal{P}_{MAC}$ at Bob, we pose an optimization problem as given below.

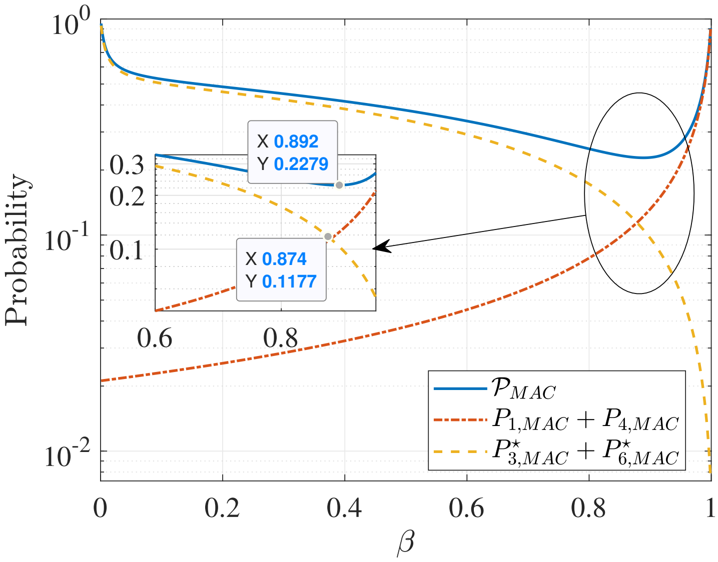

Figure 5.13: Variation of $\mathcal{P}_{MAC}$ and its increasing and decreasing terms as a function of ε at 25 dB.

$$\boxed{\varepsilon^{\dagger} = \arg\min_{\varepsilon} \quad \mathcal{P}_{MAC}; \quad \text{s.t.: } 0 < \varepsilon < 1. \qquad (5.30)}$$

Towards minimizing $\mathcal{P}_{MAC}$, we note that, it is straightforward to prove that $\mathcal{P}_{MAC}$ is a sum of increasing and decreasing terms w.r.t. ε. In particular, using the results of Lemma 14, we notice that $P_{1,MAC} + P_{4,MAC}$ is an increasing function of ε and $P^{\star}_{3,MAC} + P^{\star}_{6,MAC}$ is a decreasing function of ε and the intersection of the increasing and decreasing terms is close to the unique minima of $\mathcal{P}_{MAC}$. This observation is exemplified in Fig. 5.13 at SNR = 25 dB. Along the similar lines of Theorem 16, it is straightforward to prove that, $P_{1,MAC} + P_{4,MAC}$ and $P^{\star}_{3,MAC} + P^{\star}_{6,MAC}$ intersect at a unique value of $\varepsilon \in (0, 1)$. Therefore, the unique intersection of $P_{1,MAC} + P_{4,MAC}$ and $P^{\star}_{3,MAC} + P^{\star}_{6,MAC}$ can be computed using the NR algorithm. This near-optimal value of ε that minimizes $\mathcal{P}_{MAC}$ is denoted by $\varepsilon^{\dagger}$. In Table 5.5, we tabulate the optimal values of ε obtained by using an exhaustive search (ε_{Exact}) and by using the intersection method ($\varepsilon^{\dagger}$) for various values of SNR. Here, the resolution for the exhaustive search is 10^{-3}. It is clear from the table that ε_{Exact} is close to $\varepsilon^{\dagger}$. In the next section, we present Monte-Carlo simulations for SC-MAC scheme and showcase its error performance.

Table 5.5: EXACT AND APPROXIMATE VALUES OF ε

$\downarrow \varepsilon \setminus \underset{\rightarrow}{SNR}$	19 dB	21 dB	25 dB	29 dB
ε_{Exact}	0.8080	0.8700	0.8920	0.9250
$\varepsilon^{\dagger}$	0.7820	0.8510	0.8740	0.9190

5.5.2 Simulation Results for SC-MAC

For all simulation purposes, we use the same simulation parameters as given in Sec. 5.4.5. Assuming Charlie uses $4-$PSK constellation, in Fig. 5.14, we plot the joint error performance of Alice and Charlie, when using SC-MAC scheme, as a function of SNR. Through this plot, we show that the error performance of SC-MAC improves as a function of SNR. Further, we also compare the error performance of SC-MAC with 3ϕ DASC-MF scheme when $\Theta = 10 \log N_C^{\dagger}$ and $\Theta = \log_2 N_C^{\dagger}$, and note that SC-MAC is sub-optimal for the assumed models on Θ of 3ϕ DASC-MF. This is because, throughout 3ϕ DASC-MF scheme, Bob decodes a majority of Alice's symbols using the coherent Charlie-to-Bob link of the MAC, whereas, in SC-MAC, Bob decodes all Alice's symbols using the non-coherent Alice-to-Bob link of the MAC. Thus, unlike SC-MAC, Alice's symbols are decoded more reliably in 3ϕ DASC-MF scheme. We observe the same pattern when we plot Alice's individual performance as a function of SNR in Fig. 5.15. Overall, it is clear from the plots that SC-MAC helps Alice to evade the jamming attack from Dave within the latency constraint, however, it is sub-optimal as compared to 3ϕ DASC-MF scheme. Nevertheless, it is a still a good option when $\Theta > \frac{L}{2}$.

5.6 Covertness Analysis

As discussed in Sec. 5.2, Dave uses an ED to detect the changes in the average energy level on all the frequencies in the network after the jamming attack. Since Alice and Charlie use f_{AB} and f_{CB} to execute the countermeasures, we restrict our analysis to these frequencies only. Thus, in the context of this chapter, we refer to a mitigation scheme as covert if Dave is unable to detect changes in the average energy levels of f_{AB} and f_{CB}. Further, throughout this section, we assume that Dave has the knowledge of the channel statistics of Alice-to-Dave link and Charlie-to-Dave link, but no knowledge of the channel coefficients of these links.

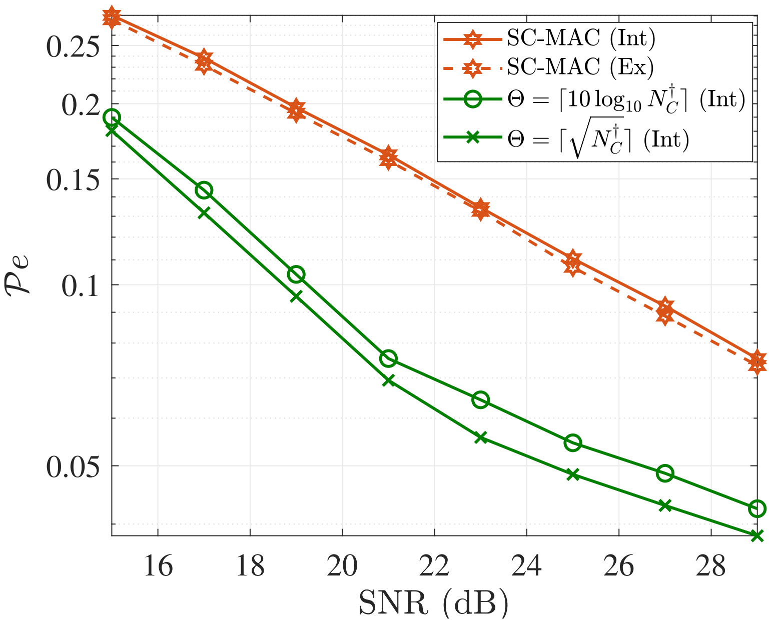

Figure 5.14: Joint error performance of SC-MAC scheme.

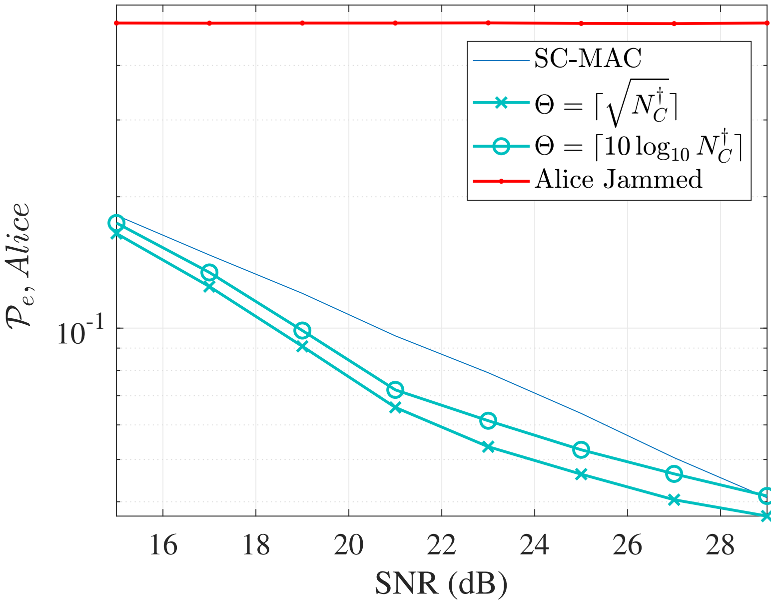

Figure 5.15: Improvement in Alice's performance when using SC-MAC.

5.6.1 Covertness Analysis for ED when using 3ϕ DASC-MF Relaying Scheme

In this section, we first discuss energy detection at Dave on f_{AB} and f_{CB} when using 3ϕ DASC-MF and then, compute probability of false-alarms and probability of miss-detections on f_{AB} and f_{CB}. Before executing the jamming attack, Dave collects a frame of L symbols on f_{AB} and f_{CB} and computes their average energy. The n^{th} symbol received at Dave, before the jamming attack on f_{AB} and f_{CB} are respectively given as

$$r_{D,AB,n} = h_{AD,n}x_n + w_{D,AB,n}, \quad 1 \leq n \leq L, \tag{5.31}$$

$$r_{D,CB,n} = h_{CD,n}y_n + w_{D,CB,n}, \quad 1 \leq n \leq L, \tag{5.32}$$

where $h_{AD,n} \sim \mathcal{CN}(0,1)$ and $h_{CD,n} \sim \mathcal{CN}(0,1+\partial)$ are the n^{th} channel coefficients of Alice-to-Dave link and Charlie-to-Dave link, respectively, such that, ∂ captures the relative difference in the variance of Alice-to-Dave link and Charlie-to-Dave link. Further, $w_{D,AB,n} \sim \mathcal{CN}(0,\tilde{N}_o)$ is the effective AWGN at Dave on f_{AB}, such that, $\tilde{N}_o = N_o + \sigma_{DD}^2$, where σ_{DD}^2 is the variance of the residual SI at Dave and N_o is the variance of the AWGN at Dave. Furthermore, $w_{D,CB,n} \sim \mathcal{CN}(0,N_o)$ is the AWGN at Dave on f_{CB}. Since $r_{D,AB,n}$ and $r_{D,CB,n}$ are statistically independent over n, using weak law of large numbers, $\frac{1}{L}\sum_{n=1}^{L}|r_{D,AB,n}|^2 \rightarrow \mathcal{E}_{AB}$ and $\frac{1}{L}\sum_{n=1}^{L}|r_{D,CB,n}|^2 \rightarrow \mathcal{E}_{CB}$, in probability, such that $\mathcal{E}_{AB} = \tilde{N}_o + 0.5$ and $\mathcal{E}_{CB} = N_o + 1 + \partial$. However, due to short packet length, the measured average energies on f_{AB} and f_{CB} are not equal to $\mathcal{E}_{AB}$ and $\mathcal{E}_{CB}$. Therefore, if $\mathcal{H}_0$ denotes the hypothesis that no countermeasure is implemented, then, probability of false-alarms on f_{AB} and f_{CB} are defined as follows.

Definition 5. *The probability of false-alarm on* f_{AB}*, denoted by,* $\mathbf{P}_{FA,AB}$ *is given as* $\mathbf{P}_{FA,AB} = \Pr\left(|\mathcal{U}_{L,AB} - \mathcal{E}_{AB}| \geq \nu_{AB}|\mathcal{H}_0\, true\right)$*, where,* $\mathcal{U}_{L,AB}$ *denotes the random variable (RV) corresponding to the average energy of L symbols received at Dave on* f_{AB} *and* $\nu_{AB} > 0$ *is a parameter of Dave's choice.*

Definition 6. *The probability of false-alarm on* f_{CB}*, denoted by,* $\mathbf{P}_{FA,CB}$ *is given as* $\mathbf{P}_{FA,CB} = \Pr\left(|\mathcal{U}_{L,CB} - \mathcal{E}_{CB}| \geq \nu_{CB}|\mathcal{H}_0\, true\right)$*, for* $\nu_{CB} > 0$*, where,* $\mathcal{U}_{L,CB}$ *denotes the RV corresponding to the average energy of L symbols received at Dave on* f_{CB} *and* ν_{CB} *is a parameter of Dave's choice.*

When $\tilde{N}_o \ll 1$, the distribution of $\mathcal{U}_{L,AB}$ is approximated as $\frac{1}{2^L}\sum_{l=0}^{L}\binom{L}{l}\mathrm{G}\left(l, \frac{1}{L}\right)$, where $\mathrm{G}(\cdot,\cdot)$ denotes the Gamma distribution [40, Theorem 5]. Along the similar lines, when $N_o \ll 1$, the distribution of $\mathcal{U}_{L,CB}$ can be approximated as $\frac{1}{2^L}\sum_{l=0}^{L}\binom{L}{l}\mathrm{G}\left(l, \frac{1+\partial}{L}\right)$. Thus, the expressions of $\mathbf{P}_{FA,AB}$ and $\mathbf{P}_{FA,CB}$ when $\tilde{N}_o \ll 1$ and $N_o \ll 1$, respectively, are approximated as

$$\mathbf{P}_{FA,AB} \approx \frac{1}{2^L}\left[\sum_{l=0}^{L}\binom{L}{l}\frac{\gamma\left(l, L\left(\mathcal{E}_{AB}-\nu_{AB}\right)\right)}{\Gamma(l)} + \frac{\Gamma\left(l, L\left(\mathcal{E}_{AB}+\nu_{AB}\right)\right)}{\Gamma(l)}\right], \tag{5.33}$$

$$\mathbf{P}_{FA,CB} \approx \frac{1}{2^L}\left[\sum_{l=0}^{L}\binom{L}{l}\frac{\gamma\left(l, \frac{L}{1+\partial}\left(\mathcal{E}_{CB}-\nu_{CB}\right)\right)}{\Gamma(l)} + \frac{\Gamma\left(l, \frac{L}{1+\partial}\left(\mathcal{E}_{CB}+\nu_{CB}\right)\right)}{\Gamma(l)}\right], \tag{5.34}$$

where ν_{AB} and ν_{CB} are decided by Dave. However, small values of ν_{AB} and ν_{CB} often result in high false-alarms, and large values of ν_{AB} and ν_{CB} result in high miss-detection. Thus, the values of ν_{AB} and ν_{CB} must be cautiously chosen by Dave so as to minimize both probability of false-alarm and probability of miss-detection. In the rest of the section, we discuss the probability of miss-detection on f_{AB} and f_{CB}, when using 3ϕ DASC-MF scheme for a given choice of ν_{AB} and ν_{CB}. Towards computing the probability of miss-detection, we first present the symbols observed at Dave on f_{AB} and then characterise the probability of miss-detection on f_{AB}. Along the similar lines, we will then characterise the probability of miss-detection on f_{CB}. We recall that Alice and Charlie use OOK symbols from a pre-shared Gold-sequence to cooperatively pour their residual energies on f_{AB}. Therefore, if $b_n \in \{0,1\}$ denotes the n^{th} OOK bit jointly transmitted by Alice and Charlie, and $r^{\dagger}_{D,AB,n}$ denotes the n^{th} baseband symbol received at Dave, then

$$r^{\dagger}_{D,AB,n} = \begin{cases} \sqrt{\alpha}h_{AD,n}b_n + \sqrt{1-\alpha}h_{CD,n}b_n + w_{D,AB,n}, \text{if } 1 \leq n \leq L-\Theta, & \text{(5.35a)} \\ \sqrt{\beta^{\dagger}}h_{AD,n}b_n + \sqrt{1-\beta^{\dagger}}h_{CD,n}b_n + w_{D,AB,n}, \text{if } L-\Theta+1 \leq n \leq L. & \text{(5.35b)} \end{cases}$$

Let $\mathcal{H}_1$ denote the hypothesis that a countermeasure is implemented, then, formally, the probability of miss-detection at Dave on f_{AB} is given as follows.

Definition 7. *Let $\mathcal{V}_{L,AB}$ denote the RV corresponding to the average energy of L symbols on f_{AB} after using 3ϕ DASC-MF scheme. Thus, probability of miss-detection denoted by, $\mathbf{P}^{3\phi}_{MD,AB}$, is $\mathbf{P}^{3\phi}_{MD,AB} = \Pr\left(|\mathcal{V}_{L,AB} - \mathcal{E}_{AB}| \leq \nu_{AB} | \mathcal{H}_1 \text{ true}\right)$, for $\nu_{AB} > 0$.*

Using (5.35a) and (5.35b), we will now characterize $\mathbf{P}^{3\phi}_{MD,AB}$. Let $v_{n_1,AB}$ denote the RV corresponding to $|r^{\dagger}_{D,AB,n_1}|^2$, such that $1 \leq n_1 \leq L-\Theta$ and $v_{n_2,AB}$ denote the RV corresponding to $|r^{\dagger}_{D,AB,n_2}|^2$, such that $L-\Theta+1 \leq n_2 \leq L$. Thus, $\mathcal{V}_{L,AB} = \mathcal{V}_{L_1,AB} + \mathcal{V}_{L_2,AB}$, such that $\mathcal{V}_{L_1,AB} = \frac{1}{L}\sum_{n_1=1}^{L-\Theta} \upsilon_{n_1,AB}$ and $\mathcal{V}_{L_2,AB} = \frac{1}{L}\sum_{n_2=L-\Theta+1}^{L} \upsilon_{n_2,AB}$. In the next lemma, we compute the PDF of $\mathcal{V}_{L_1,AB}$ and $\mathcal{V}_{L_2,AB}$.

Lemma 15. *At high SNR, such that $\tilde{N}_o \ll 1$, the distribution of $\mathcal{V}_{L_1,AB}$ is approximated as $\frac{1}{2^{L-\Theta}}\sum_{l=0}^{L-\Theta}\binom{L-\Theta}{l}\mathrm{G}\left(l, \frac{\mathcal{A}}{L}\right)$, where $\mathcal{A} = \alpha+(1-\alpha)(1+\partial)$. Similarly, the distribution of $\mathcal{V}_{L_2,AB}$ is approximated as $\frac{1}{2^{\Theta}}\sum_{l=0}^{\Theta}\binom{\Theta}{l}\mathrm{G}\left(l, \frac{\mathcal{B}}{L}\right)$, where $\mathcal{B} = \beta^{\dagger} + (1-\beta^{\dagger})(1+\partial)$.*

Finally, $\frac{1}{2^{L-\Theta}}\sum_{l=0}^{L-\Theta}\binom{L-\Theta}{l}\mathrm{G}\left(l, \frac{\mathcal{A}}{L}\right) * \frac{1}{2^{\Theta}}\sum_{l=0}^{\Theta}\binom{\Theta}{l}\mathrm{G}\left(l, \frac{\mathcal{B}}{L}\right)$ gives the distribution of $\mathcal{V}_{L,AB}$, where $*$ denotes linear convolution. Using the distribution of $\mathcal{V}_{L,AB}$, it is straightforward to compute $\mathbf{P}^{3\phi}_{MD,AB}$.

Remark 6. *If $\partial = 0$, then $\mathbf{P}_{FA,AB} + \mathbf{P}^{3\phi}_{MD,AB} = 1$ for all $\nu_{AB} > 0$.*

Although, Remark 6 theoretically guarantees that $\mathbf{P}_{FA,AB} + \mathbf{P}^{3\phi}_{MD,AB} = 1$, in Sec. 5.6.3, through Monte-Carlo simulations, we show that, $\mathbf{P}_{FA,AB} + \mathbf{P}^{3\phi}_{MD,AB}$ is close to 1 for various values of ∂.

We now compute the probability of miss-detection on f_{CB}, denoted by, $\mathbf{P}^{3\phi}_{MD,CB}$. Towards computing $\mathbf{P}^{3\phi}_{MD,CB}$, we first observe the symbol received at Dave on f_{CB}, denoted by $r^{\dagger}_{D,CB,n}$ and then characterise its PDF. Thus, the n^{th} baseband symbol received at Dave on f_{CB} is given as

$$r^{\dagger}_{D,CB,n} = \begin{cases} \sqrt{1-\alpha}\, h_{AD,n}x_n + \sqrt{\alpha}\, h_{CB,n}y_n + w_{CB,n}, \text{ if } 1 \leq n \leq \Theta, & \text{(5.36a)} \\ \sqrt{1-\alpha}\, h_{AD,n}x_n + h_{CB,n}t_n + w_{CB,n}, \text{ if } \Theta+1 \leq n \leq L-\Theta, & \text{(5.36b)} \\ \sqrt{1-\beta^{\dagger}}\, h_{AD,n}x_n + \sqrt{\beta^{\dagger}}\, h_{CB,n}s_n + w_{CB,n}, \text{ if } L-\Theta+1 \leq n \leq L, & \text{(5.36c)} \end{cases}$$

where $\alpha = 1 - \Delta N_o$. Let $\upsilon_{n_1,CB}$, $\upsilon_{n_2,CB}$, and $\upsilon_{n_3,CB}$ denote the RVs corresponding to $|r^{\dagger}_{D,CB,n_1}|^2$, $|r^{\dagger}_{D,CB,n_2}|^2$, and $|r^{\dagger}_{D,CB,n_3}|^2$, respectively, such that $1 \leq n_1 \leq \Theta$, $\Theta + 1 \leq n_2 \leq L - \Theta$, and $L - \Theta + 1 \leq n_3 \leq L$. Thus, the RV corresponding to the average energy of L symbols on f_{CB}, denoted by $\mathcal{V}_{L,CB}$ is given as $\mathcal{V}_{L,CB} = \mathcal{V}_{L_1,CB} + \mathcal{V}_{L_2,CB} + \mathcal{V}_{L_3,CB}$, such that $\mathcal{V}_{L_1,CB} = \frac{1}{L}\sum_{n_1=1}^{\Theta} \upsilon_{n_1,CB}$, $\mathcal{V}_{L_2,CB} = \frac{1}{L}\sum_{n_2=\Theta+1}^{L-\Theta} \upsilon_{n_2,CB}$, and $\mathcal{V}_{L_3,CB} = \frac{1}{L}\sum_{n_3=L-\Theta+1}^{L} \upsilon_{n_3,CB}$. Using $\mathcal{V}_{L,CB}$, we formally define probability of miss-detection at Dave when measuring the average energy level on f_{CB}.

Definition 8. *Given $\mathcal{H}_1$ is true, probability of miss-detection when Dave measures the* *average energy level on f_{CB}, denoted by $\mathbf{P}^{3\phi}_{MD,CB}$, is given as follows*

$$\mathbf{P}^{3\phi}_{MD,CB} = \Pr\left(|\mathcal{V}_{L,CB} - \mathcal{E}_{CB}| \leq \nu_{CB}|\mathcal{H}_1 \textit{ true}\right).$$

Proposition 9. *When $N_o \ll 1$ and $\alpha = 1 - \Delta N_o$, the distributions of $\mathcal{V}_{L_1,CB}$ and $\mathcal{V}_{L_2,CB}$ are approximated as $\frac{1}{2^\Theta}\sum_{l=0}^{\Theta}\binom{\Theta}{l}\mathrm{G}\left(l, \frac{1}{L}\right)$ and $\frac{1}{2^{L-2\Theta}}\sum_{l=0}^{L-2\Theta}\binom{L-2\Theta}{l}\mathrm{G}\left(l, \frac{1}{L}\right)$, respectively. Thus, the distribution of $\frac{1}{L}\sum_{n=1}^{L-\Theta}|r^{\dagger}_{D,CB,n}|^2$ can be approximated as $\frac{1}{2^{L-\Theta}}\sum_{l=0}^{L-\Theta}\binom{L-\Theta}{l}\mathrm{G}\left(l, \frac{1}{L}\right)$.*

From Proposition 9, we observe that the distribution of $|r^{\dagger}_{D,CB,n}|^2$ is approximately same as that of the distribution of $|r_{D,CB,n}|^2$, for $1 \leq n \leq L - \Theta$. This indicates that, Charlie solely controls the energy level on f_{CB} for the first $L - \Theta$ symbols after implementing 3ϕ DASC-MF scheme. However, during Phase-III, i.e., $L - \Theta + 1 \leq n \leq L$, Alice and Charlie use the energy-splitting factor $\beta^{\dagger}$ away from 1, as shown in Table 5.3. Therefore, when Alice transmits a burst of zeros, the energy observed at Dave on f_{CB} is likely to be less than $\mathcal{E}_{CB}$, thereby resulting in higher probability of detection at Dave. Although, Alice and Charlie can choose to use $\beta^{\dagger}$ close to 1, this will increase the fraction of erroneous decisions of Alice's current symbols.

While we are able to derive the probability of detection on f_{AB}, we do not derive closed-form expressions on probability of detection on f_{CB}, due to intractable density function contributed by Phase-III of the 3ϕ DASC-MF. However, we present simulation results on detection in Sec. 5.6.3.

5.6.2 Covertness Analysis for ED when using SC-MAC Scheme

Along the similar lines of Sec. 5.6.1, in this section, we define the probability of miss-detection at Dave on f_{AB} and f_{CB}, when Alice and Charlie use SC-MAC.

Definition 9. *The probability of miss-detection by Dave's ED on f_{AB} and f_{CB} are denoted by, $\mathbf{P}^{MAC}_{MD,AB}$ and $\mathbf{P}^{MAC}_{MD,CB}$, respectively, where*

$$\mathbf{P}^{MAC}_{MD,AB} = \Pr\left(|\mathcal{W}_{L,AB} - \mathcal{E}_{AB}| \leq \nu_{AB}|\mathcal{H}_1 \textit{ true}\right)$$
$$\mathbf{P}^{MAC}_{MD,CB} = \Pr\left(|\mathcal{W}_{L,CB} - \mathcal{E}_{CB}| \leq \nu_{CB}|\mathcal{H}_1 \textit{ true}\right),$$

such that, $\mathcal{W}_{L,AB}$ and $\mathcal{W}_{L,CB}$ are the RVs denoting the average energy of L symbols

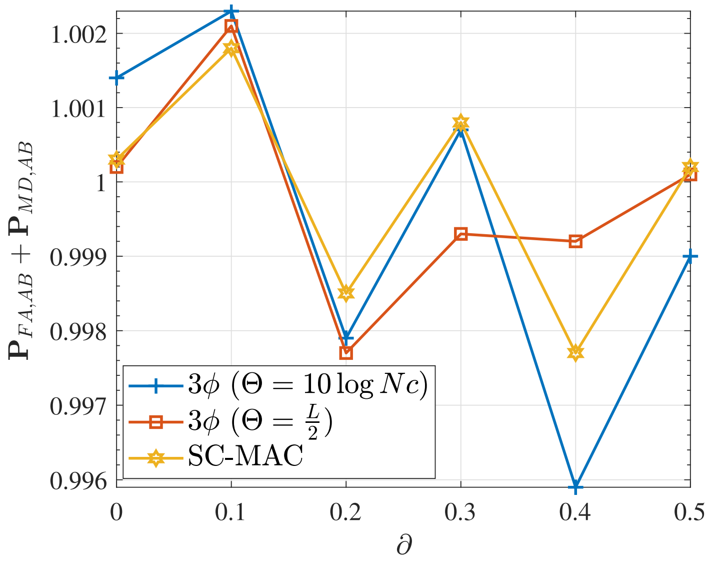

Figure 5.16: $\mathbf{P}_{FA,AB} + \mathbf{P}_{MD,AB}$ on f_{AB} as a function of ∂.

received at Dave on f_{AB} and f_{CB}, respectively.

The distributions of $\mathcal{W}_{L,AB}$ and $\mathcal{W}_{L,CB}$ can be computed along the similar lines of $\mathcal{V}_{L,AB}$ and $\mathcal{V}_{L,CB}$, respectively. It is worthwhile to note that, since the entire frame of L symbols is uncoordinated in energy, the sum $\mathbf{P}_{FA,AB} + \mathbf{P}^{MAC}_{MD,AB}$ and $\mathbf{P}_{FA,CB} + \mathbf{P}^{MAC}_{MD,CB}$ should be away from 1, indicating that Dave is more likely to detect SC-MAC as compared to 3ϕ DASC-MF scheme.

5.6.3 Simulation Results

In this section, we provide results to showcase the covertness of the proposed schemes. In addition to the parameters used in Sec. 5.4.5, we use $\nu_{AB} = \nu_{CB} = 10^{-3}$. In Fig. 5.16, we first plot $\mathbf{P}_{FA,AB} + \mathbf{P}_{MD,AB}$ for both the proposed schemes as a function of ∂ at SNR = 25 dB, and observe that the sum is close to 1 for the considered range of ∂. We also observe a similar behaviour in Fig. 5.17, where we plot $\mathbf{P}_{FA,CB} + \mathbf{P}_{MD,CB}$ for both the schemes. We note that, when $\Theta = \frac{L}{2}$, exactly $\frac{L}{2}$ symbols are transmitted in uncoordinated fashion, thus, $\mathbf{P}_{FA,CB} + \mathbf{P}_{MD,CB}$ is slightly higher than SC-MAC, where all the L symbols are uncoordinated in energy. However, since the 3ϕ DASC-MF scheme has minimum number of uncoordinated symbols, its $\mathbf{P}_{FA,CB} + \mathbf{P}_{MD,CB}$ is maximum and is close to 1 for all values of $\partial \in [0, 0.5]$.

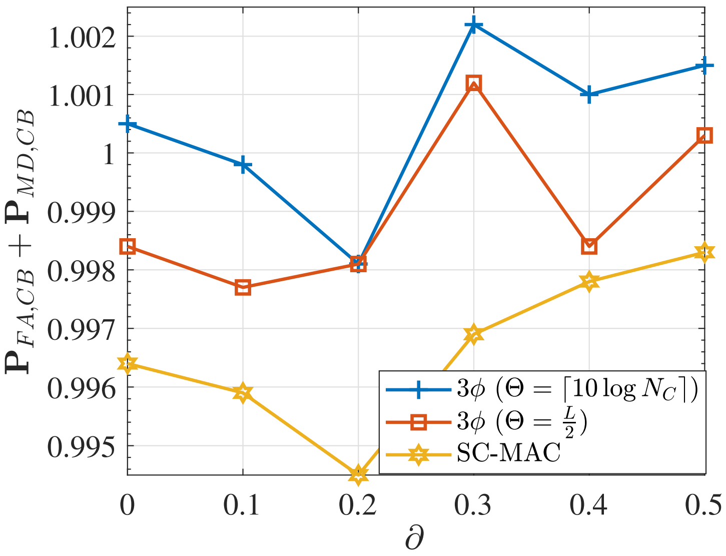

Figure 5.17: $\mathbf{P}_{FA,CB} + \mathbf{P}_{MD,CB}$ on f_{CB} as a function of ∂.

5.7 Chapter Summary

This chapter presented a delay aware cooperative framework to mitigate an FD reactive jammer. As a salient feature of this framework, the helper uses a practical FD radio to forward the victim's low-latency symbols to the destination. Here, the helper multiplexes the victim's symbols to its symbols to facilitate joint decoding at the destination. First the processing delay at the helper was modelled using a parameter, Θ and then it was shown that the symbols received from the two users arrive during different time slots at the destination, resulting in complex decoding. Further, it was also pointed out that the symbols from both the users are uncoordinated in energy, leading to detection by an energy detector at the adversary. To circumvent these problems, two mitigation schemes based on the delay parameter Θ were proposed. When $\Theta \leq \frac{L}{2}$, 3ϕ delay-aware semi-coherent multiplex-and-forward scheme was used, wherein the legitimate users transmit their symbols using two energy-splitting factors, α and β, and the destination decodes them in three-phases, parametrised by Θ. When $\Theta > \frac{L}{2}$, a semi-coherent multiple access channel scheme was proposed, wherein due to large Θ, the helper does not decode the victim's symbols, and the victim and the helper transmit their symbols to the destination using an energy-splitting factor, ε. For both the schemes, near-optimal solution on the energy-splitting factor to the optimisation problem of minimising the error rates was provided. Finally, it was shown that the victim reliably communicates with the destination while adhering to the latency constraints without getting detected by the adversary.

CHAPTER 6

CONCLUSION AND FUTURE WORK

Low-latency communication is at the heart of the next generation of wireless communication. Motivated by the recent developments in radio architectures, this thesis investigated mitigation schemes for reactive jamming attacks on low-latency communication. The adversary under consideration is a powerful full-duplex cognitive adversary capable of jamming and detecting pre-existing countermeasures, such as frequency hopping. To mitigate the full-duplex cognitive adversary, we proposed a framework of full-duplex strategies wherein the victim node seeks assistance from a nearby full-duplex node to multiplex-and-forward its symbols to the base station. Assuming various channel conditions between the helper and the base station, practical limitations of the radio architecture of the helper node, the location of the jammer, and the countermeasure detectors used by the jammer, we have shown that the proposed framework facilitates reliable low-latency communication between the victim and the helper node and also engages the adversary to the jammed band. To this end, the concluding remarks of this thesis are given in the next section.

6.1 Conclusion

In Chapter 3, we proposed semi-coherent fast-forward mitigation schemes to mitigate a full-duplex cognitive jammer capable of measuring the average energy levels on the jammed frequency band besides jamming it. Assuming the channel between the helper and the base station as slow-fading, semi-coherent fast-forward half-duplex and semi-coherent fast-forward full-duplex relaying schemes were proposed. Here, the helper node operated in half-duplex and full-duplex modes, respectively, subject to the location of the jammer w.r.t. the helper node. Assuming OOK at the victim and $M-$PSK at the helper node, for both the schemes, a joint maximum a posteriori decoder was formulated that jointly decoded the victim's and the helper's symbols at the base station. Using this decoder, near-optimal constellation designs for the victim and the helper were proposed. It was highlighted that, unlike the semi-coherent fast-forward half-duplex scheme, designing optimal constellations at the victim and the helper for the semi-coherent fast-forward full-duplex relaying scheme was non-trivial due to the use of the energy-splitting factor. An approximate joint maximum a posteriori decoder was proposed to circumvent the problem that computed a near-optimal value of the energy splitting factor. Finally, it was shown that the proposed schemes facilitate reliable, low-latency communication to the victim while successfully engaging the adversary in the jammed band.

Chapter 4 considered a more sophisticated adversary compared to the one in Chapter 3, wherein the full-duplex cognitive jammer scanned multiple frequency bands and estimated the correlation between the symbols on the jammed band and other frequency bands. Owing to a fast-fading channel between the helper and the base station, a non-coherent fast-forward full-duplex mitigation scheme was proposed, where the victim and the helper used OOK, and $M-$ary ASK signalling schemes, respectively. For this scheme, an optimization problem was formulated. Its solution provided the optimal constellations at the victim and the helper node that minimizes the joint error rates at the base station, subject to average energy constants at the victim and the helper node. Further, a delay-tolerant non-coherent fast-forward full-duplex mitigation scheme was also proposed, which solved the problem of designing constellations at the helper and the victim when the fast-forwarding at the helper node is imperfect. For both schemes, it was shown that using the proposed methods, the victim reliably communicates with the base station while successfully deceiving the countermeasure detectors at the adversary.

Unlike Chapter 3 and Chapter 4, Chapter 5 assumed a practical full-duplex helper, resulting in non-instantaneous multiplex and forward process at the helper. Although we assumed the signal model similar to that of Chapter 3, the attack model is much stronger as compared to Chapter 3 and Chapter 4. Here, the adversary scans all the frequency bands to measure the average energy level on all the frequency bands and estimates the correlation as described in Chapter 4. It was highlighted that due to the delay incurred by the helper node, the analysis given in Chapter 3 does not hold. Therefore, delay aware semi-coherent multiplex and forward mitigation scheme was proposed, wherein the delay was modelled at the helper node and then the problem of designing the optimal constellation at the victim and the helper node was solved that minimised the error rates at the base station. Through rigorous analysis and simulation results, it was shown that the proposed schemes facilitate the victim in evading the jamming attacks whilst deceiving the adversary.

6.2 Future Work

There are multiple directions for future work. Some interesting directions are enumerated as follows:

1. This thesis studied an uncoded setting, wherein the information symbols from both the victim and the helper nodes take statistically independent values. However, when one incorporates outer codes at both these nodes, temporal correlation across the transmitted symbols within one codeword is expected. Consequently, it is interesting to study the error performance and the covertness performance of the coded counterparts.
2. Designing non-coherent constellations when using practical full-duplex helper node is still an exiting direction for future work.
3. Throughout this thesis, it was assumed that the adversary can instantaneously sense and jam a specific frequency band. However, it will be interesting study the use of practical full-duplex radios at the adversary as well.
4. In the model considered hitherto the adversary constantly uses his energy to jam victim-to-base station link. However, the adversary can save its energy by attacking in bursts, this is known as sporadic attack. In this attack model, the base station will have to monitor the received symbols on both frequencies and use the channel knowledge to maximise the error performance.

REFERENCES

[1] S. K. Sharma, T. E. Bogale, L. B. Le, S. Chatzinotas, X. Wang, and B. Ottersten, "Dynamic spectrum sharing in 5G wireless networks with full-duplex technology: Recent advances and research challenges," *IEEE Communications Surveys & Tutorials*, vol. 20, no. 1, pp. 674–707, 2018.

[2] I. F. Akyildiz, W.-Y. Lee, M. C. Vuran, and S. Mohanty, "Next generation/dynamic spectrum access/cognitive radio wireless networks: A survey," *Computer Networks*, vol. 50, no. 13, pp. 2127–2159, 2006.

[3] M. T. Masonta, M. Mzyece, and N. Ntlatlapa, "Spectrum decision in cognitive radio networks: A survey," *IEEE Communications Surveys & Tutorials*, vol. 15, no. 3, pp. 1088–1107, 2013.

[4] C. Condo, V. Bioglio, H. Hafermann, and I. Land, "Practical product code construction of polar codes," *IEEE Transactions on Signal Processing*, vol. 68, pp. 2004–2014, 2020.

[5] V. Bioglio, C. Condo, and I. Land, "Design of polar codes in 5G new radio," *IEEE Communications Surveys & Tutorials*, vol. 23, no. 1, pp. 29–40, 2021.

[6] M. A. Albreem, M. Juntti, and S. Shahabuddin, "Massive MIMO detection techniques: A survey," *IEEE Communications Surveys & Tutorials*, vol. 21, no. 4, pp. 3109–3132, 2019.

[7] E. Björnson and L. Sanguinetti, "Scalable cell-free massive MIMO systems," *IEEE Transactions on Communications*, vol. 68, no. 7, pp. 4247–4261, 2020.

[8] L. Liu and W. Yu, "Massive connectivity with massive MIMO—part ii: Achievable rate characterization," *IEEE Transactions on Signal Processing*, vol. 66, no. 11, pp. 2947–2959, 2018.

[9] A. Goyal and K. Kumar, "LTE-advanced carrier aggregation for enhancement of bandwidth," in *Advances in VLSI, Communication, and Signal Processing*. Springer, 2020, pp. 341–351.

[10] X. Wang, L. Kong, F. Kong, F. Qiu, M. Xia, S. Arnon, and G. Chen, "Millimeter wave communication: A comprehensive survey," *IEEE Communications Surveys & Tutorials*, vol. 20, no. 3, pp. 1616–1653, 2018.

[11] X. Chen, G. Liu, Z. Ma, X. Zhang, P. Fan, S. Chen, and F. R. Yu, "When full-duplex wireless meets non-orthogonal multiple access: Opportunities and challenges," *IEEE Wireless Communications*, vol. 26, no. 4, pp. 148–155, 2019.

[12] A. Jee, K. Agrawal, and S. Prakriya, "A coordinated direct AF/DF relay-aided NOMA framework for low outage," *IEEE Transactions on Communications*, vol. 70, no. 3, pp. 1559–1579, 2022.

[13] C. E. Shannon, "A mathematical theory of communication," *The Bell System Technical Journal*, vol. 27, no. 3, pp. 379–423, 1948.

[14] 3GPP, "Service requirements for the 5g system," *3rd Generation Partnership Project (3GPP), Technical Specification (TS) 22.261*, 2019.

[15] M. E. Morocho-Cayamcela, H. Lee, and W. Lim, “Machine learning for 5g/b5g mobile and wireless communications: Potential, limitations, and future directions,” *IEEE Access*, vol. 7, pp. 137 184–137 206, 2019.

[16] M. Lichtman, R. P. Jover, M. Labib, R. Rao, V. Marojevic, and J. H. Reed, “LTE/LTE-A jamming, spoofing, and sniffing: Threat assessment and mitigation,” *IEEE Communications Magazine*, vol. 54, no. 4, pp. 54–61, 2016.

[17] M. Vanhoef and F. Piessens, “Advanced Wi-Fi attacks using commodity hardware,” in *Proceedings of the 30th Annual Computer Security Applications Conference*, ser. ACSAC ’14, 2014, p. 256–265.

[18] V. Navda, A. Bohra, S. Ganguly, and D. Rubenstein, “Using channel hopping to increase 802.11 resilience to jamming attacks,” in *IEEE INFOCOM 2007 - 26th IEEE International Conference on Computer Communications*, 2007, pp. 2526–2530.

[19] J. Jeung, S. Jeong, and J. Lim, “Adaptive rapid channel-hopping scheme mitigating smart jammer attacks in secure WLAN,” in *2011 - MILCOM 2011 Military Communications Conference*, 2011, pp. 1231–1236.

[20] Y. Liu and P. Ning, “Bittrickle: Defending against broadband and high-power reactive jamming attacks,” in *2012 Proceedings IEEE INFOCOM*, 2012, pp. 909–917.

[21] T. Karhima, A. Silvennoinen, M. Hall, and S.-G. Haggman, “Ieee 802.11b/g wlan tolerance to jamming,” in *IEEE MILCOM 2004. Military Communications Conference, 2004.*, vol. 3, 2004, pp. 1364–1370 Vol. 3.

[22] I. Harjula, J. Pinola, and J. Prokkola, “Performance of ieee 802.11 based WLAN devices under various jamming signals,” in *2011 - MILCOM 2011 Military Communications Conference*, 2011, pp. 2129–2135.

[23] S. Bandaru, “Investigating the effect of jamming attacks on wireless LANS,” *International Journal of Computer Applications*, vol. 99, pp. 5–9, 08 2014.

[24] Q. Yan, H. Zeng, T. Jiang, M. Li, W. Lou, and Y. T. Hou, “Jamming resilient communication using MIMO interference cancellation,” *IEEE Transactions on Information Forensics and Security*, vol. 11, no. 7, pp. 1486–1499, 2016.

[25] ——, “MIMO-based jamming resilient communication in wireless networks,” in *IEEE INFOCOM 2014 - IEEE Conference on Computer Communications*, 2014, pp. 2697–2706.

[26] W. Shen, P. Ning, X. He, H. Dai, and Y. Liu, “MCR decoding: A MIMO approach for defending against wireless jamming attacks,” in *2014 IEEE Conference on Communications and Network Security*, 2014, pp. 133–138.

[27] H. Zeng, C. Cao, H. Li, and Q. Yan, “Enabling jamming-resistant communications in wireless MIMO networks,” in *2017 IEEE Conference on Communications and Network Security (CNS)*, 2017, pp. 1–9.

[28] A. Malla and R. K. Sahu, “Security attacks with an effective solution for DOS attacks in VANET,” *International Journal of Computer Applications*, vol. 66, pp. 975–8887, 04 2013.

[29] X. Lu, D. Xu, L. Xiao, L. Wang, and W. Zhuang, “Anti-jamming communication game for UAV-aided VANETs,” in *GLOBECOM 2017 - 2017 IEEE Global Communications Conference*, 2017, pp. 1–6.

[30] H. Li and Z. Han, "Dogfight in spectrum: Jamming and anti-jamming in multichannel cognitive radio systems," in *GLOBECOM 2009 - 2009 IEEE Global Telecommunications Conference*, 2009, pp. 1–6.

[31] M. Jo, L. Han, D. Kim, and H. P. In, "Selfish attacks and detection in cognitive radio Ad-Hoc networks," *IEEE Network*, vol. 27, no. 3, pp. 46–50, 2013.

[32] D. Lentner and G. Kramer, "Stealth communication with vanishing power over binary symmetric channels," in *2020 IEEE International Symposium on Information Theory (ISIT)*, 2020, pp. 822–827.

[33] V. Chaudhary and J. Harshan, "Fast-forward relaying scheme to mitigate jamming attacks by full-duplex radios," 2020. [Online]. Available: https://arxiv.org/abs/2004.08898

[34] ——, "Fast-forward relaying scheme to mitigate jamming attacks by full-duplex radios," in *2020 IEEE 31st Annual International Symposium on Personal, Indoor and Mobile Radio Communications*, 2020, pp. 1–7.

[35] V. Chaudhary and H. Jagadeesh, "Fast-forward mitigation schemes for cognitive adversary," *IEEE Transactions on Cognitive Communications and Networking*, vol. 7, no. 4, pp. 1304–1319, 2021.

[36] V. Chaudhary and J. Harshan, "Non-coherent fast-forward relays for full-duplex jamming attack," 2021. [Online]. Available: https://arxiv.org/abs/2104.13583

[37] ——, "Non-coherent fast-forward relays for full-duplex jamming attack," in *2021 IEEE Global Communications Conference (GLOBECOM)*, 2021, pp. 1–6.

[38] ——, "Constellation design for non-coherent fast-forward relays to mitigate full-duplex jamming attacks," 2022. [Online]. Available: https://arxiv.org/abs/2205.13198

[39] ——, "Whisper when under attack: Delay tolerant fast-forward relays against full-duplex jamming," in *2022 14th International Conference on COMmunication Systems & NETworkS (COMSNETS)*, 2022, pp. 163–171.

[40] V. Chaudhary and H. Jagadeesh, "Constellation design for non-coherent fast-forward relays to mitigate full-duplex jamming attacks," *IEEE Transactions on Communications*, vol. 70, no. 7, pp. 4755–4770, 2022.

[41] K. Pelechrinis, M. Iliofotou, and S. V. Krishnamurthy, "Denial of service attacks in wireless networks: The case of jammers," *IEEE Communications Surveys & Tutorials*, vol. 13, no. 2, pp. 245–257, 2011.

[42] T. X. Brown, J. E. James, and A. Sethi, "Jamming and sensing of encrypted wireless ad hoc networks," in *Proceedings of the 7th ACM International Symposium on Mobile Ad Hoc Networking and Computing*, ser. MobiHoc '06, 2006, p. 120–130.

[43] W. Xu, W. Trappe, Y. Zhang, and T. Wood, "The feasibility of launching and detecting jamming attacks in wireless networks," in *Proceedings of the 6th ACM International Symposium on Mobile Ad Hoc Networking and Computing*, ser. MobiHoc '05. Association for Computing Machinery, 2005, p. 46–57.

[44] D. Torrieri, "Frequency hopping with multiple frequency-shift keying and hard decisions," *IEEE Transactions on Communications*, vol. 32, no. 5, pp. 574–582, 1984.

[45] R. Gummadi, D. Wetherall, B. Greenstein, and S. Seshan, "Understanding and mitigating the impact of rf interference on 802.11 networks," *SIGCOMM Computer Communications Review*, vol. 37, no. 4, p. 385–396, aug 2007.

[46] O. Besson, P. Stoica, and Y. Kamiya, “Direction finding in the presence of an intermittent interference,” *IEEE Transactions on Signal Processing*, vol. 50, no. 7, pp. 1554–1564, 2002.

[47] E. Lance and G. Kaleh, “A diversity scheme for a phase-coherent frequency-hopping spread-spectrum system,” *IEEE Transactions on Communications*, vol. 45, no. 9, pp. 1123–1129, 1997.

[48] L. Freitag, M. Stojanovic, S. Singh, and M. Johnson, “Analysis of channel effects on direct-sequence and frequency-hopped spread-spectrum acoustic communication,” *IEEE Journal of Oceanic Engineering*, vol. 26, no. 4, pp. 586–593, 2001.

[49] W. Xu, W. Trappe, Y. Zhang, and T. Wood, “The feasibility of launching and detecting jamming attacks in wireless networks,” in *Proceedings of the 6th ACM International Symposium on Mobile Ad Hoc Networking and Computing*, ser. MobiHoc ’05, 2005, p. 46–57.

[50] Z. Liu, H. Liu, W. Xu, and Y. Chen, “An error-minimizing framework for localizing jammers in wireless networks,” *IEEE Transactions on Parallel and Distributed Systems*, vol. 25, no. 2, pp. 508–517, 2014.

[51] X. Liu, G. Noubir, R. Sundaram, and S. Tan, “Spread: Foiling smart jammers using multi-layer agility,” in *IEEE INFOCOM 2007 - 26th IEEE International Conference on Computer Communications*, 2007, pp. 2536–2540.

[52] J. I. Choi, M. Jain, K. Srinivasan, P. Levis, and S. Katti, “Achieving single channel, full duplex wireless communication,” in *Proceedings of the Sixteenth Annual International Conference on Mobile Computing and Networking*, ser. MobiCom ’10, 2010, p. 1–12.

[53] M. Duarte and A. Sabharwal, “Full-duplex wireless communications using off-the-shelf radios: Feasibility and first results,” in *2010 Conference Record of the Forty Fourth Asilomar Conference on Signals, Systems and Computers*, 2010, pp. 1558–1562.

[54] M. Jain, J. I. Choi, T. Kim, D. Bharadia, S. Seth, K. Srinivasan, P. Levis, S. Katti, and P. Sinha, “Practical, real-time, full duplex wireless,” in *Proceedings of the 17th Annual International Conference on Mobile Computing and Networking*, ser. MobiCom ’11, 2011, p. 301–312.

[55] Y. Pan, C. Zhou, G. Cui, W. Wang, and X. Li, “Self-interference cancellation with RF impairments suppression for full-duplex systems,” in *2015 IEEE 82nd Vehicular Technology Conference (VTC2015-Fall)*, 2015, pp. 1–5.

[56] A. Masmoudi and T. Le-Ngoc, “Residual self-interference after cancellation in full-duplex systems,” in *2014 IEEE International Conference on Communications (ICC)*, 2014, pp. 4680–4685.

[57] D. Bharadia, E. McMilin, and S. Katti, “Full duplex radios,” *SIGCOMM Comput. Commun. Rev.*, vol. 43, no. 4, p. 375–386, aug 2013.

[58] E. Everett, M. Duarte, C. Dick, and A. Sabharwal, “Empowering full-duplex wireless communication by exploiting directional diversity,” in *2011 Conference Record of the Forty Fifth Asilomar Conference on Signals, Systems and Computers (ASILOMAR)*, 2011, pp. 2002–2006.

[59] M. Chung, M. S. Sim, J. Kim, D. K. Kim, and C.-b. Chae, “Prototyping real-time full duplex radios,” *IEEE Communications Magazine*, vol. 53, no. 9, pp. 56–63, 2015.

[60] E. Aryafar *et al.*, "MIDU: Enabling MIMO full-duplex," in *Proceedings of the 18th Annual International Conference on Mobile Computing and Networking*, ser. Mobicom '12, 2012, p. 257–268.

[61] E. Everett, A. Sahai, and A. Sabharwal, "Passive self-interference suppression for full-duplex infrastructure nodes," *IEEE Transactions on Wireless Communications*, vol. 13, no. 2, pp. 680–694, 2014.

[62] M. A. Khojastepour *et al.*, "The case for antenna cancellation for scalable full-duplex wireless communications," ser. HotNets-X, 2011.

[63] A. Sahai, G. Patel, and A. Sabharwal, "Pushing the limits of full-duplex: Design and real-time implementation," 2011. [Online]. Available: https://arxiv.org/abs/1107.0607

[64] M. Duarte, C. Dick, and A. Sabharwal, "Experiment-driven characterization of full-duplex wireless systems," *IEEE Transactions on Wireless Communications*, vol. 11, no. 12, pp. 4296–4307, 2012.

[65] M. Duarte, A. Sabharwal, V. Aggarwal, R. Jana, K. K. Ramakrishnan, C. W. Rice, and N. K. Shankaranarayanan, "Design and characterization of a full-duplex multiantenna system for WiFi networks," *IEEE Transactions on Vehicular Technology*, vol. 63, no. 3, pp. 1160–1177, 2014.

[66] D. W. Bliss, P. A. Parker, and A. R. Margetts, "Simultaneous transmission and reception for improved wireless network performance," in *2007 IEEE/SP 14th Workshop on Statistical Signal Processing*, 2007, pp. 478–482.

[67] J. Sangiamwong *et al.*, "Joint multi-filter design for full-duplex MU-MIMO relaying," in *VTC Spring 2009 - IEEE 69th Vehicular Technology Conference*, 2009, pp. 1–5.

[68] P. Lioliou, M. Viberg, M. Coldrey, and F. Athley, "Self-interference suppression in full-duplex MIMO relays," in *2010 Conference Record of the Forty Fourth Asilomar Conference on Signals, Systems and Computers*, 2010, pp. 658–662.

[69] T. Riihonen, A. Balakrishnan, K. Haneda, S. Wyne, S. Werner, and R. Wichman, "Optimal eigenbeamforming for suppressing self-interference in full-duplex MIMO relays," in *2011 45th Annual Conference on Information Sciences and Systems*, 2011, pp. 1–6.

[70] B. P. Day, A. R. Margetts, D. W. Bliss, and P. Schniter, "Full-duplex bidirectional MIMO: Achievable rates under limited dynamic range," *IEEE Transactions on Signal Processing*, vol. 60, no. 7, pp. 3702–3713, 2012.

[71] ——, "Full-duplex MIMO relaying: Achievable rates under limited dynamic range," *IEEE Journal on Selected Areas in Communications*, vol. 30, no. 8, pp. 1541–1553, 2012.

[72] T. Riihonen, S. Werner, and R. Wichman, "Mitigation of loopback self-interference in full-duplex MIMO relays," *IEEE Transactions on Signal Processing*, vol. 59, no. 12, pp. 5983–5993, 2011.

[73] T. Schenk, *RF Imperfections in High-Rate Wireless Systems: Impact and Digital Compensation*, 1st ed. Springer Publishing Company, Incorporated, 2008.

[74] L. Anttila, D. Korpi, V. Syrjälä, and M. Valkama, "Cancellation of power amplifier induced nonlinear self-interference in full-duplex transceivers," in *2013 Asilomar Conference on Signals, Systems and Computers*, 2013, pp. 1193–1198.

[75] E. Ahmed, A. M. Eltawil, and A. Sabharwal, "Self-interference cancellation with nonlinear distortion suppression for full-duplex systems," in *2013 Asilomar Conference on Signals, Systems and Computers*, 2013, pp. 1199–1203.

[76] D. Bharadia and S. Katti, "FastForward: Fast and constructive full duplex relays," vol. 44, no. 4, p. 199–210, aug 2014.

[77] K. G. Shin, H. Kim, A. W. Min, and A. Kumar, "Cognitive radios for dynamic spectrum access: From concept to reality," *IEEE Wireless Communications*, vol. 17, no. 6, pp. 64–74, 2010.

[78] S. Bhattarai, J.-M. J. Park, B. Gao, K. Bian, and W. Lehr, "An overview of dynamic spectrum sharing: Ongoing initiatives, challenges, and a roadmap for future research," *IEEE Transactions on Cognitive Communications and Networking*, vol. 2, no. 2, pp. 110–128, 2016.

[79] "Broadcasting strategies for cognitive radio networks: Taxonomy, issues, and open challenges," *Computers & Electrical Engineering*, vol. 52, pp. 349–361, 2016.

[80] J. Mitola, "Cognitive radio for flexible mobile multimedia communications," in *1999 IEEE International Workshop on Mobile Multimedia Communications (MoMuC'99) (Cat. No.99EX384)*, 1999, pp. 3–10.

[81] J. M. Iii, "Cognitive radio: An integrated agent architecture for software defined radio," 2000.

[82] C. R. Stevenson, G. Chouinard, Z. Lei, W. Hu, S. J. Shellhammer, and W. Caldwell, "Ieee 802.22: The first cognitive radio wireless regional area network standard," *IEEE Communications Magazine*, vol. 47, no. 1, pp. 130–138, 2009.

[83] Y. Zeng, Y.-C. Liang, A. T. Hoang, and R. Zhang, "A review on spectrum sensing for cognitive radio: Challenges and solutions," *EURASIP journal on advances in signal processing*, vol. 2010, pp. 1–15, 2010.

[84] I. F. Akyildiz, W.-y. Lee, M. C. Vuran, and S. Mohanty, "A survey on spectrum management in cognitive radio networks," *IEEE Communications Magazine*, vol. 46, no. 4, pp. 40–48, 2008.

[85] M. Deng, B.-J. Hu, and X. Li, "Adaptive weighted sensing with simultaneous transmission for dynamic primary user traffic," *IEEE Transactions on Communications*, vol. 65, no. 3, pp. 992–1004, 2017.

[86] J. Jia, Q. Zhang, and X. S. Shen, "Hc-mac: A hardware-constrained cognitive MAC for efficient spectrum management," *IEEE Journal on Selected Areas in Communications*, vol. 26, no. 1, pp. 106–117, 2008.

[87] Q. Zhao, L. Tong, A. Swami, and Y. Chen, "Decentralized cognitive MAC for opportunistic spectrum access in ad hoc networks: A POMDP framework," *IEEE Journal on Selected Areas in Communications*, vol. 25, no. 3, pp. 589–600, 2007.

[88] M.-L. Ku, W. Li, Y. Chen, and K. J. Ray Liu, "Advances in energy harvesting communications: Past, present, and future challenges," *IEEE Communications Surveys & Tutorials*, vol. 18, no. 2, pp. 1384–1412, 2016.

[89] J. Harshan and Y.-C. Hu, "Cognitive radio from hell: Flipping attack on direct-sequence spread spectrum," in *2018 IEEE Wireless Communications and Networking Conference (WCNC)*, 2018, pp. 1–6.

[90] H. Jagadeesh and Y.-C. Hu, "Convolution attack on frequency hopping by full-duplex radios," *IEEE Transactions on Vehicular Technology*, vol. 68, no. 6, pp. 5642–5656, 2019.

[91] M. K. Hanawal, D. N. Nguyen, and M. Krunz, “Cognitive networks with in-band full-duplex radios: Jamming attacks and countermeasures,” *IEEE Transactions on Cognitive Communications and Networking*, vol. 6, no. 1, pp. 296–309, 2020.

[92] A. Sabharwal, P. Schniter, D. Guo, D. W. Bliss, S. Rangarajan, and R. Wichman, “In-band full-duplex wireless: Challenges and opportunities,” *IEEE Journal on selected areas in communications*, vol. 32, no. 9, pp. 1637–1652, 2014.

[93] A. Sahai, G. Patel, C. Dick, and A. Sabharwal, “Understanding the impact of phase noise on active cancellation in wireless full-duplex,” in *2012 Conference Record of the Forty Sixth Asilomar Conference on Signals, Systems and Computers (ASILOMAR)*, 2012, pp. 29–33.

[94] N. H. Mahmood, I. S. Ansari, G. Berardinelli, P. Mogensen, and K. A. Qaraqe, “Analysing self interference cancellation in full-duplex radios,” in *2016 IEEE Wireless Communications and Networking Conference*, 2016, pp. 1–6.

[95] S. Akbar, Y. Deng, A. Nallanathan, M. Elkashlan, and G. K. Karagiannidis, “Massive multiuser MIMO in heterogeneous cellular networks with full duplex small cells,” *IEEE Transactions on Communications*, vol. 65, no. 11, pp. 4704–4719, 2017.

[96] X. Tian, Z. Tian, K. Pham, E. Blasch, and D. Shen, “Jamming/anti-jamming game with a cognitive jammer in space communication,” in *2012 SPIE Sensors and Systems for Space Applications V*, vol. 8385, 2012, pp. 194 – 203.

[97] Y. Liao, T. Wang, L. Song, and Z. Han, “Listen-and-talk: Protocol design and analysis for full-duplex cognitive radio networks,” *IEEE Transactions on Vehicular Technology*, vol. 66, no. 1, pp. 656–667, 2016.

[98] D. Li, J. Cheng, and V. C. Leung, “Adaptive spectrum sharing for half-duplex and full-duplex cognitive radios: From the energy efficiency perspective,” *IEEE Transactions on Communications*, vol. 66, no. 11, pp. 5067–5080, 2018.

[99] V. Towhidlou and M. Shikh-Bahaei, “Adaptive full-duplex communications in cognitive radio networks,” *IEEE Transactions on Vehicular Technology*, vol. 67, no. 9, pp. 8386–8395, 2018.

[100] W. Xiong, Y. Yao, X. Fu, and S. Li, “Covert communication with cognitive jammer,” *IEEE Wireless Communications Letters*, pp. 1–1, 2020.

[101] J. Xu, L. Duan, and R. Zhang, “Proactive eavesdropping via cognitive jamming in fading channels,” *IEEE Transactions on Wireless Communications*, vol. 16, no. 5, pp. 2790–2806, 2017.

[102] G. Zheng, I. Krikidis, J. Li, A. P. Petropulu, and B. Ottersten, “Improving physical layer secrecy using full-duplex jamming receivers,” *IEEE Transactions on Signal Processing*, vol. 61, no. 20, pp. 4962–4974, 2013.

[103] X. Hu, C. Kai, Z. Guo, and J. Gao, “A fast forward full-duplex cooperative relay scheme for securing wireless communications,” *IEEE Signal Processing Letters*, vol. 26, no. 5, pp. 775–779, 2019.

[104] 3GPP TS38.211, “NR: Physical channels and modulation,” v15.3.0, Sept.2018.

[105] N. Zlatanov, E. Sippel, V. Jamali, and R. Schober, “Capacity of the gaussian two-hop full-duplex relay channel with residual self-interference,” *IEEE Transactions on Communications*, vol. 65, no. 3, pp. 1005–1021, 2017.

[106] A. Behboodi, A. Chaaban, R. Mathar, and M. Alouini, “On full duplex gaussian relay channels with self-interference,” in *2016 IEEE International Symposium on Information Theory (ISIT)*, 2016, pp. 1864–1868.

[107] R. Yazdani and M. Ardakani, “Efficient LLR calculation for non-binary modulations over fading channels,” *IEEE transactions on communications*, vol. 59, no. 5, pp. 1236–1241, 2011.

[108] G. E. Corazza and G. Ferrari, “New bounds for the marcum Q-function,” *IEEE Transactions on Information Theory*, vol. 48, no. 11, pp. 3003–3008, 2002.

[109] M. W. Hirsch and S. Smale, “On algorithms for solving f(x)=0,” *Communications on Pure and Applied Mathematics*, vol. 32, no. 3, pp. 281–312, 1979.

[110] R. K. Mallik and R. D. Murch, “Noncoherent reception of multi-level ASK in Rayleigh fading with receive diversity,” *IEEE Transactions on Communications*, vol. 62, no. 1, pp. 135–143, 2014.

[111] M. Chowdhury, A. Manolakos, and A. J. Goldsmith, “Design and performance of noncoherent massive SIMO systems,” in *2014 48th Annual Conference on Information Sciences and Systems (CISS)*, 2014, pp. 1–6.

[112] A. Manolakos, M. Chowdhury, and A. Goldsmith, “Energy-based modulation for noncoherent massive SIMO systems,” *IEEE Transactions on Wireless Communications*, vol. 15, no. 11, pp. 7831–7846, 2016.

[113] S. Li, J.-K. Zhang, and X. Mu, “Design of optimal noncoherent constellations for SIMO systems,” *IEEE Transactions on Communications*, vol. 67, no. 8, pp. 5706–5720, 2019.

[114] X.-C. Gao, J.-K. Zhang, H. Chen, Z. Dong, and B. Vucetic, “Energy-efficient and low-latency massive SIMO using non-coherent ML detection for industrial IoT communications,” *IEEE Internet of Things Journal*, vol. 6, no. 4, pp. 6247–6261, 2019.

[115] S. Li, Z. Dong, H. Chen, and X. Guo, “Constellation design for non-coherent massive SIMO systems in URLLC applications,” *IEEE Transactions on Communications*, vol. 69, no. 7, pp. 4387–4401, 2021.

[116] M. Chowdhury, A. Manolakos, and A. Goldsmith, “Scaling laws for non-coherent energy-based communications in the SIMO MAC,” *IEEE Transactions on Information Theory*, vol. 62, no. 4, pp. 1980–1992, 2016.

[117] K.-H. Ngo, S. Yang, M. Guillaud, and A. Decurninge, “Joint constellation design for the two-user non-coherent multiple-access channel,” 2020. [Online]. Available: https://arxiv.org/abs/2001.04970

[118] R. P. Jover *et al.*, “Enhancing the security of LTE networks against jamming attacks,” *EURASIP Journal on Information Security*, vol. 2014, no. 1, pp. 1–14, 2014.

[119] A. Kraskov, H. Stögbauer, and P. Grassberger, “Estimating mutual information,” *Phys. Rev. E*, vol. 69, p. 066138, Jun 2004.

[120] D. Bharadia and S. Katti, “Full duplex MIMO radios,” in *11th USENIX Symposium on Networked Systems Design and Implementation (NSDI 14)*. USENIX Association, Apr. 2014, pp. 359–372.

[121] J. G. Proakis and M. Salehi, *Digital Communications*. McGraw-Hill Higher Education, 5th expanded ed., 2007.